Title

From Cores to Envelopes to Disks: A Multi-scale View of Magnetized Star Formation

Author

Hull, Charles Lindsay Hopkins

Publication Date

2014

From Cores to Envelopes to Disks: A Multi-scale View of Magnetized Star Formation

by

Charles Lindsay Hopkins Hull

A dissertation submitted in partial satisfaction of the
requirements for the degree of
Doctor of Philosophy

in

Astrophysics

in the

Graduate Division

of the

University of California, Berkeley

Committee in charge:

Dr. Richard Plambeck, Chair
Professor Christopher McKee
Professor Carl Heiles
Professor Adrian Lee

Fall 2014

From Cores to Envelopes to Disks: A Multi-scale View of Magnetized Star Formation

Abstract

From Cores to Envelopes to Disks: A Multi-scale View of Magnetized Star Formation

by

Charles Lindsay Hopkins Hull
Doctor of Philosophy in Astrophysics

University of California, Berkeley

Dr. Richard Plambeck, Chair

Observations of polarization in star forming regions have been made across many wavelengths, many size scales, and many stages of stellar evolution. One of the overarching goals of these observations has been to determine the importance of magnetic fields—which are the cause of the polarization—in the star formation process. We begin by describing the commissioning and the calibration of the 1.3 mm dual-polarization receiver system we built for CARMA (the Combined Array for Research in Millimeter-wave Astronomy), a radio telescope in the eastern Sierra region of California. One of the primary science drivers behind the polarization system is to observe polarized thermal emission from dust grains in the dense clumps of dust and gas where the youngest, Class 0 protostars are forming. We go on to describe the CARMA TADPOL survey—the largest high-resolution (~ 1000 AU scale) survey to date of dust polarization in low-mass protostellar cores—and discuss our main findings: (1) Magnetic fields (B-fields) on scales of $\sim$1000 AU are not tightly aligned with protostellar outflows. Rather, the data are consistent both with scenarios where outflows and magnetic fields are preferentially misaligned (perpendicular) and where they are randomly aligned. (2) Sources with high CARMA polarization fractions have consistent B-field orientations on large scales ($\sim 20''$, measured using single-dish submillimeter telescopes) and small scales ($\sim 2.5''$, measured by CARMA). We interpret this to mean that in at least some cases B-fields play a role in regulating the infall of material all the way down to the ~ 1000 AU scales of protostellar envelopes. Finally, (3) While on the whole outflows appear to be randomly aligned with B-fields, in sources with low polarization fractions there is a hint that outflows are preferentially perpendicular to small-scale B-fields, which suggests that in these sources the fields have been wrapped up by envelope rotation. This work shows that the ~ 1000 AU protostellar envelope may be a turning point: at larger scales B-fields may still retain the memory of the global B-field drawn in from the ambient medium; but at smaller scales the B-fields may be affected by the dynamics of both envelope and disk rotation. This sets the stage for ALMA (the Atacama Large Millimeter/submillimeter Array), which will soon reveal the morphology of B-fields in circumstellar disks themselves.

For Anna.

Contents

List of Figures

Acknowledgments

It has been an amazing six years, and there are so many people to thank. I think it's appropriate to begin with the largest group of people to whom I am indebted: the American taxpayers. The majority of the funding that made the last six years possible came from the National Science Foundation. The NSF Graduate Research Fellowship paid my salary for half of my time at Berkeley, and the CARMA NSF grant not only allowed me to travel regularly to my beloved CARMA and paid me in my final year, but also gave me the opportunity to travel far and wide to present my results. The experience of sharing in scientific camaraderie all over the U.S. and the world has been absolutely incredible. Thank you.

I also owe thanks to UC Berkeley donors and California taxpayers for the UC Berkeley Chancellor's Fellowship, and to the Ford Foundation both for the Dissertation Fellowship and for introducing me to the charismatic and high-powered community of Ford Fellows.

Thank you to the Berkeley Astronomy Department, which has been a wonderfully lively place to work for six years; to Nina Ruymaker, Barb Hoversten, Rayna Helgens, and the rest of the department and RES staff for keeping things humming along; and to Dexter Stewart, for shepherding us through the unfathomably complicated path to graduation (and for calling in favors for us more than a few times!).

Thank you to the members of the Radio Astronomy Laboratory—the faculty, staff, and students both present and past—for teaching me everything I know about radio astronomy. Amber Bauermeister, Statia Cook, Peter "Pedro" Williams, James McBride, Geoff Bower, Mel Wright, Dave MacMahon, Calvin Cheng, Daning Chow, Leo Blitz...I'm so glad I chose to be a radio astronomer. How exactly I made the choice is unclear, but I think it was soon after Geoff Bower informed me of the apparently undisputed fact that radio astronomers are the coolest.

Thank you to Carl Heiles: for the great advice, for the long chats when you always had so much work to do, for writing me countless letters of recommendation, and for pushing me to do things the right way.

Thank you to Jonnie Pober for being a glorious radio compadre, and for getting up early to watch the Bills lose way too many times.

Thank you to my unfailingly supportive, hilarious, and humble officemate Mike McCourt for six years of excellence: pretty much everything I know about computers I learned from you. Not to mention all of the depressing stereotypes about New York City culture that I've discovered by wallowing in the *New Yorker* comics with you every day—Sad Hour to the max! Don't worry, the East Coast won't be that bad.

Thank you to the great people of CARMA: each and every one of you made observing a joy. It was fun, exhilarating, and an incredible learning experience. Thanks in particular to those who helped make the CARMA polarization system possible: James Lamb, Michael Laxen, Mark Hodges, Dave Hawkins, Dave Woody (thanks for the letters!), Andy Beard, Ira Snyder, Steve Scott, Kevin Rauch, Doug Friedel, Marc Pound, Peter Teuben, Lisa Xu, and everyone else on the maintenance crew and in the hardware, software and correlator groups. And thanks to the other heroes of CARMA: Nikolaus Volgenau, John Carpenter, Mary Daniel, Curt Giovanine (and his sister Teri, who saved me with an emergency chiropractic visit), Paul Rasmussen (who saved me during the December 2010 blizzard right after Teri saved me), Steve Miller, Michael Cooper, Andres Rizo, Ron Lawrence, Lori McGraw and Terry Sepsey (we'll miss you), and last but most definitely not least...Cecil (Wahoowa!).

Thank you to my adviser, Dick Plambeck—you have been the best mentor I ever could have hoped for. Thank you for the countless hours you spent teaching me about the CARMA hardware system from the ground up while we were commissioning the dual-pol receivers. Thanks for staying up all night to help me with the huge proposal that would ultimately pave the way for years of exciting science. Thanks for teaching me about data reduction, star formation, and most importantly, how to be appropriately skeptical. Thanks for all of the challenges. Thanks for the incredible hikes, even if we pretty much always bit off more than we could chew. And thanks for the friendship.

Thank you to my beloved housemates for six wondrous years. For the nerd-alert discussions, the wine nights, the celebrations, and the shoulders to cry on. For incorporating me into your various wonderful families ("this is so niiice..."). And for the friendship that I have no doubt will last a lifetime.

Thank you to the boys! By the time this thesis gets published online I fully expect the boysnight thread count to have exceeded 10,000. You all are men among men: the prime rib of Penn Yan and beyond, and a group for whom I'd beer myself across the country at the drop of a hat.

Thank you so much to my family. To Betsey, Sally, and Lesley, M, and Dave Rosinus for your unfailing support. To Bo and Lizbet for being totally wonderful, and for introducing me to the lawnmower paradigm of academic funding. To the entire Hurley Clan for being the biggest and best family addition I could ever have dreamed of. And to those who supported me but are no longer with us: Tom, Carl, Poodie, Pops, and of course Twodads, whose love of science most certainly rubbed off on me.

And thanks to my Mom, Dad, David, and Anna. D: you're the best brother a guy could have, your sense of humor is ridiculous, and you're an inspiration to so many. Mom: you talk sense into me, you're always supportive, you're a blast to travel with, and you have great ideas. You're the best. Padre: the connoisseur of wine, the great polyglot, and the nerd from whom I inherited my nerditude. You've always been there when I've needed advice, and have been the first to join in the celebrations of my successes. ¿Etequetacatrá? ¡Te quiero, che! And finally, Anna: thank you for everything. You are truly an angel and a saint, abounding with patience and wisdom. I couldn't have done this without you.

This dissertation was typeset using the ucastrothesis LaTeX template. Thanks, Pedro!

Chapter 1

Introduction

How do magnetic fields affect the star formation process? The answer to that question depends both on the type of material (atomic vs. molecular) and on physical scale, and seems to change across the many orders of magnitude from the large ($\sim 100\,\mathrm{pc}$) scales of giant molecular clouds (GMCs) to the small, $\sim 0.01\,\mathrm{pc}$ ($\sim 1000\,\mathrm{AU}$) scales of what we deem "protostellar envelopes."

Magnetic fields have long been considered to be one of the key components that regulate star formation (e.g., Shu et al. 1987; McKee et al. 1993). And indeed, observations of polarization in star-forming regions have shown that magnetic fields are well ordered on large scales, from the $\sim$kpc scales of the entire galaxy (Planck Collaboration et al. 2014a,b,c) to the $\sim 100\,\mathrm{pc}$ scales of GMCs (Heiles 2000) to the $\sim 1\,\mathrm{pc}$ scales of individual clouds (Pereyra & Magalhães 2004; Goldsmith et al. 2008; Franco et al. 2010; Palmeirim et al. 2013). This is evidence that B-fields in the interstellar medium (ISM) are strong relative to the turbulence in the ISM across many orders of magnitude. In other words, the turbulence in the ISM is sub-Alfvénic: the speed of turbulent motions v is less than the Alfvén speed $v_A = B/\sqrt{4\pi\rho}$, and thus the Alfvén Mach number $M_A = v/v_A$ is < 1.[1]

In addition to comparing magnetic and turbulent energy via M_A, one can also compare magnetic and gravitational energy via the mass-to-flux ratio $\lambda = M/M_{\mathrm{crit}}$, where M_{crit} is the magnetic critical mass. (M_{crit} is defined by the condition that magnetic energy be equal to gravitational energy; see McKee & Ostriker 2007). When B-fields support star-forming material against gravitational collapse, $\lambda < 1$ and that material is said to be "subcritical." The opposite case is "supercritical," when $\lambda > 1$ and gravity overwhelms magnetic pressure, thus allowing the formation of a central protostar. Subcritical gas can be converted to a supercritical state by ambipolar diffusion (e.g., Mestel & Spitzer 1956; Fiedler & Mouschovias 1993; Tassis et al. 2009), turbulent magnetic reconnection diffusion (Lazarian 2005; Leão et al. 2013), flow along B-field lines, and shock compression (Mestel 1985; McKee et al. 1993; Chen & Ostriker 2014).

Observations of of atomic gas (e.g., Heiles & Troland 2005, and references therein) have

---

[1] Note that Crutcher et al. (1999) found approximately Alfvénic turbulence on $\sim 1\,\mathrm{pc}$ scales in the NGC 2024 molecular cloud.

shown that atomic gas is subcritical on scales $\lesssim$ the scale height of the gas; although, atomic gas does become supercritical on large enough scales, e.g., the cloud's accumulation length (see Mestel 1985; McKee & Ostriker 2007). Molecular gas, on the other hand, is always seen to be *supercritical.* Thus far, however, observations of molecular gas have been limited to scales of ~ 0.1–1 pc (see Crutcher 2012, and references therein). Further observations are needed (dare we say...critical!) to determine the state of molecular gas on larger scales.

In short, the star formation process is not a simple progression from sub- to supercritical. GMCs are presumably *supercritical* because they are gravitationally bound (McKee 1989, and references therein), having formed out of the ISM in the galactic disk via gravitational instability (Mestel 1985; McKee et al. 1993, although, as mentioned above, this has yet to be confirmed observationally). However, much of the volume of GMCs may be filled with low-density, *subcritical* atomic and molecular material (again, this needs to be confirmed). And yet, amidst these subcritical regions are dense, *supercritical* molecular regions where the majority of the mass of the GMC presumably resides, and where stars eventually form.

Millimeter-wave interferometry is an ideal technique for discovering the role magnetic fields play at the small scales of protostellar cores (~ 0.1 pc) and envelopes (~ 0.01 pc). The CARMA polarization system is the best at probing scales of $1 - 4''$ in angular extent, which correspond to approximately $200 - 8000$ AU in physical size in the nearest star-forming regions.

1.1 Observing dust polarization

Magnetic fields leave an imprint on the radiation that we detect at many scales, from the CMB to stellar coronae—that imprint is polarization. Across frequencies from the optical to the radio, we can glean information about the morphology (and sometimes the strength) of magnetic fields in interstellar clouds, clumps, and cores via spectropolarimetry of central stars, optical and infrared background starlight polarization, (sub)millimeter thermal dust emission, spectral-line polarization via the Goldreich-Kylafis effect and Zeeman splitting, and synchrotron emission.

In this work, we focus primarily on the polarization of millimeter-wave thermal dust emission. Under most circumstances, spinning dust grains are expected to align themselves with their long axes perpendicular to the magnetic field (Hildebrand 1988; Lazarian 2003, 2007; Lazarian & Hoang 2007; Hoang & Lazarian 2009; Andersson 2012), so normally the thermal radiation from these grains is polarized perpendicular to the magnetic field (see Section 1.2). Ambient fields can be probed within $\gtrsim 1$ pc of a dense core using optical observations of background stars (e.g., Heiles 2000), whose light becomes polarized after passing through regions of aligned dust grains. However, this type of observation is not possible inside the dense cores where the central protostars and their circumstellar disks form; even at infrared wavelengths the extinction through these regions is too great. Mapping the polarized thermal emission from dust grains at millimeter and submillimeter wavelengths is therefore the usual means of studying the magnetic fields in these regions.

Observations of dust polarization in dense cores were pioneered by polarimeters at the Caltech Submillimeter Observatory (CSO) and the James Clerk Maxwell Telescope (JCMT), two submillimeter single-dish telescopes with $\sim 20''$ resolution. Until the advent of interferometric (sub)millimeter polarimetry with the Berkeley-Illinois-Maryland Array (BIMA) and the Submillimeter Array (SMA), the lion's share of work on protostellar polarization had been done using the the SCUBA polarimeter at the JCMT (Matthews et al. 2009) and the Hertz (Dotson et al. 2010) and the SHARC-II (SHARP) (Attard et al. 2009; Davidson et al. 2011; Chapman et al. 2013) polarimeters at the CSO.

With the development of the polarimeters on BIMA and the SMA, it became possible to probe polarization in regions smaller than the ~ 0.1 pc dense core. The polarization system at CARMA is now one of only three (sub)millimeter interferometric full-polarization systems in the world, the others being at the SMA and the Plateau de Bure Interferometer (PdBI). CARMA's large correlator bandwidth, large collecting area, and excellent UV-coverage put it on the forefront of polarization science. The polarization system at CARMA is also a critical pathfinder for ALMA, whose polarization system is just now coming online.

Note that observations of dust polarization do not allow for direct measurements of the magnetic field strength. Under certain circumstances measurements of the strength can be made via Zeeman or synchrotron measurements in the same sources; however, in most sources these measurements are not possible, and thus one must resort to such indirect probes as the Chandrasekhar-Fermi method (Chandrasekhar & Fermi 1953; Ostriker et al. 2001) or the intensity-gradient relation presented in Koch et al. (2012).

Finally, note that polarization angles χ (and the B-field orientations inferred from them) are not vectors, but are *polars*. A polar is a "headless" vector that has an *orientation* (not a direction) with a 180° range (e.g., $0 - 180°$ or $-90 - 90°$).

1.2 Dust-grain alignment

One of the main assumptions underlying the conclusions we draw in this work is that spinning dust grains are aligned by magnetic fields, and that these grains are expected to align themselves with their long axes perpendicular to the B-field. This then allows us to use maps of dust polarization to infer B-field morphology.

An extensive review of dust alignment theories, and the observational tests that have been done to test those theories, can be found in Andersson (2012). He reviews the history of grain alignment theory, beginning with the now-less-popular theories: mechanical alignment (also known as "Gold alignment"; see e.g., Gold 1952), where collisions between streams of dust and gas with different systemic velocities cause grain alignment; and paramagnetic alignment (also known as the "Davis-Greenstein effect"; see e.g., Davis & Greenstein 1951; Purcell 1979; Mathis 1986), where the grains are aligned perpendicular to the external B-field due to the dissipation of internal magnetic energy. The most widely accepted theory for dust-grain alignment is currently that of radiative torques (RATs), proposed by Dolginov & Mitrofanov (1976), and expanded upon by Draine & Weingartner (1996); Lazarian (2007); Lazarian &

Hoang (2007); Hoang & Lazarian (2009). Other reviews of grain alignment theories include Lazarian (2003); Lazarian et al. (2014).

Dust-grain alignment depends not only on the degree of alignment between the angular momentum vector J and the B-field, but also on the alignment of the grain's short axis (which is its axis of maximal moment of inertia) with respect to J. Grains initially tumbling through space are not necessarily spinning about their short axes; however, they relax into this lowest-energy state because of "internal relaxation," which happens much faster than the alignment of J with the B-field. Internal relaxation is made possible by the Barnett effect, which is the magnetization of a rotating paramagnetic body (i.e., a body with unpaired spins; see Purcell 1979 for good explanations of both the Barnett effect and internal relaxation). When a dust grain is spinning—but not about its short axis—then the magnetic moments in the grain's atoms caused by the Barnett effect will continually be reoriented, leading to the dissipation of energy in the form of heat. This internal relaxation can occur because of the reorientation of the magnetic moments of either unpaired electrons (Purcell 1979) or the atoms' nuclei (Lazarian & Draine 1999a). The latter, known as "nuclear relaxation," is the dominant process for large grains ($10^{-5} < a < 10^{-4}$ cm), and occurs in ~ 10 s, orders of magnitude more quickly than the relaxation due to the reorientation of electron spins (10^7 s; see Table 1 in Lazarian et al. 2014 for relevant timescales). The fixed magnetization caused by the Barnett effect is what then causes the grains to undergo Larmor procession around the B-field lines.

Once internal relaxation has occurred, grains spin about their short axes and their angular momentum vectors J precess around the B-field; the question then is how J becomes aligned with the external B-field. One of the first processes proposed to explain how grains become aligned with the the B-field is paramagnetic alignment (Davis & Greenstein 1951). Similar to how internal relaxation causes the grain to rotate around its short axis, paramagnetic relaxation eventually causes the grain's short axis (i.e., its rotation axis) to align with the external B-field. However, for large grains, paramagnetic relaxation is too slow; collisions would randomize 10^{-5} cm grains more quickly than they would be aligned in a region with a typical ISM B-field of a few μG.[2]

Thus, RATs are the dominant mechanism for aligning large grains.[3] The basic RAT model, proposed in Lazarian & Hoang (2007), assumes that dust grains are oblate spheroids with net helicities (i.e., they will interact more with incident right-circularly polarized (RCP) light than with LCP light, or vice versa), being illuminated by anisotropic radiation with a wavelength $\lambda < 2a$, where a is the effective radius of the grain. This requirement for

---

[2] Note that there are other reasons besides timescales that cause paramagnetic alignment to fail for large grains. For example, Jones & Spitzer (1967) found that a difference in gas and dust temperatures was required for paramagnetic alignment; however, Jones et al. (1984) observed aligned grains in a region where the gas and dust are in thermal equilibrium. Also, the suprathermal rotation of grains proposed by Purcell (1979) could have avoided the thermal equilibrium problem, but Lazarian & Draine (1999b) found that grains could be "thermally trapped" in non-suprathermal states because of rapid flipping induced by internal thermal excitation. See Andersson (2012) for a detailed discussion.

[3] RATs align small grains ($a < 10^{-6}$ cm) less efficiently, making classical paramagnetic alignment the dominant mechanism for aligning small grains (Lazarian et al. 2014).

anisotropic radiation is normally fulfilled because there is a localized source (e.g., a protostar in the center of a dense core acting as a "light bulb"), or because the interstellar radiation field is not perfectly isotropic because of absorption by discrete clouds. Along with "pinwheel torques" such as Purcell torques (caused by H_2 formation on grain surfaces; see Purcell 1979), these RATs spin up dust grains.

Grains are subject both to "spin-up torques" (torques parallel to J), and to "alignment torques" (torques perpendicular to J; Lazarian et al. 2014). The alignment torques tend to align J with the B-field: as J becomes closer and closer to being parallel to the B-field, these alignment torques average to zero over the grain's precession period. In this situation of ideal alignment, the normal to the largest face of the grain is along the radiation direction for most of the precession period, leading to a large spin-up torque on the grain that allows it to be spun up quickly (much as a toy pinwheel spins up very fast when it faces the wind direction); the result is a grain with high angular momentum (see "high-J attractor points" below). However, sometimes the sum of the torques (averaged over the precession period) along the three axes of the grain is small, because of both the misalignment of J with the radiation direction as well as differing scattering efficiencies along the three axes of the grain; in this case the grain is not spun up as strongly, and has low angular momentum (see "low-J attractor points" below).

Note that perfect alignment of J with the B-field is not required for radiation from grains to be polarized: the J vectors of spinning grains precess around the external B-field with a Larmor precession period of $\sim 10^6$ s; averaging over all of the precessing grains will cause the polarization to appear either parallel (absorption) or perpendicular (emission) to the ISM B-field. Also note that Lazarian & Hoang (2007) found that grains can spin with their long axes either perpendicular to the B-field (the "right" way) or parallel to it (the "wrong" way). However, the "wrong" alignment is only possible at "low-J attractor points" (i.e., at low angular momentum); because of bombardment by gas particles and because the grains wobble within an angular range that is larger than the range for which the wrong alignment is possible (Lazarian 1994; Lazarian & Roberge 1997), all grains eventually end up at the more stable "high-J attractor points." Consequently, while grains can be aligned the wrong way, they eventually end up with their long axes aligned perpendicular to the B-field, as expected.

1.3 Misalignment of B-fields and outflows in protostellar cores

One of the main conclusions of this work is that at the ~ 1000 AU scales probed by CARMA, B-fields and outflows from protostellar cores tend to be randomly aligned (note that we assume that outflows are oriented perpendicular to the planes of circumstellar disks). This misalignment is not limited to CARMA scales, however. When their entire samples are taken into account, Ménard & Duchêne (2004) found that T Tauri outflows (or disk symmetry axes) are randomly aligned with B-fields on parsec scales, and Targon et al. (2011) found a similar result using a larger sample of Class 0 and I objects. On smaller scales, Poidevin et al.

(2010) found that outflows from low-mass protostars in Orion are misaligned with the B-field measured with SCUBA at ∼ 0.1 pc scales. Finally, our work with CARMA (Hull et al. 2013, 2014) confirmed the early hints from BIMA and the SMA that outflows might be randomly aligned with B-fields at ∼ 1000 AU scales (Girart et al. 1999, 2006; Rao et al. 2009).

Considering the evidence that B-fields and outflows are misaligned at multiple scales, and presuming that outflows have the same orientation regardless of physical scale, then a reasonable question to ask would be, Are B-fields consistent across all of those scales? Indeed, Li et al. (2009) showed that B-field orientations are consistent over many orders of magnitude, from scales of ∼ 100 pc to ∼ 0.1 pc. We take the next step in our work (Hull et al. 2014, see Chapter 3) by comparing B-field orientations from scales of ∼ 0.1 pc to ∼ 0.01 pc. We do find that some sources continue to have consistent B-field orientations down to ∼ 0.01 pc scales; however, a subset of the sources have B-fields that not only are inconsistent from ∼ 0.1 pc to ∼ 0.01 pc, but also tend to be *preferentially perpendicular* to the sources' bipolar outflows, suggesting that the B-fields have been toroidally wrapped by rotation. In short, at the ∼ 0.01 pc (∼ 1000 AU) scales of the protostellar envelope, we may finally be probing the scale where the B-field loses its "memory" of the larger scale B-field, having been affected by small-scale dynamical processes such as rotation.

Early models of magnetized core collapse assumed initial alignment between the angular momentum and B-field axes of collapsing protostellar cores (Galli & Shu 1993a,b). While this was partially because cylindrically symmetric models were simpler, it was later shown that magnetic braking will force the angular momentum of a rotating core back into alignment with a strong poloidal B-field (e.g., Machida et al. 2006). The fact that B-fields and outflows are misaligned thus suggests that in most protostellar cores the B-fields are not, in fact, strong enough to maintain alignment with core rotation axes (N.B. when it comes to forming disks, this turns out to be a good thing; see Section 1.4).

This begs the question: why the misalignment? Three possible avenues to investigate come to mind: multiplicity, environment, and age.

Stars in multiple systems are known to exhibit the effects of binary interaction. Examples include objects such as L1157 (Looney et al. 2007, and references therein), whose outflows and disks precess over time; and objects whose outflows are no longer perpendicular to the circumstellar disks that launch them (Stapelfeldt et al. 2014). However, these effects usually cause alignment perturbations of $10 - 20°$ at most, and are thus unlikely to cause the ∼ 90° misalignment seen in objects such as the low-mass protostellar binary NGC 1333-IRAS 2A, which has perpendicular (or "quadrupolar") outflows (Sandell et al. 1994; Engargiola & Plambeck 1999).

The environment surrounding the protostar may also play a role in B-field/outflow misalignment. Unlike Hull et al. (2013), Chapman et al. (2013) find that outflows and B-fields tend to be aligned in their sample of protostellar cores. However, their sample of eight sources were chosen to include only cores that are isolated, whose outflows are nearly in the plane of the sky, and which are not known binaries. In more isolated, quiescent sources devoid of binary interactions it is entirely possible that the classic picture of magnetically regulated collapse is still viable.

But what about in the rest of the sources? In less quiescent regions, it may be that asymmetric infall causes the angular momentum of a protostellar core to twist around as material accretes, especially early in the accretion process when infalling clumps have masses comparable to the forming protostar. Hydrodynamic simulations (e.g., Smith et al. 2011) have shown that the angular momentum of infalling material as a function of radius in a core can vary widely; however, high resolution magnetohydrodynamic (MHD) simulations will be necessary to reveal whether asymmetric infall of material onto cores is sufficient to randomize the cores' angular momentum vectors in the presence of B-fields.

An argument in favor of asymmetric accretion over time involves observations of Herbig Ae/Be stars, which are more massive than the low mass Class 0, Class I, and T Tauri stars discussed thus far. Rodrigues et al. (2009) found that younger Ae/Be stars tend to have disk symmetry axes that are preferentially aligned with ambient B-fields, whereas the older Ae/Be stars tend to have B-fields and symmetry axes that are randomly aligned. And in fact, this may be seen in the samples of low-mass stars studied by Ménard & Duchêne (2004) and Targon et al. (2011): when they limited their sample to younger sources, there were (statistically marginal) hints that younger sources are better aligned with ambient B-fields.

This evolutionary story seems plausible, but in addition to the lack of corroborating evidence from simulations, there are other issues. First, OMC3-MMS6, a Class 0 source in Orion, has a very small bipolar outflow with a dynamical age of only 100 yr (Takahashi & Ho 2012), too young to have either perturbed the B-field in the core or changed direction. The outflow is not aligned with either the large- (~ 0.1 pc) or the small-scale (~ 0.01 pc) B-field around MMS6, suggesting that the orientation of the disk launching the outflow truly is misaligned with the B-field in the envelope, despite the fact that the source is so young. And second, aside from the outflow precession discussed above, outflows are not known to change direction appreciably over the course of a protostar's lifetime: many sources show bipolar ejections with consistent position angles over parsec scales. Some examples include HH 211 mm (Lee et al. 2009), L1448 IRS 2 (Tobin et al. 2007; O'Linger et al. 1999), L1157 (Gueth et al. 1996; Bachiller & Perez Gutierrez 1997), L1527 (Hogerheijde et al. 1998), and VLA 1623 (Andre et al. 1990). However, this might be a selection effect, in that the bipolar outflows that can be traced the furthest are more likely to be straight; connecting periodic ejections from a source whose outflow position angle has changed significantly could be very difficult.

Finally, one could imagine that a protostar would be the most prone to having its angular momentum changed in the very earliest stages of accretion before and outflow has even turned on. MHD simulations will shed light on this and other aspects of this problem, as mentioned above; much remains to be done.

1.4 Probing polarization in protoplanetary disks

The next question is, What do B-fields look like at scales even smaller than those we've probed with CARMA?

Some simulations (e.g., Machida et al. 2006; Myers et al. 2013) find that the B-fields in a protostar are wrapped up at disk scales, regardless of the larger-scale B-field morphology in the envelope and the core. In Hull et al. (2014) we reported hints of this toroidal wrapping in the sources with lower polarization fractions. Evidence for toroidal wrapping of B-fields from $\sim$100–1000 AU scales in high-mass protostars has also been seen in mid-infrared absorption (Aitken et al. 1993); although, intriguingly, mid-infrared emission suggests that B-fields may be *aligned* with outflows at smaller scales, in spite of the large-scale toroidal B-fields! (Wright 2007).

If B-fields are indeed toroidally wrapped in protostellar envelopes, it could have important consequences for circumstellar disk formation, since preferential misalignment of the B-field and the rotation axis should allow circumstellar disks to form more easily (Hennebelle & Ciardi 2009; Krasnopolsky et al. 2012; Joos et al. 2012; Li et al. 2013). Objects with misaligned B-fields and rotation axes are less susceptible to the "magnetic braking catastrophe," where magnetic braking prevents the formation of a rotationally supported Keplerian disk (Allen et al. 2003; Galli et al. 2006; Mellon & Li 2008; Hennebelle & Fromang 2008; Li et al. 2011). Indeed, some of these models suggest that misalignment may be a necessary condition for the formation of disks (see also Krumholz et al. 2013).

It is important to emphasize that even if we are in fact seeing toroidally wrapped B-fields in the CARMA results, the scales we are probing are $\sim$500–1000 AU scales, *not* $\sim$100 AU disk scales. Consequently, the B-fields would have been wrapped up by the envelopes and not by the disks. However, polarization indicating toroidally wrapped B-fields at the $\sim$100 AU scale of circumstellar disks has been detected in IRAS 16293 (Rao et al. 2014) with the SMA, and in HL Tau (Stephens et al. 2014) and L1527 (Looney et al., in prep.) with CARMA. ALMA observations of dust polarization will be needed to confirm these results and to reveal whether B-fields are indeed toroidally wrapped on even smaller scales.

1.5 B-field evolution over time during protostellar formation

The term "multi-scale" in the title of this thesis refers to multiple physical scales. However, the change in B-field morphology over time is equally interesting. In the protostellar phase, magnetic fields become harder to detect with time. Take, for example, several Class II sources such as HD 163296, TW Hya, and DG Tau, which show no ordered polarization on $\sim$500 AU scales (Hughes et al. 2009, 2013). This is surprising, since many of these Class II sources presumably evolved from significantly polarized cores, and thus one would thus expect to see polarized emission from the dusty disk.

MHD turbulence in magnetized protoplanetary disks is thought to influence a wide array of physical processes relevant for planet formation, including dust and gas transport and mixing (e.g., Ciesla 2007), meteoritic composition (e.g., Boss 2004), disk chemistry (e.g., Semenov et al. 2006), and the migration of planetary embryos through the disk (e.g., Chambers 2006). But perhaps the greatest impact of MHD turbulence is that it can provide the source of viscosity that drives disk evolution. The mechanism most commonly invoked as the source of this turbulence is the magnetorotational instability (MRI), in which magnetic interactions between fluid elements in the disk combine with an outwardly decreasing velocity field to produce torques that transfer angular momentum from the inner disk outward (e.g., Balbus & Hawley 1991, 1998). Indeed, it is unlikely that turbulence in an unmagnetized, azimuthally symmetric Keplerian disk can sufficiently redistribute angular momentum: B-fields must be invoked to enable Shakura-Sunyaev viscosity (e.g., Balbus et al. 1996). The ionization fraction is most likely high enough to allow magnetic coupling of material over much of the outer disk (see, e.g., Sano et al. 2000; Turner et al. 2007), and the observed Keplerian rotation of protoplanetary disks provides the requisite velocity shear. However, the B-field properties far from the central star remain unconstrained.

In the presence of MHD turbulence, B-fields should only be detectable at very small scales. Turbulent motions are expected to occur on size scales comparable to the scale height in the disk; however, all of the observations undertaken so far have a spatial resolution of many tens to hundreds of AU, far larger than the scale height at comparable distances from the central star. Even if magnetic fields are ordered at some level on small scales, any structure will be entirely washed out by integration across such a large beam. Using ALMA to probe scale-height-sized regions within the disk will resolve ordered structures in the turbulent cells, thus allowing detection of polarized emission. In addition, higher resolution observations of the inner disk, where the strengths of B-fields induced by the MRI are predicted to be higher, will improve the probability of detection if low magnetic field strengths are responsible for the lack of alignment of large grains (see discussion in Bai 2011).

Interestingly, magnetic fields seem to reveal themselves again in the very latest stages of stellar evolution, e.g., in protoplanetary nebulae (PPN; see Sabin et al. 2014, and references therein), presumably being the result of dynamos in the rotating PPN systems. Opining on the dust polarization of these very evolved objects is outside of the scope of this work; we mention it simply as an illustration of the fact that B-fields are ever-present, even if their origins are distinct at different times and physical scales.

1.6 Thesis outline

In Chapter 2 we will discuss the development, testing, and calibration of the 1.3 mm dual-polarization receiver system at CARMA that made all of our protostellar polarization work possible. We will then discuss the scientific contributions we have made using the system. In Chapter 3 we discuss the misalignment of B-fields and outflows in protostellar cores (Hull et al. 2013). And in Chapter 4 we present the results of the entire TADPOL survey (Hull et al. 2014); we find that B-fields are not always consistent from core to envelope scales, and we see hints that the B-fields in some protostellar envelopes may be toroidally wrapped by envelope rotation.

Acknowledgements (Chapter 1)

C.L.H.H. would like to thank Chris McKee for the excellent discussion that led to great improvements in this introduction; and Alex Lazarian and B-G Andersson for helping to elucidate the mysteries of dust-grain alignment.

Chapter 2

The 1.3 mm Full-Stokes Polarization System at CARMA

We have constructed dual-polarization 1.3 mm receivers for the CARMA array. A key science goal for these receivers is to map the linearly polarized thermal emission from dust grains in interstellar clouds; maps of this polarized emission can then be used to infer the magnetic-field morphologies in these regions. Polarization fractions of a few percent are typical of this radiation. For an aperture synthesis array like CARMA it is advantageous to measure this weak linear polarization by cross-correlating the signals from circularly polarized feeds. To observe circular polarization, we install a waveguide polarizer between the feed horn and the orthomode transducer (OMT), at a temperature of 4 K, to convert incoming circularly polarized signals into linearly polarized signals. The receivers use waveguide OMTs to split the incoming radiation into orthogonal linear polarizations. The two OMT outputs are coupled to separate SIS (superconductor-insulator-superconductor) mixers and WBA-13 low-noise amplifiers (LNAs). Here we introduce the basics of polarization before briefly describing the system itself. We then discuss the commissioning and calibration of the system, including an exhaustive list of the aspects of the system that we tested, the difficulties and systematic limitations we encountered, and the solutions we devised.

2.1 Introduction to Polarization

A source is considered partially polarized if the power in any polarization is greater than in its orthogonal state (i.e., more vertically than horizontally, or more right- than left-circularly polarized). Polarization is produced by a number of processes, including many that involve magnetic fields (e.g., synchrotron radiation, Zeeman splitting, dust emission, etc.); and others that do not (e.g., scattering). In this work we will focus primarily on the polarization of thermal emission from dust grains that have been aligned by magnetic fields.

Note that when you measure a single polarization, you only get half of the power (assuming an unpolarized source). So when you measure both polarizations, you gain a factor of $\sqrt{2}$ in sensitivity.

An excellent introduction to the basics of polarization, including an extensive discussion of monochromatic polarization, plane waves, Stokes and Jones vectors, bases, conventions, and history can be found in Tim Robishaw's Ph.D. thesis (Robishaw 2008). And of course, detailed descriptions of just about every concept in radio astronomy can be found in such classic texts as Thompson et al. (2004, a.k.a. "TMS"). Here we simply highlight some of the concepts that are particularly useful for understanding interferometric polarization.

2.1.1 Polarization ellipse

An incoming monochromatic signal can be polarized in various ways: circularly, linearly, or elliptically. The generic polarization ellipse can be described as follows:

- $+x$ points up (from South to North), $+y$ points to the left (from West to East), and $+z$ comes out of the page toward the reader. Note that this follows Thompson et al. (2004), where the X and Y axes are rotated 90° counterclockwise relative to standard Cartesian axes.
- The position angle (PA) χ is measured east of north.
- Linear polarization: when the orthogonal vibrations have the same phase. Amplitudes can be different or the same.
- Circular polarization: when the orthogonal vibrations have exactly a 90° phase difference and have the same amplitude.
- Elliptical polarization: when the amplitudes of the orthogonal vibrations are different and there's any phase difference; or when the amplitudes are the same and there's a phase difference $\phi \neq 90°$.

The position angle χ is the angle of orientation of the long axis of the ellipse. If you observed linear polarization, the angle of the linear polarization would also be χ.

Note that polarization angles χ (and the B-field orientations inferred from them) are not vectors, but are *polars*. A polar is a "headless" vector that has an *orientation* (not a direction) with a 180° range (e.g., 0 to 180° or –90 to 90°).

2.1.1.1 Definition of handedness (LCP vs. RCP)

The IEEE (Institute of Electrical and Electronics Engineers) has defined handedness in the following way: light is right-circularly polarized (RCP) when the radiation phasor travels clockwise *as viewed by the emitter* (IEEE 1997). As we look up in the sky, RCP looks as if it's going around counterclockwise. As Robishaw (2008) points out, a good way to remember this is to point both of your own thumbs toward yourself and curl your fingers. The apparent direction of your fingers will give you the IEEE-sanctioned handedness of the signal: left hand (LCP) → clockwise, right hand (RCP) → counterclockwise.

Note that this IEEE convention, which is used by engineers and radio astronomers, is the *opposite* of the convention used by physicists and optical astronomers! See Section 2.2.1 of Robishaw (2008) for more details.

2.1.2 Stokes parameters

Stokes parameters describe the polarization properties of the radiation field, and may be measured with either linearly or circularly polarized feeds. By using four Stokes parameters, one can fully describe the characteristics of a fully polarized, partially polarized, or unpolarized signal that has four parameters:

- X-amplitude
- Y-amplitude
- Phase angle ϕ between the orthogonal polarizations
- Polarization fraction Π

Dual-polarization receivers comprise either orthogonal linear or circular feeds. Using the incoming electric fields E detected by the orthogonal *linear* feeds, you can get all four Stokes parameters by calculating the following time-averaged products of the voltages E_X and E_Y (Rybicki & Lightman 1979):

$$I = \langle E_X E_X^* \rangle + \langle E_Y E_Y^* \rangle \tag{2.1}$$

$$Q = \langle E_X E_X^* \rangle - \langle E_Y E_Y^* \rangle \tag{2.2}$$

$$U = \langle E_X E_Y^* \rangle + \langle E_X^* E_Y \rangle \tag{2.3}$$

$$V = -i \left(\langle E_X E_Y^* \rangle - \langle E_X^* E_Y \rangle \right) \ , \tag{2.4}$$

where E_X^* denotes the complex conjugate of E_X.

One can convert from linear to circular using the Mueller matrix $\mathbf{M}_{\text{lin-to-circ}}$ (Heiles et al. 2001b, Equation 14; see Section 2.1.3 for a discussion of Mueller matrices):

$$\mathbf{M}_{\text{lin-to-circ}} = \begin{bmatrix} 1 & 0 & 0 & 0 \\ 0 & 0 & 0 & 1 \\ 0 & 0 & 1 & 0 \\ 0 & -1 & 0 & 0 \end{bmatrix} \ . \tag{2.5}$$

The conversion leads us to the following reorganization of Equations 2.1–2.4 [essentially, $I \rightarrow I$; $Q \rightarrow V$; $U \rightarrow U$; and $V \rightarrow -Q$, or $(I, Q, U, V) \rightarrow (I, V, U, -Q)$], where the subscripts $x \rightarrow R$ and $y \rightarrow L$:

$$\begin{aligned} I &= \langle E_R E_R^* \rangle + \langle E_L E_L^* \rangle && (2.6) \\ Q &= i\left(\langle E_R E_L^* \rangle - \langle E_R^* E_L \rangle \right) && (2.7) \\ U &= \langle E_R E_L^* \rangle + \langle E_R^* E_L \rangle && (2.8) \\ V &= \langle E_R E_R^* \rangle - \langle E_L E_L^* \rangle \ . && (2.9) \end{aligned}$$

Equation 2.9 is in agreement with the standard convention, defined by the IAU in Contopoulos & Jappel (1974), which deems Stokes V to be positive if the signal has net RCP:

$$V \equiv \mathrm{RCP} - \mathrm{LCP} \ . \tag{2.10}$$

While this is the accepted convention, the sign choice is arbitrary, and many publications define Stokes V in the opposite way (i.e., LCP − RCP). One must use caution when reviewing the literature, and should be sure to define clearly the Stokes V convention one has chosen.

Note that the above Equations 2.1–2.4 and 2.6–2.9 are appropriate for a single dish telescope. However, since CARMA is an interferometer, what we really measure are Stokes visibilities from cross correlations between antennas. Thus, an interferometer would actually measure E_X (or E_R) for antenna i and E_Y (or E_L) for antenna j for all baseline pairs ij.

Another common way to express the four Stokes parameters combines both linear and circular polarizations:

$$\begin{aligned} I &= E_{0^\circ}^2 + E_{90^\circ}^2 && (2.11) \\ Q &= E_{0^\circ}^2 - E_{90^\circ}^2 && (2.12) \\ U &= E_{45^\circ}^2 - E_{-45^\circ}^2 && (2.13) \\ V &= E_{RCP}^2 - E_{LCP}^2 \ . && (2.14) \end{aligned}$$

Stokes I represents the total power in the incoming radiation. You can get the total power by sampling two orthogonal polarizations (no matter which two they are). That is, if you were to take any of the differences listed above and turn them into sums, you'd get total intensity. For example:

$$\begin{aligned} I &= E_{0^\circ}^2 + E_{90^\circ}^2 && (2.15) \\ &= E_{45^\circ}^2 + E_{-45^\circ}^2 && (2.16) \\ &= E_{RCP}^2 + E_{LCP}^2 \ . && (2.17) \end{aligned}$$

Stokes Q and U fully describe linear polarization. Two parameters are needed because for linear polarization one must find both an amplitude and a position angle, and thus one needs two equations. Q and U can also be written this way:

$$\frac{Q}{I} = \Pi_l \cos(2\chi) \tag{2.18}$$

$$\frac{U}{I} = \Pi_l \sin(2\chi) \ \ , \tag{2.19}$$

where Π_l is the total fractional linear polarization:

$$\Pi_l = \frac{\sqrt{Q^2 + U^2}}{I} \ . \tag{2.20}$$

Fractional circular polarization is:

$$\Pi_c = \frac{V}{I} \ . \tag{2.21}$$

The total fraction of polarized light Π is calculated in the following way:

$$\Pi = \frac{\sqrt{Q^2 + U^2 + V^2}}{I} \tag{2.22}$$

$$\Pi \leq 1 \ . \tag{2.23}$$

If both Π_l and Π_c are nonzero, the polarization is elliptical.

The argument of the sine and cosine in Equations 2.18 and 2.19 is 2χ because χ is periodic in π. You can take Equations 2.18 and 2.19 and divide them to get a relation between Q, U, and χ:

$$\chi = \frac{1}{2} \arctan \frac{U}{Q} \ , \quad 0 < \chi < \pi \ . \tag{2.24}$$

2.1.3 Jones and Mueller matrices

Jones matrices (Jones 1941) are 2×2 matrices that are transfer functions, which can be used to describe the effect of any linear system on the real and imaginary parts of a sinusoidal wave, e.g., a polarized light wave, or the voltage signals output by a telescope receiver.

$$\begin{bmatrix} E_X \\ E_Y \end{bmatrix}_{\text{out}} = \mathbf{J} \begin{bmatrix} E_X \\ E_Y \end{bmatrix}_{\text{in}} \tag{2.25}$$

where $\mathbf{J}$ is the Jones matrix. Jones matrices are useful for describing the the response of the telescope to polarized radiation and can represent a large number of effects, each corresponding to a step in the signal path that causes an amplitude and/or phase change in the original signal. For example, gain differences $\mathbf{G}$ (including pointing, atmospheric, and electronic effects) between the two orthogonal polarizations, cross-polarization (leakage) terms $\mathbf{D}$, and the polarization characteristics of the feed $\mathbf{F}$ can be represented using the following Jones matrices (Hamaker et al. 1996; Heiles et al. 2001b; Marrone 2006, these are for a telescope with *linearly* polarized feeds):

$$\mathbf{G} = \begin{bmatrix} g_X\, e^{i\Psi_X} & 0 \\ 0 & g_Y\, e^{i\Psi_Y} \end{bmatrix} \tag{2.26}$$

$$\mathbf{D} = \begin{bmatrix} 1 & \epsilon_X\, e^{i\phi_X} \\ \epsilon_Y\, e^{-i\phi_Y} & 1 \end{bmatrix} \tag{2.27}$$

$$\mathbf{F} = \begin{bmatrix} \cos\alpha & e^{i\theta}\sin\alpha \\ -e^{-i\theta}\sin\alpha & \cos\alpha \end{bmatrix} \tag{2.28}$$

In $\mathbf{G}$, g_X and g_Y are the voltage gains (the power gains are g_X^2 and g_Y^2) and ψ_X and ψ_Y are the phase delays. In $\mathbf{D}$, ϵ_X and ϵ_Y represent the cross-coupling between the two polarizations, and ϕ_X and ϕ_Y are the phase angles of the coupled voltages. In $\mathbf{F}$, α characterizes the amount of coupling into the orthogonal polarization, and θ is the angle of that coupling (i.e., if the feed is mixing incoming linear polarizations, then a native linear feed has $\alpha = 0$ and $\theta = 0$; a native circular feed has $\alpha = 45°$ and $\theta = 90°$, etc.). These effects combine linearly, and thus the total Jones matrix in Equation 2.25 would be $\mathbf{J} = \mathbf{GDF}$.

Unfortunately, with the Jones formalism it is not possible to represent E_X and E_Y as partially polarized waves. Since no astronomical sources are 100% polarized, we turn to Mueller matrices and Stokes parameters. Instead of describing the electric field, the 4×4 Mueller matrices $\mathbf{M}$ (which are formed by taking the outer product of individual Jones matrices), relate the true and measured Stokes parameters.

$$\begin{bmatrix} I \\ Q \\ U \\ V \end{bmatrix}_{\text{measured}} = \mathbf{M} \begin{bmatrix} I \\ Q \\ U \\ V \end{bmatrix}_{\text{true}} . \tag{2.29}$$

Ultimately, you get the true signal by measuring $\mathbf{M}$ and then inverting it to get the true Stokes parameters. Mueller matrices can also be used to describe the cross-correlation of two antennas (i.e., the interferometer response; see Hamaker et al. 1996).

Heiles et al. (2001b) report the Mueller matrices associated with the each one of the above Jones matrices. Note that the Jones matrices we list above correspond to those in Heiles et al. (2001b), just with slightly different variables and matrix-name subscripts. Our Jones matrices $\mathbf{G}$ (gains), $\mathbf{D}$ (leakages), and $\mathbf{F}$ (feed) correspond to Heiles's Mueller matrices $\mathbf{M_A}$, $\mathbf{M_{IF}}$, and $\mathbf{M_F}$ (Equations 20, 17, and 11 in Heiles et al. 2001b, respectively).

The full Mueller matrix $\mathbf{M_{TOT}}$ for a telescope can be produced by multiplying the above Mueller matrices together; Heiles et al. (2001b) do so, and report it in Equation 22. One can determine all of the relevant parameters in the Mueller by doing a least-squares fit to suitably chosen astronomical data (see, for example, Figure 2.1 in Robishaw 2008).

2.1.4 Debiasing polarimetric images

Polarization measurements have a positive bias because the polarization $P = \sqrt{Q^2 + U^2}$ is always positive, even though the Stokes parameters Q and U from which P is derived can be either positive or negative. This bias has a significant effect in low signal-to-noise (SNR) measurements, i.e., when $P \lesssim 3\,\sigma_P$, where σ_P is the rms noise in the polarization maps. (The rms noise values in the Q and U maps are generally comparable, such that we set $\sigma_P \approx \sigma_Q \approx \sigma_U$). The bias can be taken into account by calculating the bias-corrected polarized intensity P_c (e.g., Vaillancourt 2006; see also Naghizadeh-Khouei & Clarke 1993 for a discussion of the statistics of position angles in low SNR measurements).

The probability density function for the observed polarization P of a signal with true polarization P_c is given by the Rice distribution (Killeen et al. 1986, Equation B1, and Vaillancourt 2006, Equation 6):

$$\mathrm{PDF}(P|P_c, \sigma_P) = \frac{P}{\sigma_P^2}\, I_0\left(\frac{P P_c}{\sigma_P^2}\right) \exp\left[-(P^2 + P_c^2)/2\sigma_P^2\right] . \tag{2.30}$$

However, to calculate the debiased intensity of the true polarization P_c one needs the opposite: $\mathrm{PDF}(P_c|P, \sigma_P)$. If one assumes a uniform prior for the true polarization P_c, then by Bayes's theorem $\mathrm{PDF}(P_c|P, \sigma_P)$ is the same as Equation 2.30:

$$\mathrm{PDF}(P_c|P, \sigma_P) = \frac{P}{\sigma_P^2}\, I_0\left(\frac{P P_c}{\sigma_P^2}\right) \exp\left[-(P^2 + P_c^2)/2\sigma_P^2\right] . \tag{2.31}$$

Thus, given the observed polarization P, one can be calculate the true polarization P_c by finding the maximum (i.e., the most probable value) of the PDF in Equation 2.31.

For very significant polarization detections ($P \gtrsim 5\,\sigma_P$), one can use the simple high-SNR limit (see Vaillancourt 2006, Equation 12):

$$P_c \approx \sqrt{Q^2 + U^2 - \sigma_P^2}\,. \tag{2.32}$$

However, for low-SNR detections ($P \lesssim 5\,\sigma_P$), things are not so simple, and one must use Equation 2.31 to calculate the debiased polarization intensity.

The position angle χ and uncertainty $\delta\chi$ (calculated using standard error propagation) of the incoming radiation are

$$\chi = \frac{1}{2} \arctan\left(\frac{U}{Q}\right) , \tag{2.33}$$

$$\delta\chi = \frac{1}{2}\frac{\sigma_P}{P_c}\,. \tag{2.34}$$

I.e., for a detection $P_c = 2\,\sigma_P$, the uncertainty in the position angle is 1/4 of a radian, or $\pm\,14^\circ$.

2.2 The CARMA dual-polarization receiver system

The CARMA polarization system consists of dual-polarization receivers that are sensitive to right- (R) and left-circular (L) polarization, and a spectral-line correlator that measures all four cross polarizations (RR, LL, LR, RL) on each of the 105 baselines connecting the 15 telescopes (six with 10 m diameters and nine with 6 m diameters). Each receiver comprises a single feed horn, a waveguide circular polarizer, an orthomode transducer (OMT), two heterodyne mixers, and two low-noise amplifiers (LNAs), all mounted in a cryogenically cooled dewar. The local oscillator (LO) and sky signals are combined using a mylar beamsplitter in front of the dewar window. See Figure 2.2 for a photo of the receiver module.

Figure 2.1: CARMA, the Combined Array for Research in Millimeter-wave Astronomy. Photo credit: John Carlstrom (University of Chicago).

The waveguide polarizer is a two-section design with half-wave and quarter-wave retarder sections rotated axially with respect to one another to achieve broadband (210–270 GHz) performance; the retarders are sections of faceted circular waveguide (Plambeck & Engargiola 2010); these facets, or “flats,” essentially make the waveguide elliptical in specific places, and act as phase shifters. The polarizer converts the R and L circularly polarized radiation from the sky into orthogonal X and Y linear polarizations, which then are separated by an OMT (Navarrini & Plambeck 2006). The mixers use ALMA Band 6 SIS (superconductor-insulator-superconductor) tunnel junctions fabricated at the University of Virginia by Arthur Lichtenberger. Although at ALMA these devices are used in sideband-separating mixers (Kerr et al. 2013), at CARMA they are used in double-sideband mixers that are sensitive to signals in two bands, one 1–9 GHz below (lower sideband, or LSB), and the other 1–9 GHz above (upper sideband, or USB) the LO frequency. A phase-switching pattern applied to the LO allows the LSB and USB signals to be separated in the correlator. The 1–9 GHz intermediate frequency (IF) from each mixer is amplified with a WBA13 low noise amplifier (Weinreb 1998; Pandian et al. 2006).

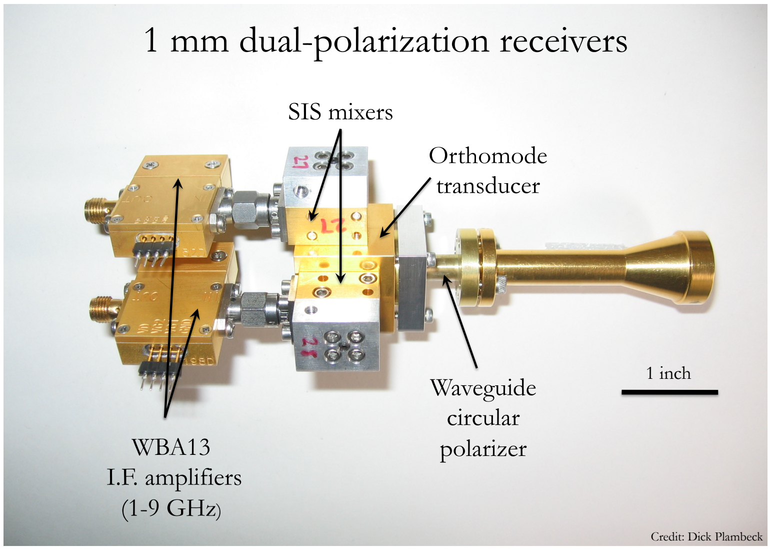

Figure 2.2: The 1.3 mm dual-polarization receiver module, installed on all 15 six- and ten-meter antennas at CARMA.

In addition to the usual gain, passband, and flux calibrations, two additional calibrations are required for polarization observations: "`XYphase`"[1] and leakage. The `XYphase` calibration corrects for the phase difference between the R and L channels on each telescope (i.e., the R–L phase) caused by delay differences in the receiver, underground cables, and correlator cabling. The `XYphase` is not a single number, but is a function of frequency, due to fiber- and cable-length differences. That is, you can look at the same piece of the IF in different correlator sections and get completely different R–L phases. Note that while we are actually measuring the R–L phases at CARMA, we will continue to refer to the quantity as `XYphase`, which is a term from `MIRIAD` (Sault et al. 1995), one of the standard data-reduction software packages for (sub)millimeter-wave interferometry.

To calibrate the `XYphase` one must observe a linearly polarized source with known position angle. Since most astronomical sources at millimeter wavelengths are weakly polarized and time-variable, CARMA uses artificial linearly polarized noise sources for this purpose. The noise sources are created by inserting wire grid polarizers into the beams of the 10 m telescopes. With the grid in place, one linear polarization reaching the receiver originates from the sky, while the other originates from a room temperature load. Since the room temperature load is much hotter than the sky, the receiver sees thermal noise that is strongly polarized. The R–L phase difference is then derived, channel by channel, from the R vs. L autocorrelation spectrum obtained with the grid in place (this is, in essence, a "cross-auto" passband, using the LR cross-correlation from the RCP and LCP receivers on the same antenna). One of the 10 m telescopes is always used as the reference for the regular passband observations, thus

---

[1] This font signifies the data reduction package `MIRIAD` itself; a task, procedure, or keyword within `MIRIAD`; or a Python task.

transferring the R–L phase calibration to all other telescopes. See Section 2.3 for a detailed discussion of `XYphase`- and position-angle calibration.

The leakage corrections compensate for cross-coupling between the R and L channels, caused by imperfections in the polarizers and OMTs, and by crosstalk in the analog electronics that precede the correlator. Leakages are measured in terms of voltage amplitudes (1% leakage (voltage) corresponds to 10^{-4} in power), and are defined in the following way (Thompson et al. 2004, Equation 4.42):

$$v'_R = v_R + D_R\, v_L \tag{2.35}$$

$$v'_L = v_L + D_L\, v_R \ , \tag{2.36}$$

where v'_R and v'_L are the observed signals, v_R and v_L are the true signals, D_R is the leakage from L into R, and D_L is the leakage from R into L.

In `MIRIAD`, $D_x \rightarrow D_R$, and $D_y \rightarrow D_L$.

Leakages are calibrated by observing a strong source (usually the gain calibrator) over a range of parallactic angles. There are no moving parts in the CARMA dual-polarization receivers, so the measured leakages are stable with time. A typical telescope has a band-averaged leakage amplitude (i.e., a voltage coupling from R into L, or vice versa) of 6%. See Section 2.4 for a detailed discussion of leakage calibration.

2.2.1 Observing modes of the 1.3 mm receiver system

The 1 mm receiver system operates in four modes: single-polarization mode (LL or RR) dual-polarization (LL and RR simultaneously), and full-Stokes (LL, RR, LR, RL). All four modes use the full 8 GHz bandwidth of the CARMA correlator (4 GHz per sideband), but with different combinations of correlator bands and polarizations (see Table 2.1).

In the nomenclature of `MIRIAD`, on the labels in the correlator room, and in the high-level software used to run the CARMA system, "POL1" corresponds to LCP and "POL2" to RCP. When referring to correlator bands, in single- or dual-polarization modes there are eight bands (labeled "band 1" through "band 8"). However, in full-Stokes mode, pairs of bands are coupled to produce the RL and LR cross-correlations, and thus full-Stokes bands 1, 2, 3, and 4 correspond to single-polarization bands 1/2, 3/4, 5/6, and 7/8, respectively. In the full-Stokes pairings of the single-polarization correlator bands, the odd bands correspond to LCP and the even correspond to RCP.

There is no benefit to using dual-polarization mode for wideband (continuum) observing. Typically the RCP receivers have higher noise temperatures than the LCP receivers, so it is better to use the available correlator bandwidth for LL observations only. The dual-polarization mode offers higher sensitivity only for spectral line (or mixed spectral line/continuum) observations. The reason for this is because for either spectral line or continuum observations you get independent information by observing the second polarization. However, for continuum observations that independent information can equally well be

Table 2.1: CARMA 1.3 mm Wideband Observing Modes

Mode	Bands (#)	BW/band (MHz)	Pol. (#)	SB (#)	Total BW (GHz)	Cross-corr.	Channels[†] (# per band)
Single-pol	8	500	1	2	8	RR *or* LL	95
Dual-pol	4	500	2	2	8	RR *and* LL	95
Full-Stokes	4	500	2	2	8	RR, LL, RL, LR	47

[†] These channel numbers are for 2-bit mode, which is the only mode allowed for wideband (500 MHz) full-Stokes mode. Full-Stokes data have fewer channels because some of the correlator's processing power is used to create the RL and LR cross-correlations.

Note. — 1.3 mm CARMA wideband (500 MHz/band) observing modes. The total bandwidth of each mode is 8 GHz, and is equal to the number of correlator bands × the bandwidth per correlator band (BW/band) × the number of polarizations (Pol.) × the number of sidebands (SB).

obtained by observing a different frequency slice of the available IF passband using the LCP receivers.

Incidentally, for the 1 mm receivers it is also best to avoid the extreme ends of the 1–9 GHz IF bandpass; the system temperature is worse below 2 GHz and above 8 GHz.

2.2.2 Correcting delays prior to full-Stokes observations

After the CARMA telescopes are moved, a certain prescription must be followed before engaging in full-Stokes observations. The general outline includes running both `fringeCheck`, a CARMA test observation of a quasar that reveals post-move phase slopes in the passband; and `fitDelays`, a Python program written to analyze `fringeCheck` data. `fitDelays` measures phase slopes in the 3 mm and 1 mm passbands, and then computes new 3 mm geometric delay "offsets" and 1 mm receiver delay differences (or "diffs," which are computed relative to the 3 mm offsets), thus flattening the passbands. The general procedure is:

- Run 3 mm `fringeCheck`; run `fitDelays` to correct 3 mm delay offsets.
- Run 1 mm LCP `fringeCheck`; run `fitDelays` to correct LCP receiver diffs.
- Run 1 mm RCP `fringeCheck`; run `fitDelays` to correct RCP receiver diffs.
- Check `XYphase` passband of 10 m antennas; if there is an overall slope in all 10 m passbands, calculate it with `fitDelays` and apply the same correction to the 1 mm LCP receiver diffs for all 15 antennas.

The above calibrations can also be accomplished in fewer steps by running a `fringeCheck` with `conf='FULLSTOKES'` followed by `fitDelays` with the keyword `RX1MM_FULLSTOKES`.

A note for posterity about the sign of the delays necessary to correct phase slopes: adding a positive number to the existing 1 mm LCP delay of an antenna makes the slope more positive. Consequently, to remove the wholesale RCP vs. LCP slope, one must *subtract* the fitted delay diff from the LCP diff of all antennas.[2]

After each array change, large delay diffs (~ 2 ns) tend to appear in the 1 mm RCP passbands. This is probably because the 1 mm RCP diffs are set using the 1 mm LCP fiber length, which is stored in the CARMA real-time system (RTS). The 1 mm RCP fiber length, however, is not stored in the RTS, and each pad's LCP fiber probably differs a bit from its RCP fiber—sometimes by quite a bit, probably because of repeated cable splicing, which requires cutting off pieces of cable before re-splicing.

2.3 Calibration of the Absolute Polarization Position Angle χ

2.3.1 Absolute position angle and the CARMA system

For a dual-linear receiver system, a fundamental quantity is the position angle of the X-feed relative to the local vertical. However, for the dual-circular case of CARMA, we define the fundamental quantity to be the position angle between the local vertical and the reference plane in which both RCP and LCP radiation are in phase (combining to create linear polarization).

The position angle χ of that reference plane on the sky is

$$\chi = q + \texttt{evector} \ . \qquad (2.37)$$

The parallactic angle q is the angle between the great circle through a celestial object and the zenith, and the hour circle[3] of the object. In the triangle with zenith–object–celestial pole at the corners, the parallactic angle will be the angle of the celestial object's corner. The parallactic angle is zero when the object crosses the meridian. `evector` is defined in `MIRIAD` as the position angle between the local vertical and the reference plane (note that `evector` should not be confused with the "E-vector," which is the position angle of the polarization of polarized radiation). We use the wire grids to produce horizontally polarized emission, and thus `evector` = 90° for CARMA (see Section 2.3.3 for more details).

2.3.2 `XYphase` signal path modeling

Because of differences in correlator cabling, the `XYphase` is frequency dependent. Consequently, prior to the realization that we could correct for the `XYphase` with grid data taken

---

[2] When computing new delay diffs, `fitDelays` processes the USB `fringeCheck` data only, so the rule of thumb described here only applies to USB data.

[3] The hour circle of an object is the great circle through the object and the celestial poles; it is perpendicular to the celestial equator. The hour circle is analogous to longitude lines on a globe.

during each observation, we endeavored to model the signal path and measure the `XYphase` as a function of correlator band and LO frequency.

We attempt to fit phases (deg) vs. IF frequency (GHz); the function we see (Figure 2.4) is piecewise and discontinuous because the second LO (LO2) has discrete steps, and because when we cross 5 GHz in the IF the signal takes a different path through the block downconverter. The function

$$\phi = f(\nu_{\rm IF}) \tag{2.38}$$

depends on LO2 as well as the geometric delays τ_1, τ_2, $\tau_{3,\rm lo}$, $\tau_{3,\rm hi}$, and τ_4, all of which are measured in nanoseconds, and which manifest themselves as phase slopes or offsets in the plot. (The units work out because the slope of ϕ vs. ν (in GHz) is in units of ns.)

A basic schematic of the CARMA signal path can be seen in Figure 2.3. It shows the critical components of the system, and highlights where in the system delay differences (and thus phase slopes) can arise. Note that from the point in the figure where it says "all phases flat," the correlator software guarantees that the path lengths from the noise source through the rest of the correlator are precisely equal; consequently, we only worry about delays up to that point.

Figure 2.4 shows the `XYphase` passbands at many frequencies in the 1–9 GHz IF passband. In the plotted example we used only one correlator band (band 4) from one telescope ("C1," one of the 10 m antennas), and stepped that band through many IF frequencies in an attempt to characterize the various delays τ in the system:

- τ_1: front-end delays inside the receiver itself
- τ_2: underground fiber and correlator cabling delays between the receiver and the block downconverter
- $\tau_{3,\rm hi}$: delay from the block downconverter mixer to the baseband mixer
- $\tau_{3,\rm lo}$: delay from the equivalent non-mixer position in the block downconverter to the baseband mixer
- τ_4: delay between LO2 and the baseband mixer

Note that all of the above delays except τ_1 are different for each correlator band.

We assume τ_1 is zero, because the path lengths between the feed horn and each output of the OMT are nearly identical for each receiver (they differ by $\sim$0.1 inch). 0.1 in is a significant path-length difference at 230 GHz; however, both the LO and the incoming radiation travel through the same path, and each suffer virtually the same delay through the OMT. The delay we need to be concerned with is that suffered by the IF, which is the frequency difference between the LO and the sky signal. An 0.1 in path-length difference at the 1–9 GHz IF frequency causes a minimal phase shift.

τ_2 causes an overall phase slope across the entire IF bandpass. This is caused by differences in fiber lengths between the receivers and the correlator.

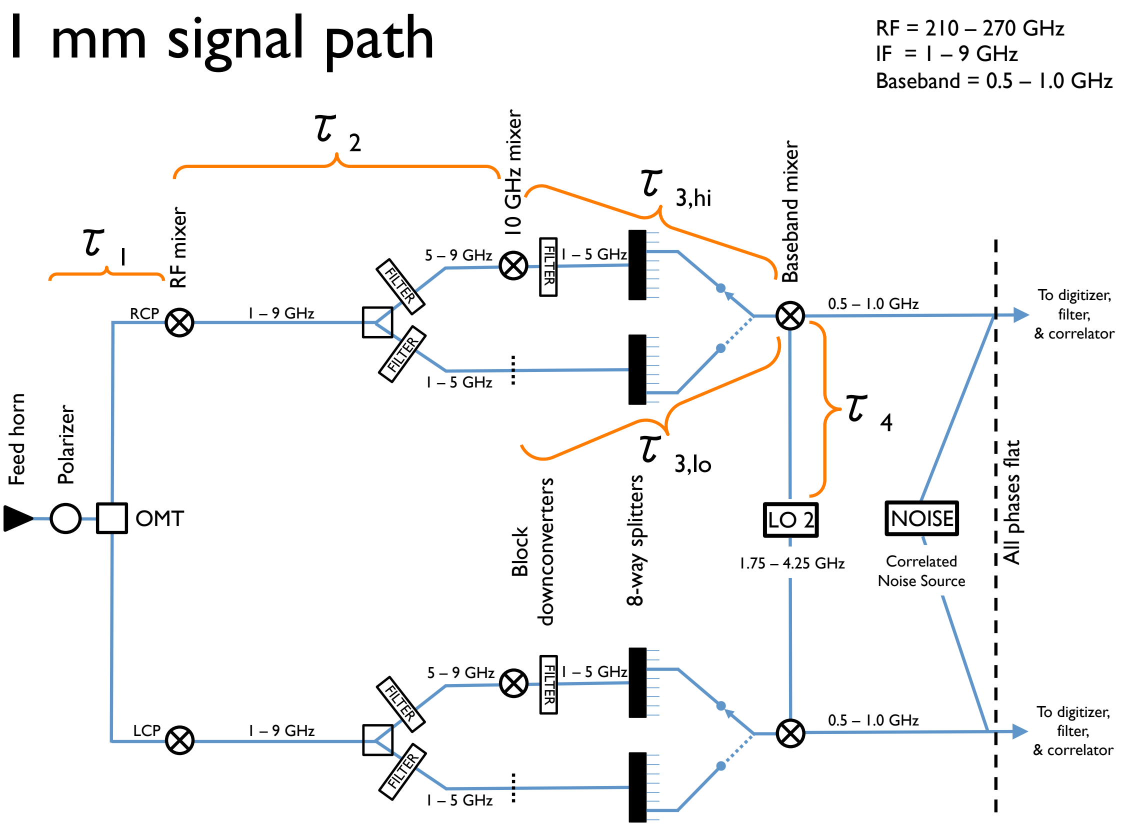

Figure 2.3: Basic schematic of the signal path of the 1.3 mm dual-polarization receiver system at CARMA.

$\tau_{3,\text{lo}}$ and $\tau_{3,\text{hi}}$ (combined with τ_2) cause the slope across the band for each tuning below (lo) and above (hi) 5 GHz. These delays are the result of cable-length differences between the upper (> 5 GHz) path in the block downconverter (the path with the mixer) and the lower (< 5 GHz) path (without the mixer). These delays tended to be a few × 0.1 ns.

τ_4 causes the phase jumps between tunings, because LO2 has discrete values.

See Figure 2.4 for a sample fit to real `XYphase` data.

2.3.3 XYphase calibration using wire-grid polarizers

When the 10 m dish is pointed at zenith the following statements hold:

- Wire grids are vertical (see Figure 2.5).

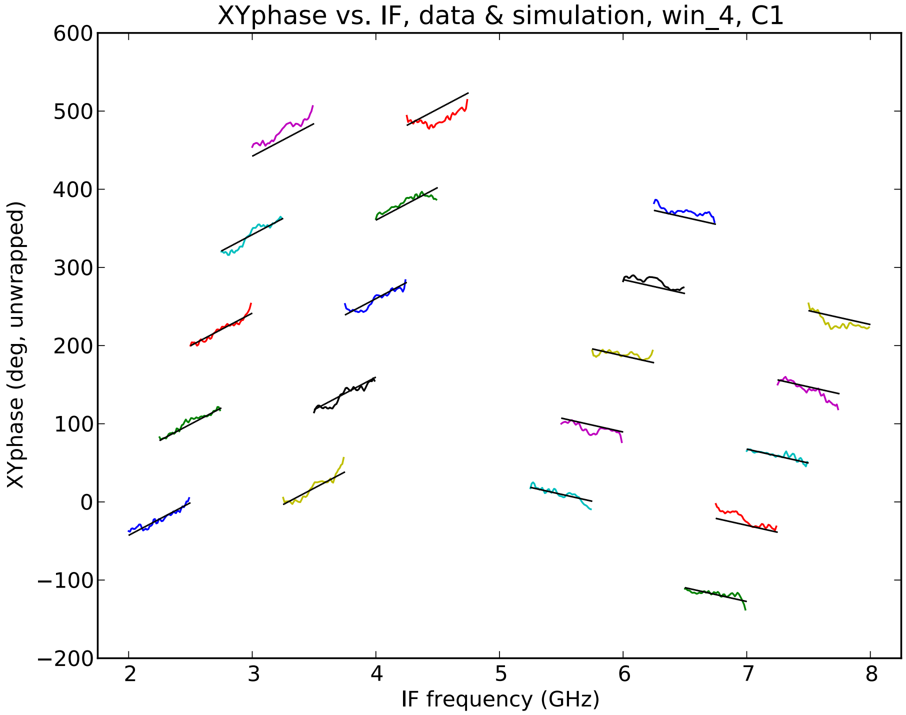

Figure 2.4: `XYphase` passbands for one correlator band on one telescope, stepped through many frequencies in the 1–9 GHz IF passband.

- The 1 mm receiver looks through the grid, and the transmitted E-vector is *horizontal*.
- At the tertiary, the E-vector is *horizontal*, and is perpendicular to the elevation axis (i.e., it is fore-aft).
- An astronomical source that is vertically polarized ($\chi = 0°$) will be transmitted through the grid.
- An astronomical source that is horizontally polarized ($\chi = 90°$) will *not* be transmitted through the grid.
- The polarized noise source (i.e., radiation reflected off of the grids) is equivalent to a source on the sky with a PA of $\chi = 90°$.

For the standard grid observations, the grid wires reflect hot ($\sim$300 K) ambient radiation from the telescope cabin into the receiver, making a strongly polarized noise source with an effective $\chi = 90°$. Using the `MIRIAD` task `XYAUTO`, we define the `XYphase` to be 0° (i.e., we define RCP and LCP to be in phase) when the receiver is looking at the noise source.

As a test, we observed the bright quasar 3C279 *with the grids in place;* the radiation from the quasar, after passing through the grids, had an effective $\chi = 0°$. As expected, we found that the RL and LR phases (i.e., the `XYphase`) on all baselines that included a 10 m antenna were ± 180° (as opposed to the case above when the receiver is observing ambient radiation from the grids with $\chi = 90^\circ$ and an `XYphase` of 0°).

A 90° rotation of χ is equivalent to a 180° rotation of the `XYphase`. This is because of the circular-to-linear conversion: an R–L phase change of 90° will transform the radiation from linear (in phase) to circular (90° out of phase); another 90° change will transform the radiation from circular to the linear (180° out of phase, with a position angle perpendicular to the original linear orientation).

The reference plane where RCP and LCP are in phase corresponds to a position angle on the sky of $\chi = 90^\circ$. Consequently, in order to derive the correct polarization position angle for sources on the sky, in the CARMA install of MIRIAD we define

$$\texttt{evector} = 90^\circ \ . \tag{2.39}$$

Note that while changing `evector` does affect χ, it *does not* affect the leakage terms, because no matter how you rotate the frame of reference of the feeds, their complex leakage into one another should be the same.

Also note that the when viewing raw data with UVPLT, for example, the parallactic-angle- and `evector`-based rotation matrices *have not* been applied. Only when the Stokes parameters I, Q, U, V are finally created—i.e., with INVERT or UVFLUX—are the rotation corrections applied on a record-by-record basis.

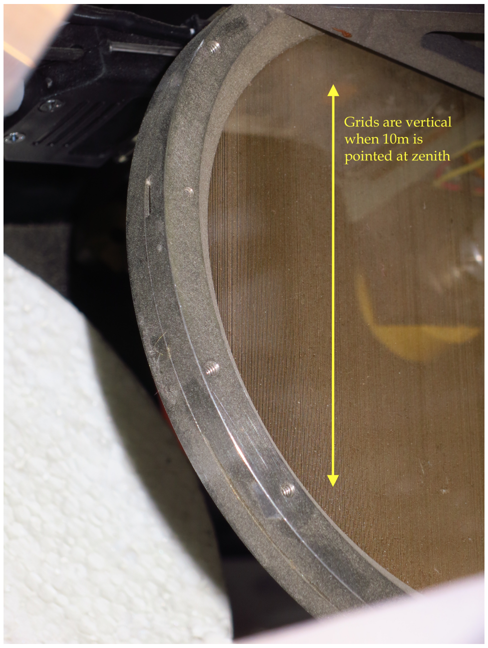

Figure 2.5: A photo of the wire-grid polarizers in the 10 m receiver cabins. The orientation of the grid is vertical when the telescope is pointed at zenith.

Figure 2.6 shows a schematic of how the wire grid polarizers produce a highly polarized noise source by reflecting ambient radiation into the receiver.

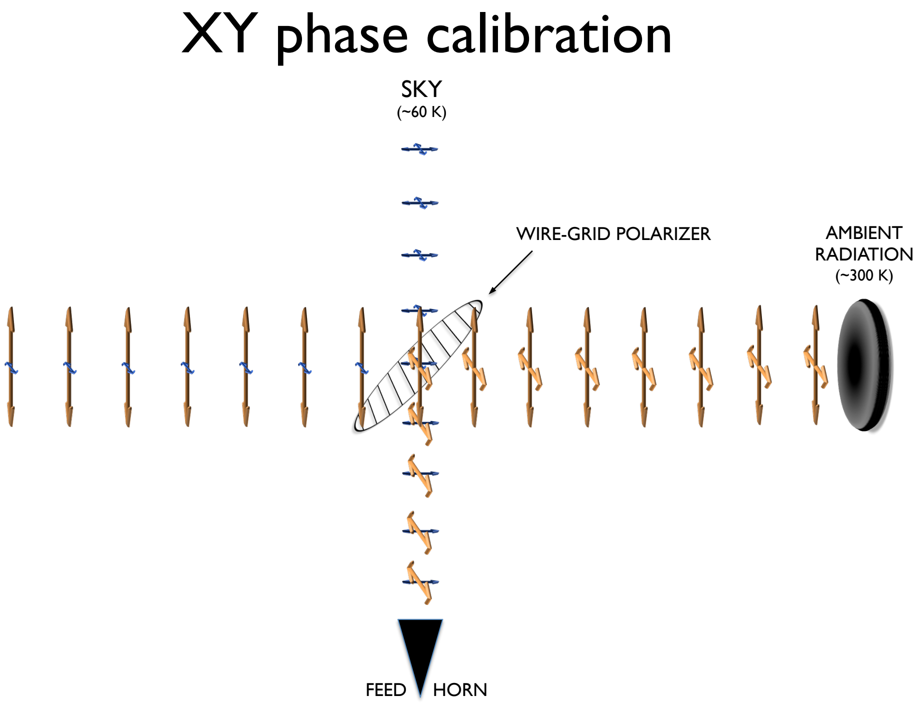

Figure 2.6: A schematic showing how the wire grid polarizers produce a highly polarized noise source by reflecting ambient radiation into the receiver.

On 26 October 2011 we adjusted the angles of the grids on the 10 m telescopes. The grids are driven by a computer controlled motor; after pointing each telescope at zenith[4], we adjusted the grid position offsets in the motor drives until the grids were level (according to a bubble level). The new offsets put into the system ranged from roughly 1–4°. The resolution of the motion of the motor moving the grid is about 0.2°. After correction, the grid positions should be accurate to within $\sim 1°$.

---

[4] Note that to point exactly at zenith one must use the hand paddle, override the limits, and put in the ambient load to prevent the receivers from getting fried by CloudSat.

2.3.4 Systematic limits to `XYphase` measurements

2.3.4.1 SNR of polarized signal with the grids in place

Even without the wire grids in place, the cross-auto `XYphase` passband has phase structure due to coupling between R and L, either from polarization leakage or from noise that is common to both channels. In order to derive a reliable `XYphase` passband, the noise source signal must be much larger than this, or the measurements will be corrupted.

Fortunately, in typical 1 mm weather, with the grids in place the amplitude of the RL cross-auto spectrum is ~ 20 times higher than the amplitude with the grids out. That is good for `XYphase` measurement: 1 part in 20 leads to an error of 1/20 radians, which corresponds to an error of $\sim 1.5°$ in position angle.

2.3.4.2 Effect of bad weather (via high T_{sys}) on `XYphase` measurements

Good `XYphase` observations require good weather, since the strength of noise source depends on sky temperature. In cases when the sky temperature is close to the ambient temperature in the telescope cabin, the reflected (ambient) component and the transmitted component (from the sky) have approximately the same power, and thus the radiation entering the receiver is no longer strongly polarized. However, even though bad weather affects the apparent polarization fraction of the noise source, it should not create a bias in the absolute phase measurements.

2.3.4.3 High leakages may affect position angle measurements

Leakages could potentially perturb the cross-auto `XYphase` measurement, thus affecting the final PA we calculate. This error could arise because we measure phase differences using the R vs. L correlation on the same antenna. Some R leaks into L, and vice versa; the worst leakage amplitudes are 12%, and would cause twice that fractional error in `XYphase`: $\sim 25\%$ of a radian, or 15°. This would correspond to a PA error of 7.5°.

So far we have assumed that this is a minor effect, and thus we calibrate the R–L phases first and compute leakages later (also, there is no easy way of taking out channel-dependent leakages first and then fitting the `XYphase`). As described in Section 2.3.6, we have seen differences in PA when using different 10 m antennas as the reference; however, we don't see a correlation between high leakages and large PA offsets. This suggests that the PA offsets are not being caused by high leakage terms.

2.3.4.4 Phase-lock loop (PLL) jitter

Each correlator band uses separate digitizers for R and L, and the digitizers are not directly run off of a single 1 GHz clock, but instead are run off of independent clocks that are phase-locked to a common reference signal. One systematic effect that limits our ability to measure absolute position angle is rapid variation in `XYphase` solutions caused by jitter (phase noise) in the 1 GHz PLL outputs. See Figure 2.7 for plots of the `XYphase` residuals (after correction), which show 1–2° variations in the R–L phase every 0.5 s.

See Figure 2.8 for two plots, each showing the relative change in phase for a few channels of a single cross-correlation spectrum over a series of 500 ms integrations. The baseline used is the one calculated within the digitizer between its A and B inputs. The left-hand plot shows the results with the board in "normal" mode, where each digitizer channel is clocked by a separate 1 GHz PLL; it exhibits the same 1–2° of rapid phase variability that we see in the `XYphase` measurements. The right-hand plot shows the same test performed using a single clock for both channels, and the phase is steady (the boards are capable of operating in this mode, but currently do not).

2.3.5 Absolute position angle calibration using 3C286

Absolute PA calibration at centimeter wavelength is usually performed using observations of 3C286, a quasar known to have a very stable polarization position angle $\chi = 33°$ (measured counterclockwise from north). However, the position angle begins to increase at higher frequencies: our CARMA observations yield $\chi = 39.9°$ (see Table 2.2), which is roughly consistent with recent measurements by Agudo et al. (2012): $\chi = 37.3 \pm 0.8°$ at $\lambda\,3$ mm and $\chi = 33.1 \pm 5.7°$ at $\lambda\,1.3$ mm. Our results are also consistent with ALMA (Atacama Large Millimeter-submillimeter Array) commissioning results at $\lambda\,1.3$ mm ($\chi = 39°$; Stuartt Corder, priv. comm., 2013), as well as with centimeter observations compiled by Perley & Butler (2013), who showed that the polarization position angle of 3C286 increases slowly from $\chi = 33°$ at $\lambda \gtrsim 3.7$ cm to $\chi = 36°$ at $\lambda\,0.7$ cm.

Because of the uncertainty in the PA of 3C286 and high frequencies, and because we get different answers using different antennas (see Section 2.3.6.1), we find that it is preferable to use the polarization of Mars to calibrate 3C286 (see Section 2.3.6).

2.3.6 Absolute position-angle calibration using Mars

One way to perform absolute position-angle calibration without using a quasar like 3C286 is to observe a rocky planet or satellite, since these bodies are known to be polarized. The reflectivity of a surface depends on whether the incident radiation's plane of polarization is parallel or perpendicular to the plane of incidence (i.e., the plane defined by the incident and reflected rays). For spherical, solid bodies emitting blackbody radiation, the polarization orientations should be radial with respect to the planet.

If we were transmitting radiation toward the planet, then radiation polarized perpendicular to the plane of incidence (i.e., tangentially with respect to the surface) is able to reflect better than radiation parallel to the plane of incidence (i.e., radial with respect to the surface); at Brewster's angle, the latter is completely absorbed into the planet. In the case of thermal emission, we can simply reverse this scenario, finding that we see thermal emission that is polarized radially. This phenomenon has been seen before in, for example, observations of the Moon (Heiles & Drake 1963; Davies & Gardner 1966; White & Cogdell 1973); Heiles &

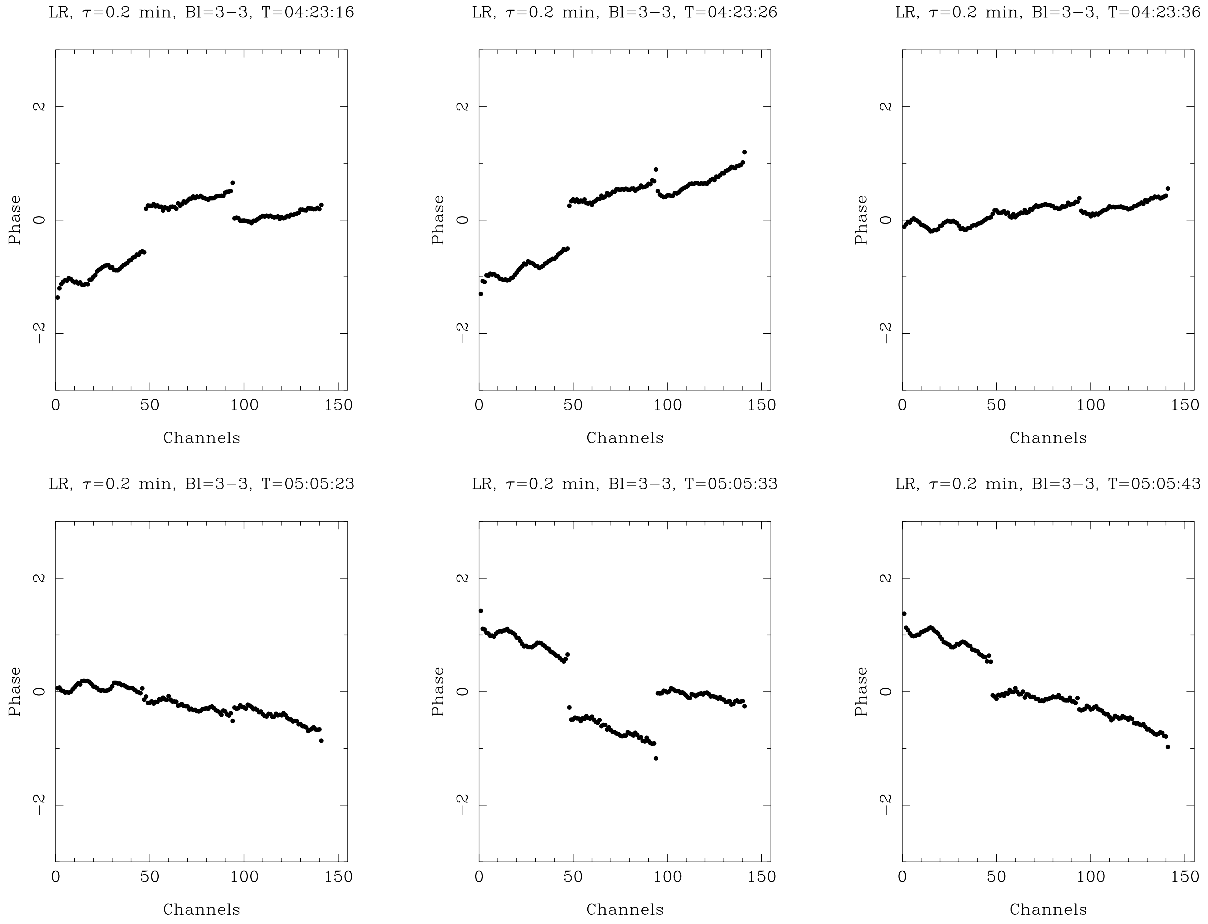

Figure 2.7: 1–2° jitter in the `XYphase` residuals (after correction). This is caused by jitter (phase noise) in the 1 GHz PLL outputs. The data are the cross-auto (LR) data from antenna C3 with the grid in place.

Drake (1963) found that the maximum polarization of the Moon was ~20% when observed at $\lambda\,21\,$cm.

Mars is generally small enough to fit in the primary beams (fields of view) of CARMA and ALMA. Early attempts to calibrate the absolute position angle of the polarization system at ALMA used observations of Mars (Bryan Butler and Stuartt Corder, priv. comm., 2013).

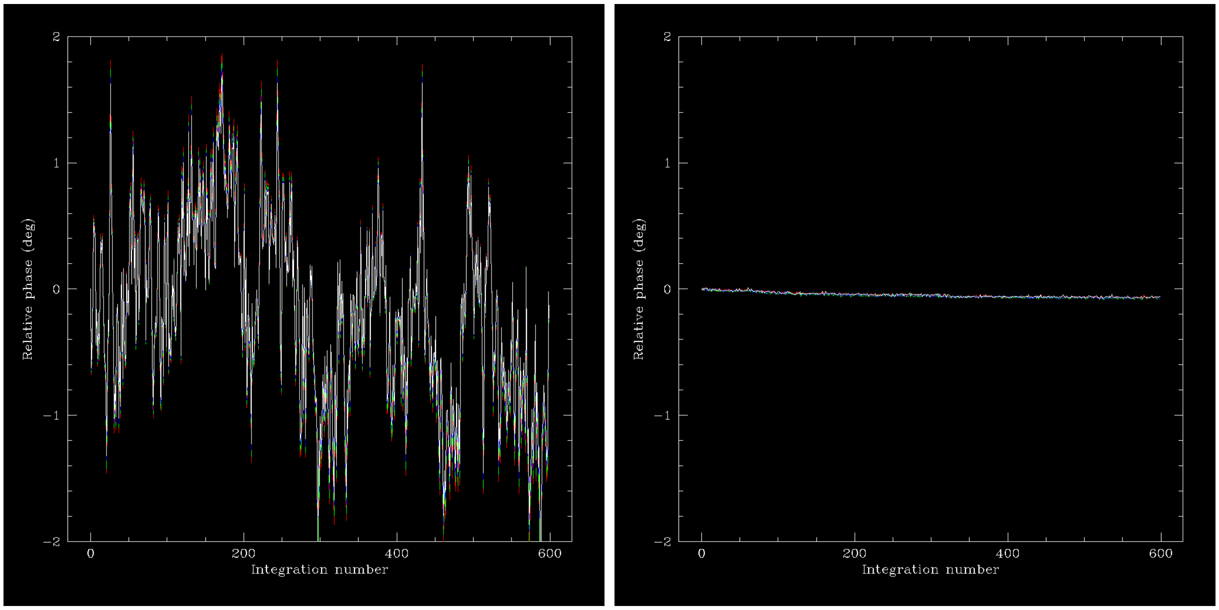

Figure 2.8: **Left:** 1–2° jitter (phase noise) in the 1 GHz PLL outputs. **Right:** Jitter goes away when a single clock is used for both channels. Credit: Kevin Rauch (University of Maryland at College Park).

2.3.6.1 Differing PA values from different 10 m antennas

Normally we use antenna C1 as the passband reference antenna (and, therefore, as the R–L phase calibration antenna) since it has relatively low leakages. For the data taken on 04 May 2014 we checked the absolute position angle calibration from polarization maps of Mars; near the limb of the planet the polarization orientations are expected to be perfectly radial, as described above.

Unfortunately, a different choice of reference antenna leads to a different absolute position angle calibration. As shown in column 5 of Table 2.2, for the 04 May 2014 data the offset ranges from –0.56° for C5 up to 8.7° for C6. These discrepancies are unlikely to originate from leakages; C3 has the worst leakages (magnitudes of order 10%), but its PA deviation is no larger than average. The deviations may originate in the optics between the wire grids and the primary mirrors of the 10 m telescopes, but further tests should be made.

For each choice of R–L reference antenna we also computed the PA for 3C286. Column 10 of Table 2.2 shows the corrected 3C286 PA values for each reference antenna; we corrected them by calculating the systematic deviation from radial of the Mars polarization orientations, and then subtracting those systematic offsets from the PA of 3C286. The answers are surprisingly consistent, with an average PA value of 39.9°.

Table 2.3 shows a summary of Mars polarization observations on two different days: 04 May 2014 (see Table 2.2) and 17 Jan 2014. The difference in the final corrected PA for 3C286

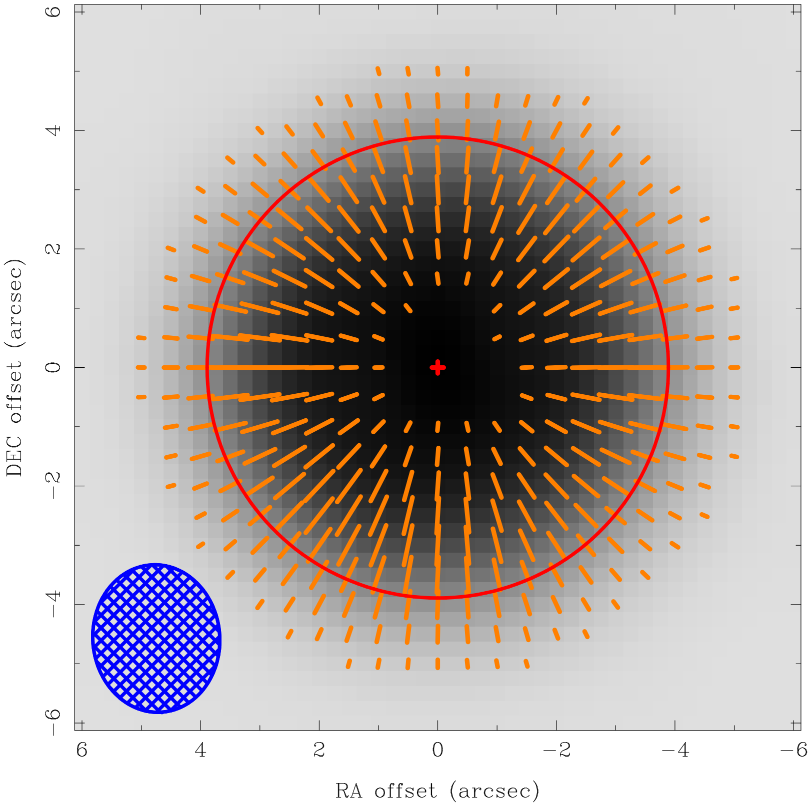

Figure 2.9: Polarization of Mars. Line segments indicate polarization orientation from the CARMA data; segment lengths are proportional to polarization intensity. The red circle indicates the diameter of Mars. The blue ellipse indicates the synthesized beam (resolution element). The polarization of spherical, solid bodies like Mars should be radial.

between the two days is unexplained, but may be because the 17 Jan track was a short, snapshot observation and the 04 May track had wide parallactic angle coverage.

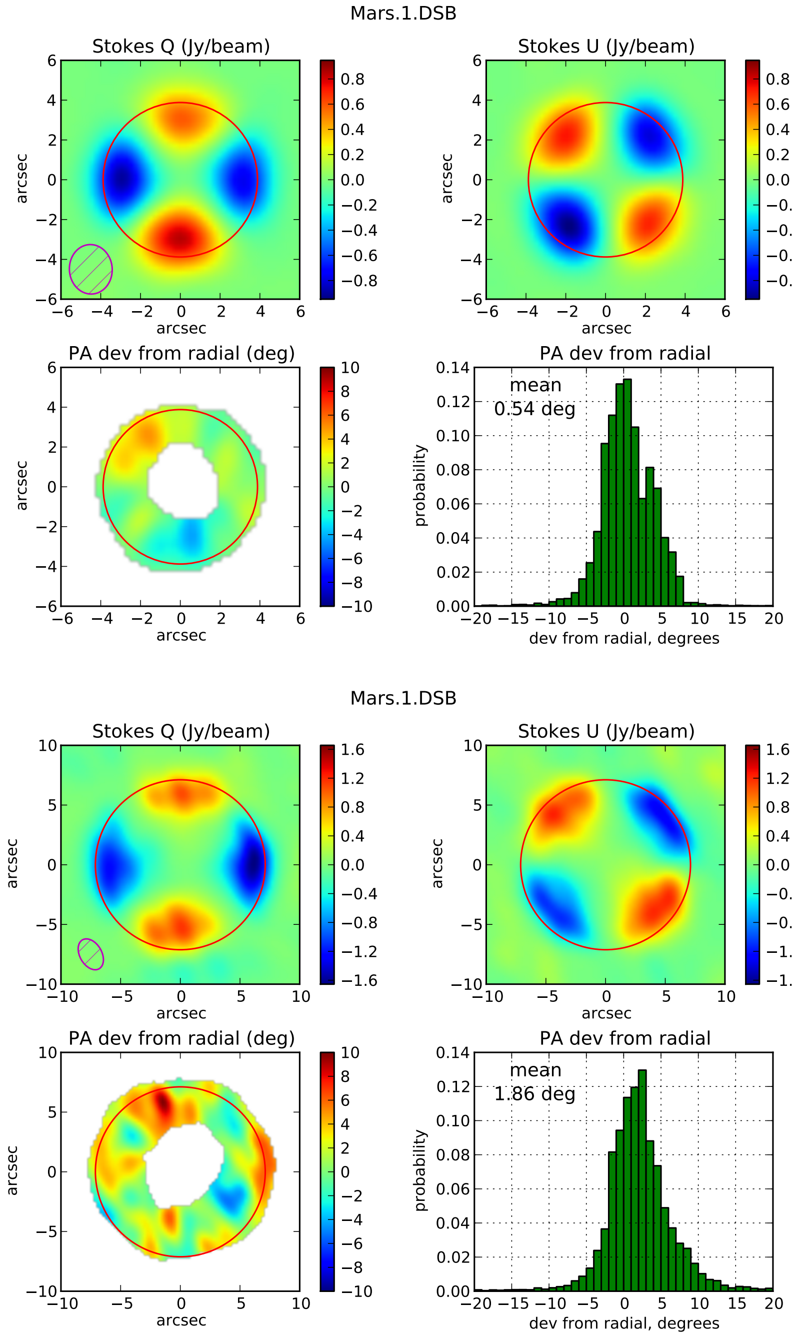

Figure 2.10: Analysis of deviation from radial of Mars polarization data. The red circle indicates the diameter of Mars. Radial deviations are computed only at pixels where the polarized intensity is > 0.3 Jy/beam. The color scale on the deviation map runs from –10 to 10°. Values are weighted by polarized intensity when computing the mean deviation. Data were taken on 17 January 2014 (top) during a snapshot observation, and on 04 May 2014 (bottom) during an observation with wide parallactic-angle coverage.

Table 2.2: PA deviations in measurements of Mars and 3C286

(1)	(2)	(3)	(4)	(5)	(6)	(7)	(8)	(9)	(10)
R–*L* cal	Mars radial dev (deg)				3C286 PA (deg)				3C286 PA (deg)
antenna	LSB	USB	USB−LSB	DSB	LSB	USB	USB−LSB	DSB	corrected
C1	0.69	3.50	2.81	1.77	40.71	42.25	1.54	41.62	39.85
C2	4.96	6.20	1.24	5.29	44.92	45.07	0.15	45.13	39.84
C3	4.21	4.86	–0.53	3.97	44.15	43.51	–0.64	43.95	39.98
C4	5.73	6.87	1.14	5.74	45.63	45.51	–0.12	45.69	39.95
C5	–0.14	–0.02	0.12	–0.56	39.71	38.62	–1.09	39.29	39.85
C6	8.23	9.74	1.51	8.70	48.19	48.80	0.61	48.63	39.93

Table 2.2: Deviation from radial of the Mars polarization orientations, and 3C286 position angles, as a function of the *R*–*L* phase calibration antenna. Leakages derived on 04 May 2014 were used. Lower sideband (LSB; 217.75 GHz), upper sideband (USB; 232.25 GHz), and double sideband (DSB; 225 GHz) values are given. For reasons that aren't clear, the DSB values are not necessarily the mean of the LSB and USB values. The last column shows the 3C286 DSB position angles corrected by the Mars DSB radial deviations. Data were taken on 04 May 2014 during an observation with wide parallactic-angle coverage.

Table 2.3: Average PA deviations in measurements of Mars and 3C286

Date	Mars diameter	Beam size	3C286 PA dev, DSB (deg)						3C286 PA (deg)
			C1	C2	C3	C4	C5	C6	corrected
17 Jan 2014	$7.8''$	$2.49 \times 2.15''$	0.54	4.96	2.54	4.39	–1.83	4.54	38.5
04 May 2014	$14.2''$	$2.92 \times 1.71''$	1.77	5.29	3.97	5.74	–0.56	8.70	39.9

Table 2.3: Same as Table 2.2, but for two separate observations on 17 Jan 2014 and 04 May 2014. The difference in the final corrected PA for 3C286 is unexplained, but may be because the 17 Jan track was a short, snapshot observation and the 04 May track had wide parallactic angle coverage.

2.4 Leakage Calibration

One can measure the leakages by observing a strong calibrator, polarized or not, over a range of parallactic angles; ideally the observation will be centered on the time when the calibrator transits. Over the course of the observation the RL and LR cross correlations will change in a predictable way if source is polarized, but will be constant if leakage is responsible.

The `MIRIAD` task `GPCAL` fits for both the intrinsic and the instrumental polarization from the leakages. Given good weather and normal antenna performance, a 4–6 hr observation in which the calibrator crosses transit yields a reliable leakage solution.

2.4.1 Instrumental polarization and position-angle errors caused by scatter in leakage values

Leakage solutions can vary slightly from track to track, with the Re and Im parts of the leakages varying by up to a few × 0.01. To test the effects of these variations on the solutions of polarization position angle and fraction, we performed simulations using `UVGEN`.

The simulated UV data included thermal noise consistent with typical 1 mm weather at CARMA: system temperatures of 300 K and opacity $\tau \approx 0.3$. The data comprised 8 GHz of continuum bandwidth, and included a point-source with a flux of 1 Jy and at an elevation of 30°. We used actual leakage terms from CARMA polarization data as the initial set of values.

We performed two tests, examining how variations in leakage terms affect the polarization fraction and PA of (1) a snapshot observation (i.e., when we're finding the polarization of the passband calibrator, which is only observed for 10 min), and (2) a longer, ∼ 6 hr observation of the calibrator or the science target.

The simulations proceeded as follows:

- Used `UVGEN` to simulate leakage-free data: either a 10 min snapshot, or a long track covering ±3 hr around transit
- Copied "real" leakages (from a typical 1 mm CARMA polarization track) into the data file
- Rewrote the data to apply the leakages, thus corrupting the data
- Copied a negated version of the above leakages into the dataset after varying the leakages' Re and Im parts using Gaussian random errors with standard deviations between 0.01 and 0.03
- Used `UVFLUX` to find the % and PA of the source
- Ran a Monte-Carlo test for point sources with 0%, 1%, and 10% polarization, and calculated the standard deviation of the polarization fraction and PA for each value of the leakage error

Copying negated leakages into the dataset would have corrected the previously corrupted data exactly. However, copying a set of leakages whose Re and Im parts were modified slightly resulted in slight differences in the calculated PA and %. Performing these simulations gave us a handle on how robust our calculated PA and % values were to typical leakage variations.

See Figure 2.11 for the results. Looking from the left-hand to the right-hand plots, it is clear that snapshot observations are more susceptible to scatter in PA and % than longer tracks. Additionally, sources with higher polarization fraction are more robust to scatter in leakage terms.

Looking at the plots of the scatter in the polarization fraction, we conclude that the instrumental polarization caused by the typical leakage errors of ~ 0.01 is $\sim 0.3\%$ for a snapshot and $\sim 0.1\%$ for a longer track. The corresponding variations in position angle are $\sim 8^\circ$ and $\sim 3^\circ$ for a 1% polarized source (PA errors are larger for sources with weaker polarizations).

See Figure 2.12 for a histogram of the scatter in leakage solutions from several different datasets obtained over a two-month interval. In that case the standard deviation of the Re and Im parts of the leakage terms was ~ 0.009; however, in other cases the standard deviation can be as small as ~ 0.002.

2.4.2 The dynamic range limit: unreliable solutions for very weakly polarized sources

When a source is very weakly polarized ($P_c/I \lesssim 0.5\%$), very small changes to the leakages can cause drastic changes to the resulting polarization position angles across the source. For example, when analyzing CARMA data toward the protoplanetary nebula CRL 618 (see Sabin et al. 2014) we saw position angles that varied by up to 90° from night to night depending on how exactly we reduced the data. The reason for this was that the source was extremely bright at 1.3 mm ($\sim 2\,\mathrm{Jy\,bm^{-1}}$), but was very weakly polarized ($\sim 0.5\%$ polarization at the intensity peak), which caused us to hit a dynamic range limit where the polarization detected at very low levels can be caused by imperfections in the leakage solutions.

The scatter in the Re and Im parts of the leakage solutions on the two nights was ~ 0.01, which is standard; however, in this case those slight differences led to significantly different maps for Q and U. These small changes in leakages caused virtually no variations in the maps for the TADPOL sources, which were on average at least a few percent polarized, and which tended to be much fainter sources where the ability to detect polarization was limited by the system temperature instead of by dynamic range.

We therefore urge caution when interpreting sources with polarization fractions of $< 0.5\%$.

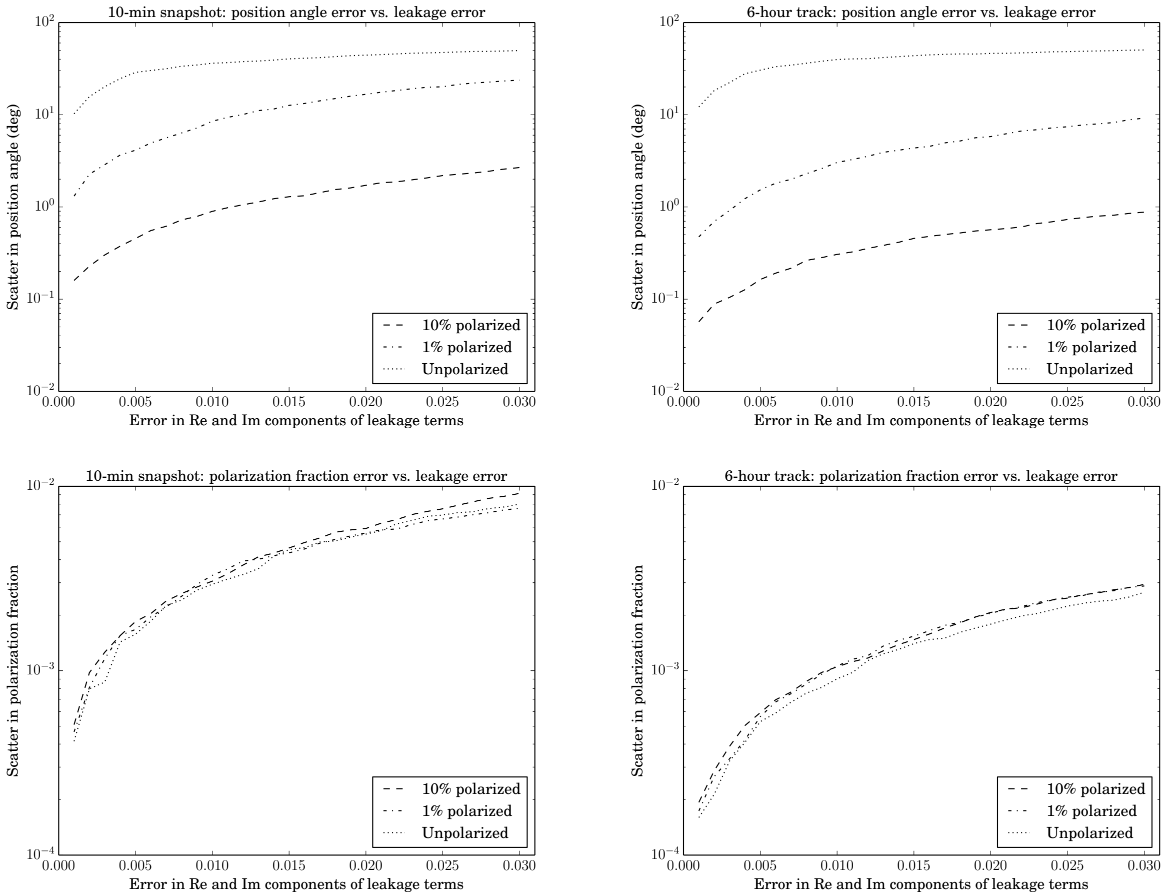

Figure 2.11: Errors in PA and fractional polarization as a function of leakage errors.

2.4.3 Leakage ripples as a function of frequency

2.4.3.1 Reflections in the receiver

See Figure 2.13 for plots showing leakage amplitudes for C1 (a good antenna) and C13 (a particularly bad antenna) based on 5 datasets from 2012 to 2014. These plots show that some antennas have ripples in the leakage amplitudes as a function of frequency, and also that the leakages are quite stable with time.

C13 (particularly for D_R) shows ripples with a period of about 1 GHz, which corresponds to a reflection with a round-trip distance of 30 cm ($\approx$ 12 in). This could indicate a reflection from the mixer back to the dewar window and then back to the other mixer, since the path length through the OMT is $\sim$ 1 in, the circular polarizer is 0.75 in long, the feed horn is about 2 in long, and then there is another $\sim$ 2 in to the dewar window (for a total of $\sim$ 6 in).

To test the reflection hypothesis, we attempted to reduce the reflection off of the RCP

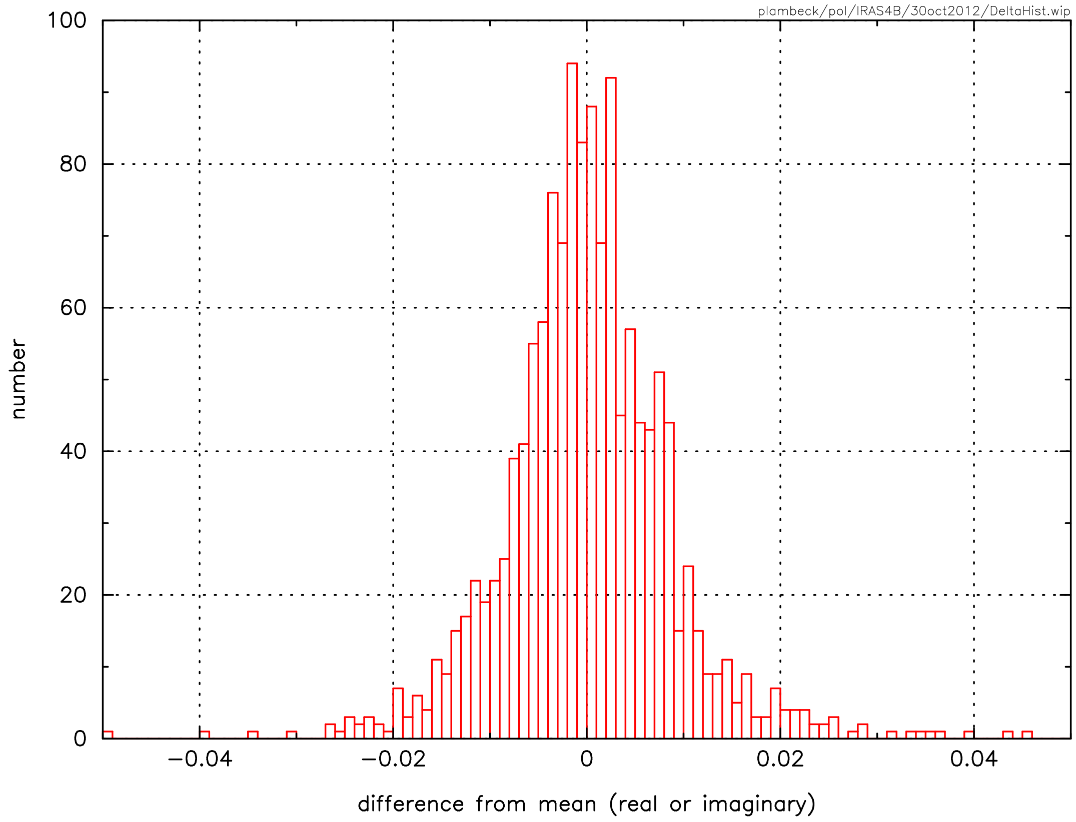

Figure 2.12: A histogram of the differences of 4 leakage solutions from their mean. The values encompass the real and imaginary components for D_R (leakage from LCP into RCP) and D_L (leakage from RCP into LCP), for 6 correlator windows and all 15 telescopes. The leakage solutions are from 02 September 2012, 25 September 2012, 25 October 2012, and 30 October 2012. The standard deviation is 0.0089.

mixer in antenna C9 by changing the mixer bias (see Figure 2.14). Reducing the reflection off of one mixer would reduce the leakage ripples in the opposite receiver. For the data shown in cyan in Figure 2.14, the RCP mixer was biased to 13 mV. This is above the superconducting energy gap, so no RCP astronomical signals would have been downconverted. However, the SIS mixer reflection coefficient probably is lower at this bias, so the RCP signal bouncing off the mixer may have been reduced.

What would we expect if the reflection were reduced? First, we expect to see just noise for the RCP leakages, because there is no signal in that band. And indeed, we see very noisy values (see the cyan data in Figure 2.14, lower panel). For the LCP leakages, the amplitude of the ripples appears to be smaller (cyan data, upper panel). This is consistent with the hypothesis that the RCP signal reflects off the RCP mixer, bounces off the dewar window as LCP, and thus appears as an LCP leakage. We reduced the reflection, so we reduced the ripple.

Unfortunately, there is still some ambiguity regarding where in the receiver the ripple originates. This mixer-bias result could also mean that all the cross-coupling happens at the downconverters (see Section 2.4.3.2): since we eliminated the RCP signal, there would have been nothing to cross-couple to the LCP channel. We also tried both tilting the dewar lens to change this reflection and adding a thick sheet of Mylar in front of the lens to increase the reflection; we did not see much change in either case.

2.4.3.2 Cross-coupling in the block downconverter

Another potential source of the leakage ripples is cross-coupling in the block downconverter. See Figure 2.15 for a plot of leakage ripples from antennas C1–C4. Two correlator sections were positioned above 5 GHz in the IF (middle columns), and two below 5 GHz (outer columns). One sees a very pronounced ripple in D_R (but not D_L), and only below 5 GHz. This means that LCP was leaking into RCP but not vice versa.

The output of the block downconverter has a switch that selects either low-band RCP, high-band RCP, low-band LCP, or high-band LCP, and sends that signal on to the downconverter. The switch has 40–50 dB isolation between ports, but this is not enough if one signal is much stronger than another. For example, suppose the switch has 45 dB isolation but that the RCP signal is 15 dB stronger than the LCP signal. Then the relative level of RCP in the LCP IF is –30 dB, which means that the RCP voltage is 0.03 × the LCP voltage. There is an extra path length for the RCP voltage, so it gets in and out of phase with the RCP that leaks through the polarizer (for example), causing a 6% peak-to-peak ripple in the leakage, comparable with what we see in the broadband leakage terms. By attenuating the RCP relative to the LCP, we found we could make the leakage ripples move from D_R to D_L.

See Figure 2.16 for evidence that additional attenuation in the block downconverter can indeed reduce ripple amplitudes. Before additional attenuation, the RCP power into the block downconverter was greater than the LCP power by 16 dB for C9 and 9 dB for C13. We installed 10 dB pads for RCP on C9 and C13, and saw that pads reduced the ripples in the two correlator sections below 5 GHz. The pads had little effect on the sections above 5 GHz.

2.5 Primary-beam Polarization

If a source is not perfectly on-axis, then additional distortions are introduced across the primary beams of the telescopes. To check for these variations in the instrumental polarization, we observed BL Lac (a bright, highly polarized quasar) at 16 offset positions, eight of which were 12″ and eight of which were 24″ from the field center.[5] Our aim was to

---

[5] The analysis presented below only uses the data taken 12″ from the field center.

characterize the “beam squint” and “beam squash.”

Beam squint arises when the feeds of the telescope are tilted with respect to the optical axis of the primary reflector, causing the LCP and RCP responses to be slightly offset from the symmetry axis. Beam squint is discussed in Chu & Turrin (1973); Adatia & Rudge (1975); Rudge & Adatia (1978). Squint manifests itself as a double-lobed pattern in Stokes V, which is the difference of RCP and LCP.

Beam squash is caused by differences in the beam widths of the orthogonal polarizations. These beam width differences are caused by two phenomena: (1) the way the linearly polarized radiation reflects off of a curved parabolic reflector, and (2) the fact that linearly polarized radiation propagating through a circular waveguide has a non-circular beam width (this is because the beam width is larger is the direction where the polarization is perpendicular to the waveguide wall, but smaller in the direction where the polarization is parallel to the wall; when radiation is parallel to the wall it essentially “shorts out.”). Most feeds are now designed to minimize the waveguide effect, and thus the dominant effect would be reflection. Squash manifests itself as a four-lobed “cloverleaf” pattern in the linearly polarized Stokes Q and U maps. This phenomenon is discussed in Napier (1994, 1999); the term “beam squash” was coined in Heiles et al. (2001a).

Maps of both squint and squash have been made by Robishaw (2008) for the Green Bank Telescope (GBT) and Heiles et al. (2001a) for Arecibo.

2.5.1 Beam squint

While the CARMA system is almost always used for measuring linear polarization, we are still able to make maps of Stokes V, and are thus able to measure squint. Beam squint is normally characterized using the squint angle Ψ_s (Rudge & Adatia 1978, Equation 25; see also Napier 1994):

$$\begin{aligned}\Psi_s &= \arcsin \frac{\lambda \sin\theta_0}{4\pi F} && (2.40)\\ &\approx \frac{\lambda\theta_0}{4\pi F}\ , && (2.41)\end{aligned}$$

where λ is the observing wavelength, θ_0 is the angular offset between the feed and the telescope’s optical axis, and F is the focal length of the primary reflector. The approximation in Equation 2.41 is good when the angular offset θ_0 is small, which is usually the case.

The 6 m antennas have a Cassegrain design, with feed horn offset by $\Delta\mathrm{az} = 7.126'$ and $\Delta\mathrm{el} = 1.91'$ (Plambeck 2000). Using Equation 2.41 with an effective focal length of $F = 1186$ inches, the theoretical squint produced by these offsets should be incredibly small: $\approx 0.002''$. The measured squint is significantly larger ($\approx 0.45''$; see Figure 2.17, right panel). The 10 m antennas are on-axis (and should thus be squint-free); however, there are multiple reflections in the optical path, including three curved mirrors with $\sim 90°$ bends that are all in different planes. The odd number of off-axis reflections may be the cause of the 10 m squint, which is even worse than the 6 m squint ($\approx 2.16''$; see Figure 2.17, left panel). The significant squint that we measure in the 6 m and (especially) the 10 m antennas suggests that there are optical effects causing the squint that cannot be explained by the standard squint model.

In order to fit for the squint we solved for Stokes V at each ($12''$) offset position and for each 30 s integration on BL Lac. Note that we applied the gain and leakage corrections solved at the center position only. We calculated the offsets in the frame of the dish (in azimuth and elevation) by de-rotating the offset position (in RA and DEC) by the parallactic angle χ associated with the given integration. In order to derive the squint, we fit the data to the difference of two circular Gaussians $G_2 - G_1$:

$$G_1 = \exp(-\left[(\mathrm{az} - \Delta\mathrm{az}/2)^2 + (\mathrm{el} - \Delta\mathrm{el}/2)^2\right]/(2\sigma^2)) \tag{2.42}$$

$$G_2 = \exp(-\left[(\mathrm{az} + \Delta\mathrm{az}/2)^2 + (\mathrm{el} + \Delta\mathrm{el}/2)^2\right]/(2\sigma^2)) \ , \tag{2.43}$$

where $\sigma = \mathrm{FWHM}/(2\sqrt{2\log 2})$, and FWHM is the full-width at half-maximum of the primary beam at $\lambda\,1.3$ mm ($30''$ for the 10 m antennas and $56''$ for the 6 m antennas); Δaz and Δel are the vertical and horizontal components of the offset between the RCP and LCP beams, and the angle of the beam offset in the frame of the dish $\theta = \arctan(\Delta\mathrm{el}/\Delta\mathrm{az}) - 90^\circ$, measured east from north (or counterclockwise from vertical, in the reference frame of the antenna). We assume that the amplitudes of the Gaussians are identical, and that the two beams are offset by equal and opposite amounts ($\pm\Delta\mathrm{az}/2$ and $\pm\Delta\mathrm{el}/2$) from the pointing center.

2.5.2 Beam squash

Telescopes with native circular feeds like CARMA should see squash in both Stokes Q and U, which are both combinations of the cross-polarizations RL and LR (see Equations 2.7 and 2.8). For telescopes like the GBT and Arecibo with native linear feeds, it should be easier to see squash in Stokes U, which is calculated using the cross-polarizations XY and YX (see Equation 2.3) and is thus unaffected by XX and YY gain variations that can plague Stokes Q (see Equation 2.2). Maps of beam squash have been made in Stokes U for the GBT (Robishaw 2008) and in both Stokes Q and U for Arecibo (Heiles et al. 2001a) (note that for Arecibo the gain variations had a minimal effect, allowing excellent maps of both Stokes parameters).

We see no evidence in the Q or U CARMA maps for a quadrupolar squash pattern, which should have twice the frequency of the squint as one moves around the dish. However, variations in Q and U do lead to squint-like variations (i.e., a single crest and trough) in the polarization fraction and position angle (see Section 2.5.3).

2.5.3 Variation in polarization fraction and position angle across the primary beam

While we saw no evidence of squash in the data, we did see squint-like behavior in Q, U, and the PA and polarization fraction derived from them. This behavior is not expected theoretically, but is seen at Arecibo and discussed in various publications and technical memos including Heiles (1999); Heiles et al. (2001a, 2003); Heiles & Crutcher (2005).

We fit a sinusoid to find the peak-to-peak variation in the calculated PA and polarization fraction of both the 10 m and 6 m dishes. The 6 m dishes showed very little variation in PA and polarization fraction, whereas the 10 m dishes showed more (possibly because observations were further out into the primary beam). The 10 m antennas had peak-to-peak variations of $\sim 8^\circ$ in PA and ~ 0.02 in polarization fraction (0.02 represents a $\sim 25\%$ variation in the mean of the BL Lac polarization fraction). See Figure 2.18.

2.6 Summary

Above we describe the 1.3 mm dual-polarization receiver system built for CARMA. One of the key science goals for the system is to map the linearly polarized thermal emission from dust grains in interstellar clouds; maps of this polarized emission can then be used to infer the magnetic-field morphologies in these regions. We describe our work on this front in Chapters 3 and 4.

Here we have focused on the commissioning and calibration of the system. We began by briefly describing the basics of polarization, the receiver hardware, and the observing modes of the CARMA system. We then discussed in detail the two additional calibration steps required for interferometric polarization observations: leakages and absolute position angle χ. We have included an exhaustive list of the aspects of the system that we tested, the difficulties and systematic limitations we encountered, and the solutions we devised.

Acknowledgments (Chapter 2)

C.L.H.H. would like to acknowledge the advice and guidance of the members of the Berkeley Radio Astronomy Laboratory, the Berkeley Astronomy Department, the Owens Valley Radio Observatory, and the CARMA consortium. He would also like to thank Tim Robishaw for his clear and concise thesis introduction, which provided an excellent review of polarization basics.

C.L.H.H. acknowledges support from an NSF Graduate Fellowship and from a Ford Foundation Dissertation Fellowship.

Support for CARMA construction was derived from the states of California, Illinois, and Maryland, the James S. McDonnell Foundation, the Gordon and Betty Moore Foundation, the Kenneth T. and Eileen L. Norris Foundation, the University of Chicago, the Associates of the California Institute of Technology, and the National Science Foundation. Ongoing

CARMA development and operations are supported by the National Science Foundation under a cooperative agreement, and by the CARMA partner universities.

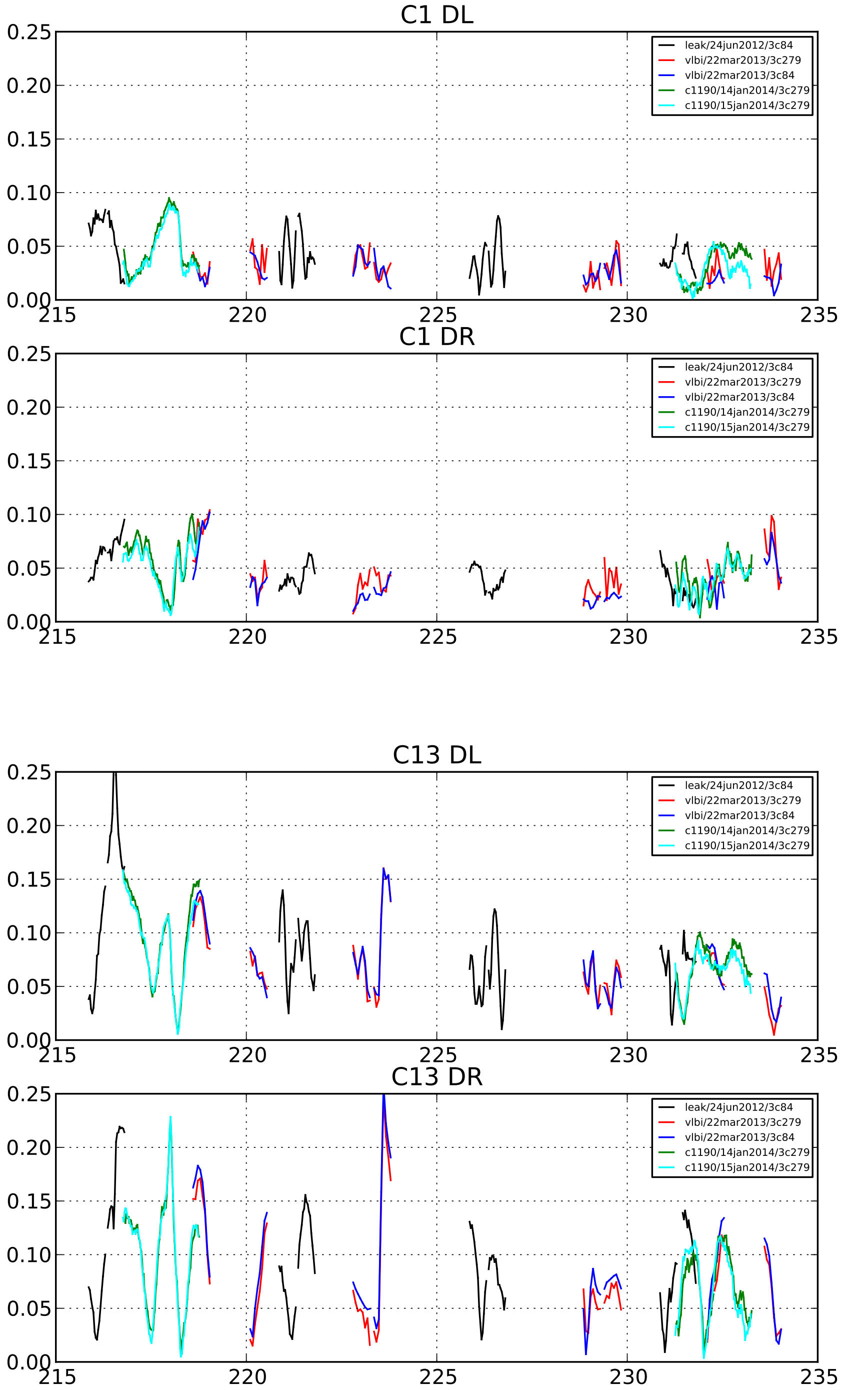

Figure 2.13: Leakage amplitudes as a function of frequency for antennas C1 and C13, based on five datasets from 2012–2014. “DR” is the leakage from LCP into RCP, and “DL” is the leakage from RCP into LCP. These plots exhibit ripples in the leakage terms as a function of frequency, and also show that the leakages are quite stable over time.

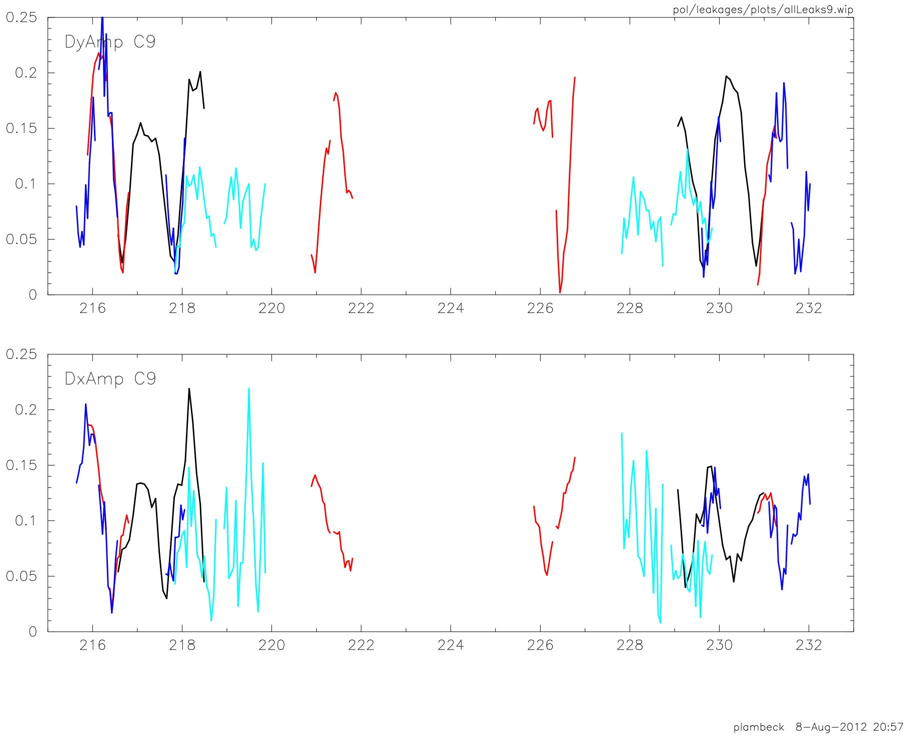

Figure 2.14: Leakage amplitudes as a function of frequency for antenna C9. For the data shown in cyan, the RCP mixer was biased to 13 mV, the SIS mixer reflection coefficient probably is lower at this bias, and thus the RCP signal bouncing off the mixer may have been reduced. "Dx" corresponds to D_R, or reflection of LCP into RCP; the cyan data show noise for the RCP leakages, because there was no signal coming from the RCP receiver.

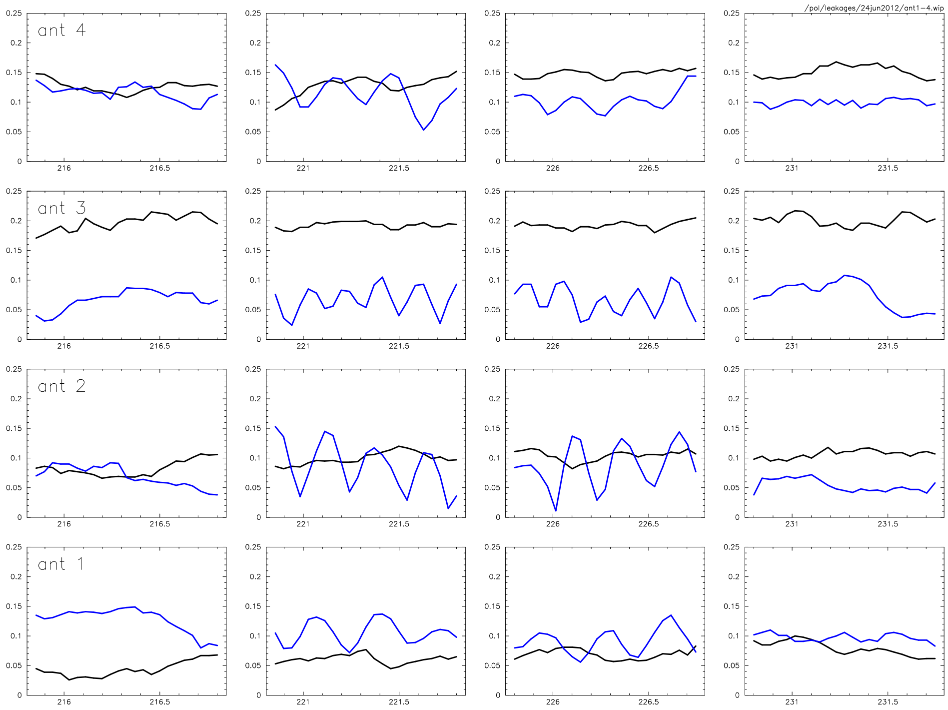

Figure 2.15: Leakage amplitudes as a function of frequency for antennas C1–C4. Two correlator sections were positioned above 5 GHz in the IF (the middle columns), and two below 5 GHz (the outer two columns). Black curves are D_L and blue curves are D_R. Data are from 24 June 2012, and are leakage solutions on 3C84.

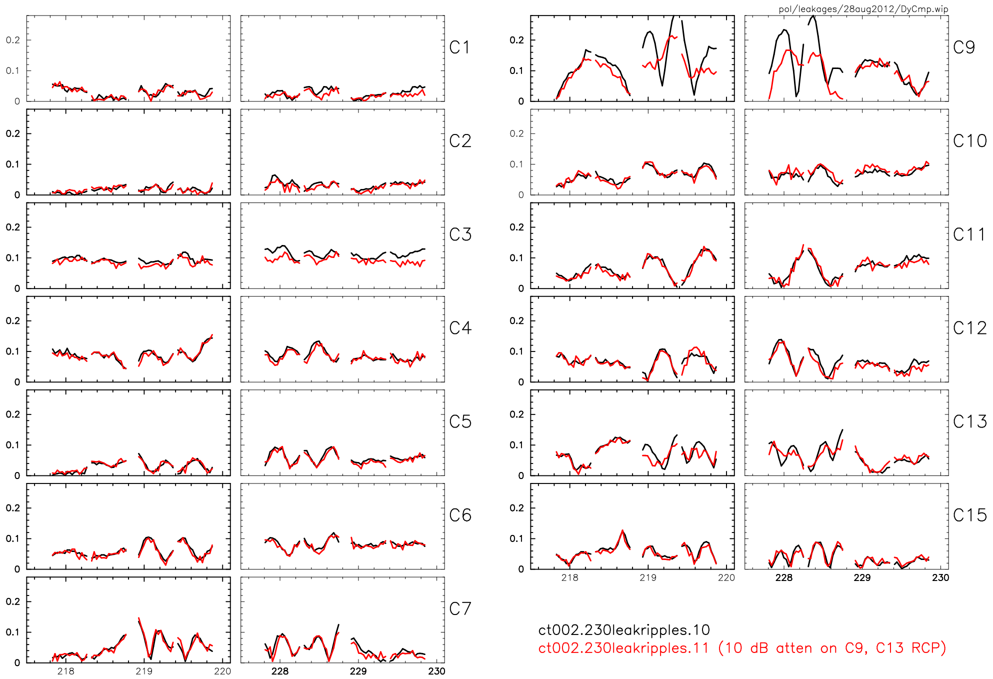

Figure 2.16: Leakage amplitudes as a function of frequency for antennas C1–C15. The curves show the leakage solutions before (black) and after (red) installing 10 dB attenuator pads on the RCP inputs to the block downconverters on C9 and C13. Inserting these pads reduced the ripples in the two correlator sections below 5 GHz, and had little effect on the sections above 5 GHz. Data are from 28 August 2012, and are leakage solutions on 3C84.

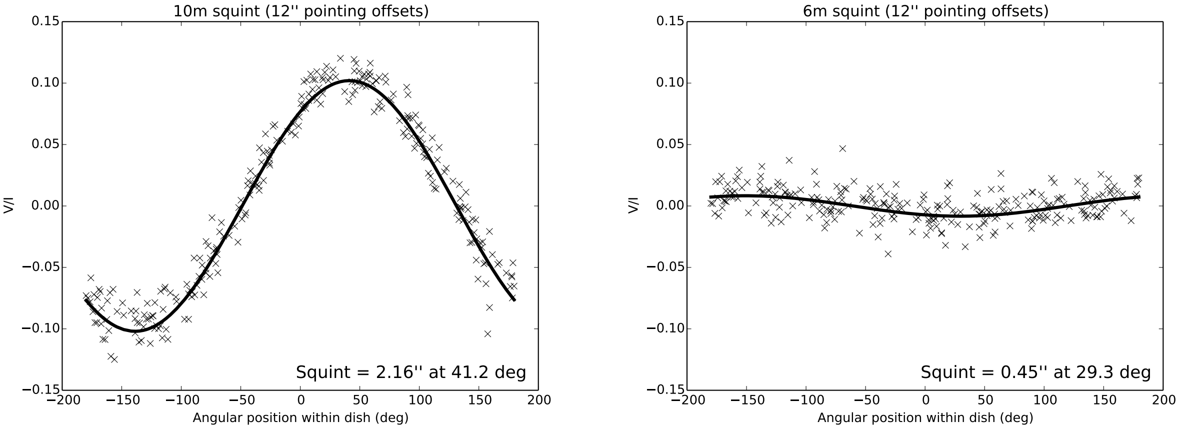

Figure 2.17: 6 m and 10 m beam squint, fit using data positions offset by 12″ from the pointing center. The solid curve is the the best-fit squint model (see Equation 2.43).

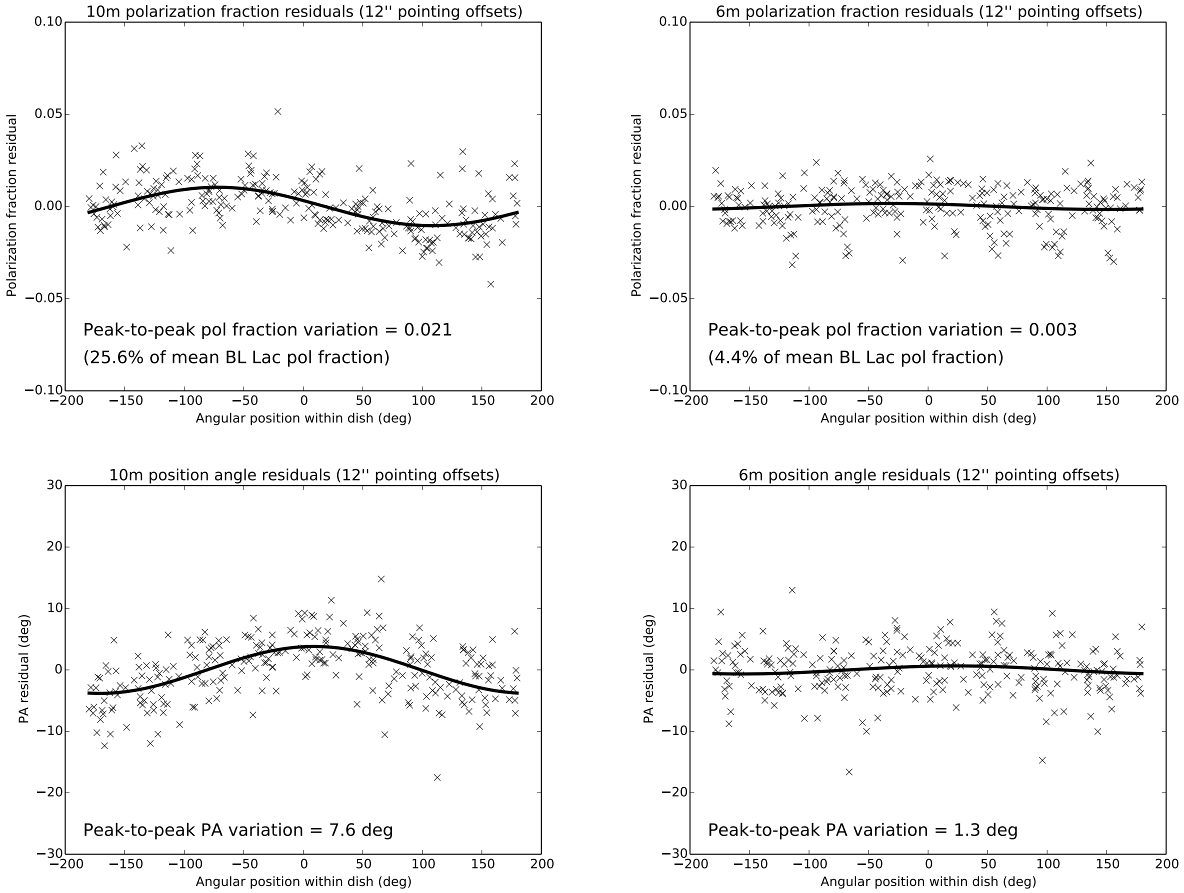

Figure 2.18: Variations of PA and polarization fraction across the 6 m and 10 m primary beams, fit using data positions offset by $12''$ from the pointing center. The solid curves are sinusoids fit to the data to find the peak-to-peak variations.

Chapter 3

Misalignment of Magnetic Fields and Outflows in Protostellar Cores

Previously published: Hull, C. L. H., Plambeck, R. L., et al. 2013, Astrophysical Journal, 768, 159.

We present results of λ1.3 mm dust polarization observations toward 16 nearby, low-mass protostars, mapped with ~2.5″ resolution at CARMA. The results show that magnetic fields in protostellar cores on scales of ~1000 AU are not tightly aligned with outflows from the protostars. Rather, the data are consistent with scenarios where outflows and magnetic fields are preferentially misaligned (perpendicular), or where they are randomly aligned. If one assumes that outflows emerge along the rotation axes of circumstellar disks, and that the outflows have not disrupted the fields in the surrounding material, then our results imply that the disks are not aligned with the fields in the cores from which they formed.

3.1 Introduction

Magnetic fields have long been considered to be one of the key components that regulate star formation (e.g., Shu et al. 1987; McKee et al. 1993). And indeed, observations of polarization in star-forming regions have shown that magnetic fields are well ordered on large scales, from the ~ kpc scales of the entire galaxy (Planck Collaboration et al. 2014a,b,c) to the ~ 100 pc scales of GMCs (Heiles 2000) to the ~ 1 pc scales of individual clouds (Pereyra & Magalhães 2004; Goldsmith et al. 2008; Franco et al. 2010; Palmeirim et al. 2013). This is evidence that B-fields in the interstellar medium (ISM) are strong relative to the turbulence in the ISM across many orders of magnitude. In other words, the turbulence in the ISM is sub-Alfvénic: the speed of turbulent motions v is less than the Alfvén speed $v_A = B/\sqrt{4\pi\rho}$, and thus the Alfvén Mach number $M_A = v/v_A$ is < 1.[1]

---

[1] Note that Crutcher et al. (1999) found approximately Alfvénic turbulence on ~ 1 pc scales in the NGC 2024 molecular cloud.

In addition to comparing magnetic and turbulent energy via M_A, one can also compare magnetic and gravitational energy via the mass-to-flux ratio $\lambda = M/M_{\text{crit}}$, where M_{crit} is the magnetic critical mass. (M_{crit} is defined by the condition that magnetic energy be equal to gravitational energy; see McKee & Ostriker 2007). When B-fields support star-forming material against gravitational collapse, $\lambda < 1$ and that material is said to be "subcritical." The opposite case is "supercritical," when $\lambda > 1$ and gravity overwhelms magnetic pressure, thus allowing the formation of a central protostar. Subcritical gas can be converted to a supercritical state by ambipolar diffusion (e.g., Mestel & Spitzer 1956; Fiedler & Mouschovias 1993; Tassis et al. 2009), turbulent magnetic reconnection diffusion (Lazarian 2005; Leão et al. 2013), flow along B-field lines, and shock compression (Mestel 1985; McKee et al. 1993; Chen & Ostriker 2014). In the simplest axisymmetric case, one expects the field lines within a supercritical dense core to be drawn into an hourglass shape by gravitational collapse, forming a ∼1000 AU diameter "pseudodisk" (Galli & Shu 1993b).

Although the magnetic field (B-field) may not be strong enough to prevent the formation of a protostar within the pseudodisk, it can have a significant impact on the accretion rate onto the star, and on the formation of a rotationally supported circumstellar disk in which planets will form. In the limiting case of flux freezing, the field close to the protostar becomes strong enough to brake the rotation of the infalling gas completely, preventing the formation of a rotationally supported disk (Galli et al. 2006). Even if ambipolar diffusion allows the field to escape the central core, the redistributed flux tends to be trapped in a ring surrounding the star, greatly reducing the infall rate (Li et al. 2011).

Magnetic braking is less effective, and disks should form more easily, if the rotation axis of the cloud is at an angle to the magnetic field (Joos et al. 2012; Krumholz et al. 2013). Indeed, from an observational perspective it is clear that circumstellar disks typically are *not* well-aligned with the parsec-scale magnetic fields in the surrounding molecular cloud. If they were, the bipolar outflows and jets that emerge along the axes of these disks would all be parallel with the ambient B-field, but this is not observed: Ménard & Duchêne (2004) have shown that the optical jets from classical T Tauri stars in the Taurus-Auriga molecular cloud are randomly oriented with respect to the parsec-scale magnetic field in this cloud; Targon et al. (2011) obtained a similar result for 28 regions spread over the Galaxy, although they do find some evidence for alignment of jets from younger, Class 0 and Class I, protostars.

Polarization observations of background stars are unable to probe the magnetic field morphologies inside the dense cores where circumstellar disks form; even at infrared wavelengths the extinction through these regions is too great. Mapping the polarized thermal emission from dust grains at millimeter and submillimeter wavelengths is the usual means of studying the magnetic fields in these regions. Under most circumstances, spinning dust grains are expected to align themselves with their long axes perpendicular to the magnetic field (Hoang & Lazarian 2009), so normally the thermal radiation from these grains is weakly polarized perpendicular to the field.

Dust polarization maps of many sources have been obtained at submillimeter wavelengths with single-dish instruments, *e.g.,* with the SCUBA polarimeter on the JCMT at 850 μm (Matthews et al. 2009), and with the Hertz polarimeter on the CSO at 350 μm (Dotson et al. 2010). These maps have angular resolutions of about 20″, corresponding to scales of 3000–8000 AU in nearby molecular clouds. Curran & Chrysostomou (2007) found that on these scales, outflows and inferred B-fields are randomly aligned.

Higher angular resolution is required to study the field geometry in the innermost regions of the cores where circumstellar disks form. Thus far, interferometric polarization maps with resolutions of a few arcseconds have been published for about a dozen sources, using data from OVRO, BIMA, and the SMA. Most of this work has focused on detailed analyses of individual objects: examples include maps of NGC 1333-IRAS 4A (Girart et al. 2006), IRAS 16293 (Rao et al. 2009), and Orion KL (Rao et al. 1998; Tang et al. 2010). In this limited set of sources, outflows often were found to be skewed with respect to the inferred magnetic field directions, hinting that circumstellar disks may not be tightly aligned with the magnetic fields on ∼1000 AU scales.

The 1 mm dual-polarization receiver system at CARMA (the Combined Array for Research in Millimeter-wave Astronomy) allows us to map the dust polarization toward many more sources. Here we present results from the TADPOL[2] survey, a CARMA key project to study dust polarization in protostellar cores. This paper focuses on results from nearby, low-mass protostars. We compare the field direction inferred from dust-polarization measurements with the outflow direction, which indicates the axis of the rotationally supported disk. On the ∼1000 AU scales probed by our data, magnetic fields appear to be either preferentially misaligned (perpendicular) or randomly aligned with respect to outflows.

3.2 Observations and Data Reduction

Observations were made with CARMA between May 2011 and October 2012. We selected sources from catalogs of young stellar objects, including Jørgensen et al. (2007), Matthews et al. (2009), Tobin et al. (2010), and Enoch et al. (2011). We focus on Class 0 and Class I objects at distances of $d \lesssim 400$ pc that are known to have bipolar outflows.

The polarization system consists of dual-polarization receivers that are sensitive to right- (R) and left-circular (L) polarization, and a spectral-line correlator that measures all four cross polarizations (RR, LL, LR, RL) on the 105 baselines connecting the 15 antennas. The receivers comprise a single feed horn, a waveguide circular polarizer (Plambeck & Engargiola 2010), an orthomode transducer (Navarrini & Plambeck 2006), and two mixers. The receivers are double-sideband; a phase-switching pattern applied to the local oscillator (LO) allows signals in the lower (LSB) and upper sidebands (USB) to be separated in the correlator.

For these observations, the correlator was set up with three 500 MHz-wide bands to measure the dust continuum, and one 31 MHz-wide band to map bipolar outflows. The frequency of the first LO was 223.821 GHz. The three continuum bands were centered at 6.0, 7.5, and 8.0 GHz in the intermediate frequency (IF). The corresponding RF frequencies are equal to the difference (LSB) or the sum (USB) of the LO and the IF. The spectral-line band

---

[2] **T**elescope **A**rray **D**oing **POL**arization: `tadpol.astro.illinois.edu/`

was centered at IF = 6.717 GHz, allowing simultaneous observations of the SiO(5–4) line in the LSB, and the CO(2–1) line in the USB. For the spectral line measurements, the channel spacing is 0.2 $\mathrm{km\,s^{-1}}$.

In addition to the usual gain, passband, and flux calibrations, polarization observations require two additional calibrations: "XYphase" and leakage. The XYphase calibration corrects for phase differences between the L and R receivers, and is done by observing an artificially polarized noise source of known position angle. The leakage corrections compensate for cross-coupling between the L and R receivers, and are calibrated by observing a strong source (usually the gain calibrator) over a range of parallactic angles. There are no moving parts in the CARMA dual polarization receivers, so the measured leakages are stable with time. A typical antenna has a band-averaged leakage amplitude (*i.e.,* a voltage coupling from L into R, or vice versa) of 6%.

We perform calibration and imaging with the MIRIAD data reduction package (Sault et al. 1995). Using multi-frequency synthesis and natural weighting, we create dust-continuum maps of all four Stokes parameters (I, Q, U, V). The typical beam size is 2.5″, which corresponds to a resolution of 750 AU at a distance of 300 pc. We produce polarization position-angle and intensity maps from the Stokes I, Q, and U data, where the position angle of the incoming radiation is $\chi = 0.5\arctan(U/Q)$, and the bias-corrected polarized intensity is $P_\mathrm{c} = \sqrt{Q^2 + U^2 - \sigma_\mathrm{P}^2}$ (Vaillancourt 2006) (σ_P is the median rms noise in the Stokes Q and U maps).

In good weather $\sigma_\mathrm{P} \approx 0.4$ mJy/beam for a single 6-hour observation, and can be as low as ∼0.2 mJy/beam when multiple observations are combined. We consider it a detection only if $P_\mathrm{c} \geq 3\sigma_\mathrm{P}$ and the location of the polarized emission coincides with a detection of total intensity $I \geq 2\sigma_\mathrm{I}$, where σ_I is the rms noise in the Stokes I map.

We also generate maps of the red- and blueshifted CO and SiO line wings to measure outflow directions. We generally use CO maps to measure the outflow direction, but occasionally we use SiO if the CO emission is too complex. We do not attempt to measure polarization in the spectral line data because of fine-scale frequency structure in the polarization leakages.

3.3 Results & Analysis

Of the 27 TADPOL sources within ∼400 pc, we detected dust polarization toward 16, which we focus on in this paper. The full set of TADPOL results will be presented in a separate paper.

Figures 3.1 and 3.2 shows some example results. In all of the plots, the dust-polarization vectors have been rotated by 90° to show the inferred magnetic field direction and are plotted at the Nyquist spatial frequency (two vectors per synthesized beam).

Table 3.1 lists the results for the 16 TADPOL sources, as well as for IRAS 16293, which was previously published by Rao et al. (2009). Two of the sources each have two distinct outflows, which we consider as independent data, thus making a total of 19 entries. Note that NGC 1333-IRAS 4A, one of the sources in the TADPOL sample, has been mapped in detail

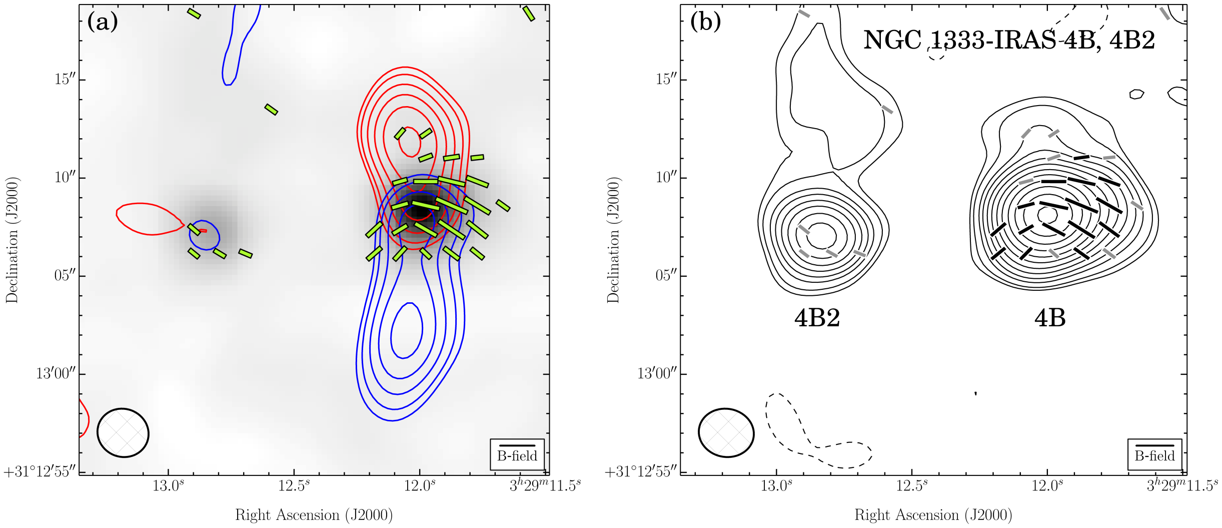

Figure 3.1: Sample maps from the TADPOL survey: NGC 1333-IRAS 4B. The line segments show the inferred magnetic field orientations; they have been rotated by 90° relative to the polarization orientations. Segments are plotted twice per synthesized beam (resolution element) in locations where $I > 2\,\sigma_I$ and $P_c > 2\,\sigma_P$, where I is the total intensity of the dust emission, P_c is the bias-corrected polarized intensity, and σ_I and σ_P are the rms noise values in the total and polarized intensity maps, respectively. **(a)** The segment lengths are proportional to the square root of polarized intensity, *not* fractional polarization. The grayscale is proportional to the total intensity (Stokes I) dust emission. The bipolar outflows are shown by the blue and red contours, which represent the blue- and redshifted spectral line wings. The velocity ranges of the CO($J = 2 \rightarrow 1$) in IRAS 4B are 22.5 to 9.8 $\mathrm{km\,s^{-1}}$ (redshifted) and 3.4 to –12.5 $\mathrm{km\,s^{-1}}$ (blueshifted). The contour levels in all spectral line maps are $4, 6, 10, 16, 25, 40, 64, 102 \times \sigma_{\mathrm{SL}}$, where σ_{SL} is the rms noise measured in the spectral line moment maps. For IRAS 4B, $\sigma_{\mathrm{SL}} = 3.28$ $\mathrm{K\,km\,s^{-1}}$. **(b)** Line segments are black where $P_c > 3.5\,\sigma_P$ and gray where $2\,\sigma_P < P_c < 3.5\,\sigma_P$. The grid on which the line segments are plotted is centered on the polarization intensity peak $P_{\mathrm{c,pk}}$, which is not necessarily spatially coincident with the total intensity peak I_{pk}. The ellipses show the synthesized beams. The dust continuum contours in all dust maps are $-3, 2, 3, 5, 7, 10, 14, 20, 28, 40, 56, 79, 111, 155, 217 \times \sigma_I$. For IRAS 4B, $\sigma_I = 7.3$ $\mathrm{mJy\,bm^{-1}}$.

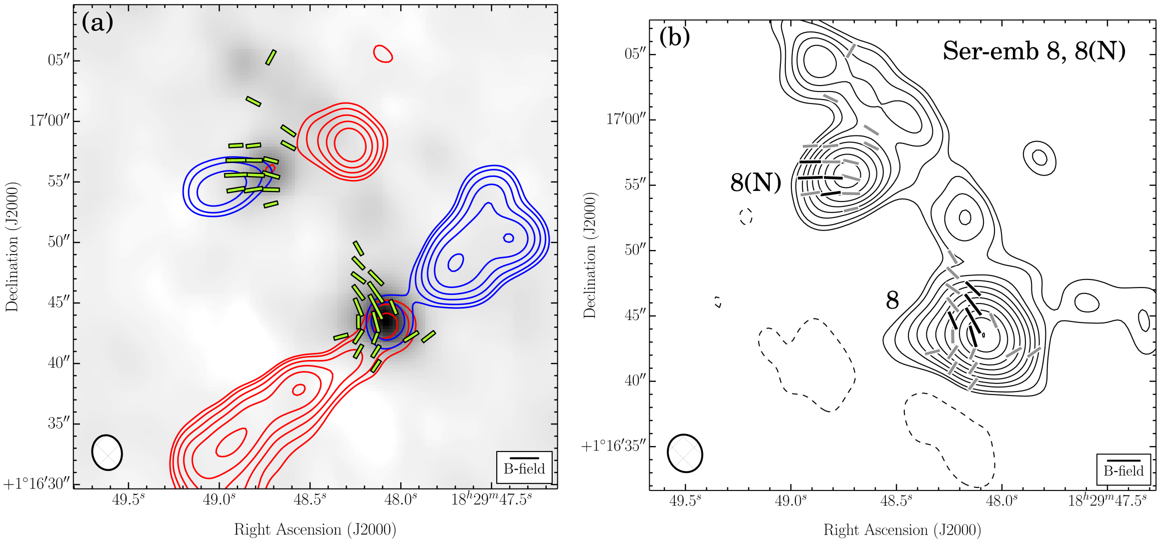

Figure 3.2: Sample maps from the TADPOL survey: Ser-emb 8 & 8(N). Same as above. **(a)** The velocity ranges of the SiO($J = 5 \rightarrow 4$) in Ser-emb 8 are 23.7 to 10.2 $\mathrm{km\,s^{-1}}$ (redshifted) and 4.6 to –6.6 $\mathrm{km\,s^{-1}}$ (blueshifted). (Note: in the published version of Hull et al. (2013), the colors of the red- and blueshifted outflow lobes were accidentally reversed in the Ser-emb 8 & 8(N) map). $\sigma_{\mathrm{SL}} = 0.69$ $\mathrm{K\,km\,s^{-1}}$. **(b)** $\sigma_I = 2.1$ $\mathrm{mJy\,bm^{-1}}$.

before (Girart et al. 2006), and was included in our survey as a cross-check. The polarization directions at the intensity peaks of the 230 GHz CARMA map and the previously published 345 GHz SMA map are in excellent agreement.

To estimate the outflow direction, we measure the position angles of lines connecting the center of the continuum source and the intensity peaks of the red and blue outflow lobes; we take the average of the two position angles as the outflow direction. As a crude estimate of the uncertainty σ_{o}, we use half the difference of the position angles. The B-field direction is calculated by averaging the B-field position angles, weighted by the Stokes I total intensity, which gives the field direction in the densest part of the core. The uncertainty in the B-field σ_{B} is the average of the B-field position angle uncertainties, also weighted by the Stokes I total intensity. The total uncertainty in the angle between the B-field and the outflow is $\sigma_{\mathrm{o-B}} = \sqrt{\sigma_{\mathrm{o}}^2 + \sigma_{\mathrm{B}}^2}$.

Figure 3.3 shows the cumulative distribution function (CDF) of the projected angles between the B-fields and outflows of the sources in Table 3.1. The B-field and outflow position angles we observe are projected onto the plane of the sky. To determine if the large scatter in position angle differences could be due to projection effects, we compare the results with Monte Carlo simulations where the outflows and B-fields are tightly aligned, preferentially misaligned (perpendicular), or randomly aligned.

For the tightly aligned case, the simulation randomly selects pairs of vectors in three dimensions that are within 20° of one another, and then projects the vectors onto the plane of the sky and measures their angular differences. The resulting CDF is shown by the upper dotted curve in Figure 3.3. In this case projection effects are not as problematic as one might think: to have a projected separation larger than 20°, the two vectors must point almost along the line of sight.

For the preferentially misaligned case, the simulation randomly selects pairs of vectors that are separated by 70–90°. The resulting CDF is shown by the lower dotted curve in Figure 3.3. In this case projection effects are more important, and result in a CDF that is similar to that expected for random alignment, shown by the solid curve.

A Kolmogorov-Smirnov (K-S) test shows that the probability that our data were drawn from the same population as the tightly aligned model is 3×10^{-9}, ruling out this scenario. The probability that the results were drawn from a preferentially misaligned population is 0.79, and from a random population is 0.64. Although the probability is slightly higher for the misaligned case, either of the latter two models are consistent with the data.

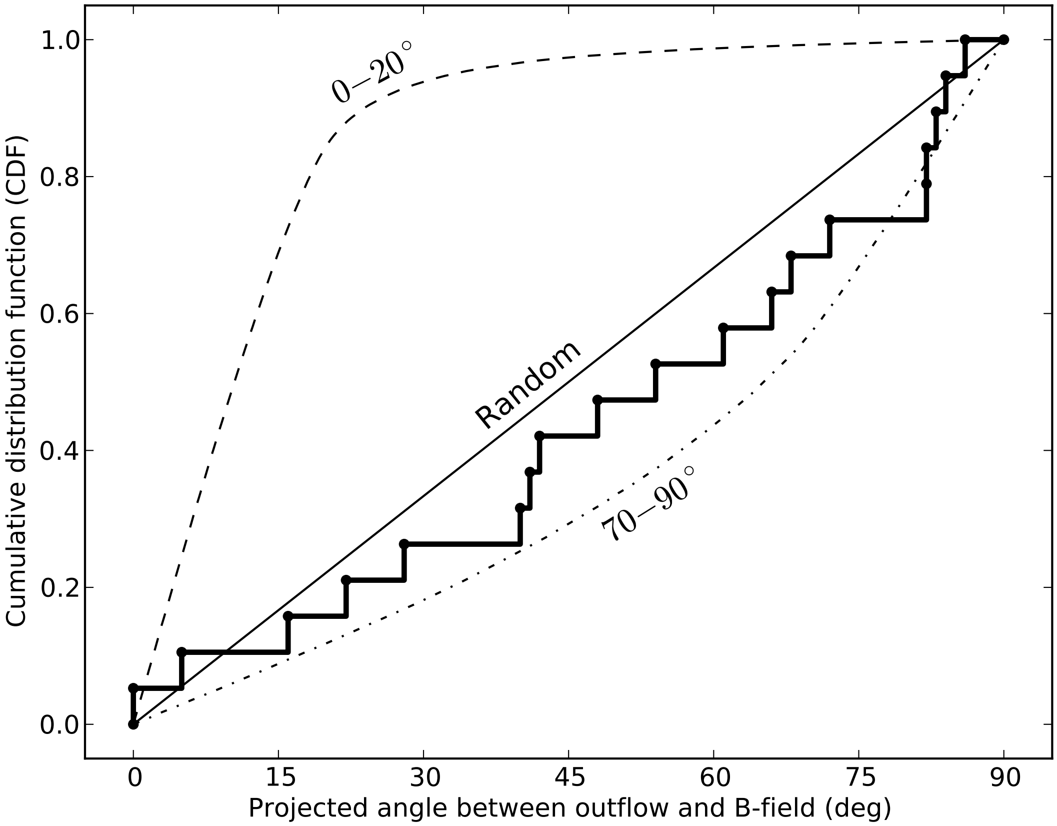

Figure 3.3: The thick solid curve shows the cumulative distribution function (CDF) of the (projected) angles between the mean magnetic field and outflow directions for the sources in Table 3.1. The upper dashed curve is the CDF from a Monte-Carlo simulation where outflow and B-field directions are oriented within 20° of one another (tightly aligned). The lower dot-dashed curve is the CDF from a simulation where outflow and B-field directions are separated by 70–90° (preferentially misaligned). The straight line is the CDF for random orientation.

Table 3.1: Observations: TADPOL first results

Source	α (J2000)	δ (J2000)	$\chi_{\rm B}$ ($\sigma_{\rm B}$) (°)	$\chi_{\rm o}$ ($\sigma_{\rm o}$) (°)	$\theta_{\rm o-B}$ ($\sigma_{\rm o-B}$) (°)	$\theta_{\rm bm}$ (″)	d (pc)	Distance ref.[d]
L1448 IRS 2	03:25:22.4	30:45:13.2	139 (9)	134 (5)	5 (10)	3.63	230	1
L1448N(B)	03:25:36.3	30:45:14.8	31 (6)	97 (2)	66 (6)	2.04	230	1
NGC 1333-IRAS 2A[a]	03:28:55.6	31:14:37.1	82 (6)	98 (6)	16 (8)	3.45	230	1
			82 (6)	21 (9)	61 (11)			1
NGC 1333-IRAS 4A	03:29:10.5	31:13:31.3	58 (2)	18 (10)	40 (10)	2.52	230	1
NGC 1333-IRAS 4B	03:29:12.0	31:13:08.1	86 (5)	0 (5)	86 (7)	2.09	230	1
HH 211	03:43:56.8	32:00:50.0	164 (6)	116 (1)	48 (6)	3.95	230	1
L1551 NE	04:31:44.5	18:08:31.5	165 (4)	67 (5)	82 (6)	2.18	140	2
L1527	04:39:53.9	26:03:09.6	174 (8)	92 (7)	82 (11)	3.06	140	2
OMC3-MMS5[b]	05:35:22.4	–05:01:14.5	52 (9)	80 (6)	28 (11)	3.22	415	3
OMC3-MMS6	05:35:23.4	–05:01:30.6	45 (2)	171 (8)	54 (8)	3.22	415	3
VLA 1623	16:26:26.4	–24:24:30.4	36 (9)	120 (5)	84 (10)	2.89	120	4
IRAS 16293 A[a,c]	16:32:22.9	–24:28:36.3	5 (9)	77 (9)	72 (13)	2.46	178	5
			5 (9)	143 (9)	42 (13)			5
Ser-emb 8	18:29:48.1	01:16:43.6	39 (6)	129 (2)	90 (6)	2.63	415	6
Ser-emb 8 (N)	18:29:48.7	01:16:55.8	88 (7)	107 (1)	19 (7)	2.63	415	6
Ser-emb 6	18:29:49.8	01:15:20.3	157 (3)	135 (3)	22 (4)	2.71	415	6
L1157	20:39:06.2	68:02:16.0	146 (4)	146 (7)	0 (8)	2.39	250	7
CB 230	21:17:38.7	68:17:32.4	89 (6)	172 (4)	83 (7)	3.05	400	8

[a] Source has two outflows.

[b] Coordinates from Takahashi et al. (2009)

[c] Results from Rao et al. (2009).

[d] Distance references. 1: Hirota et al. (2011). 2: Loinard et al. (2007). 3: Menten et al. (2007). 4: Loinard et al. (2008). 5: Imai et al. (2007). 6: Dzib et al. (2010). 7: Looney et al. (2007). 8: Launhardt et al. (2010).

Note. — Coordinates are fitted positions of dust emission peaks. The outflow angle $\chi_{\rm o}$ and inferred magnetic-field angle $\chi_{\rm B}$ are measured counter-clockwise from north. The angle difference $\theta_{\rm o-B}$ between the outflow and the B-field is always between 0–90°. The B-field direction is assumed to be perpendicular to the direction of the polarized dust emission. d is the distance to the source. $\theta_{\rm bm}$ is the geometric mean of the major and minor axes of the synthesized beam. (Note: in the published version of Hull et al. (2013), L1551 NE was mistakenly labeled as L1551 IRS 5. Also, the values for the outflow angles of Ser-emb 8 and 8(N) were switched; these numbers (and the values of $\theta_{\rm o-B}$) have been modified, but the plot in Figure 3.3 has not been modified.)

3.4 Discussion

Most analytical models of star formation assume that the rotation axis of a protostellar core, its magnetic field direction, and its outflow direction all are parallel (Shu et al. 2000; Konigl & Pudritz 2000). Our results appear to contradict this simple picture.

We have assumed that dust grains always are aligned with their long axes perpendicular to the magnetic fields, and thus that B-fields are perpendicular to the polarization directions. This may not always be the case. For example, if grains are mechanically aligned by outflows, then the polarization is expected to be *parallel* to the B-field (Gold 1952). Mechanical alignment should affect only a small portion of a protostellar core, however: the maximum opening angle of the outflows in our sample is $\sim 60°$, corresponding to $\sim 10\%$ of the core volume. Lazarian (2007) and Hoang & Lazarian (2009) show that grains aligned by radiative torques can also be stably aligned parallel to the B-field under some conditions, but this is unlikely in the densest part of a protostellar core.

Outflows may also affect magnetic field morphologies. Because of magnetic tension, the influence of an outflow is not restricted to the outflow cavity, and potentially could extend over a significant fraction of the core volume. Additionally, simulations by Tomisaka (2011) have shown that B-field morphologies can depend on the outflow launching mechanism: the B-field is predominantly toroidal in a magnetocentrifugally driven wind, and is predominantly poloidal in a jet-driven outflow with entrained molecular material. These differences in morphology, combined with projection effects, could result in random orientations between outflows and B-fields.

Finally, some simulations, such as those by Hennebelle & Ciardi (2009), Joos et al. (2012), and Li et al. (2013) suggest that misalignment of the B-field and the core rotation axis can *aid* in the formation of circumstellar disks, given a mass-to-flux ratio in the core of $\gtrsim 2$. Li et al. (2011) find that disk formation is suppressed in the case where fields and core rotation axes are parallel, even when non-ideal MHD effects are considered. Hence, these models suggest that misalignment may be a necessary condition for the formation of disks.

3.5 Summary

Results from the TADPOL survey show that magnetic fields on scales of $\sim$1000 AU are not tightly aligned with protostellar outflows. Rather, the data are consistent both with scenarios where outflows and magnetic fields are preferentially misaligned (perpendicular), and where they are randomly aligned. If one assumes that outflows emerge along the rotation axes of circumstellar disks, and that the outflows have not disrupted the fields in the surrounding material, then our results imply that the disks are not aligned with the fields in the cores from which they formed.

It could be fruitful to investigate whether alignment correlates with core rotation, field strength, outflow velocity, multiplicity, or age. Higher resolution polarization observations with ALMA will test these correlations at the $\sim$100 AU scale of circumstellar disks.

Acknowledgments (Chapter 3)

We thank the referee for his/her insightful comments.

C.L.H.H. thanks Chris McKee, Richard Klein, Mark Krumholz, and Andrew Myers for a helpful discussion, and would like to acknowledge the advice and guidance of the members of the Berkeley Radio Astronomy Laboratory and the Berkeley Astronomy Department.

C.L.H.H. acknowledges support from an NSF Graduate Fellowship. J.D.F. acknowledges support from an NSERC Discovery grant. J.J.T. acknowledges support provided by NASA through Hubble Fellowship grant #HST-HF-51300.01-A awarded by the Space Telescope Science Institute, which is operated by the Association of Universities for Research in Astronomy, Inc., for NASA, under contract NAS 5-26555. A.D.B. acknowledges support from a CAREER grant NSF-AST0955836, NSF-AST1139998, and a Research Corporation for Science Advancement Cottrell Scholar award.

Support for CARMA construction was derived from the states of California, Illinois, and Maryland, the James S. McDonnell Foundation, the Gordon and Betty Moore Foundation, the Kenneth T. and Eileen L. Norris Foundation, the University of Chicago, the Associates of the California Institute of Technology, and the National Science Foundation. Ongoing CARMA development and operations are supported by the National Science Foundation under a cooperative agreement, and by the CARMA partner universities.

Chapter 4

TADPOL: A 1.3 mm Survey of Dust Polarization in Star-forming Cores and Regions

Previously published: Hull, C. L. H., Plambeck, R. L., et al. 2014, Astrophysical Journal Supplement, 213, 13.

We present $\lambda\,1.3$ mm CARMA observations of dust polarization toward 30 star-forming cores and 8 star-forming regions from the TADPOL survey. We show maps of all sources, and compare the $\sim 2.5''$ resolution TADPOL maps with $\sim 20''$ resolution polarization maps from single-dish submillimeter telescopes. Here we do not attempt to interpret the detailed B-field morphology of each object. Rather, we use average B-field orientations to derive conclusions in a statistical sense from the ensemble of sources, bearing in mind that these average orientations can be quite uncertain. We discuss three main findings: (1) A subset of the sources have consistent magnetic field (B-field) orientations between large ($\sim 20''$) and small ($\sim 2.5''$) scales. Those same sources also tend to have higher fractional polarizations than the sources with inconsistent large-to-small-scale fields. We interpret this to mean that in at least some cases B-fields play a role in regulating the infall of material all the way down to the ~ 1000 AU scales of protostellar envelopes. (2) Outflows appear to be randomly aligned with B-fields; although, in sources with low polarization fractions there is a hint that outflows are *preferentially perpendicular* to small-scale B-fields, which suggests that in these sources the fields have been wrapped up by envelope rotation. (3) Finally, even at $\sim 2.5''$ resolution we see the so-called "polarization hole" effect, where the fractional polarization drops significantly near the total intensity peak. All data are publicly available in the electronic edition of this article.

4.1 Introduction

Magnetic fields have long been considered to be one of the key components that regulate star formation (e.g., Shu et al. 1987; McKee et al. 1993). And indeed, observations of polarization in star-forming regions have shown that magnetic fields are well ordered on large scales, from the $\sim$kpc scales of the entire galaxy (Planck Collaboration et al. 2014a,b,c) to the ~ 100 pc scales of GMCs (Heiles 2000) to the ~ 1 pc scales of individual clouds (Pereyra & Magalhães 2004; Goldsmith et al. 2008; Franco et al. 2010; Palmeirim et al. 2013). This is evidence that B-fields in the interstellar medium (ISM) are strong relative to the turbulence in the ISM across many orders of magnitude. In other words, the turbulence in the ISM is sub-Alfvénic: the speed of turbulent motions v is less than the Alfvén speed $v_A = B/\sqrt{4\pi\rho}$, and thus the Alfvén Mach number $M_A = v/v_A$ is < 1.[1]

In addition to comparing magnetic and turbulent energy via M_A, one can also compare magnetic and gravitational energy via the mass-to-flux ratio $\lambda = M/M_{\mathrm{crit}}$, where M_{crit} is the magnetic critical mass. (M_{crit} is defined by the condition that magnetic energy be equal to gravitational energy; see McKee & Ostriker 2007). When B-fields support star-forming material against gravitational collapse, $\lambda < 1$ and that material is said to be "subcritical." The opposite case is "supercritical," when $\lambda > 1$ and gravity overwhelms magnetic pressure, thus allowing the formation of a central protostar. Subcritical gas can be converted to a supercritical state by ambipolar diffusion (e.g., Mestel & Spitzer 1956; Fiedler & Mouschovias 1993; Tassis et al. 2009), turbulent magnetic reconnection diffusion (Lazarian 2005; Leão et al. 2013), flow along B-field lines, and shock compression (Mestel 1985; McKee et al. 1993; Chen & Ostriker 2014).

Under most circumstances, spinning dust grains align themselves with their long axes perpendicular to the B-field (e.g., Hildebrand 1988; Lazarian 2003, 2007; Hoang & Lazarian 2009; Andersson 2012), so the thermal radiation from these grains is polarized perpendicular to the B-field. Ambient B-fields can be probed on scales of $\gtrsim 1$ pc using optical observations of background stars (e.g., Heiles 2000), whose light becomes polarized after passing through regions of aligned dust grains. However, this type of observation is not possible inside the dense cores where the central protostars and their circumstellar disks form; even at infrared wavelengths the extinction through these dense regions is too great.

Mapping the polarized thermal emission from dust grains at millimeter and submillimeter wavelengths is the usual means of studying the B-fields in these regions. The 1.3 mm dual-polarization receiver system at CARMA (the Combined Array for Research in Millimeter-wave Astronomy; Bock et al. 2006), described in Hull et al. (2011), has allowed us to map the dust polarization toward a sample of several dozen nearby star-forming cores and a few star-forming regions (SFRs) as part of the TADPOL[2] survey—a CARMA key project.

Previous results from the TADPOL survey have touched on several topics including the consistency of B-fields from large to small scales (Stephens et al. 2013), the low levels of dust

---

[1] Note that Crutcher et al. (1999) found approximately Alfvénic turbulence on ~ 1 pc scales in the NGC 2024 molecular cloud.

[2] TADPOL: **T**elescope **A**rray **D**oing **POL**arization

polarization in the circumstellar disks around more evolved Class II sources like DG Tau (Hughes et al. 2013; see Figure 4.15), and the misalignment of bipolar outflows and small-scale B-fields in low-mass protostars (Hull et al. 2013). The latter result has been used to place limits on the fraction of protostars that should harbor circumstellar disks (Krumholz et al. 2013).

Here we present the data from the full survey. We compare these $\sim 2.5''$ resolution data with $\sim 20''$ resolution polarization maps from single-dish submillimeter telescopes to analyze the consistency of B-field orientations down to the ~ 1000 AU scale of protostellar envelopes. We also revisit the correlation of B-fields with bipolar outflows and see hints that sources with low polarization fractions have outflows and small-scale B-field orientations that are preferentially perpendicular. Finally, even at $\sim 2.5''$ resolution we see the so-called “polarization hole” effect, where the fractional polarization drops significantly near the total intensity peak.

4.2 Source Selection & Observations

We selected sources from catalogs of young stellar objects (e.g., Jørgensen et al. 2007; Matthews et al. 2009; Tobin et al. 2010; Enoch et al. 2011). While several well known, high-mass SFRs are included in the survey, we focus mainly on nearby ($d \lesssim 400$ pc) Class 0 and Class I objects that are known to have bipolar outflows, and that had been observed previously with the polarimeters on the JCMT (James Clerk Maxwell Telescope) and the CSO (Caltech Submillimeter Observatory), two submillimeter single-dish telescopes with $\sim 20''$ resolution. See Section 4.8 for source descriptions. Since the survey spanned five observing semesters, sources were selected to cover a wide range of hour angles to allow most observations to be scheduled during the more stable nighttime weather.

Observations were made with CARMA between May 2011 and April 2013. Three different array configurations were used: C (26–370 m baselines, or telescope spacings), D (11–148 m), and E (8.5–66 m), which correspond to angular resolutions at 1.3 mm of approximately $1''$, $2''$, and $4''$, respectively.

4.3 Calibration & Data Reduction

The CARMA polarization system consists of dual-polarization receivers that are sensitive to right- (R) and left-circular (L) polarization, and a spectral-line correlator that measures all four cross polarizations (RR, LL, LR, RL) on each of the 105 baselines connecting the 15 telescopes (six with 10 m diameters and nine with 6 m diameters). Each receiver comprises a single feed horn, a waveguide circular polarizer, an orthomode transducer (OMT), two heterodyne mixers, and two low-noise amplifiers, all mounted in a cryogenically cooled dewar. The local oscillator (LO) and sky signals are combined using a mylar beamsplitter in front of the dewar window.

The waveguide polarizer is a two-section design with half-wave and quarter-wave retarder sections rotated axially with respect to one another to achieve broadband (210–270 GHz) performance; the retarders are sections of reduced-height, faceted circular waveguide (Plambeck & Engargiola 2010). The polarizer converts the R and L circularly polarized radiation from the sky into orthogonal X and Y linear polarizations, which then are separated by the OMT (Navarrini & Plambeck 2006). The mixers use ALMA Band 6 SIS (superconductor-insulator-superconductor) tunnel junctions fabricated at the University of Virginia by Arthur Lichtenberger. Although at ALMA these devices are used in sideband-separating mixers (Kerr et al. 2013), at CARMA they are used in double-sideband mixers that are sensitive to signals in two bands, one 1–9 GHz above (upper sideband, or USB), and the other 1–9 GHz below (lower sideband, or LSB) the LO frequency. A phase-switching pattern applied to the LO allows the LSB and USB signals to be separated in the correlator. The 1–9 GHz intermediate frequency (IF) from each mixer is amplified with WBA13 low-noise amplifiers (Weinreb 1998; Pandian et al. 2006).

For the TADPOL observations the LO frequency was 223.821 GHz. The correlator was set up with three 500 MHz-wide bands centered at IF values of 6.0, 7.5, and 8.0 GHz, and one 31 MHz wide band centered at 6.717 GHz.[3,4] The corresponding sky frequencies are equal to the difference (LSB) or the sum (USB) of the LO and the IF. The narrowband section allowed simultaneous spectral line observations of the SiO($J = 5 \rightarrow 4$) line (217.105 GHz) in the LSB and the CO($J = 2 \rightarrow 1$) line (230.538 GHz) in the USB, with a channel spacing of $\sim 0.2\,\mathrm{km\,s^{-1}}$. These lines were used to map bipolar outflows.

In addition to the usual gain, passband, and flux calibrations, two additional calibrations are required for polarization observations: "XYphase" and leakage. The XYphase calibration corrects for the phase difference between the L and R channels on each telescope, caused by delay differences in the receiver, underground cables, and correlator cabling. To calibrate the XYphase one must observe a linearly polarized source with known position angle. Since most astronomical sources at millimeter wavelengths are weakly polarized and time-variable, CARMA uses artificial linearly polarized noise sources for this purpose. The noise sources are created by inserting wire grid polarizers into the beams of the 10 m telescopes. With the grid in place, one linear polarization reaching the receiver originates from the sky, while the other originates from a room temperature load. Since the room temperature load is much hotter than the sky, the receiver sees thermal noise that is strongly polarized. The L–R phase difference is then derived, channel by channel, from the L vs. R autocorrelation spectrum obtained with the grid in place. One of the 10 m telescopes is always used as the reference for the regular passband observations, thus transferring the L–R phase calibration to all other

---

[3] Some or all of the data for the following six sources are from another CARMA project led by Kwon et al.: L1448 IRS 2, HH 211 mm, L1527, Ser-emb 1, HH 108 IRAS, and L1165. These observations had a different correlator setup, with an LO frequency of 228.5988 GHz; three 500 MHz-wide bands centered at IF values of 1.9392, 2.4392, and 2.9392 GHz; and one 31 MHz wide band centered at 1.9392 GHz. Dust continuum and CO($J = 2 \rightarrow 1$) data from these datasets are reported in this paper.

[4] The following sources have narrow-band windows with widths of 62 MHz and corresponding channel spacings of $\sim 0.4\,\mathrm{km\,s^{-1}}$: W3 Main, W3(OH), OMC3-MMS5/6, OMC2-FIR3/4, G034.43+00.24 MM1, and DR21(OH).

telescopes.

The leakage corrections compensate for cross-coupling between the L and R channels, caused by imperfections in the polarizers and OMTs and by crosstalk in the analog electronics that precede the correlator. Leakages are calibrated by observing a strong source (usually the gain calibrator) over a range of parallactic angles. There are no moving parts in the CARMA dual polarization receivers, so the measured leakages are stable with time. A typical telescope has a band-averaged leakage amplitude (i.e., a voltage coupling from L into R, or vice versa) of 6%.

Observations of 3C286, a quasar known to have a very stable polarization position angle χ, yield $\chi = 41 \pm 3^\circ$ (measured counterclockwise from north), consistent with recent measurements by Agudo et al. (2012): $\chi = 37.3 \pm 0.8^\circ$ at $\lambda\,3\,\mathrm{mm}$ and $\chi = 33.1 \pm 5.7^\circ$ at $\lambda\,1.3\,\mathrm{mm}$. Our results also are consistent with ALMA (Atacama Large Millimeter-submillimeter Array) commissioning results at $\lambda\,1.3\,\mathrm{mm}$ ($\chi = 39^\circ$; Stuartt Corder, priv. comm., 2013), as well as with centimeter observations compiled by Perley & Butler (2013), who showed that the polarization position angle of 3C286 increases slowly from $\chi = 33^\circ$ at $\lambda \gtrsim 3.7\,\mathrm{cm}$ to $\chi = 36^\circ$ at $\lambda = 0.7\,\mathrm{cm}$. The uncertainty of $\pm\,3^\circ$ in the CARMA value is the result of systematic errors in the R–L phase correction, and is estimated from the scatter in the χ values derived using different 10 m reference antennas.

To check for variations in the instrumental polarization across the primary beams of the telescopes, we observed BL Lac (a bright, highly polarized quasar) at 8 offset positions, each $12''$ from the field center. The deviations in position angle and polarization fraction from the field-center values were $\pm\,4^\circ$ and $\pm\,8\%$, respectively. Primary beam polarization will therefore have a relatively small effect on the results presented here, since most of the sources in the TADPOL survey are less than $10''$ across and are centered in the primary beam.

We perform calibration and imaging with the MIRIAD data reduction package (Sault et al. 1995). We calibrate the complex gains by observing a nearby quasar every 15 minutes; the passband by observing a bright quasar for 10 minutes; and the absolute flux using observations of Uranus, Mars, or MWC 349.[5] Using multi-frequency synthesis and natural weighting, we create dust-continuum maps of all four Stokes parameters (I, Q, U, V) by inverting the calibrated visibilities, deconvolving the source image from the synthesized beam pattern with `CLEAN` (Högbom 1974), and restoring them with a Gaussian fit to the synthesized beam. The typical beam size is $2.5''$.

We produce polarization position-angle and intensity maps from the Stokes I, Q, and U data. (Note that since we are searching for linear dust polarization, we do not use the Stokes V maps, which are measures of circular polarization.) The rms noise values in the Q and U maps are generally comparable, such that we define the rms noise σ_P in the polarization maps as $\sigma_P \approx \sigma_Q \approx \sigma_U$. The polarized intensity P is

$$P = \sqrt{Q^2 + U^2}\,. \tag{4.1}$$

---

[5] CARMA absolute flux measurements at 1.3 mm are estimated to be uncertain by ± 15%, due in part to uncertainties in planet models, pointing, and antenna focus. However, these uncertainties do not affect the conclusions drawn in this paper.

However, polarization measurements have a positive bias because the polarization P is always positive, even though the Stokes parameters Q and U from which P is derived can be either positive or negative. This bias has a significant effect in low signal-to-noise (SNR) measurements ($P \lesssim 3\,\sigma_P$) and can be taken into account by calculating the bias-corrected polarized intensity P_c (e.g., Vaillancourt 2006; see also Naghizadeh-Khouei & Clarke 1993 for a discussion of the statistics of position angles in low SNR measurements).

All of the maps we present here have been bias-corrected. For polarization detections with $P \lesssim 5\,\sigma_P$, we calculated P_c by finding the maximum of the probability distribution function (i.e., the most probable value) of the true polarization P_c given the observed polarization P (see Vaillancourt 2006). For very significant polarization detections ($P \gtrsim 5\,\sigma_P$), we used the high-SNR limit:

$$P_c \approx \sqrt{Q^2 + U^2 - \sigma_P^2}\,. \tag{4.2}$$

The fractional polarization is

$$P_{\text{frac}} = \frac{P_c}{I}\,. \tag{4.3}$$

The position angle χ and uncertainty $\delta\chi$ (calculated using standard error propagation) of the incoming radiation are

$$\chi = \frac{1}{2}\arctan\left(\frac{U}{Q}\right), \tag{4.4}$$

$$\delta\chi = \frac{1}{2}\frac{\sigma_P}{P_c}\,. \tag{4.5}$$

Note that polarization angles (and the B-field orientations inferred from them) are not vectors, but are *polars.* A polar is a “headless” vector that has an *orientation* (not a direction) with a 180° range (e.g., 0 to 180° or –90 to 90°).

In good weather $\sigma_P \approx 0.4\,\text{mJy}\,\text{bm}^{-1}$ for a single 6-hour observation, and can be as low as $\sim 0.2\,\text{mJy}\,\text{bm}^{-1}$ when multiple observations are combined. We consider it a detection if $P_c \geq 2\,\sigma_P$ (corresponding to $\delta\chi \approx \pm 14^\circ$) and if the location of the polarized emission coincides with a detection of $I \geq 2\,\sigma_I$, where σ_I is the rms noise in the Stokes I map. We also generate maps of the red- and blueshifted CO($J = 2 \rightarrow 1$) and SiO($J = 5 \rightarrow 4$) line wings, but we do not attempt to measure polarization in the spectral line data because of fine-scale frequency structure in the polarization leakages.

4.4 Data Products & Results

Maps of all sources are shown in Section 4.7. Note that all of the polarization orientations have been rotated by 90° to show the inferred B-field directions in the plane of the sky.

There are typically three plots per source:

(a) **Small-scale (CARMA) B-fields, with outflows overlaid.** These plots include B-field orientations as well as red- and blueshifted outflow lobes, all overlaid on the total intensity (Stokes I) dust emission in gray. The outflow data are CO($J = 2 \rightarrow 1$) for all sources except for Ser-emb 8 and 8(N) (Figure 4.26), which have more clearly defined outflows in SiO($J = 5 \rightarrow 4$).

(b) **Small-scale B-fields overlaid on Stokes I dust contours.** In these plots the B-field orientations are black for significant detections ($P_c > 3.5\,\sigma_P$) or gray for marginal detections ($2\,\sigma_P < P_c < 3.5\,\sigma_P$), and are overlaid on total intensity dust emission contours. The B-field orientations are the same as those plotted in (a). These plots zoom in on the source to provide a clearer view of the small-scale B-field morphology.

(c) **Comparison of large- and small-scale B-fields.** These plots include the same dust contours and small-scale B-field orientations as in (b), but zoomed out so that the large-scale B-fields from the SCUBA (orange), Hertz (light blue), and SHARP (purple) polarimeters (see below) can be plotted. These plots show how the B-field morphology changes from the ~ 0.1 pc scales probed by single-dish submillimeter telescopes to the ~ 0.01 pc scales probed by CARMA.

To show the B-field morphologies as clearly as possible, we have chosen to plot the lengths of the line segments on a square-root scale.

at the CSO, the segment lengths are proportional to the square root of the polarized intensity.

All maps from the TADPOL survey are publicly available as FITS images and machine readable tables for each figure in Section 4.7. For each figure we include maps of Stokes I, Q, and U; bias-corrected polarization intensity P_c; polarization fraction $P_{\rm frac} = P_c/I$; and inferred B-field orientation $\chi_{\rm sm}$. Additionally, we include FITS cubes of total intensity (Stokes I) spectral-line data, as well as machine readable tables listing the RA, DEC, I, P_c, $P_{\rm frac}$, $\chi_{\rm sm}$, and associated uncertainties of each line segment plotted in the figures. These files are available in a .tar.gz package available via the link in the figure caption.

The results for each source are summarized in Table 4.1. We give fitted coordinates of the dust emission peaks, maximum total intensity $I_{\rm pk}$, maximum bias-corrected polarized intensity $P_{\rm c,pk}$, average polarization fraction $\overline{P}_{\rm frac}$, average small-scale B-field orientation $\chi_{\rm sm}$, outflow orientation $\chi_{\rm o}$, source type, distance d to the source, and synthesized-beam size $\theta_{\rm bm}$ (resolution element) of the maps.

We also tabulate the average large-scale B-field orientation $\chi_{\rm lg}$ from the SCUBA, Hertz, and SHARP data. We averaged $\chi_{\rm lg}$ values within a radius of $\sim 40''$ of the CARMA field center; all of these detections are shown in the figures in Section 4.7.

The values $\overline{P}_{\rm frac}$, $\chi_{\rm lg}$, and $\chi_{\rm sm}$ are averages of quantities that vary across each source, and hence are sensitive to the weighting schemes used to derive them. Since the locations of the intensity and polarization peaks for each source are not necessarily spatially coincident, we chose to calculate a measure of fractional polarization $\overline{P}_{\rm frac}$ using the mean polarized and total intensities across the entire source. To do this, we average only pixels where $P_c > 3.5\,\sigma_P$.

We average I and P_c separately over this set of pixels, and define $\overline{P}_{\rm frac} = \overline{P_c}\,/\,\overline{I}$. For the typical source P_c has a much flatter distribution than I over these pixels, so that our average is biased toward the minimum of the "polarization hole" in each source (see Section 4.5.3). The uncertainty in the fractional polarization is calculated rather differently: it is the median of the uncertainties in the fractional polarization in each pixel.

Note that when calculating $\overline{P}_{\rm frac}$ we average only the magnitude of P_c (and not the orientation χ of the B-field) across the source, which makes our measurements sensitive only to depolarization along the line of sight (LOS) or in the plane of the sky at scales smaller than the resolution of our CARMA maps.

We should note that interferometric measurements of fractional polarization can be problematic because an interferometer acts as a spatial filter, and is insensitive to large scale structure. This makes direct comparisons of fractional polarization results from single dish telescopes and interferometers extremely difficult. For example, in cases where polarized emission (Stokes Q or U) is localized, but total intensity (Stokes I) is extended, it is possible to overestimate the polarization fraction with an interferometer. The comparison of polarization angles should be less problematic, however, as it is unlikely that Stokes Q would be very localized and U would be very extended, or vice versa.

To calculate $\chi_{\rm sm}$ we performed a total-intensity-weighted average of each small-scale B-field orientation χ where $P_c > 2\,\sigma_P$:

$$\chi_{\rm sm} = \frac{\sum \chi I}{\sum I}\,. \tag{4.6}$$

This method gives more weight to the B-field orientations in the highest density regions of the source, and is the same method used in Hull et al. (2013).

To calculate $\chi_{\rm lg}$ we performed total-intensity-weighted averages of the large-scale B-field orientations from SCUBA, Hertz, and/or SHARP. For sources that had detections from more than one telescope, we weighted each of the averages by the number of detections present in the map (i.e., for a source with 40 SCUBA and 5 Hertz detections, more weight is given to the average of the SCUBA detections).

The dispersions in $\chi_{\rm sm}$ and $\chi_{\rm lg}$ are calculated using the circular standard deviation of the B-field orientations across each source. Note that these dispersions reflect the spread in B-field orientations in each source, not the uncertainty in the measurements. For example, a source with complicated B-field morphology such as NGC 7538 IRS 1 (see Figure 4.36) has a large scatter in $\chi_{\rm sm}$ because of the widely varying B-field orientations across the source. Nevertheless, any given B-field orientation in the map has an uncertainty of $\lesssim 14°$, since we only plot detections where $P_c > 2\,\sigma_P$.

The value $|\chi_{\rm lg} - \chi_{\rm sm}|$ was used to characterize the consistency between large- and small-scale B-field orientations. The dispersion in $|\chi_{\rm lg} - \chi_{\rm sm}|$ is equal to the dispersions in $\chi_{\rm sm}$ and $\chi_{\rm lg}$ added in quadrature.

Generally the outflow angle $\chi_{\rm o}$ is determined by connecting the center of the continuum source and the intensity peaks of the red and blue outflow lobes, and taking the average of the two position angles. Of course, this is somewhat arbitrary because it depends on the selected velocity ranges for the red and blue lobes, and because outflows can have complex morphology. We do not report outflow orientations in sources where the morphology is extremely complex. The outflow orientation is indicated in the first panel of most plots in Section 4.7.

Note that as a test, we performed polarized-intensity-weighted (as opposed to total-intensity-weighted) averages of $\chi_{\rm lg}$ and $\chi_{\rm sm}$ and found that our main conclusions were unchanged. For the low-mass cores plotted in Figures 4.1 and 4.2, the two weighting schemes resulted in $\lesssim 20^\circ$ differences in the consistency angle $|\chi_{\rm lg} - \chi_{\rm sm}|$.

Table 4.1: Observations: TADPOL data release

Source	α (J2000)	δ (J2000)	$I_{\rm pk}$[a] $\left(\frac{\rm mJy}{\rm bm}\right)$	$P_{\rm c,pk}$[a,*b*] $\left(\frac{\rm mJy}{\rm bm}\right)$	$\overline{P}_{\rm frac}$ (%)	$\chi_{\rm lg}$ (°)	$\chi_{\rm sm}$[b] (°)	$\lvert\chi_{\rm lg}-\chi_{\rm sm}\rvert$ (°)	$\chi_{\rm o}$ (°)	Type	d (pc)	$\theta_{\rm bm}$ (″)
W3 Main	02:25:40.6	62:05:51.6	374	3.3	2.0 (0.5)	135 (49)	100 (36)	35 (60)	—	SFR	1950	2.9
W3(OH)	02:27:03.9	61:52:24.6	2760	13.8	1.0 (0.4)	22 (25)	82 (53)	60 (58)	—	SFR	2040	2.7
L1448 IRS 2	03:25:22.4	30:45:13.2	136	3.4	3.7 (0.9)	148 (12)	135 (43)	13 (44)	134*	0	232	3.8
L1448N(B)	03:25:36.3	30:45:14.7	596	5.4	1.3 (0.2)	14 (33)	26 (37)	12 (49)	97*	0	232	2.5
L1448C	03:25:38.9	30:44:05.3	186	<2.4	—	110 (39)	112 (32)	2 (50)	161	0	232	2.5
L1455 IRS 1	03:27:39.1	30:13:03.0	43	<2.0	—	72 (19)	150 (24)	78 (30)	66	I	320	2.7
NGC 1333-IRAS 2A[c]	03:28:55.6	31:14:37.0	322	3.1	1.8 (0.4)	135 (56)	70 (23)	65 (60)	21* 98*	0	320	3.5
SVS 13	03:29:03.7	31:16:03.5	276	3.8	2.0 (0.5)	171 (24)	6 (24)	15 (33)	—	0/I	235	3.3
NGC 1333-IRAS 4A	03:29:10.5	31:13:31.3	1680	46.1	4.5 (0.5)	53 (25)	56 (20)	3 (32)	18*	0	320	2.4
NGC 1333-IRAS 4B	03:29:12.0	31:13:08.1	866	9.7	1.7 (0.3)	55 (27)	84 (34)	29 (43)	0*	0	320	2.5
NGC 1333-IRAS 4B2	03:29:12.8	31:13:07.1	244	<2.0	—	55 (27)	55 (20)	0 (33)	76	0	320	2.5
HH 211 mm	03:43:56.8	32:00:50.0	196	4.8	4.1 (1.2)	168 (17)	164 (32)	4 (36)	116*	0	320	4.1
DG Tau	04:27:04.5	26:06:15.9	296	<2.8	—	—	84 (14)	—	—	II	140	2.4
L1551 NE	04:31:44.5	18:08:31.5	418	8.3	2.0 (0.3)	46 (32)	164 (15)	62 (35)	67*	I	140	2.6
L1527	04:39:53.9	26:03:09.6	161	3.4	2.2 (0.3)	38 (42)	3 (8)	35 (42)	92*	0/I	140	3.0
CB 26	04:59:50.8	52:04:43.5	77	<1.8	—	81 (21)	87 (66)	6 (69)	147	I	140	2.5
Orion-KL	05:35:14.5	–05:22:31.6	3270	91.7	5.3 (1.2)	119 (13)	140 (34)	21 (36)	—	SFR	415	2.7
OMC3-MMS5	05:35:22.6	–05:01:16.5	123	5.2	4.4 (0.7)	49 (10)	59 (12)	10 (15)	80*	0	415	3.0
OMC3-MMS6	05:35:23.4	–05:01:30.6	984	20.2	3.0 (0.3)	51 (12)	44 (8)	7 (14)	171*	0	415	3.0
OMC2-FIR4	05:35:26.9	–05:09:55.8	57	2.2	7.9 (2.2)	43 (27)	146 (64)	77 (69)	—	SFR	415	3.0
OMC2-FIR3	05:35:27.6	–05:09:34.2	76	2.8	5.8 (1.4)	50 (30)	166 (7)	64 (30)	—	0	415	3.0
CB 54	07:04:20.8	–16:23:22.2	93	<2.8	—	173 (38)	32 (42)	39 (56)	108	I	1100	3.0
VLA 1623	16:26:26.4	–24:24:30.5	283	3.8	1.7 (0.4)	60 (32)	23 (48)	37 (57)	120*	0	125	3.3
Ser-emb 17	18:29:06.2	00:30:43.3	156	<2.2	—	—	73 (39)	—	—	I	415	3.0
Ser-emb 1	18:29:09.1	00:31:31.1	220	<1.6	—	—	127 (52)	—	12	0	415	3.3
Ser-emb 8	18:29:48.1	01:16:43.6	165	3.5	3.0 (0.6)	94 (35)	7 (44)	87 (56)	129*	0	415	2.6
Ser-emb 8 (N)	18:29:48.7	01:16:55.8	72	2.5	5.2 (1.2)	92 (31)	83 (15)	9 (34)	107*	0	415	2.6
Ser-emb 6	18:29:49.8	01:15:20.3	1230	17.1	1.4 (0.2)	86 (29)	172 (33)	86 (43)	135*	0	415	2.7
HH 108 IRAS	18:35:42.1	–00:33:18.4	198	<2.3	—	—	4 (34)	—	34	0/I	310	4.1
G034.43+00.24 MM1	18:53:18.0	01:25:25.4	1160	12.6	1.9 (0.4)	—	41 (22)	—	47	SFR	1560	2.6

Table 4.1 (cont'd): Observations: TADPOL data release

Source	α (J2000)	δ (J2000)	$I_{\mathrm{pk}}^{\mathrm{a}}$ $\left(\frac{\mathrm{mJy}}{\mathrm{bm}}\right)$	$P_{\mathrm{c,pk}}^{\mathrm{a},b}$ $\left(\frac{\mathrm{mJy}}{\mathrm{bm}}\right)$	$\overline{P}_{\mathrm{frac}}$ (%)	χ_{lg} (°)	$\chi_{\mathrm{sm}}^{\mathrm{b}}$ (°)	$\lvert\chi_{\mathrm{lg}} - \chi_{\mathrm{sm}}\rvert$ (°)	χ_{o} (°)	Type	d (pc)	θ_{bm} ($''$)
G034.43+00.24 MM3	18:53:20.6	01:28:26.4	66	< 2.4	—	—	57 (41)	—	—	SFR	1560	2.6
B335 IRS	19:37:00.9	07:34:09.3	71	< 3.0	—	18 (35)	123 (40)	75 (53)	99	0	150	3.5
DR21(OH)	20:39:01.1	42:22:49.0	615	8.5	2.2 (0.4)	89 (22)	42 (37)	47 (43)	—	SFR	1500	2.6
L1157	20:39:06.2	68:02:15.8	197	7.7	5.8 (1.2)	143 (23)	147 (29)	4 (37)	146*	0	250	2.2
CB 230	21:17:38.7	68:17:32.4	104	2.1	5.4 (3.2)	113 (34)	96 (35)	17 (48)	172*	0/I	325	3.0
L1165	22:06:50.5	59:02:45.9	128	< 2.9	—	—	113 (4)	—	52	I	300	3.9
NGC 7538 IRS 1	23:13:45.4	61:28:10.3	3230	11.6	1.7 (0.8)	145 (26)	52 (62)	87 (67)	—	SFR	2650	2.4
CB 244	23:25:46.6	74:17:38.3	43	< 1.5	—	168 (79)	170 (49)	2 (92)	42	0	200	2.7

Note. — Coordinates are fitted positions of dust emission peaks measured in the CARMA maps. I_{pk} and $P_{\mathrm{c,pk}}$ are the maximum total intensity and bias-corrected polarized intensity, respectively. The polarization fraction $\overline{P}_{\mathrm{frac}} = \overline{P}\,/\,\overline{I}$, where $\overline{P}$ and $\overline{I}$ are the unweighted averages of the polarization and total intensities in locations where $P_c > 3.5\,\sigma_P$. The bipolar outflow orientations χ_{o} and the large- and small-scale B-field orientations χ_{lg} and χ_{sm} are measured counterclockwise from north. Sources included in Figure 4.2 are marked with an asterisk (*) next to their outflow orientations. $\lvert\chi_{\mathrm{lg}} - \chi_{\mathrm{sm}}\rvert$ is the angle difference between the large- and small-scale B-field orientations. The uncertainties in χ_{lg} and χ_{sm} are in parentheses; these numbers are the circular standard deviations of the B-field orientations used in the averages, and thus reflect the dispersion of the B-field orientations in each source. The uncertainty in $\lvert\chi_{\mathrm{lg}} - \chi_{\mathrm{sm}}\rvert$ is equal to the uncertainties in χ_{sm} and χ_{lg} added in quadrature. The B-field is assumed to be perpendicular to the position angle of the dust polarization. Source types are: 0 (Class 0 young stellar object [YSO]), I (Class I YSO), II (Class II YSO), and SFR (star-forming region). d is the distance to the source. θ_{bm} is the geometric mean of the major and minor axes of the synthesized beam.

[a] Polarized and total intensity maxima do not necessarily coincide spatially.

[b] Upper limits on the polarized intensity $P_{\mathrm{c,pk}}$ are given for sources with $P_{\mathrm{c,pk}} < 3.5\,\sigma_P$. Because of low-level calibration artifacts, the small-scale B-field angles χ_{sm} for such sources are not always reliable.

[c] NGC 1333-IRAS 2A has two well defined outflows. Both outflow orientations are listed here, and both are included in Figure 4.2.

4.5 Analysis & Discussion

In this paper, we do not attempt to interpret the detailed B-field morphology of each object. Rather, our goal is to use average B-field orientations to derive conclusions in a statistical sense from the ensemble of sources. The large uncertainties in $\chi_{\rm lg}$ and $\chi_{\rm sm}$ in Table 4.1 reflect the large dispersions in the B-field orientations across each of these objects. The mean B-field orientation is necessarily determined by detections of polarization in locations where the observations have sufficient signal-to-noise, and may not reflect the B-field orientation across the entirety of the source. Furthermore, the B-fields may have been distorted by collapse, pinching, or outflows, and thus caution must be used when interpreting the source-averaged values that we report in Table 4.1.

4.5.1 Consistency of B-fields from large to small scales

While $\sim$kpc-scale galactic B-fields do not seem to be correlated with smaller-scale B-fields in clouds and cores (e.g., Stephens et al. 2011), Li et al. (2009) did find evidence that B-field orientations are consistent from the ~ 100 pc scales of molecular clouds to the ~ 0.1 pc scales of dense cores. We take the next step by examining the consistency of B-field orientations from the ~ 0.1 pc core to ~ 0.01 pc envelope scales.

In Figure 4.1 we plot $|\chi_{\rm lg} - \chi_{\rm sm}|$ as a function of the polarization fraction. This plot is limited to sources with (1) B-field detections at both scales, (2) CARMA polarization detections $P_c > 3.5\,\sigma_P$, and (3) distances $d \lesssim 400$ pc.

The most notable feature of the plot is the relative absence of star-forming cores in the upper-right quadrant, i.e., sources that are strongly polarized but have inconsistent large-to-small-scale B-field orientations. With the exception of OMC2-FIR3 and Ser-emb 8, we see that the cores with high CARMA polarization fractions ($\overline{P}_{\rm frac} \geq 3\%$) have B-field orientations that are consistent from large to small scales. These "high-polarization" sources are L1448 IRS 2 (Figure 4.6), NGC 1333-IRAS 4A (Figure 4.12), HH 211 mm (Figure 4.14), Orion-KL (Figure 4.19), OMC3-MMS5 and MMS6 (Figure 4.20), OMC2-FIR3 and 4 (Figure 4.21), Ser-emb 8 and 8(N) (Figure 4.26), L1157 (Figure 4.33), and CB 230 (Figure 4.34).

In these sources the consistency of the B-fields from large to small scales suggests that the fields have not been twisted by turbulent motions as the material collapses to form the protostellar cores. This is in turn consistent with the sources' higher fractional polarization, because more ordered B-fields would lead to less averaging of disordered polarization along the LOS. In this subset of sources the B-fields appear to be dynamically important, and may play a role in regulating the infall of material down to ~ 0.01 pc scales.

The remaining "low-polarization" sources ($\overline{P}_{\rm frac} < 3\%$) are L1448N(B) (Figure 4.7), NGC 1333-IRAS 2A (Figure 4.10), SVS 13 (Figure 4.11), NGC 1333-IRAS 4B (Figure 4.13), L1551 NE (Figure 4.16), L1527 (Figure 4.17), VLA 1623 (Figure 4.23), and Ser-emb 6 (Figure 4.27).

Unlike the high-polarization sources, these low-polarization sources may have low ratios of magnetic to turbulent energy, which would result in more twisted small-scale B-fields and thus

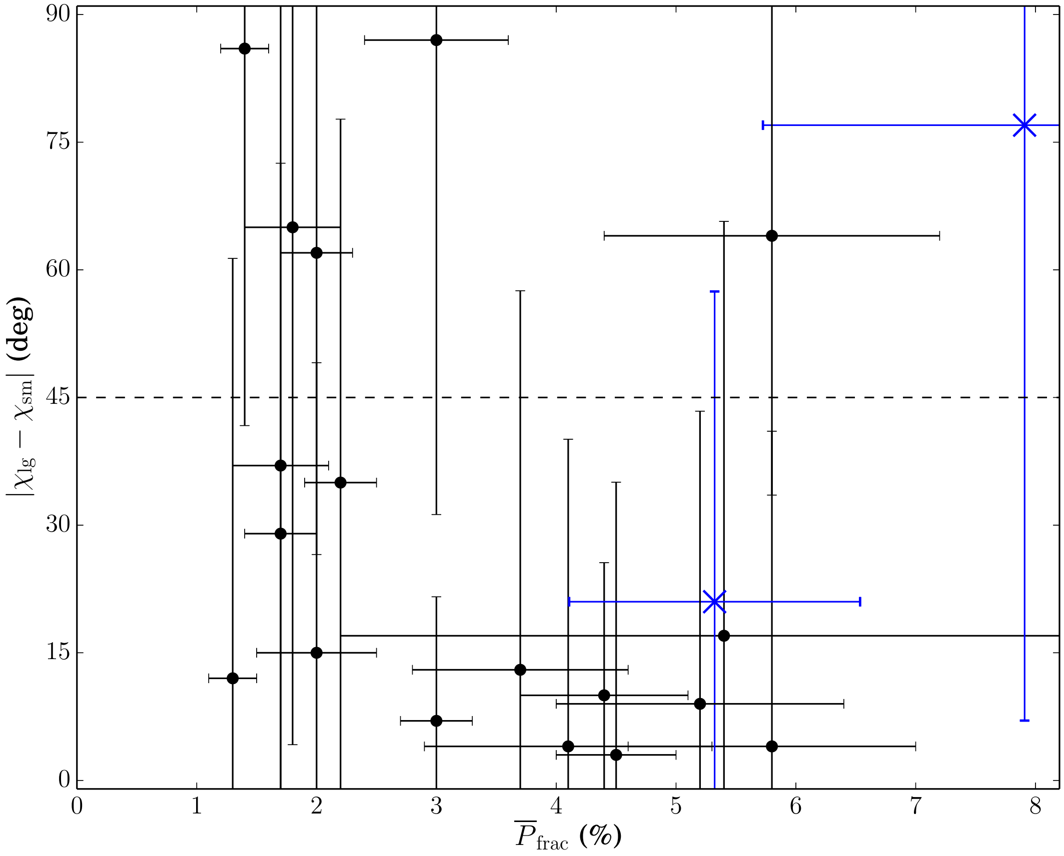

Figure 4.1: Large- vs. small-scale B-field orientation $|\chi_{\rm lg} - \chi_{\rm sm}|$ as a function of polarization fraction $\overline{P}_{\rm frac}$. Sources are included if they have (1) B-field detections at both scales, (2) CARMA polarization detections $P_c > 3.5\,\sigma_P$, and (3) distances $d \lesssim 400\,$pc. The plotted uncertainty in $|\chi_{\rm lg} - \chi_{\rm sm}|$ is equal to the uncertainties in $\chi_{\rm sm}$ and $\chi_{\rm lg}$ added in quadrature, where those uncertainties reflect the dispersion of the B-field orientations in each source. The fractional polarization $\overline{P}_{\rm frac} = \overline{P}\,/\,\overline{I}$, where $\overline{P}$ and $\overline{I}$ are the unweighted averages of the polarized and total intensities in locations where $P_c > 3.5\,\sigma_P$. Points below the 45° line exhibit overall alignment between large- and small-scale fields.

low CARMA polarization fractions. Note that straight B-fields with a high inclination angle relative to the LOS would also result in low fractional polarization; however, the likelihood of observing B-fields nearly pole-on is low.

Note that we are not asserting that higher polarization is caused directly by stronger B-fields, or that weak polarization occurs because of weak B-fields or poor grain alignment. We simply assume that high and low polarization fractions are caused by B-fields that are less or more twisted, respectively.

We have not yet discussed the more distant sources in our sample, which are all massive star-forming regions (SFRs). Four of these have been observed previously by SCUBA, Hertz, and/or SHARP: W3 Main (Figure 4.4), W3(OH) (Figure 4.5), DR21(OH) (Figure 4.32), and NGC 7538 IRS 1 (Figure 4.36). It is important to note that we are probing different structures in these objects than we are in the nearby star-forming cores: at the distances to the more distant SFRs, the angular resolution of our CARMA maps corresponds to a spatial resolution of $\sim 0.1\,\mathrm{pc}$. It is evident from our maps that at these scales the B-fields in the SFRs have been twisted, most likely by dynamic processes, as high-mass SFRs are known to be highly turbulent (Elmegreen & Scalo 2004). This suggests that for massive SFRs the ratio of magnetic to turbulent energy is low at $\sim 0.1\,\mathrm{pc}$ scales.

4.5.2 Misalignment of B-fields and bipolar outflows

We first addressed the question of B-field and outflow misalignment in Hull et al. (2013), where we found that bipolar outflows were randomly aligned with—or perhaps preferentially perpendicular to—the small-scale B-fields in their associated protostellar envelopes. In this paper we use the same sample of nearby ($d \lesssim 400\,\mathrm{pc}$) low-mass cores with well defined outflows used by Hull et al. (2013), minus IRAS 16293 A, which was not a TADPOL source.

The outflow angles are the same as those used in Hull et al. (2013); the values for χ_{sm} typically differ by a few degrees because of the inclusion of additional data. Note that we do not include SFRs in this analysis, nor do we include sources with complicated outflow structure such as SVS13 (Figure 4.11) and OMC2-FIR3/4 (Figure 4.21). All sources included in Figure 4.2 have an asterisk (*) next to their outflow orientation in Table 4.1.

In this paper we extend this analysis to include a comparison of outflow orientations vs. large-scale B-fields. Additionally, for each of these comparisons we split the sources into high- and low-polarization subsamples and plot a separate CDF for each. The heavy dashed and solid curves in Figure 4.2 correspond to the high- and low-polarization subsamples, respectively.

As discussed in Hull et al. (2013), the B-field and outflow position angles we observe are projected onto the plane of the sky. To determine if the large scatter in position angle differences could be due to projection effects, we compare the results with Monte Carlo simulations where the outflows and B-fields are tightly aligned, somewhat aligned, preferentially perpendicular, or randomly aligned.

For the tightly aligned case, the simulation randomly selects pairs of vectors in three dimensions that are within 20° of one another, and then projects the vectors onto the plane of the sky and measures their angular differences. The resulting CDF is shown in Figure 4.2. In this case projection effects are not as problematic as one might think: to have a projected separation larger than 20° the two vectors must point almost along the line of sight.

For the somewhat-aligned and preferentially-perpendicular cases the simulation randomly selects pairs of vectors that are separated by 0–45° or 70–90°, respectively. In these cases projection effects are more important and result in CDFs that are closer to that expected for random alignment, shown by the thin straight line (see Figure 4.2).

In all four cases in Figure 4.2 a Kolmogorov–Smirnov (K-S) test rules out the scenario where outflows and B-fields are tightly aligned (the K-S probabilities for all distributions are < 0.002). This is consistent with the results from Hull et al. (2013), who found that outflows and small-scale B-fields are not tightly aligned.

The K-S test also shows that all of the distributions are consistent with random alignment. However, in low-polarization sources the K-S test gives a probability of only 0.12 that the outflows and small-scale B-fields are randomly aligned, hinting[6] that they may be preferentially perpendicular. (Note that the K-S test does not take into account the dispersions in the B-field orientations reported in Table 4.1.)

We speculate that the polarization fractions are low in these sources because B-fields have be wrapped up toroidally by envelope rotation. Rotation at $\sim$1000 AU scales has been detected in at least two of the sources: see N_2H^+ observations of CB 230 and CB 244 by Chen et al. (2007) using OVRO (the Owens Valley Radio Observatory). The envelope rotation axes are roughly aligned with the outflow axes in both of these sources.

This result could have important consequences for the formation of circumstellar disks within rotating envelopes, since preferential misalignment of the B-field and the rotation axis should allow disks to form more easily (Hennebelle & Ciardi 2009; Krasnopolsky et al. 2012; Joos et al. 2012; Li et al. 2013). Objects with misaligned B-fields and rotation axes are less susceptible to the "magnetic braking catastrophe," where magnetic braking prevents the formation of a rotationally supported Keplerian disk (Allen et al. 2003; Li et al. 2011). Indeed, these models suggest that misalignment may be a necessary condition for the formation of disks (see also Krumholz et al. 2013).

What about the high-polarization population? These could be sources where we do not have the angular resolution to see B-field twisting and instead are seeing a bright sheath of polarized material that has retained the "memory" of the global B-field. Perhaps these are younger sources, or perhaps cores can form with a wide range of B-field strengths (e.g., Vázquez-Semadeni et al. 2011) and some are strong enough to resist twisting.

It is important to emphasize that even if we are seeing wrapped small-scale B-fields in the low-polarization sample, the scales we are probing are $\sim$500–1000 AU envelope scales, *not* $\sim$100 AU disk scales. Consequently, the B-fields would have been wrapped up by the envelopes and not by the disks. However, many simulations (e.g., Machida et al. 2006; Myers et al. 2013) expect the B-fields in a protostar to be wrapped up at disk scales, regardless of the larger-scale B-field morphology in the envelope and the core. If this is the case, then with sufficient angular resolution ALMA should see perpendicular B-fields and outflows even in our high-polarization sample.

---

[6] We use the word "hint" because typically a K-S test is considered to be definitive only when the statistic is < 0.1.

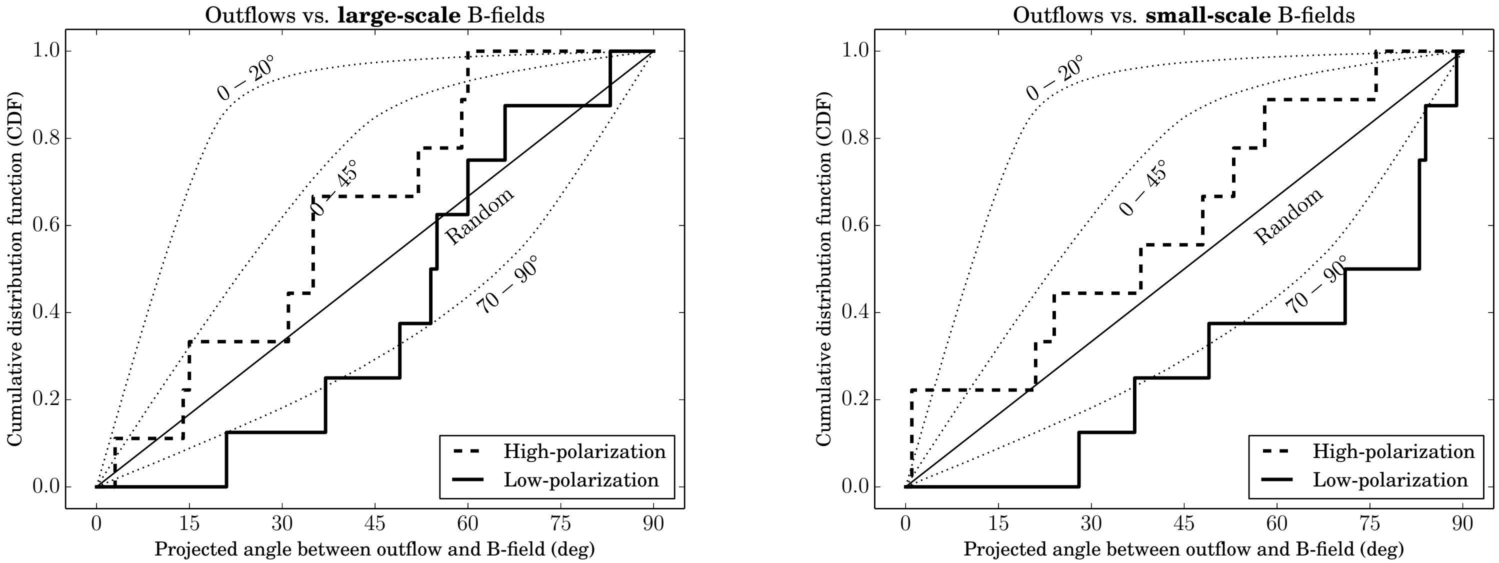

Figure 4.2: The thick, stepped curves show the cumulative distribution functions (CDF) of the (projected) angles between the bipolar outflows and the mean large-scale (left) and small-scale (right) B-field orientations in the low-mass protostellar cores listed in Table 4.1. Sources included in the plot have an asterisk (*) next to their outflow orientation in the table. Large-scale B-fields are from archival CSO and JCMT data, and have $\sim 20''$ resolution; small-scale B-fields are from the CARMA data, and have $\sim 2.5''$ resolution. The dashed curves include the "high-polarization" sources, and the solid curves include the "low-polarization" sources (see Section 4.5.1 for a discussion of high- vs. low-polarization sources). Sources are included if they have (1) B-field detections at both large and small scales, (2) CARMA polarization detections $P_c > 3.5\,\sigma_P$, (3) distances $d \lesssim 400\,\mathrm{pc}$, and (4) well defined bipolar outflows. The dotted curves are the CDFs from Monte Carlo simulations where the B-fields and outflows are oriented within 20°, 45°, and 70–90° of one another, respectively. The straight line is the CDF for random orientation. The two plots show that outflows appear to be randomly aligned with B-fields; although, in sources with low polarization fractions there is a hint that outflows are preferentially perpendicular to small-scale B-fields, which suggests that in these sources the fields have been wrapped up by envelope rotation (see Section 4.5.2).

One possible concern with this analysis is that outflows could disrupt the small-scale B-fields in the protostellar envelopes. And indeed, in a few sources we see hints that the fields are stretched along the direction of the outflow [e.g., NGC-1333 IRAS 2A (Figure 4.10), HH 211 mm (Figure 4.14), Ser-emb 6 (Figure 4.27), and L1157 (Figure 4.33)]. However, these detections tend to be quite far from the central intensity peak, where the B-field orientation is usually different. This suggests that while outflows may drag B-fields along with them, the outflows do not disrupt the B-fields in the densest parts of the protostellar envelope.

Another concern is that over time outflows could have changed direction, and that deep in the core the outflows and B-fields could actually be aligned. However, many sources show bipolar ejections with consistent position angles over parsec scales. Some examples of such sources from the TADPOL survey include HH 211 mm (Lee et al. 2009), L1448 IRS 2 (Tobin et al. 2007; O'Linger et al. 1999), L1157 (Gueth et al. 1996; Bachiller & Perez Gutierrez 1997), L1527 (Hogerheijde et al. 1998), and VLA 1623 (Andre et al. 1990).

A source that helps dispel the above concerns is OMC3-MMS6, which has a very small bipolar outflow with a dynamical age of only 100 yr (Takahashi & Ho 2012), too young to have either perturbed the B-field or changed direction appreciably. As is clear in the maps in Figure 4.20, the outflow is not aligned with either the large- or the small-scale fields around MMS6, suggesting that the orientation of the disk launching the outflow truly is misaligned with the B-field in the envelope.

4.5.3 Fractional polarization "hole"

The "polarization hole" effect, where the fractional polarization of protostellar cores drops near their dust emission peaks, is a well known phenomenon that has been seen in many previous observations (e.g., Dotson 1996; Matthews et al. 2002; Girart et al. 2006; Liu et al. 2013). We see the same effect in all of our maps, for both nearby low-mass sources and distant high-mass sources; this shows that the polarization hole effect is present across many size scales, although the reasons for the effect may be different at different scales. See Figure 4.3 for sample maps of polarization fraction in L1157 and DR21(OH); these maps show that in both cores and SFRs, the polarization fraction is higher at the edges and lower near the total intensity peaks.

For low resolution maps (e.g., those with $\sim 20''$ resolution from SCUBA, Hertz, and SHARP), a plausible explanation of the polarization holes was unresolved structure that was averaged across the beam. However, in some of the higher resolution ($\sim 2.5''$ resolution) maps presented here and in previous interferometric observations, these twisted plane-of-sky B-field morphologies have been resolved, and yet the drop in fractional polarization persists.

There are multiple possible explanations. First, except for a very few lines of sight through the densest parts of protostellar disks, millimeter-wavelength thermal dust emission is optically thin, and thus we are integrating along the LOS. If the B-field orientation is not consistent along the LOS (due to turbulence or rotation, for example), averaging will result in reduced fractional polarization. Second, there could still be unresolved B-field structure in the plane of the sky at scales smaller than the $\sim 2.5''$ resolution of the CARMA data (e.g., Rao et al. 1998). And third, grains at the centers of cores could be poorly aligned because grain alignment is less efficient in regions with high extinction, or because collisions knock grains out of alignment at higher densities. Simulations of polarized emission from turbulent cores that include the above effects show the polarization hole (e.g., Padoan et al. 2001; Lazarian 2005; Bethell et al. 2007; Pelkonen et al. 2009).

4.6 Summary

We have presented polarization maps of low-mass star-forming cores and high-mass star-forming regions from the TADPOL survey. Using source-averaged B-field orientations and polarization fractions, we have studied the statistical properties of the ensemble of sources and have come to the following key conclusions:

(1) Sources with high CARMA polarization fractions also have consistent B-field orientations on large ($\sim 20''$) and small ($\sim 2.5''$) scales. We interpret this to mean that in at least some cases B-fields play a role in regulating the infall of material all the way down to the ~ 1000 AU scales of protostellar envelopes.

(2) Outflows appear to be randomly aligned with B-fields; although, in sources with low polarization fractions there is a hint that outflows are preferentially perpendicular to small-scale B-fields, which suggests that in these sources the fields have been wrapped up by envelope rotation.

(3) Finally, even at $\sim 2.5''$ resolution we see the so-called “polarization hole” effect, where the fractional polarization drops significantly near the total intensity peak.

As the largest survey of low-mass protostellar cores to date, the TADPOL project sets the stage for observations with ALMA. ALMA’s unprecedented sensitivity will allow us to answer the question of what happens to magnetic fields in very young Class 0 protostars between the ~ 1000 AU scales we probe in this work and the ~ 100 AU scales of the circumstellar disks. The addition of ALMA data to the TADPOL sample will also enable more robust statistical analyses of the types done in both this work and in Hull et al. (2013), and will allow us to see trends in B-field morphology with source mass, age, environment, multiplicity, envelope rotation, outflow velocity, and B-field strength.

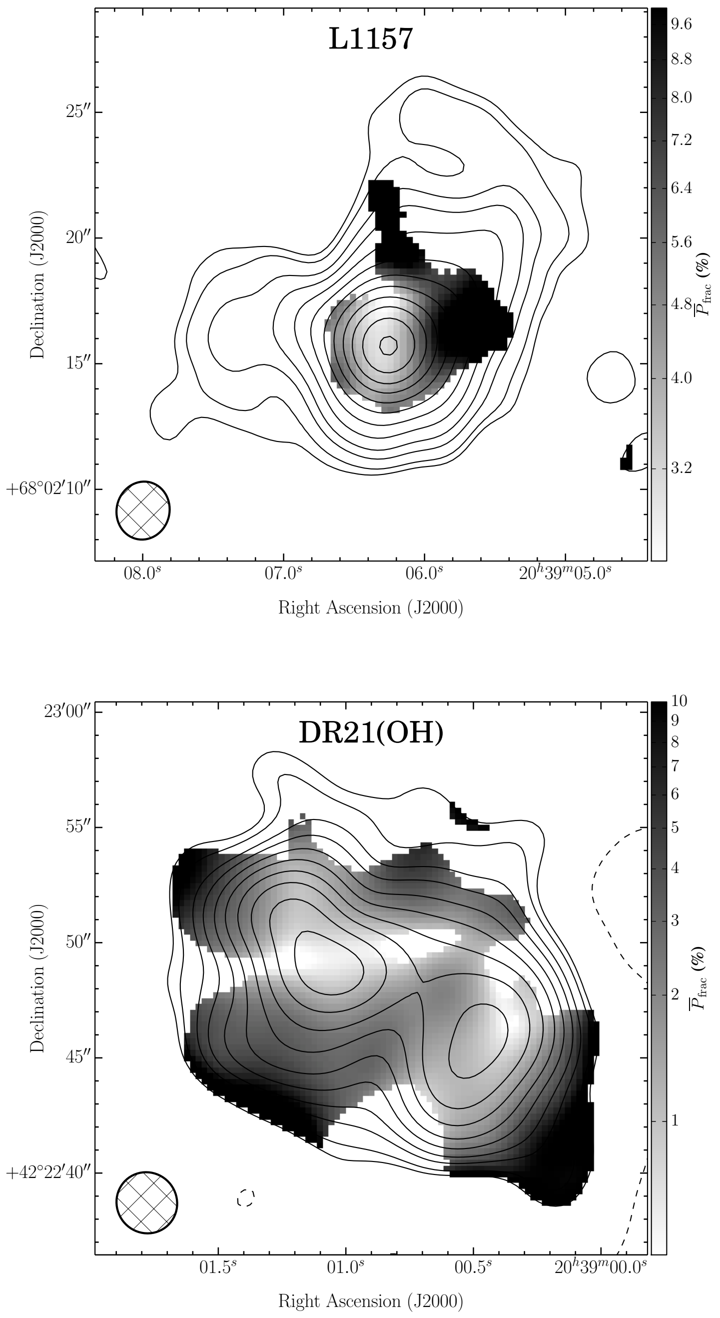

Figure 4.3: Sample maps of polarization fraction (grayscale), with dust continuum contours overlaid. The grayscale saturates at 10% in order to emphasize the low polarization fraction near the center of each object; however, the polarization fraction near the edge can be significantly higher. The dust continuum contours in all dust maps are $-3, 2, 3, 5, 7, 10, 14, 20, 28, 40, 56, 79, 111, 155, 217 \times \sigma_I$ (see Section 4.7). Polarization fraction has only been plotted in locations with significant polarization detections (i.e., $P_c > 3.5\,\sigma_P$).

Acknowledgements (Chapter 4)

We would like thank the referee for the thorough and insightful comments, which improved the paper significantly.

C.L.H.H. would like to acknowledge the advice and guidance of the members of the Berkeley Radio Astronomy Laboratory and the Berkeley Astronomy Department. In particular he would like to thank James Gao and James McBride, as well as the authors of the APLpy plotting package, for helping make the Python plots of TADPOL sources a reality. He would also like to thank Nicholas Chapman for helping to compile the SHARP data.

C.L.H.H. acknowledges support from an NSF Graduate Fellowship and from a Ford Foundation Dissertation Fellowship. J.D.F. acknowledges support from an NSERC Discovery grant. J.J.T. acknowledges support provided by NASA through Hubble Fellowship grant #HST-HF-51300.01-A awarded by the Space Telescope Science Institute, which is operated by the Association of Universities for Research in Astronomy, Inc., for NASA, under contract NAS 5-26555. N.R. acknowledges support from South Africa Square Kilometer Array (SKA) Postdoctoral Fellowship program.

Support for CARMA construction was derived from the states of California, Illinois, and Maryland, the James S. McDonnell Foundation, the Gordon and Betty Moore Foundation, the Kenneth T. and Eileen L. Norris Foundation, the University of Chicago, the Associates of the California Institute of Technology, and the National Science Foundation. Ongoing CARMA development and operations are supported by the National Science Foundation under a cooperative agreement, and by the CARMA partner universities.

4.7 Appendix A: Source Maps

All maps from the TADPOL survey are publicly available as FITS images and machine readable tables. For each figure below we include maps of Stokes I, Q, and U; bias-corrected polarization intensity P_c; polarization fraction $P_{\rm frac} = P_c/I$; and inferred B-field orientation $\chi_{\rm sm}$. Additionally, we include FITS cubes of total intensity (Stokes I) spectral-line data, as well as machine readable tables listing the RA, DEC, I, P_c, $P_{\rm frac}$, $\chi_{\rm sm}$, and associated uncertainties of each line segment plotted in the figures. These files are available in a .tar.gz package available via the link in the figure caption.

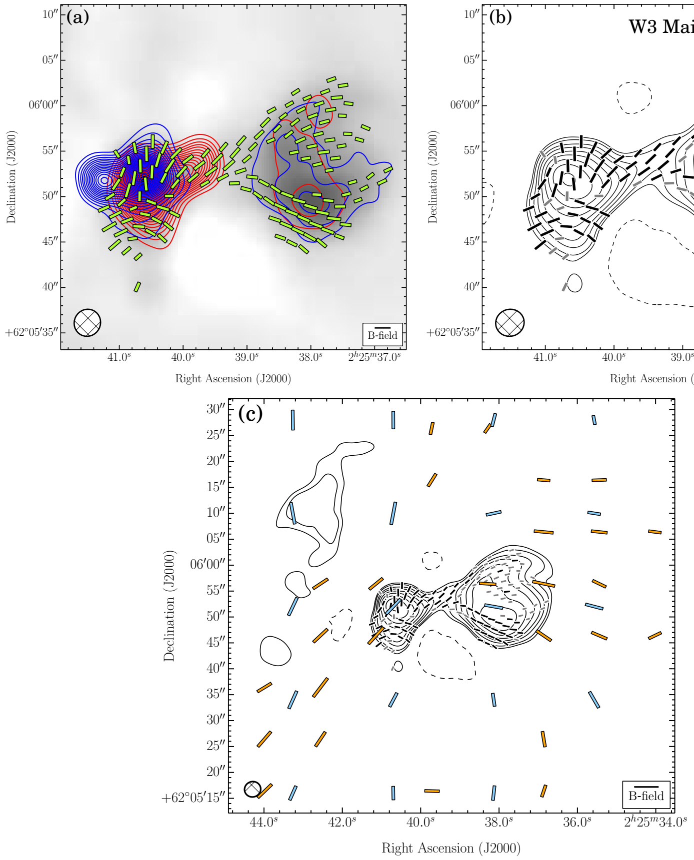

Figure 4.4: Maps of W3 Main. The line segments show the inferred magnetic field orientations; they have been rotated by 90° relative to the polarization orientations. Segments are plotted twice per synthesized beam (resolution element) in locations where $I > 2\,\sigma_I$ and $P_c > 2\,\sigma_P$, where I is the total intensity of the dust emission, P_c is the bias-corrected polarized intensity, and σ_I and σ_P are the rms noise values in the total and polarized intensity maps, respectively. **(a)** The segment lengths are proportional to the square root of polarized intensity, *not* fractional polarization. The grayscale is proportional to the total intensity (Stokes I) dust emission. The blue and red contours are the blue- and redshifted spectral line wings. The outflow orientation is indicated by a gray line for sources with outflows listed in Table 4.1. The velocity ranges of the CO($J = 2 \rightarrow 1$) emission in this map are –2.3 to –10.8 $\mathrm{km\,s^{-1}}$ (redshifted) and –67.9 to –80.6 $\mathrm{km\,s^{-1}}$ (blueshifted). The contour levels in all spectral line maps are $4, 8, 12, 16$ and $20, 25, 30 \ldots 190, 195, 200 \times \sigma_{\mathrm{SL}}$, where σ_{SL} is the rms noise measured in the spectral line moment maps. In this map, $\sigma_{\mathrm{SL}} = 0.50\ \mathrm{K\,km\,s^{-1}}$. **(b)** Line segments are black where $P_c > 3.5\,\sigma_P$ and gray where $2\,\sigma_P < P_c < 3.5\,\sigma_P$. The grid on which the line segments are plotted is centered on the polarization intensity peak $P_{\mathrm{c,pk}}$, which is not necessarily spatially coincident with the total intensity peak I_{pk}. The ellipses show the synthesized beams. The dust continuum contours in all dust maps are $-3, 2, 3, 5, 7, 10, 14, 20, 28, 40, 56, 79, 111, 155, 217 \times \sigma_I$. In this map, $\sigma_I = 8.8\ \mathrm{mJy\,bm^{-1}}$. **(c)** Same dust contours and B-field orientations as in (b), with data from three submillimeter polarimeters overlaid: SCUBA (in orange, from Matthews et al. 2009), Hertz (in light blue, from Dotson et al. 2010), and SHARP (in purple, from Attard et al. 2009; Davidson et al. 2011; Chapman et al. 2013). For SCUBA, Hertz, and SHARP data the segment lengths are proportional to the square root of the polarized intensity.

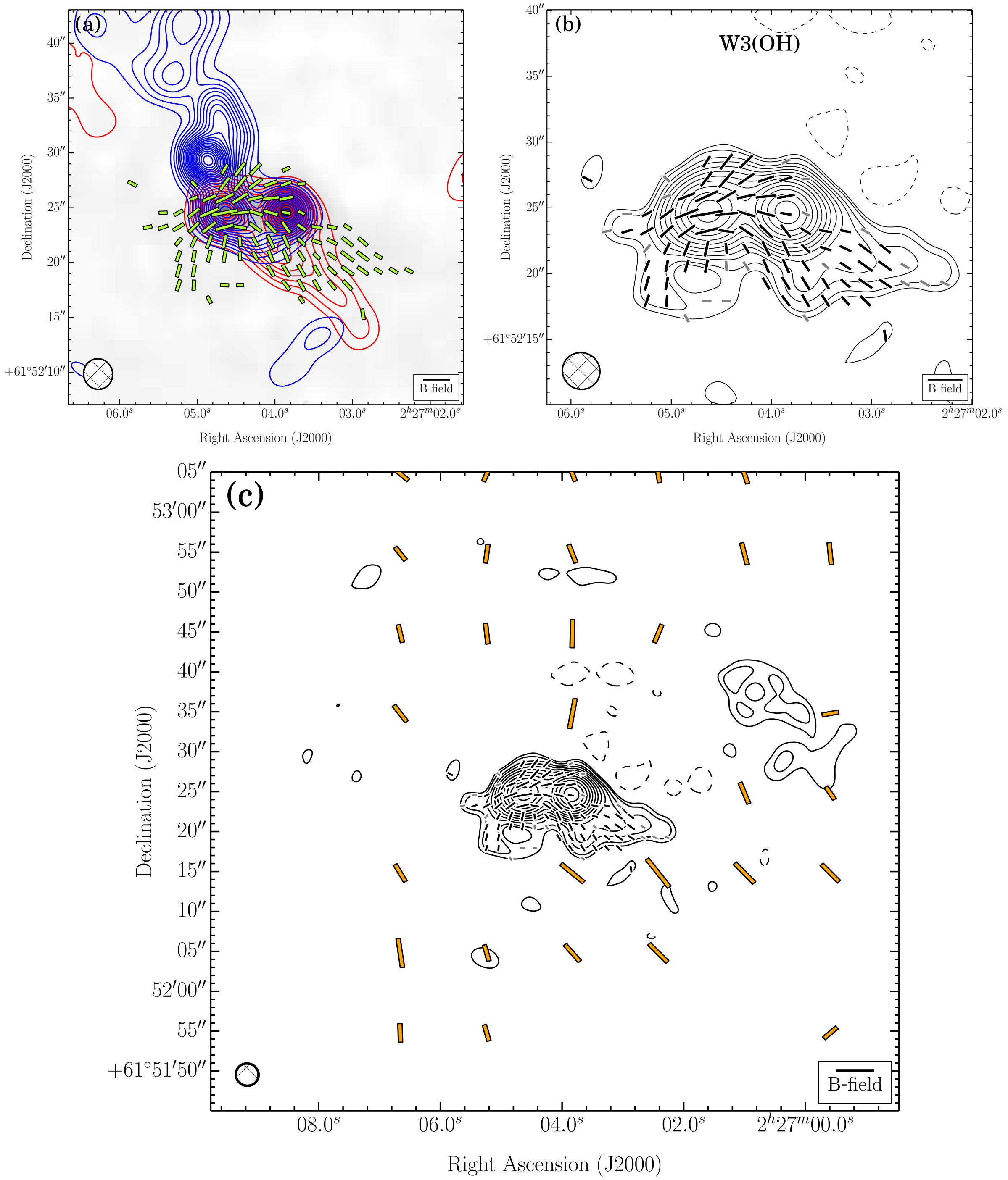

Figure 4.5: W3(OH). Same as Figure 4. **(a)** The velocity ranges of the CO($J = 2 \rightarrow 1$) line wing emission are –13.4 to –34.5 $\mathrm{km\,s^{-1}}$ (redshifted) and –57.8 to –72.6 $\mathrm{km\,s^{-1}}$ (blueshifted). $\sigma_{\mathrm{SL}} = 1.97\ \mathrm{K\,km\,s^{-1}}$. **(b)** $\sigma_I = 14.4\ \mathrm{mJy\,bm^{-1}}$.

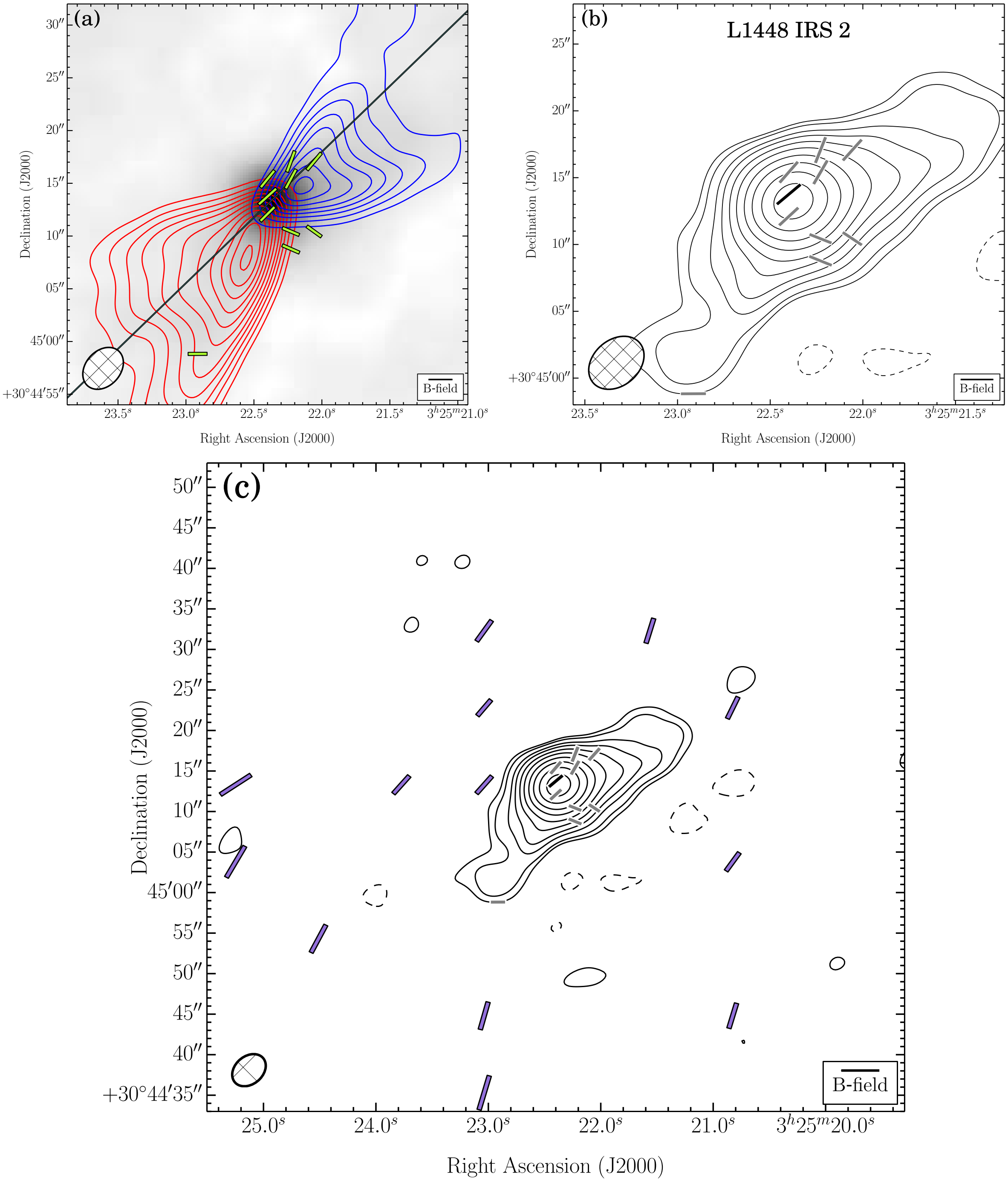

Figure 4.6: L1448 IRS 2. Same as Figure 4. **(a)** The velocity ranges of the CO($J = 2 \rightarrow 1$) line wing emission are 18.0 to 7.5 km s^{-1} (redshifted) and 1.1 to –6.3 km s^{-1} (blueshifted). $\sigma_{\mathrm{SL}} = 1.39$ K km s^{-1}. **(b)** $\sigma_I = 2.0$ mJy bm^{-1}.

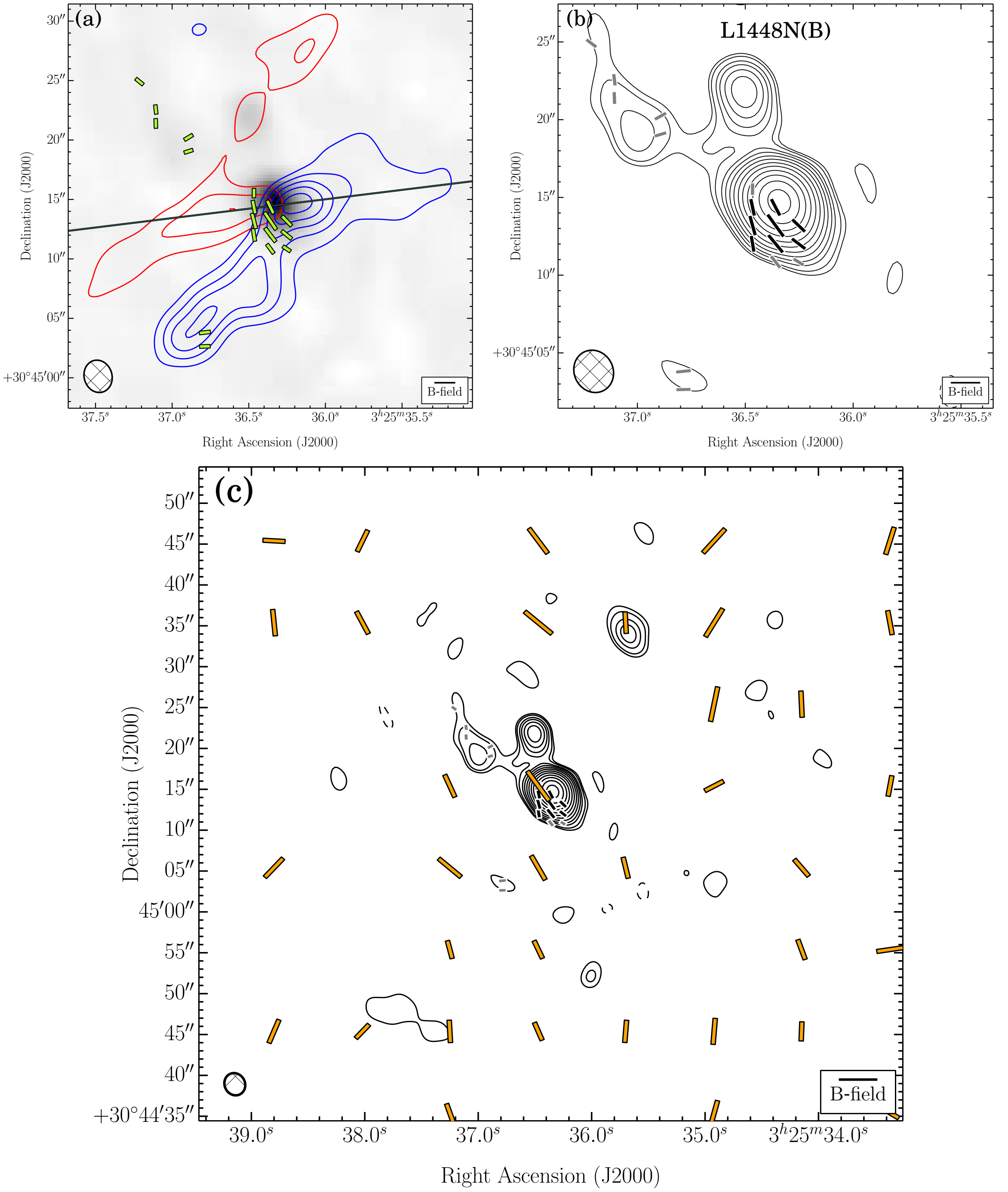

Figure 4.7: L1448N(B). Same as Figure 4. **(a)** The velocity ranges of the CO($J = 2 \rightarrow 1$) line wing emission are 25.4 to 11.6 km s^{-1} (redshifted) and –0.0 to –11.7 km s^{-1} (blueshifted). $\sigma_{\mathrm{SL}} = 4.33$ K km s^{-1}. **(b)** $\sigma_I = 4.5$ mJy bm^{-1}.

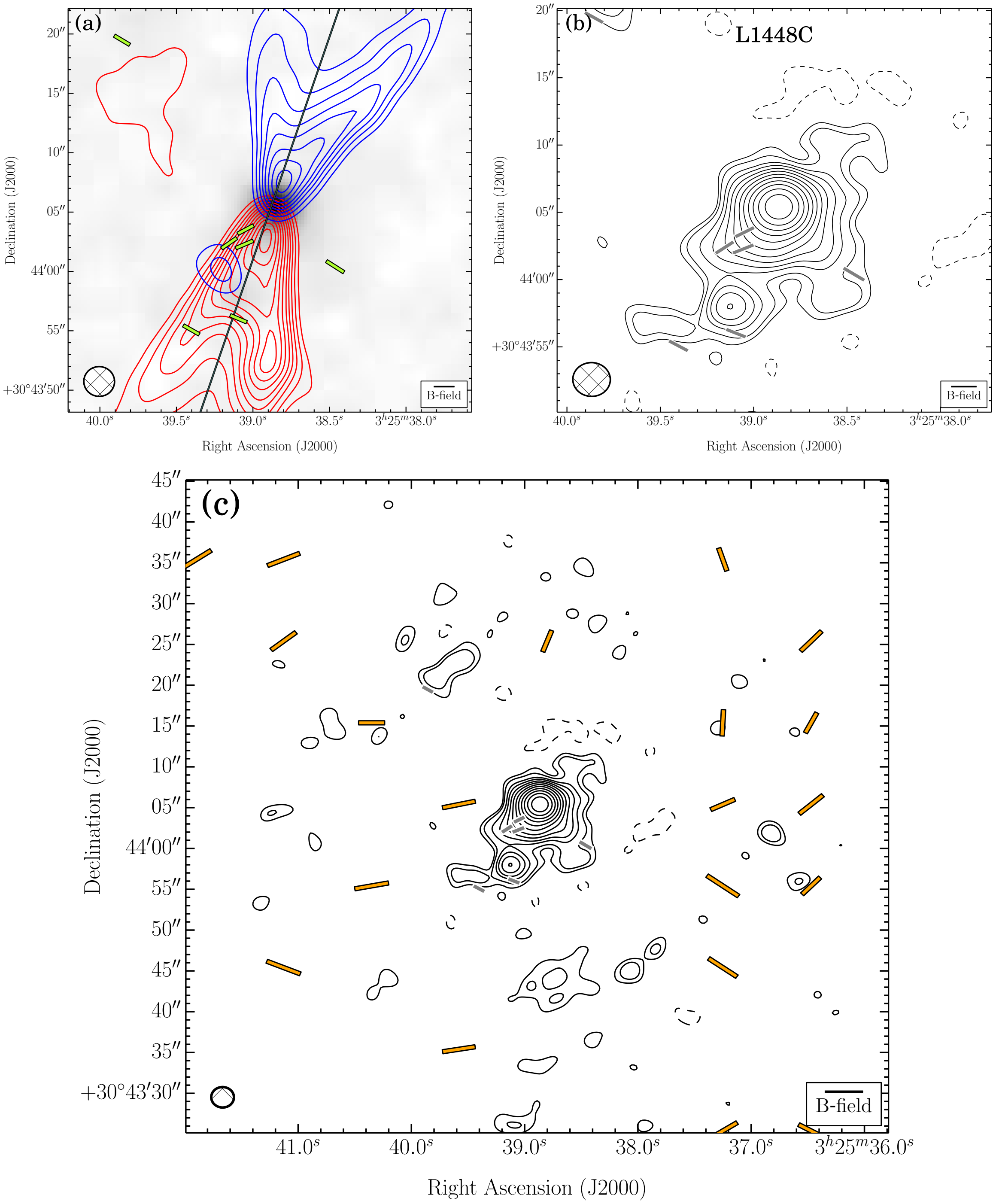

Figure 4.8: L1448C. Same as Figure 4. **(a)** The velocity ranges of the CO(J = 2 → 1) line wing emission are 15.0 to 7.6 km s^{-1} (redshifted) and 1.3 to –12.5 km s^{-1} (blueshifted). $\sigma_{\rm SL} = 3.01$ K km s^{-1}. **(b)** $\sigma_I = 1.2$ mJy bm^{-1}.

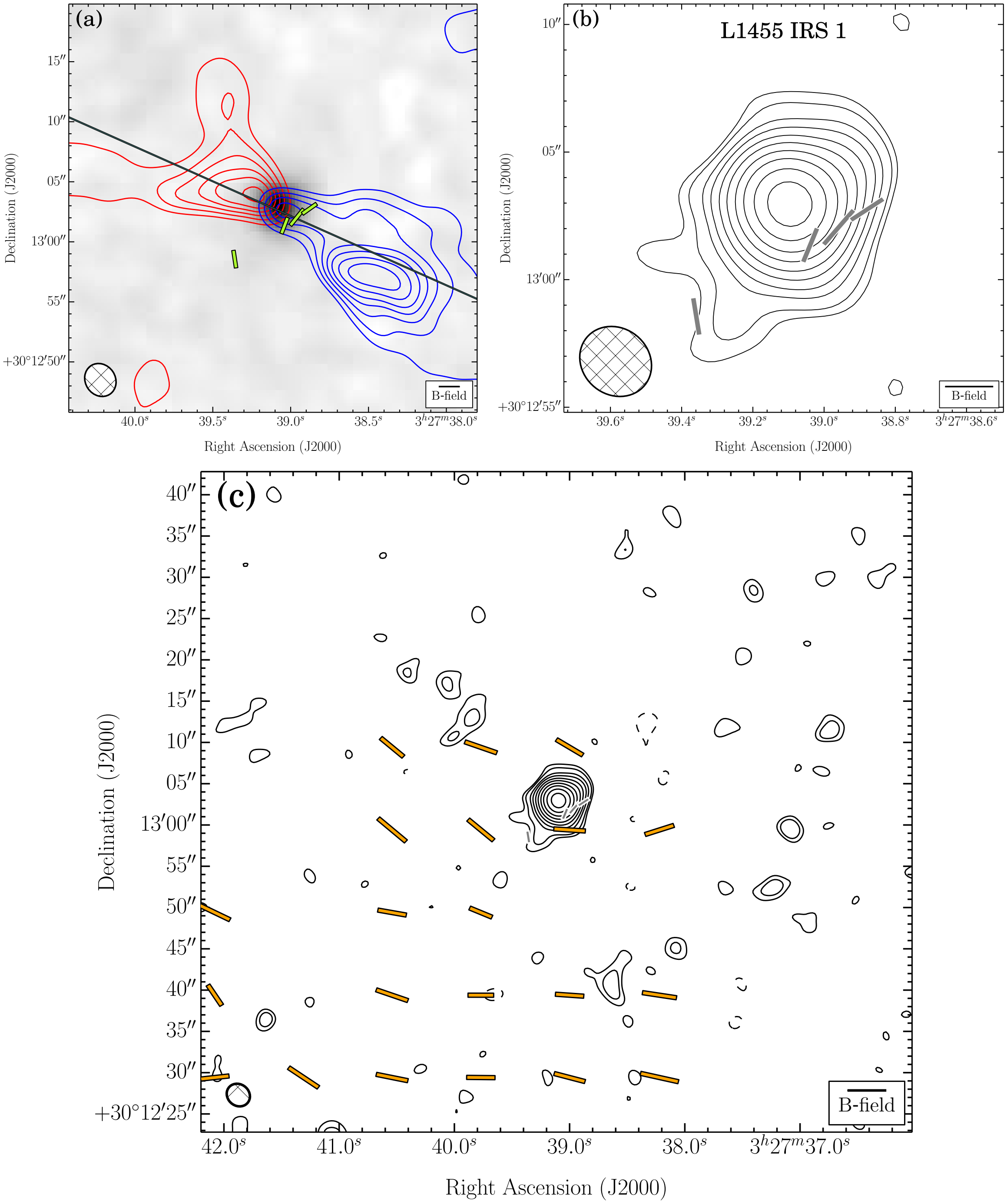

Figure 4.9: L1455 IRS 1. Same as Figure 4. **(a)** The velocity ranges of the CO($J = 2 \rightarrow 1$) line wing emission are 15.7 to 7.2 km s^{-1} (redshifted) and 3.0 to –2.3 km s^{-1} (blueshifted). $\sigma_{\rm SL} = 1.26$ K km s^{-1}. **(b)** $\sigma_I = 0.6$ mJy bm^{-1}.

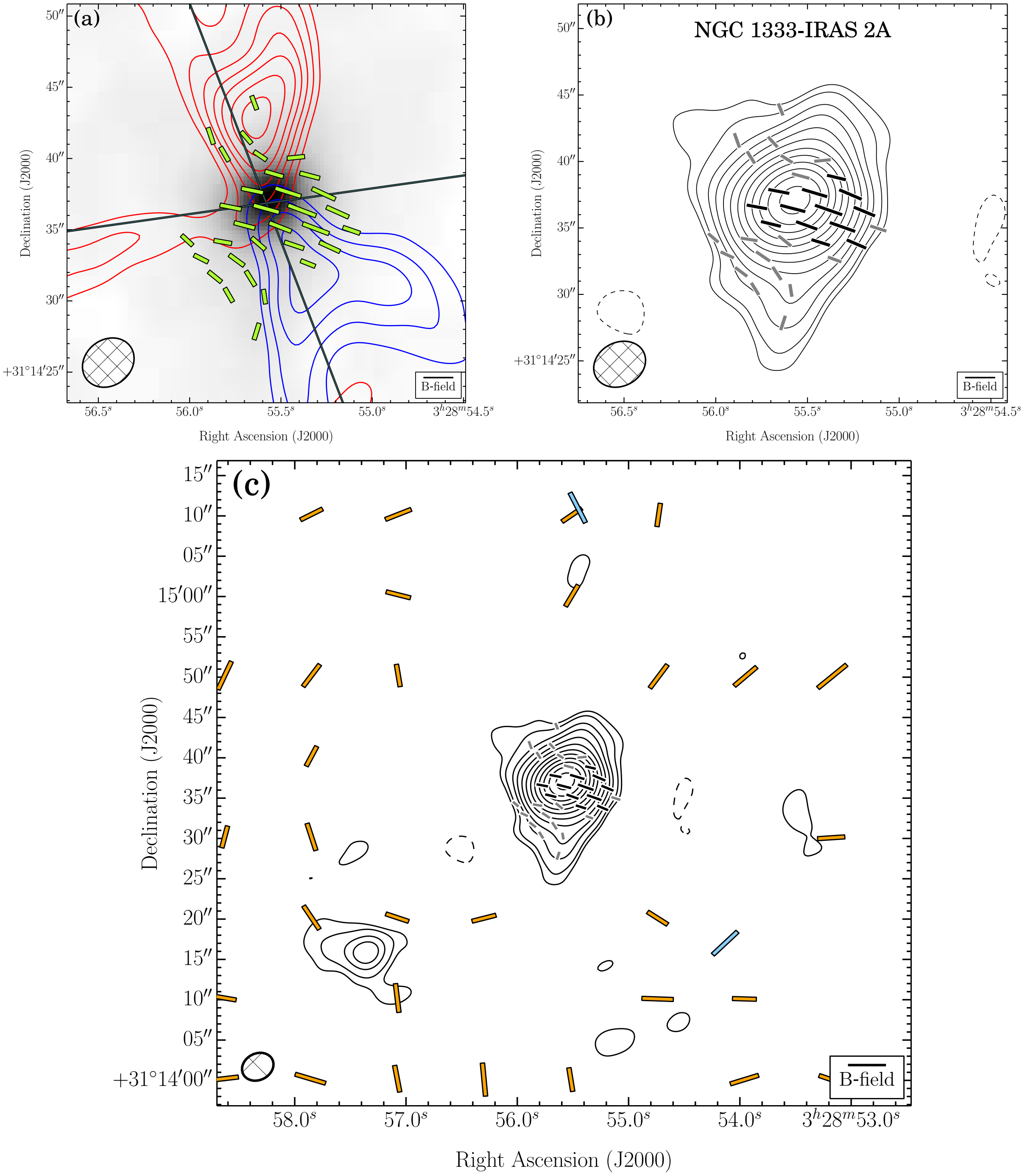

Figure 4.10: NGC 1333-IRAS 2A. Same as Figure 4. **(a)** The velocity ranges of the CO($J = 2 \rightarrow 1$) line wing emission are 27.0 to 10.1 km s^{-1} (redshifted) and 2.6 to –5.8 km s^{-1} (blueshifted). $\sigma_{\rm SL} = 2.07$ K km s^{-1}. **(b)** $\sigma_I = 2.4$ mJy bm^{-1}.

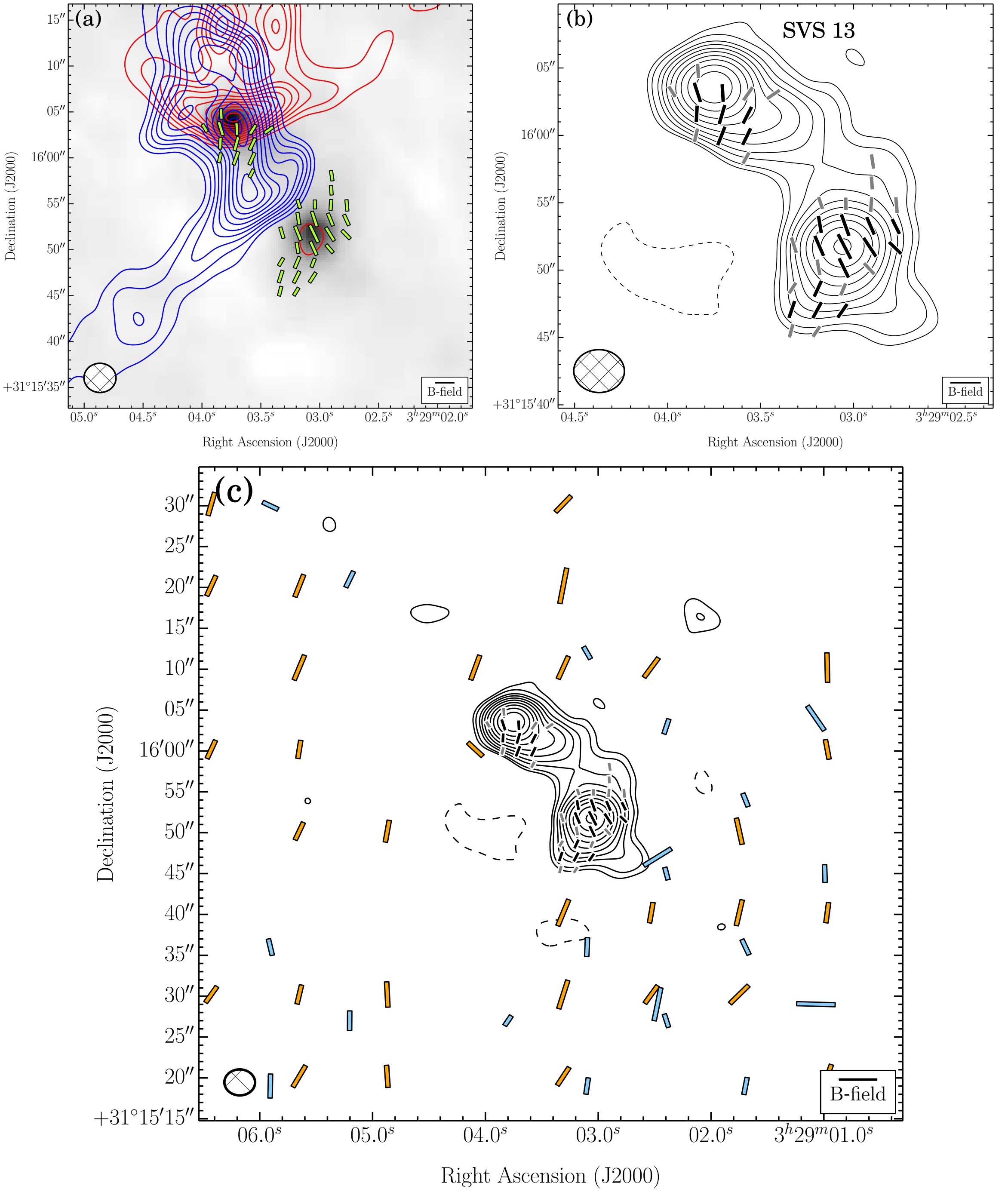

Figure 4.11: SVS 13. Same as Figure 4. **(a)** The velocity ranges of the CO($J = 2 \rightarrow 1$) line wing emission are 27.0 to 19.6 km s^{-1} (redshifted) and –6.9 to –12.2 km s^{-1} (blueshifted). $\sigma_{\mathrm{SL}} = 0.59$ K km s^{-1}. **(b)** $\sigma_I = 3.6$ mJy bm^{-1}.

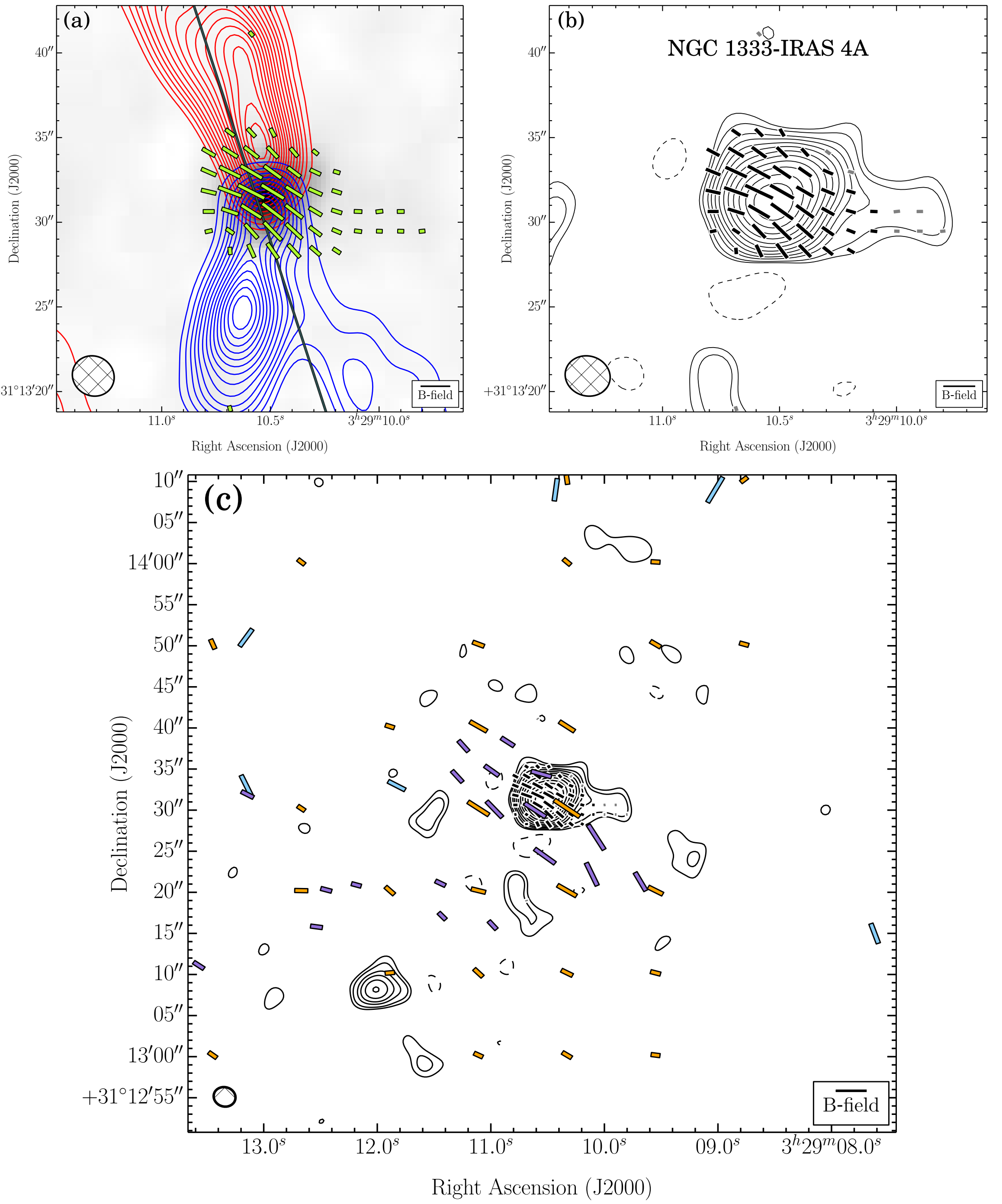

Figure 4.12: NGC 1333-IRAS 4A. Same as Figure 4. **(a)** The velocity ranges of the CO($J = 2 \rightarrow 1$) line wing emission are 11.2 to 3.8 km s^{-1} (redshifted) and –4.6 to –14.2 km s^{-1} (blueshifted). $\sigma_{\mathrm{SL}} = 2.41$ K km s^{-1}. **(b)** $\sigma_I = 10.9$ mJy bm^{-1}.

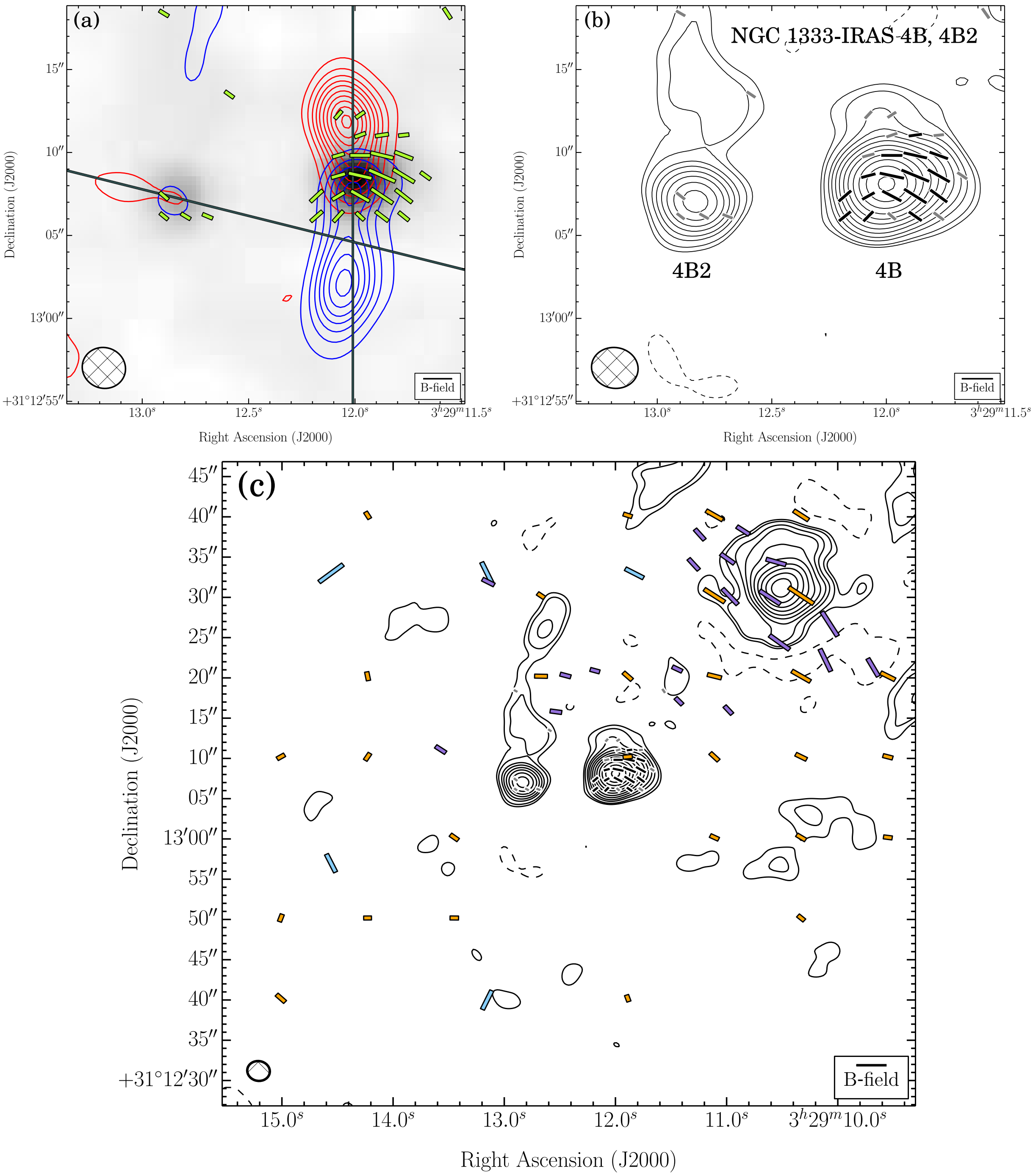

Figure 4.13: NGC 1333-IRAS 4B and 4B2. Same as Figure 4. **(a)** The velocity ranges of the CO($J = 2 \rightarrow 1$) line wing emission are 22.5 to 9.8 km s^{-1} (redshifted) and 3.4 to –12.5 km s^{-1} (blueshifted). $\sigma_{\rm SL} = 3.12$ K km s^{-1}. **(b)** $\sigma_I = 7.3$ mJy bm^{-1}.

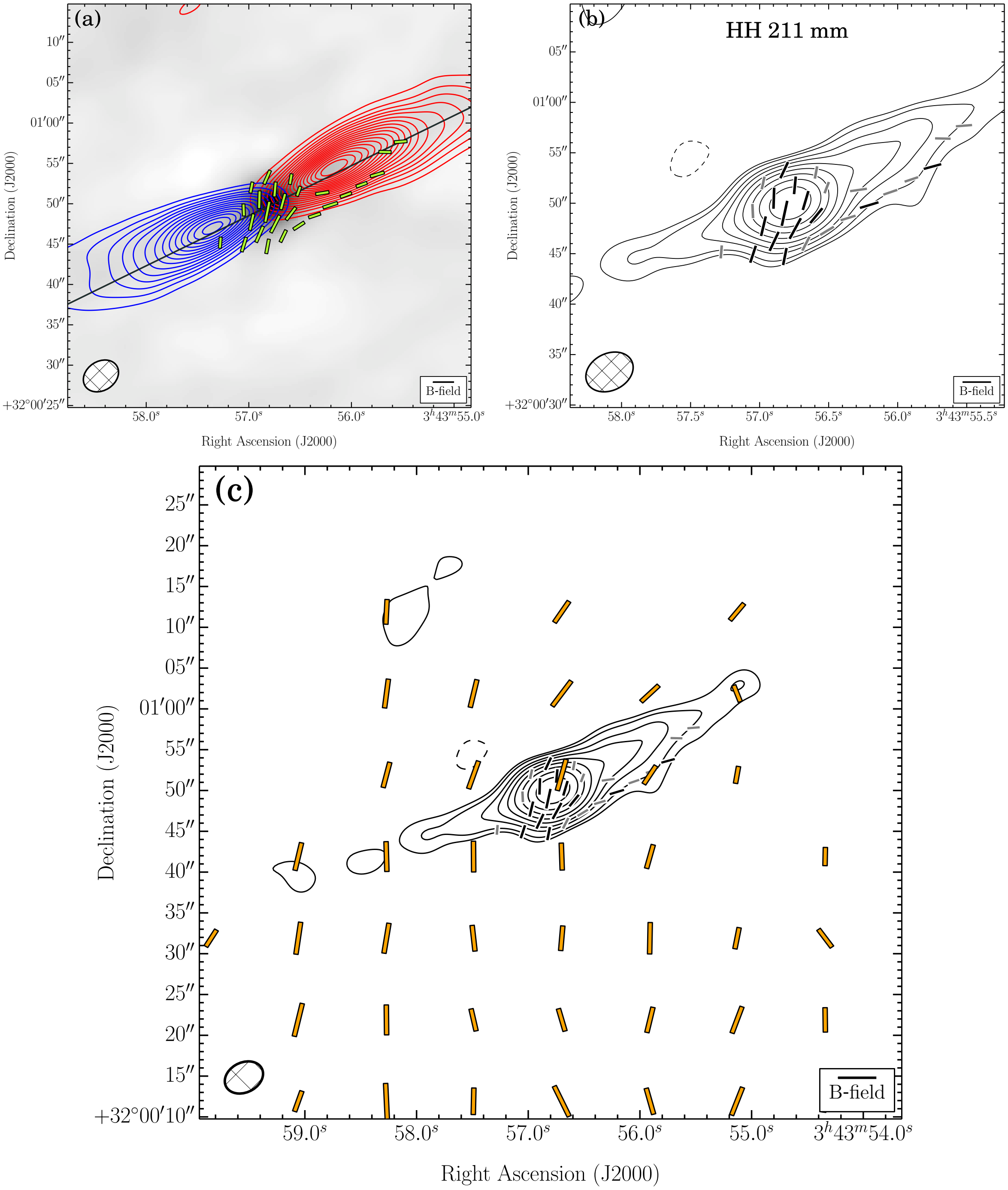

Figure 4.14: HH 211 mm. Same as Figure 4. **(a)** The velocity ranges of the CO($J = 2 \rightarrow 1$) line wing emission are 29.6 to 12.6 $\mathrm{km\,s^{-1}}$ (redshifted) and 6.3 to –3.2 $\mathrm{km\,s^{-1}}$ (blueshifted). $\sigma_{\mathrm{SL}} = 1.03$ $\mathrm{K\,km\,s^{-1}}$. **(b)** $\sigma_I = 3.5$ $\mathrm{mJy\,bm^{-1}}$.

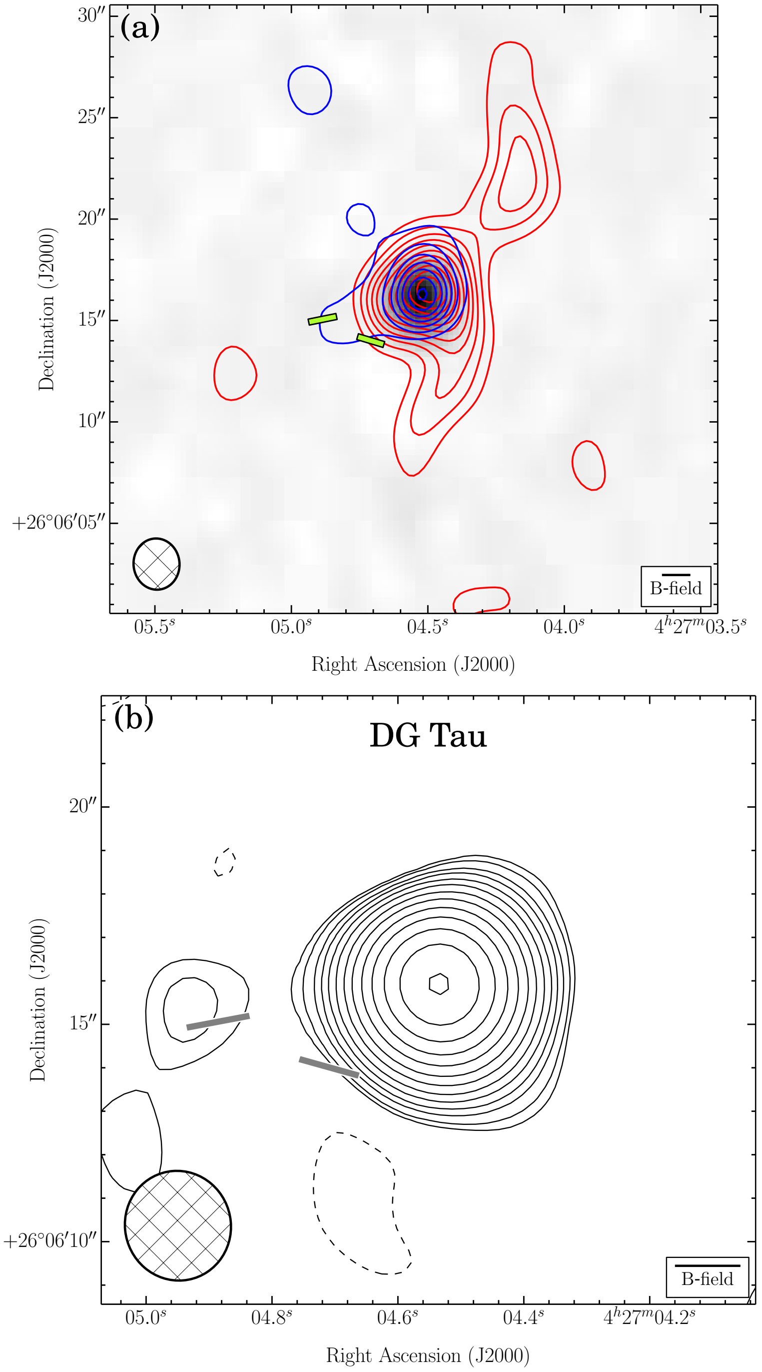

Figure 4.15: DG Tau. Same as Figure 4. **(a)** The velocity ranges of the CO($J = 2 \to 1$) line wing emission are 13.3 to 8.0 $\mathrm{km\,s^{-1}}$ (redshifted) and 4.9 to 0.6 $\mathrm{km\,s^{-1}}$ (blueshifted). $\sigma_{\rm SL} = 0.85$ $\mathrm{K\,km\,s^{-1}}$. **(b)** $\sigma_I = 1.9$ $\mathrm{mJy\,bm^{-1}}$. There is no **(c)** plot because there were no SCUBA, SHARP, or Hertz data to overlay.

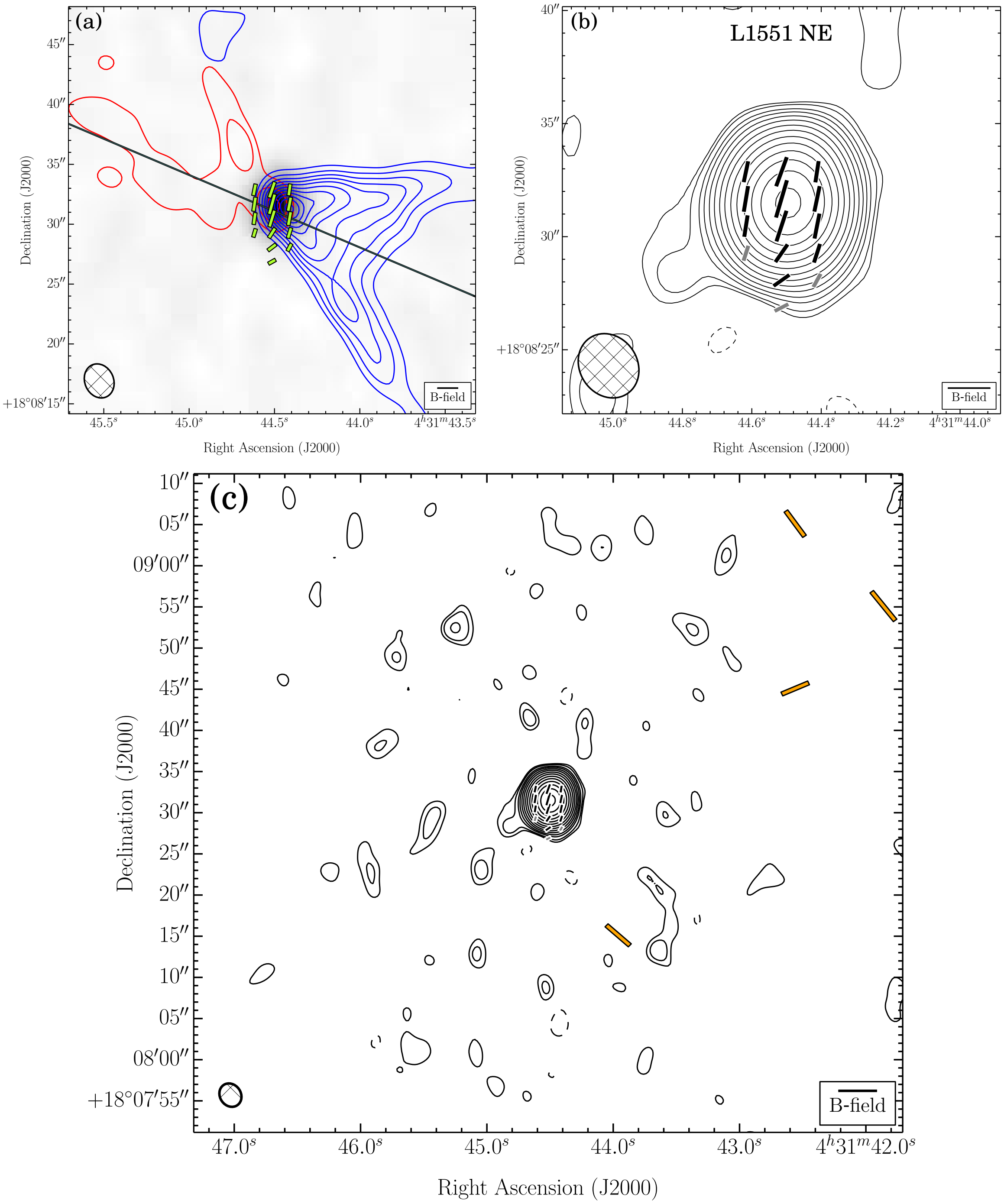

Figure 4.16: L1551 NE. Same as Figure 4. **(a)** The velocity ranges of the CO($J = 2 \rightarrow 1$) line wing emission are 22.5 to 15.0 km s^{-1} (redshifted) and 3.4 to –1.9 km s^{-1} (blueshifted). $\sigma_{\mathrm{SL}} = 0.75$ K km s^{-1}. **(b)** $\sigma_I = 1.8$ mJy bm^{-1}.

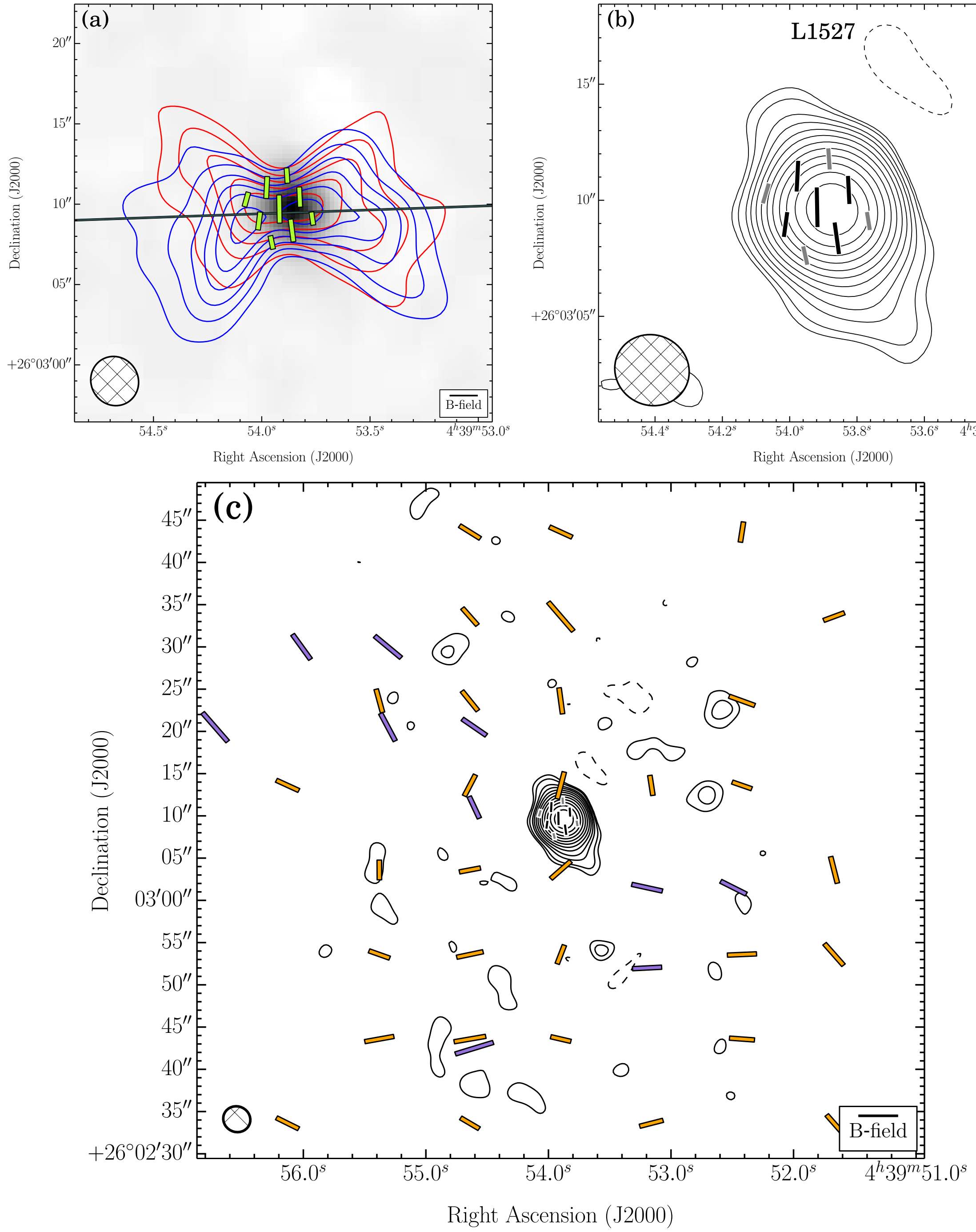

Figure 4.17: L1527. Same as Figure 4. **(a)** The velocity ranges of the CO($J = 2 \rightarrow 1$) line wing emission are 12.9 to 9.7 km s^{-1} (redshifted) and 2.3 to –0.9 km s^{-1} (blueshifted). $\sigma_{\rm SL} = 0.32$ K km s^{-1}. **(b)** $\sigma_I = 1.0$ mJy bm^{-1}.

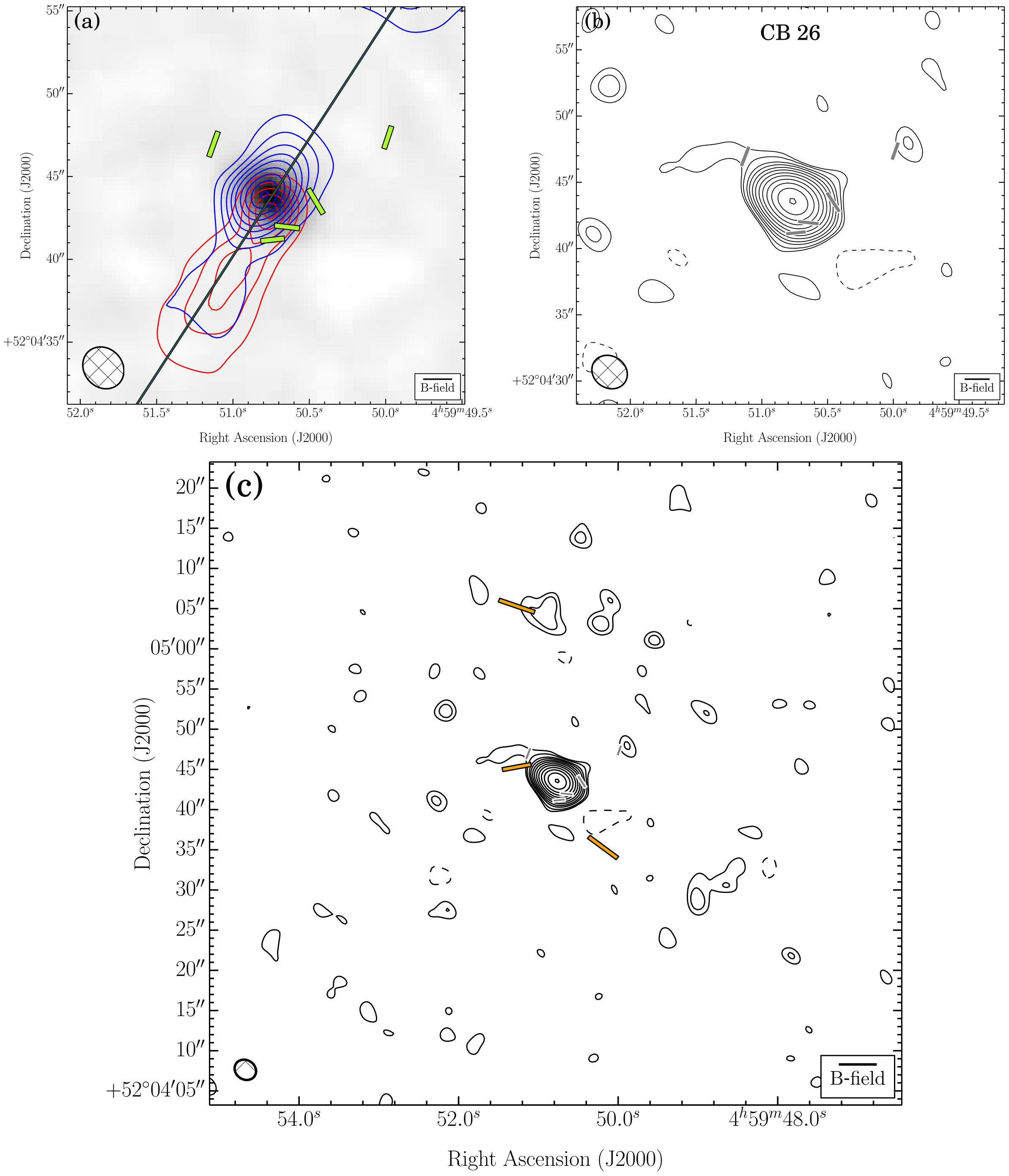

Figure 4.18: CB 26. Same as Figure 4. **(a)** The velocity ranges of the CO($J = 2 \rightarrow 1$) line wing emission are 11.4 to 8.3 km s^{-1} (redshifted) and 4.0 to –0.2 km s^{-1} (blueshifted). $\sigma_{\mathrm{SL}} = 0.46$ K km s^{-1}. **(b)** $\sigma_I = 0.7$ mJy bm^{-1}.

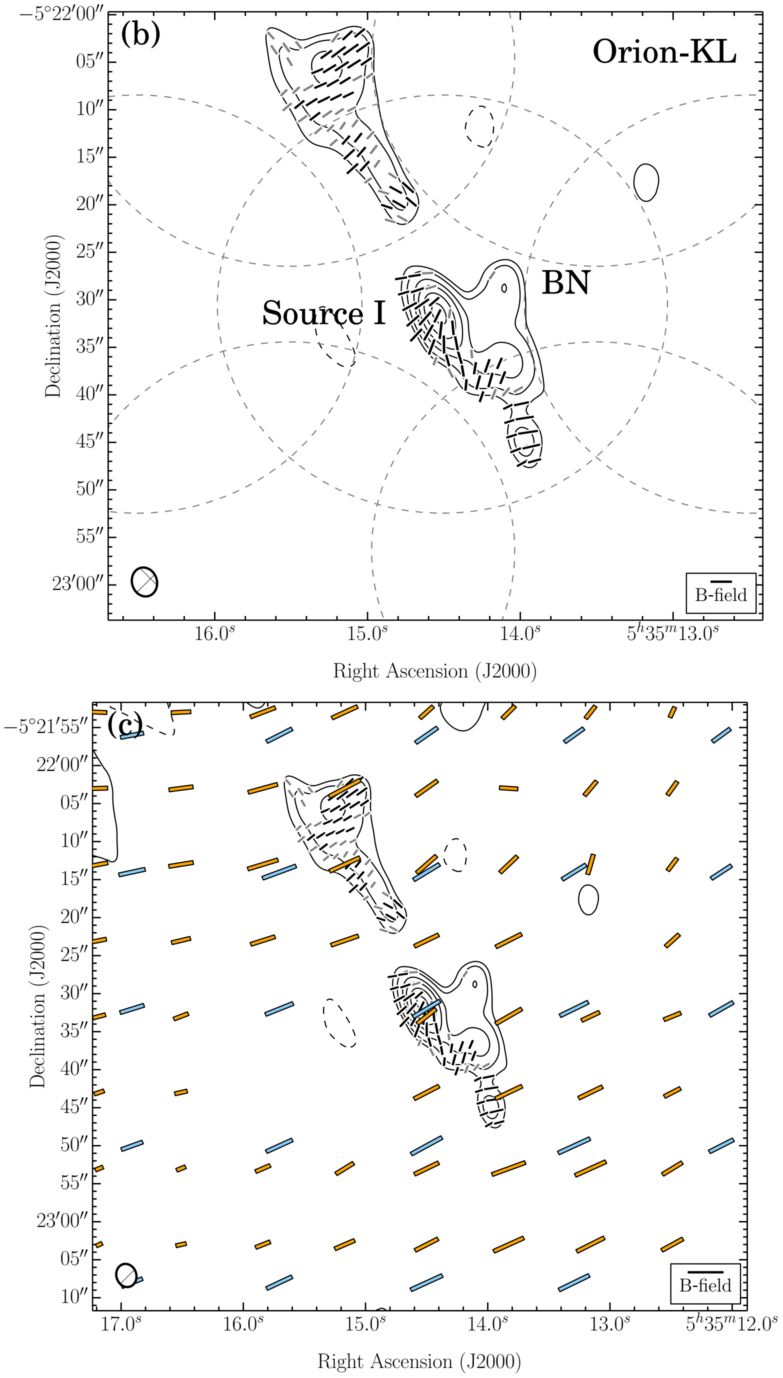

Figure 4.19: Orion-KL. Same as above. **(b)** $\sigma_I = 211.0$ mJy bm^{-1}. The full-width-half-max (FWHM) of the 7 mosaic pointings are plotted as gray, dotted circles. Their diameters ($\sim 44''$) reflect the average primary beam size of the 6 and 10 m telescopes. There is no **(a)** plot because there were no spectral-line data to plot.

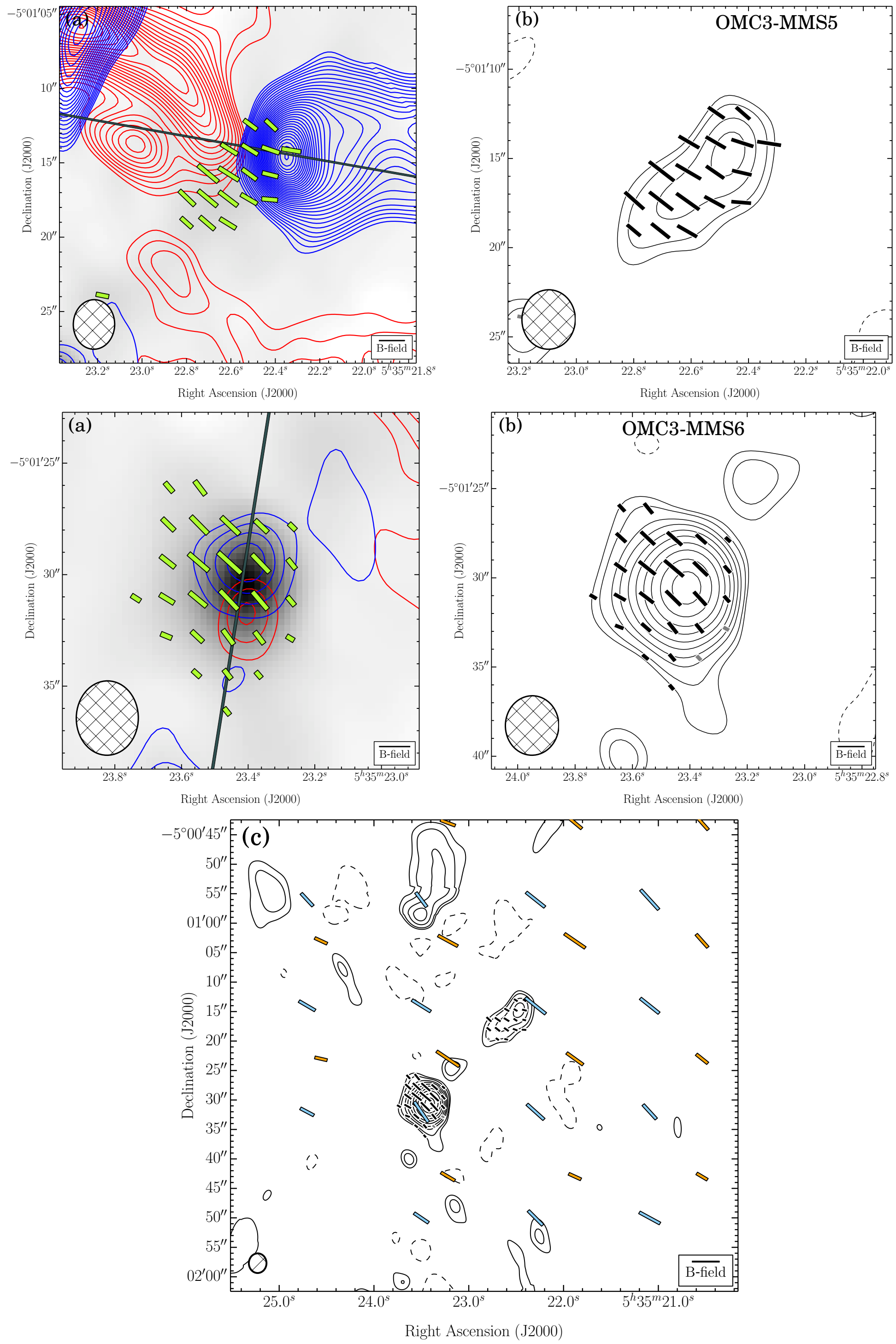

Figure 4.20: OMC3-MMS5 and MMS6. Same as Figure 4. **(a)** The velocity ranges of the CO($J = 2 \rightarrow 1$) line wing emission are 20.7 to 16.5 $\mathrm{km\,s^{-1}}$ (redshifted) and 5.9 to 3.8 $\mathrm{km\,s^{-1}}$ (blueshifted). $\sigma_{\mathrm{SL}} = 0.24\ \mathrm{K\,km\,s^{-1}}$. **(b)** $\sigma_I = 15.0$ $\mathrm{mJy\,bm^{-1}}$.

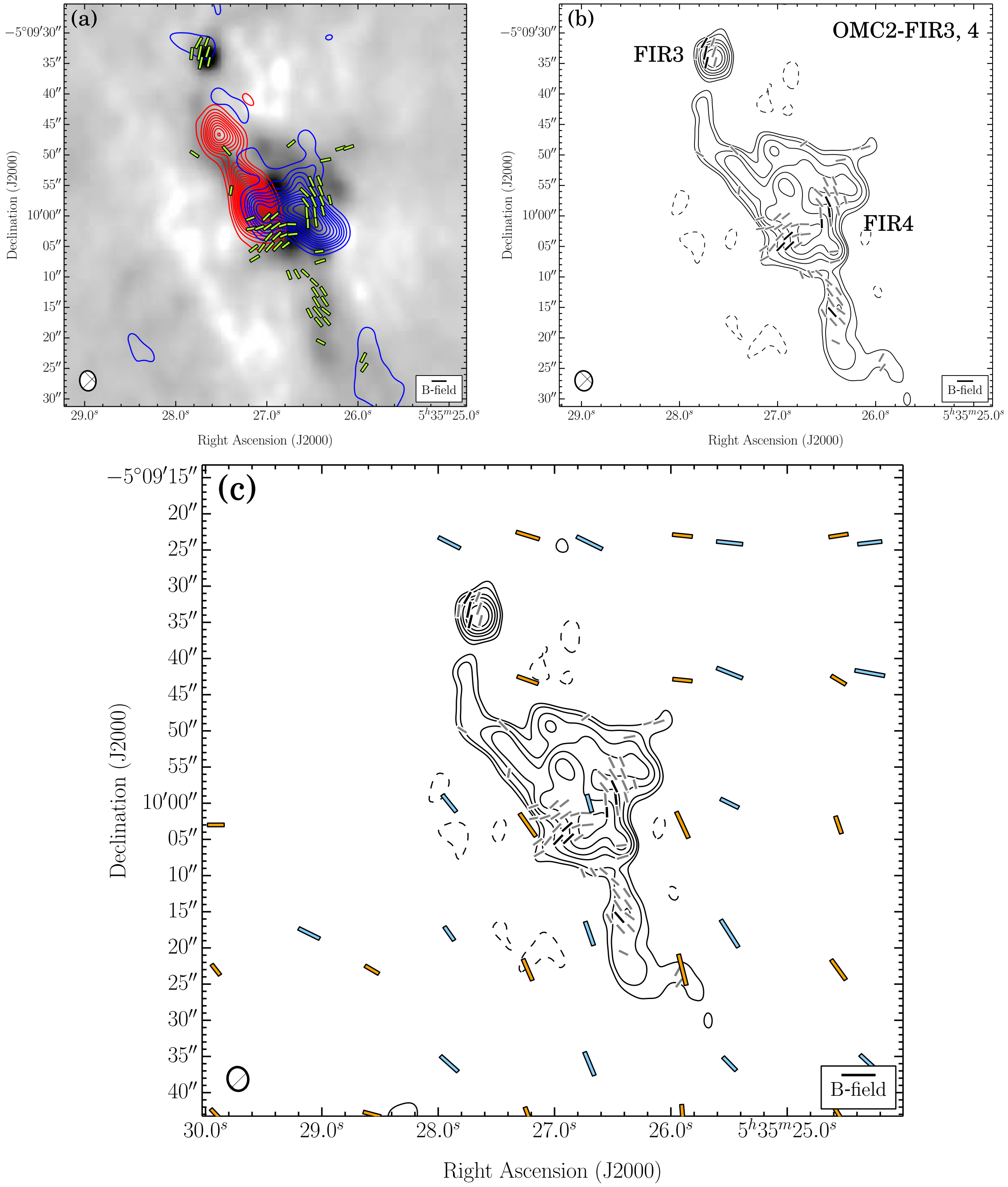

Figure 4.21: OMC2-FIR3 and 4. Same as Figure 4. **(a)** The velocity ranges of the CO($J = 2 \rightarrow 1$) line wing emission are 33.1 to 20.4 $\mathrm{km\,s^{-1}}$ (redshifted) and 1.4 to –11.3 $\mathrm{km\,s^{-1}}$ (blueshifted). $\sigma_{\rm SL} = 1.35\ \mathrm{K\,km\,s^{-1}}$. **(b)** $\sigma_I = 3.5\ \mathrm{mJy\,bm^{-1}}$.

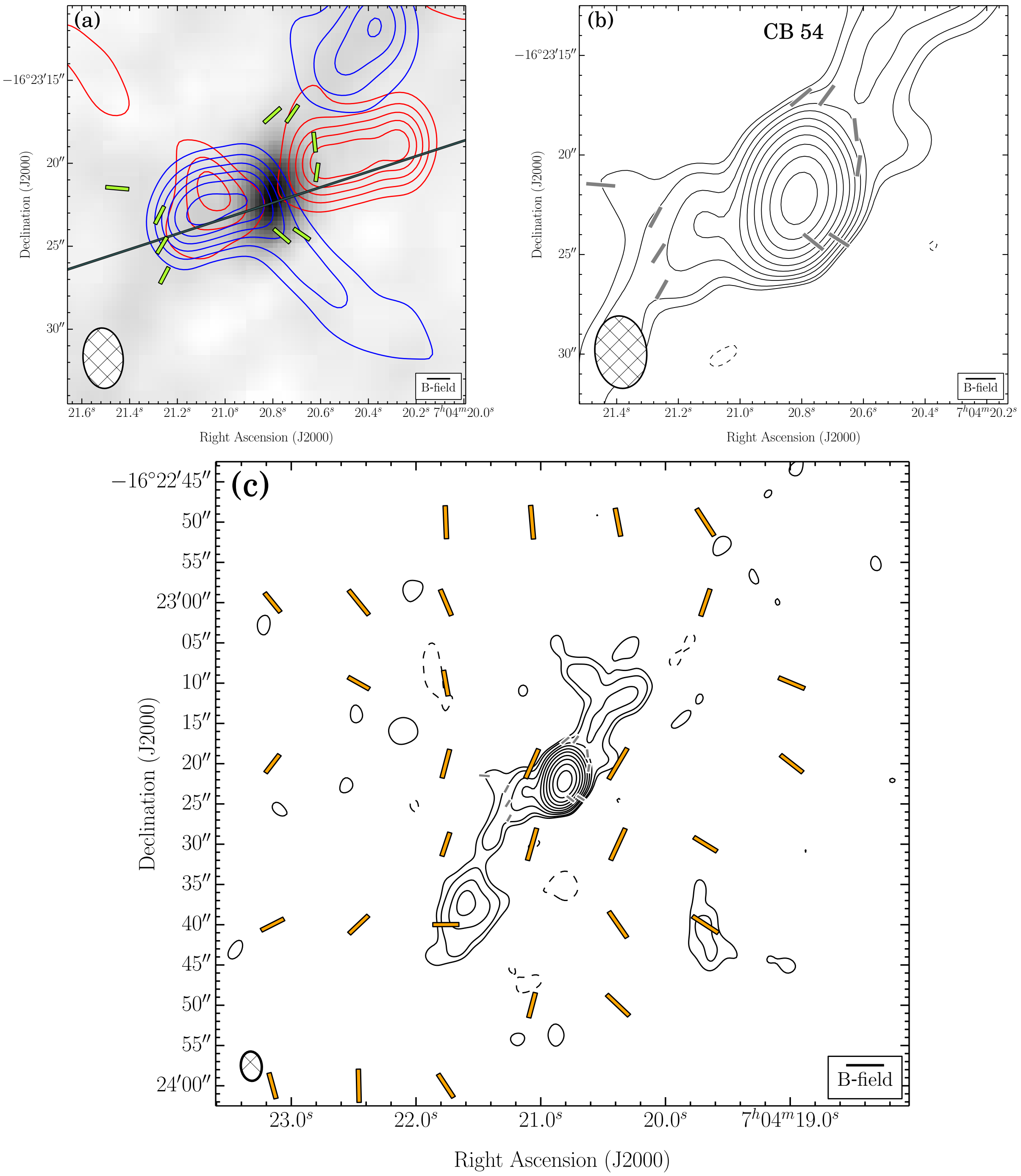

Figure 4.22: CB 54. Same as Figure 4. **(a)** The velocity ranges of the CO($J = 2 \rightarrow 1$) line wing emission are 28.0 to 23.8 $\mathrm{km\,s^{-1}}$ (redshifted) and 14.3 to 9.0 $\mathrm{km\,s^{-1}}$ (blueshifted). $\sigma_{\mathrm{SL}} = 1.28\ \mathrm{K\,km\,s^{-1}}$. **(b)** $\sigma_I = 1.3\ \mathrm{mJy\,bm^{-1}}$.

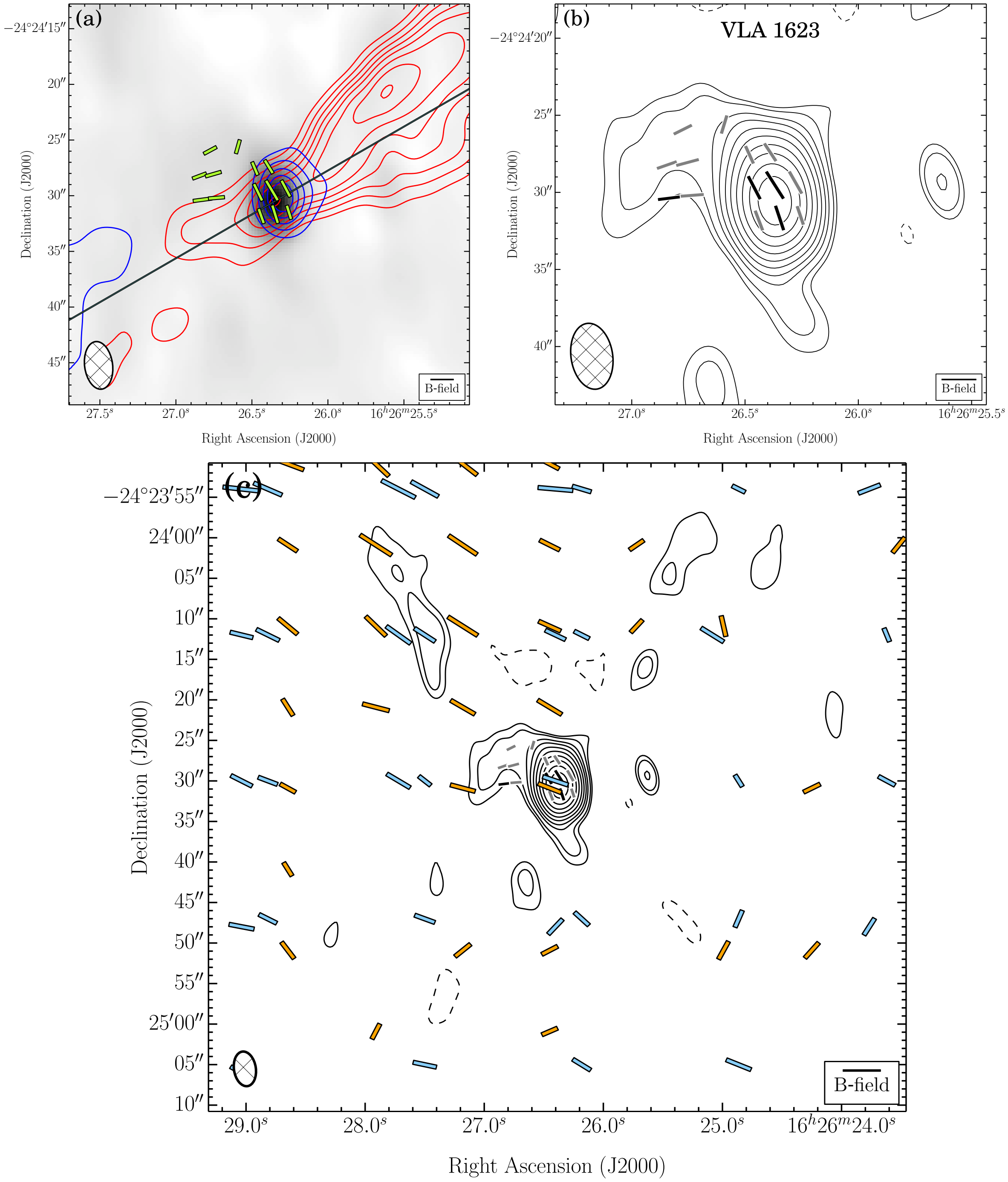

Figure 4.23: VLA 1623. Same as Figure 4. **(a)** The velocity ranges of the CO($J = 2 \rightarrow 1$) line wing emission are 15.2 to 5.7 $\mathrm{km\,s^{-1}}$ (redshifted) and –1.7 to –9.1 $\mathrm{km\,s^{-1}}$ (blueshifted). $\sigma_{\mathrm{SL}} = 0.98$ $\mathrm{K\,km\,s^{-1}}$. **(b)** $\sigma_I = 3.8$ $\mathrm{mJy\,bm^{-1}}$.

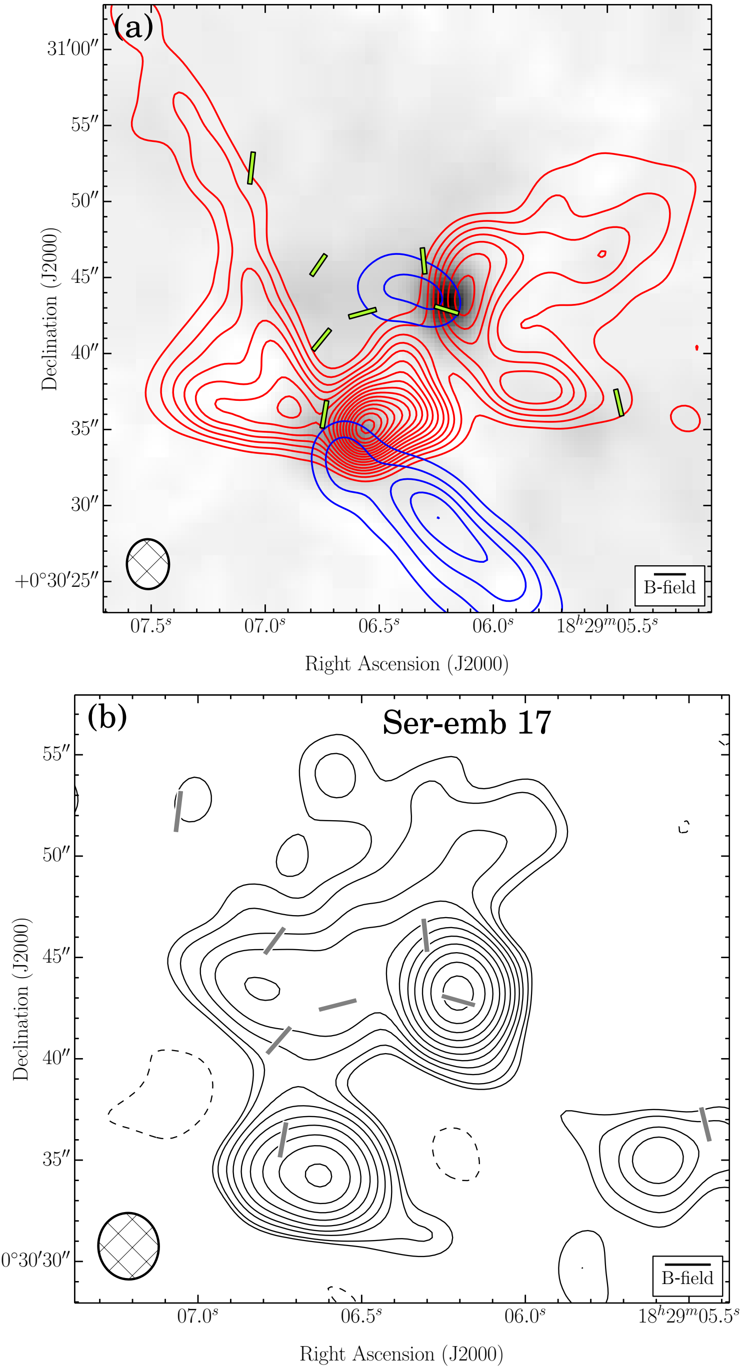

Figure 4.24: Ser-emb 17. Same as Figure 4. **(a)** The velocity ranges of the CO($J = 2 \to 1$) line wing emission are 15.4 to 12.2 km s^{-1} (redshifted) and −2.6 to −11.1 km s^{-1} (blueshifted). $\sigma_{\rm SL} = 1.13$ K km s^{-1}. **(b)** $\sigma_I = 1.7$ mJy bm^{-1}. There is no **(c)** plot because there were no SCUBA, SHARP, or Hertz data to overlay.

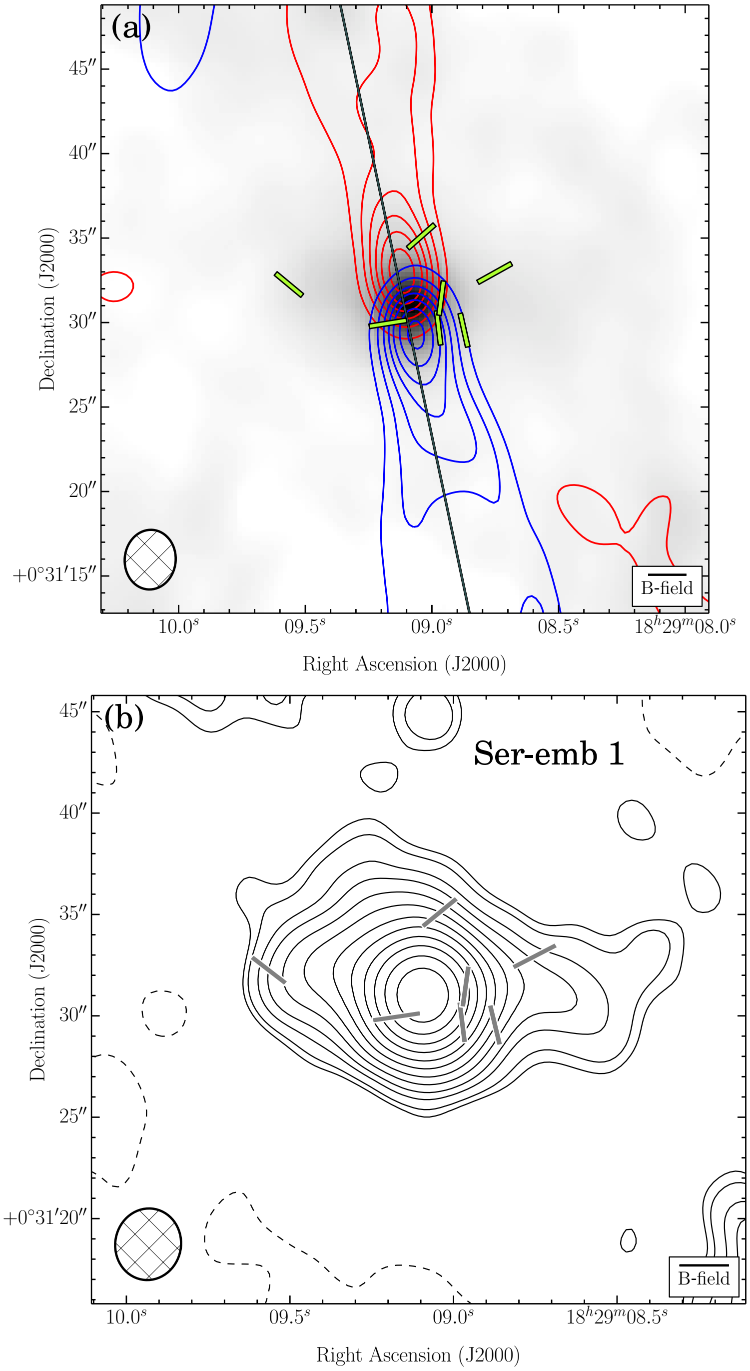

Figure 4.25: Ser-emb 1. Same as Figure 4. **(a)** The velocity ranges of the CO($J = 2 \rightarrow 1$) line wing emission are 27.0 to 13.3 $\mathrm{km\,s^{-1}}$ (redshifted) and 3.8 to –11.1 $\mathrm{km\,s^{-1}}$ (blueshifted). $\sigma_{\mathrm{SL}} = 2.16\ \mathrm{K\,km\,s^{-1}}$. **(b)** $\sigma_I = 1.4\ \mathrm{mJy\,bm^{-1}}$. There is no **(c)** plot because there were no SCUBA, SHARP, or Hertz data to overlay.

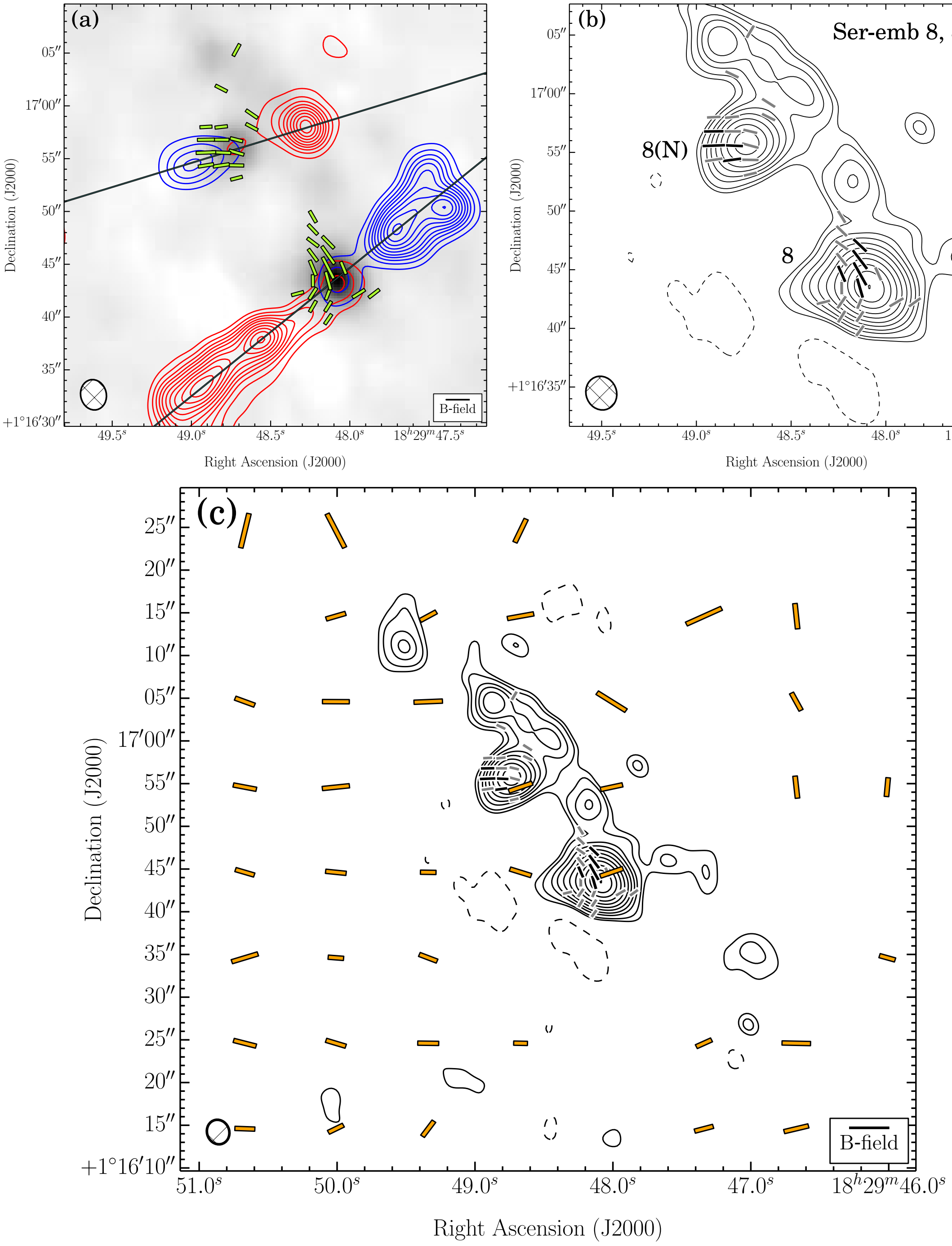

Figure 4.26: Ser-emb 8 and 8(N). Same as Figure 4. **(a)** The velocity ranges of the SiO($J = 5 \rightarrow 4$) line wing emission are 23.7 to 10.2 km s^{-1} (redshifted) and 4.6 to –6.6 km s^{-1} (blueshifted). $\sigma_{\rm SL} = 0.62$ K km s^{-1}. **(b)** $\sigma_I = 2.1$ mJy bm^{-1}. Note: in Hull et al. (2013), the colors of the red- and blueshifted outflow lobes were accidentally reversed.

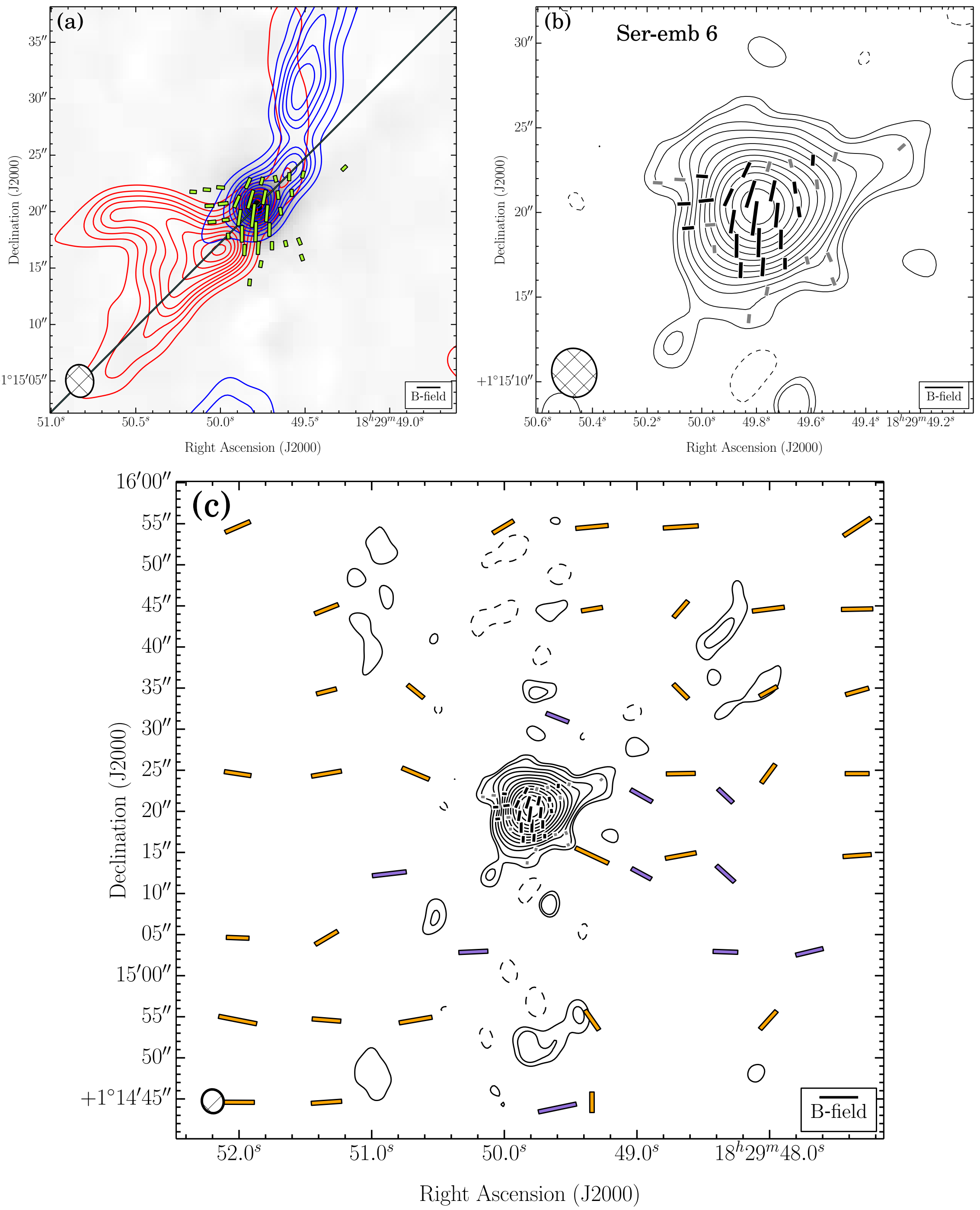

Figure 4.27: Ser-emb 6. Same as Figure 4. **(a)** The velocity ranges of the CO($J = 2 \rightarrow 1$) line wing emission are 23.9 to 16.4 $\mathrm{km\,s^{-1}}$ (redshifted) and 1.6 to −11.1 $\mathrm{km\,s^{-1}}$ (blueshifted). $\sigma_{\mathrm{SL}} = 2.35\ \mathrm{K\,km\,s^{-1}}$. **(b)** $\sigma_I = 6.2\ \mathrm{mJy\,bm^{-1}}$.

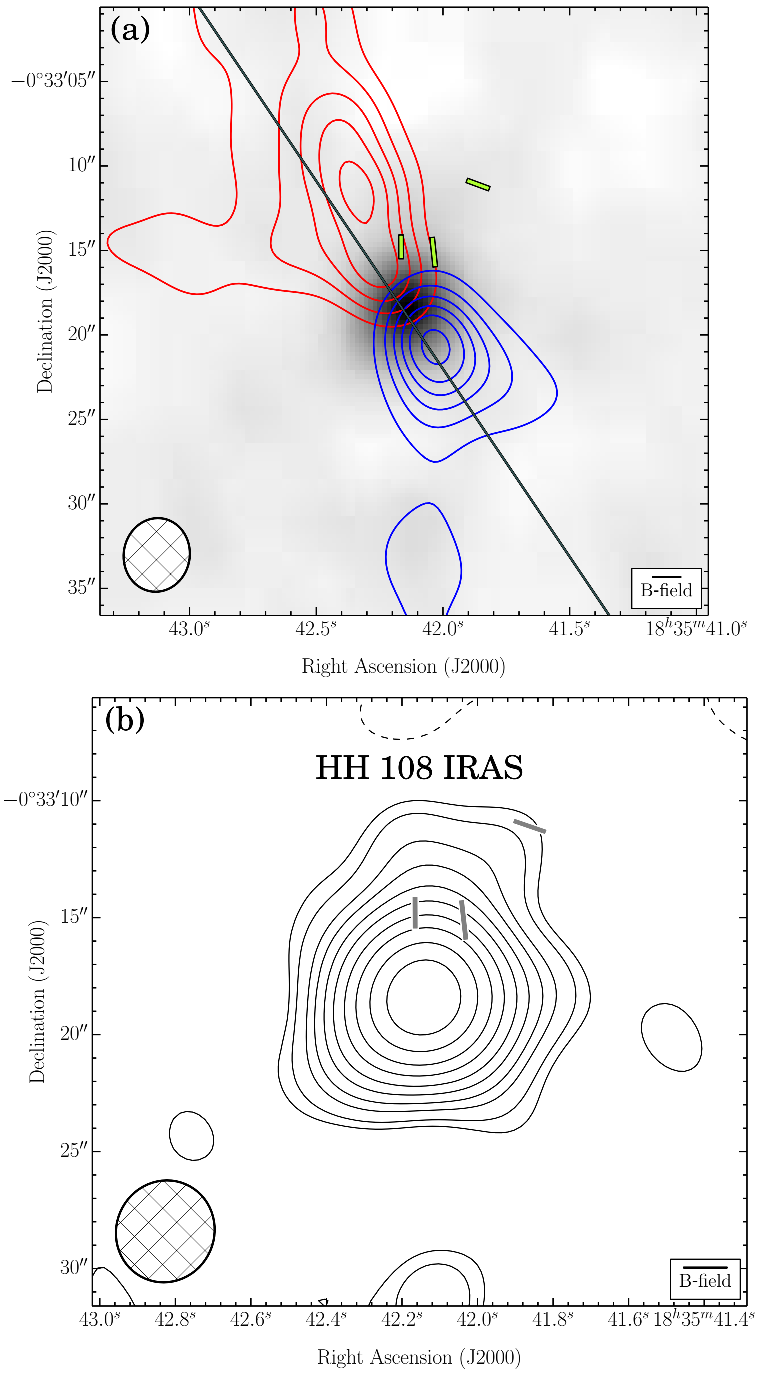

Figure 4.28: HH 108 IRAS. Same as Figure 4. **(a)** The velocity ranges of the CO($J = 2 \rightarrow 1$) line wing emission are 22.3 to 13.8 $\mathrm{km\,s^{-1}}$ (redshifted) and 9.6 to 2.2 $\mathrm{km\,s^{-1}}$ (blueshifted). $\sigma_{\mathrm{SL}} = 0.86$ $\mathrm{K\,km\,s^{-1}}$. **(b)** $\sigma_I = 2.6$ $\mathrm{mJy\,bm^{-1}}$. There is no **(c)** plot because there were no SCUBA, SHARP, or Hertz data to overlay.

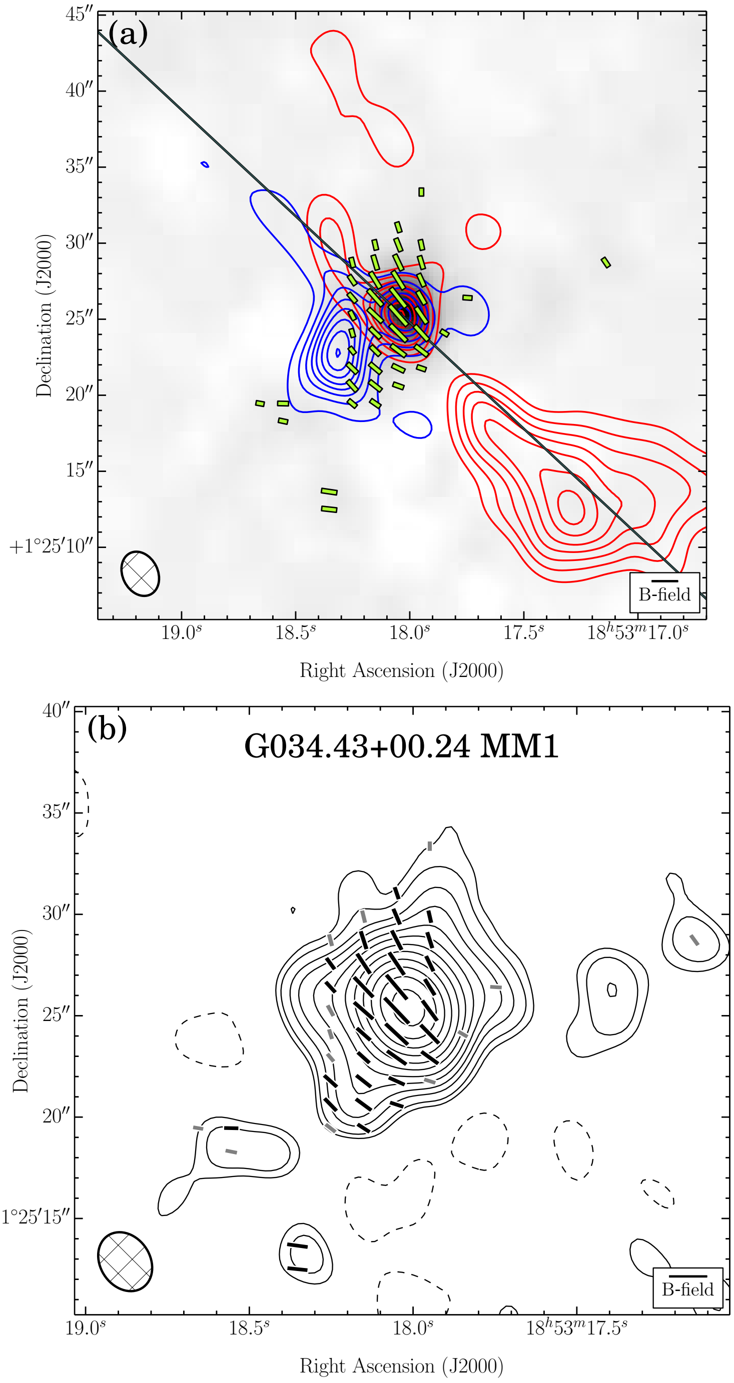

Figure 4.29: G034.43+00.24 MM1. Same as Figure 4. **(a)** The velocity ranges of the CO($J = 2 \rightarrow 1$) line wing emission are 96.5 to 66.8 km s^{-1} (redshifted) and 49.9 to 18.2 km s^{-1} (blueshifted). $\sigma_{\mathrm{SL}} = 5.81$ K km s^{-1}. **(b)** $\sigma_I = 8.8$ mJy bm^{-1}. There is no **(c)** plot because there were no SCUBA, SHARP, or Hertz data to overlay.

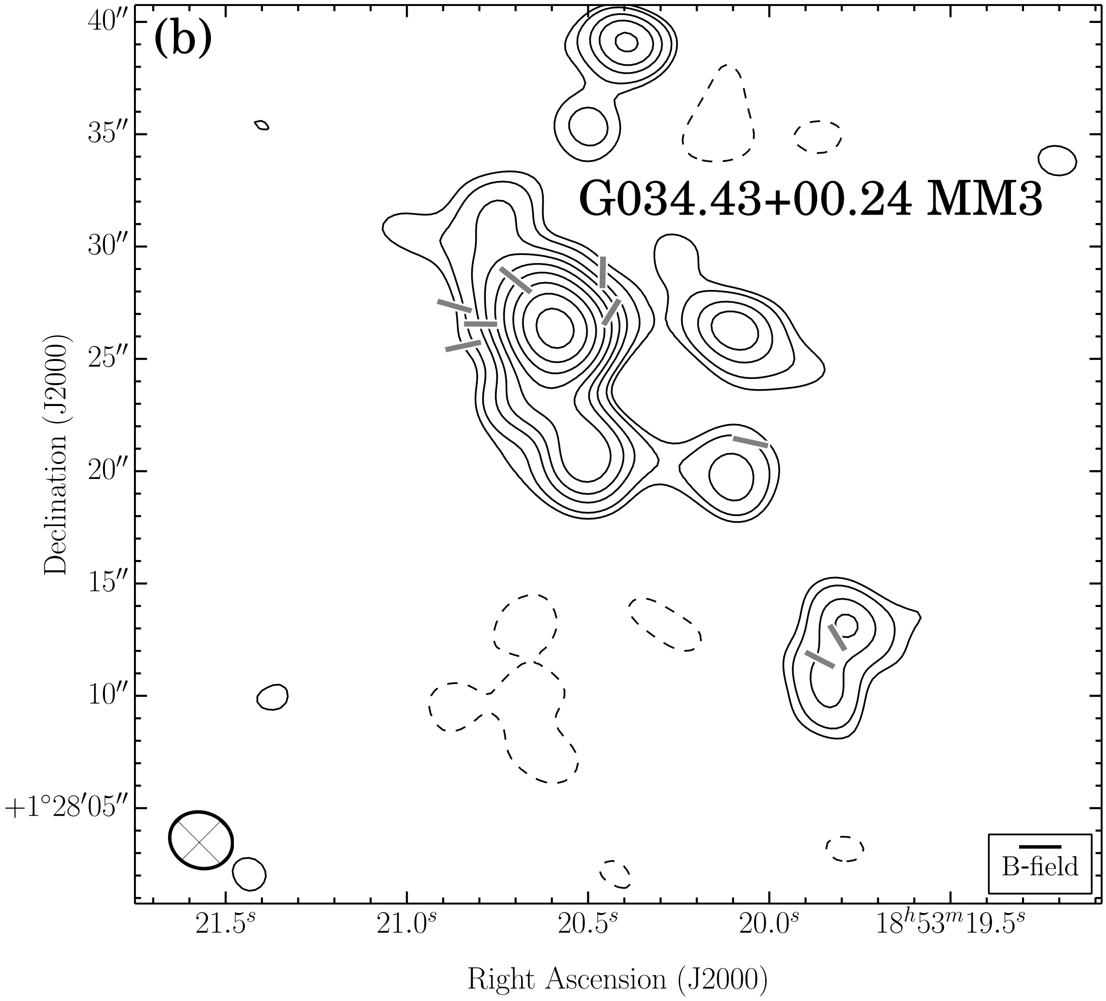

Figure 4.30: G034.43+00.24 MM3. Same as above. **(b)** σ_I = 1.4 mJy bm^{-1}. There is no **(a)** plot because there were no spectral-line data to plot. There is no **(c)** plot because there were no SCUBA, SHARP, or Hertz data to overlay.

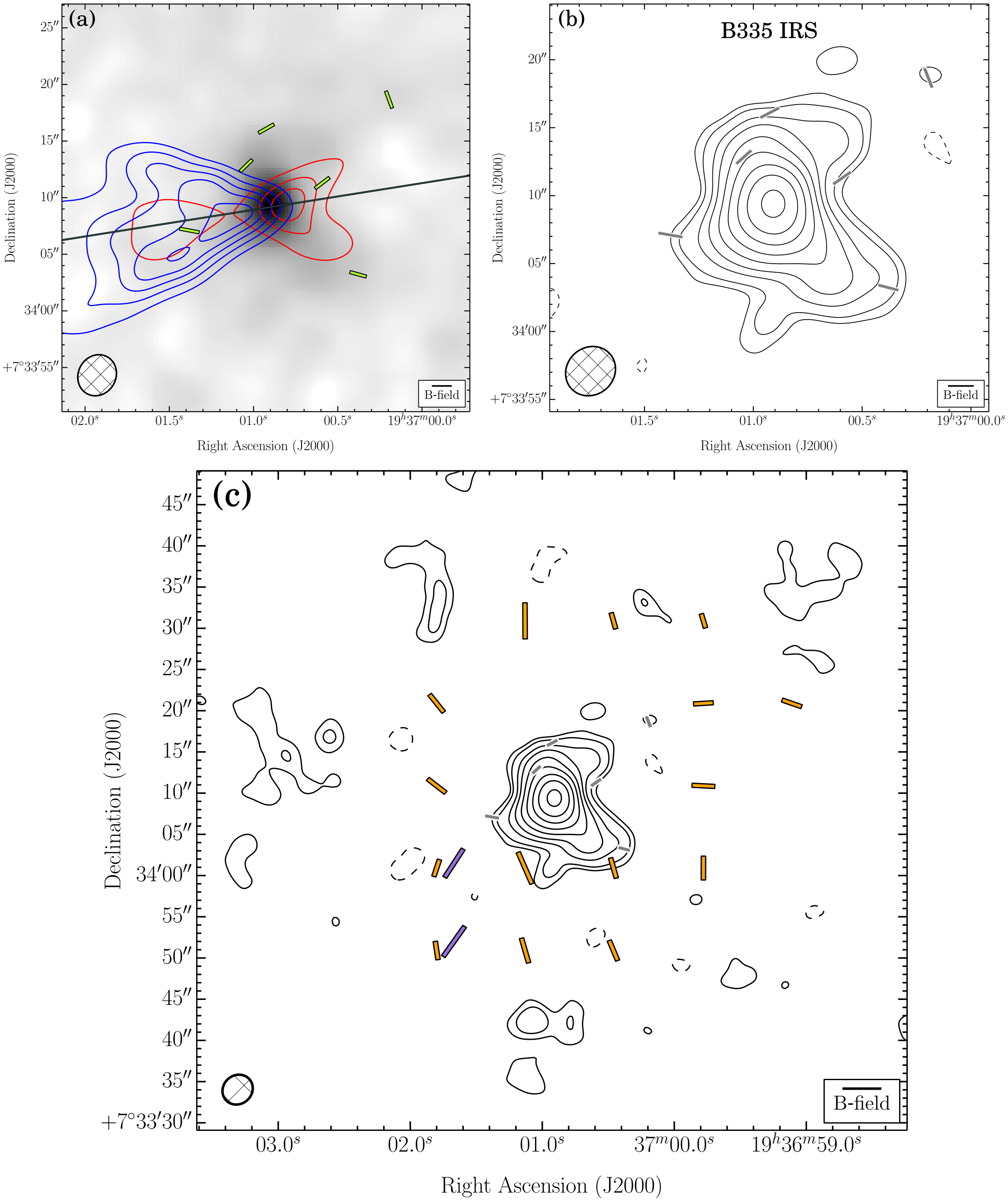

Figure 4.31: B335 IRS. Same as Figure 4. **(a)** The velocity ranges of the CO($J = 2 \rightarrow 1$) line wing emission are 19.7 to 12.3 $\mathrm{km\,s^{-1}}$ (redshifted) and 6.0 to –0.4 $\mathrm{km\,s^{-1}}$ (blueshifted). $\sigma_{\mathrm{SL}} = 1.33\ \mathrm{K\,km\,s^{-1}}$. **(b)** $\sigma_I = 1.6\ \mathrm{mJy\,bm^{-1}}$.

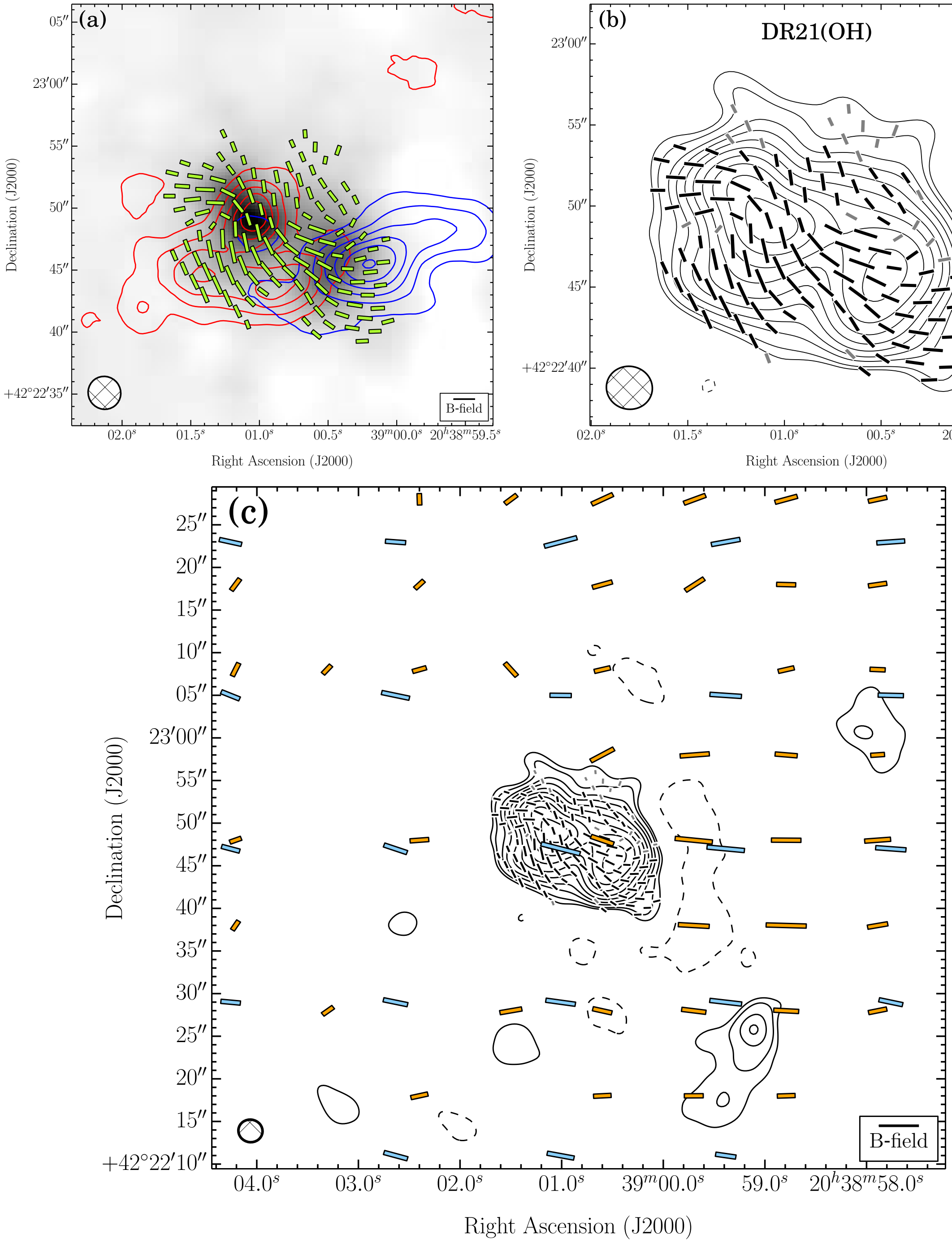

Figure 4.32: DR21(OH). Same as Figure 4. **(a)** The velocity ranges of the CO($J = 2 \rightarrow 1$) line wing emission are 36.9 to 7.2 km s^{-1} (redshifted) and –24.5 to –41.4 km s^{-1} (blueshifted). $\sigma_{\mathrm{SL}} = 2.64$ K km s^{-1}. **(b)** $\sigma_I = 8.6$ mJy bm^{-1}.

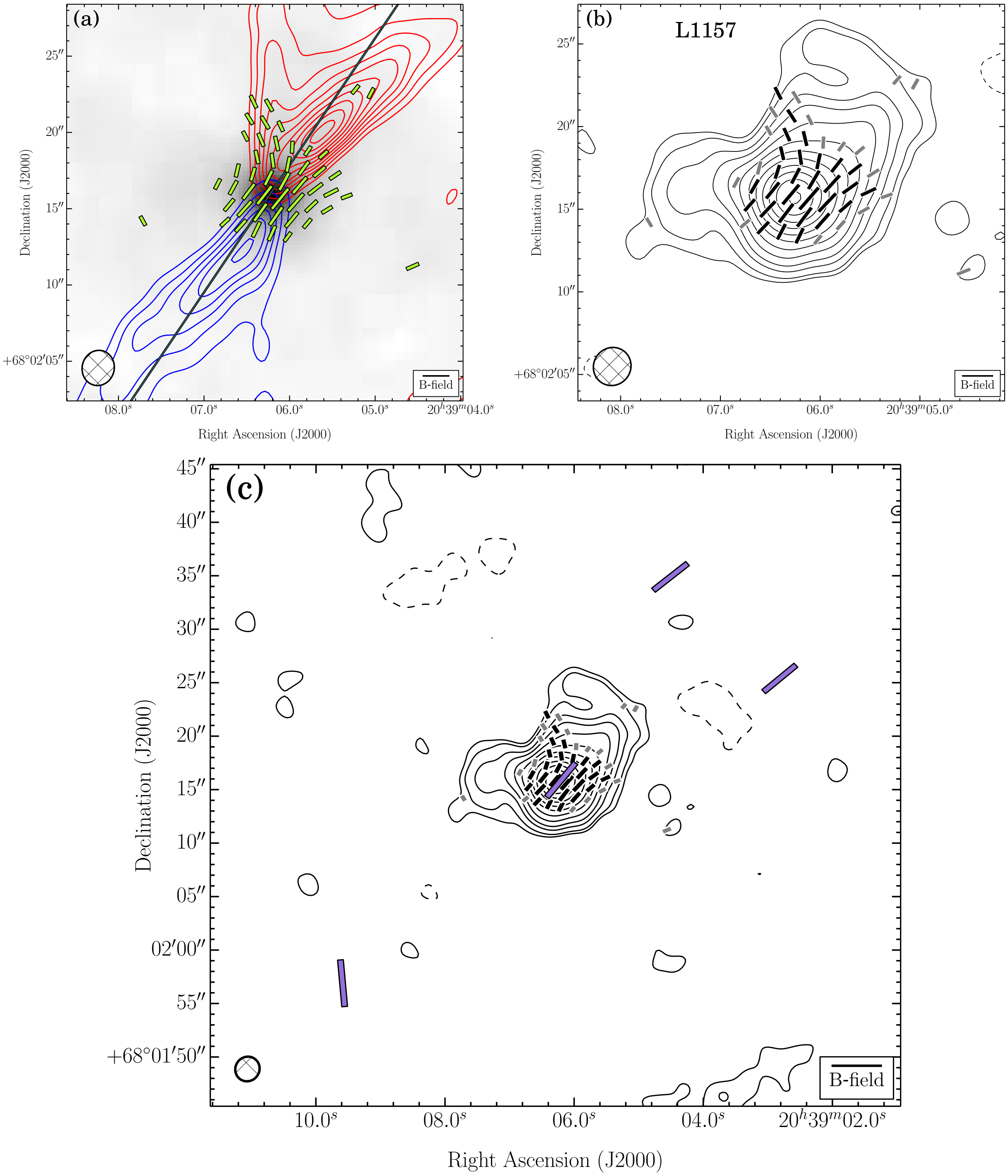

Figure 4.33: L1157. Same as Figure 4. **(a)** The velocity ranges of the CO($J = 2 \rightarrow 1$) line wing emission are 14.7 to 5.2 $\mathrm{km\,s^{-1}}$ (redshifted) and –2.2 to –14.9 $\mathrm{km\,s^{-1}}$ (blueshifted). $\sigma_{\mathrm{SL}} = 2.52\ \mathrm{K\,km\,s^{-1}}$. **(b)** $\sigma_I = 1.7\ \mathrm{mJy\,bm^{-1}}$.

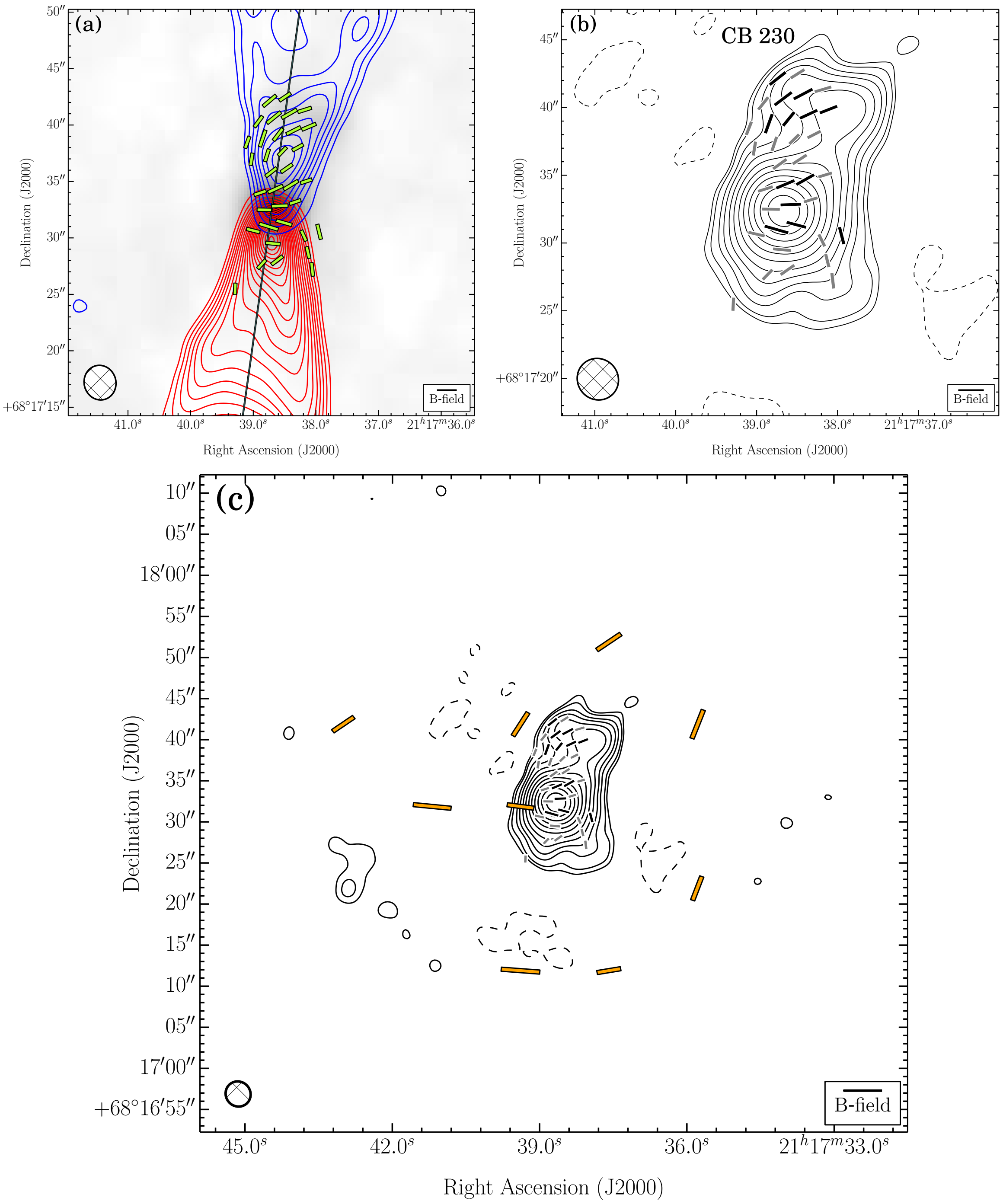

Figure 4.34: CB 230. Same as Figure 4. **(a)** The velocity ranges of the CO($J = 2 \rightarrow 1$) line wing emission are 13.1 to 5.7 km s^{-1} (redshifted) and –1.8 to –16.6 km s^{-1} (blueshifted). $\sigma_{\rm SL} = 0.47$ K km s^{-1}. **(b)** $\sigma_I = 0.7$ mJy bm^{-1}.

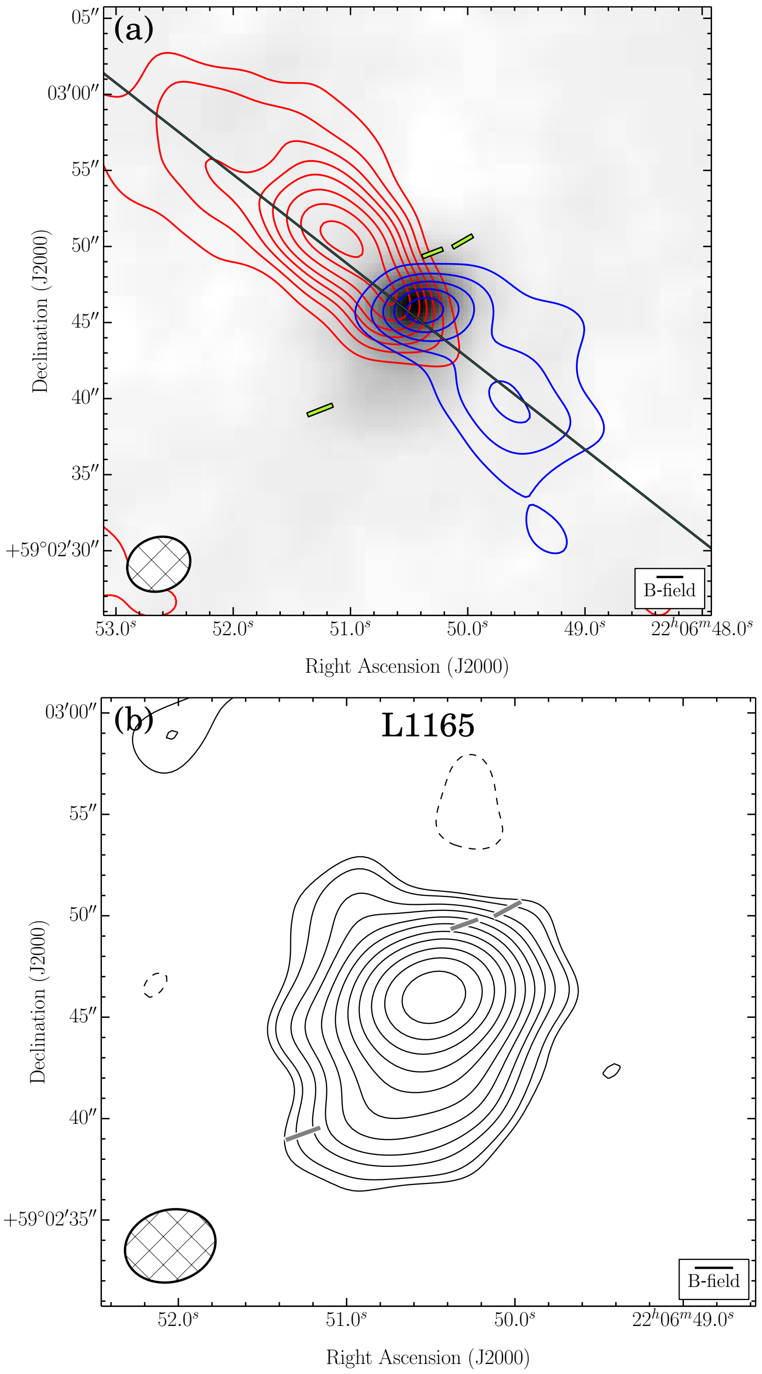

Figure 4.35: L1165. Same as Figure 4. **(a)** The velocity ranges of the CO($J = 2 \rightarrow 1$) line wing emission are 4.9 to –0.4 $\mathrm{km\,s^{-1}}$ (redshifted) and –2.5 to –7.8 $\mathrm{km\,s^{-1}}$ (blueshifted). $\sigma_{\mathrm{SL}} = 0.81\ \mathrm{K\,km\,s^{-1}}$. **(b)** $\sigma_I = 1.2\ \mathrm{mJy\,bm^{-1}}$. There is no **(c)** plot because there were no SCUBA, SHARP, or Hertz data to overlay.

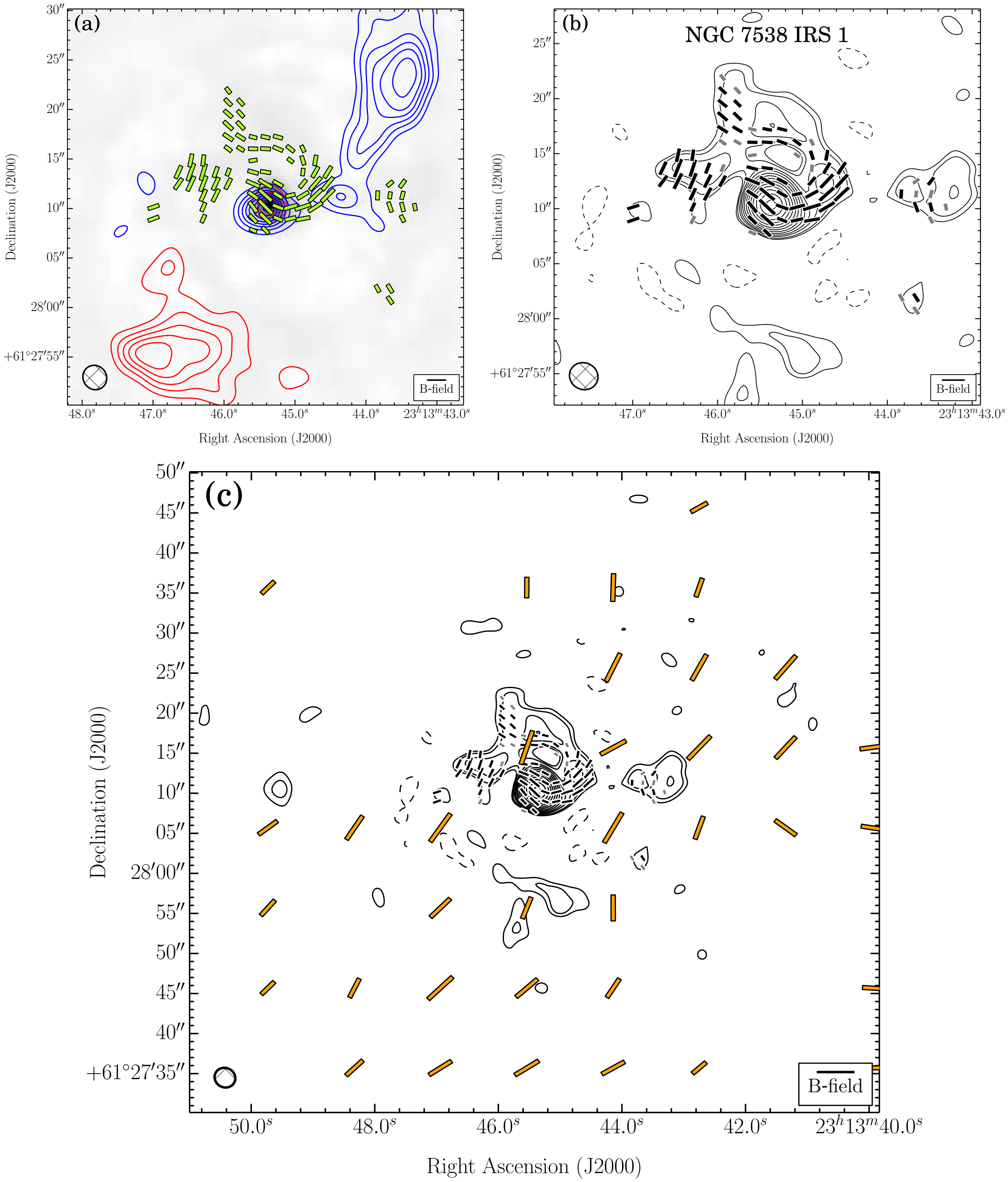

Figure 4.36: NGC 7538 IRS 1. Same as Figure 4. **(a)** The velocity ranges of the CO($J = 2 \rightarrow 1$) line wing emission are –36.3 to –39.5 $\mathrm{km\,s^{-1}}$ (redshifted) and –69.1 to –75.5 $\mathrm{km\,s^{-1}}$ (blueshifted). $\sigma_{\mathrm{SL}} = 3.2\ \mathrm{K\,km\,s^{-1}}$. **(b)** $\sigma_I = 19.3\ \mathrm{mJy\,bm^{-1}}$.

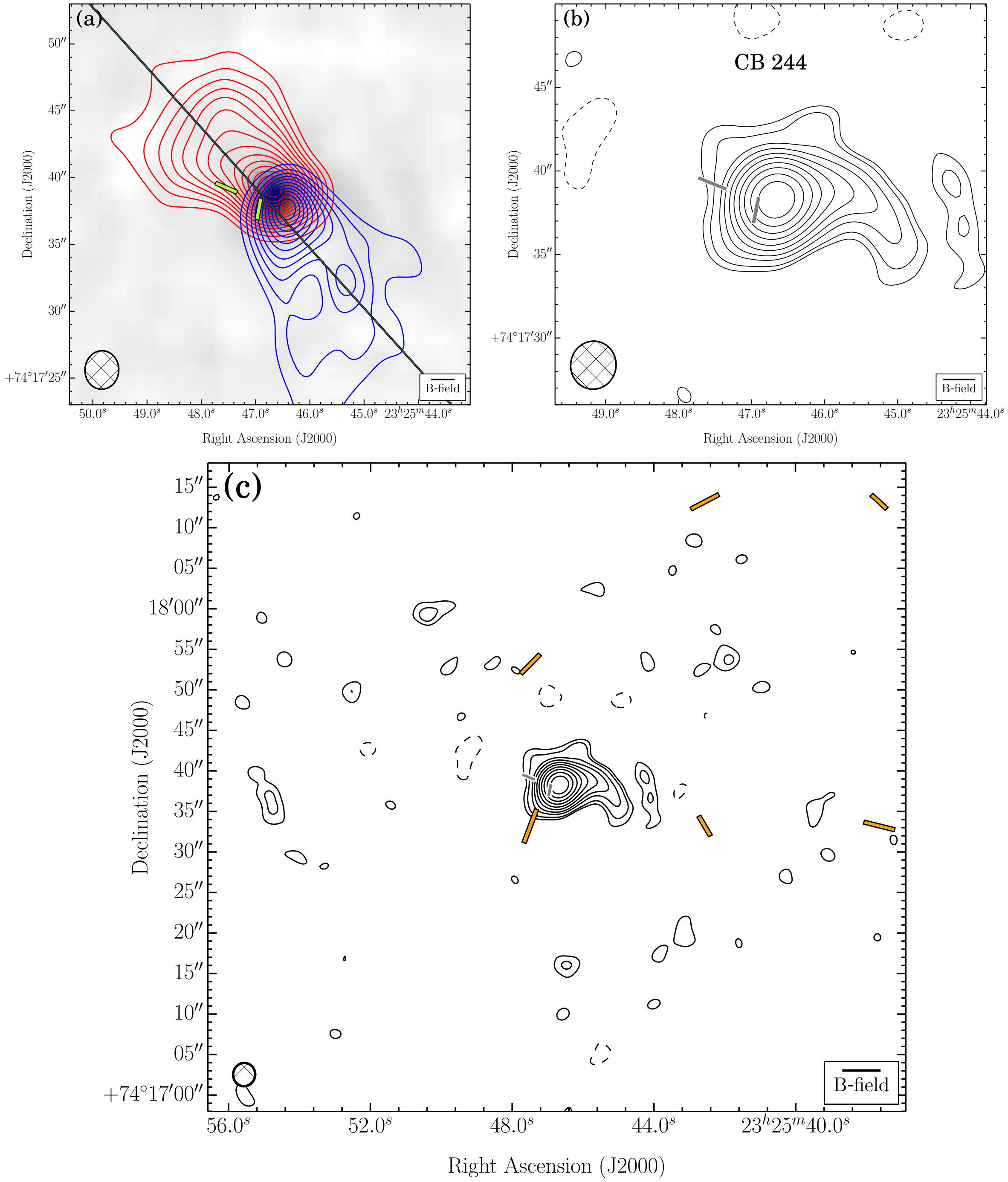

Figure 4.37: CB 244. Same as Figure 4. **(a)** The velocity ranges of the CO($J = 2 \rightarrow 1$) line wing emission are 11.7 to 6.4 $\mathrm{km\,s^{-1}}$ (redshifted) and 2.2 to –3.1 $\mathrm{km\,s^{-1}}$ (blueshifted). $\sigma_{\mathrm{SL}} = 0.98$ $\mathrm{K\,km\,s^{-1}}$. **(b)** $\sigma_I = 0.6$ $\mathrm{mJy\,bm^{-1}}$.

4.8 Appendix B: Description of Sources

4.8.1 W3 Main

The W3 molecular cloud, located at a distance of 1.95 kpc (Xu et al. 2006), is one of the massive molecular clouds in the outer galaxy, with an estimated total gas mass of $3.8\times10^5\,\mathrm{M}_\odot$ (Moore et al. 2007). It contains several young, massive star-forming complexes, the most active of which is W3 Main. Early thermal dust continuum observations identified three sources: W3 SMS1, SMS2, and SMS3 (Ladd et al. 1993). Our polarization observations are toward W3 SMS1 and are centered on the luminous infrared source IRS5 ($2\times10^5\,\mathrm{L}_\odot$, Campbell et al. 1995).

Discovered by Wynn-Williams et al. (1972), IRS5 is a double infrared source (Howell et al. 1981); both sources are associated with radio continuum emission that is consistent with very young, hyper-compact H II regions (van der Tak et al. 2005). Millimeter interferometer observations have resolved the brightest dust continuum source associated with IRS5 into at least five compact cores (MM1–MM5, Rodón et al. 2008). Hubble Space Telescope observations also revealed seven near-IR sources within IRS5 (Megeath et al. 2005). Multiple outflows associated with IRS5 have also been observed in various molecular tracers (Rodón et al. 2008; Wang et al. 2012). It has been proposed that IRS5 is a Trapezium cluster in the making and thus holds valuable clues to high mass cluster formation.

Low resolution infrared and submillimeter polarization observations have revealed low polarization, with a notable decline toward IRS 5 and a spread of values away from the dust peak (Schleuning et al. 2000; Matthews et al. 2009). Water-maser polarization observations have revealed an hourglass-shaped field toward IRS5 (Imai et al. 2003).

The more extended structure to the west of IRS5 observed in our TADPOL image is the free-free emission associated with the H II region W3 B, better known for its infrared association IRS3 (Wynn-Williams et al. 1972; Megeath et al. 1996). The associated stellar source (designated as IRS3a) is consistent with a star of spectral type O6 (Megeath et al. 1996).

See Figure 4.4 for maps.

4.8.2 W3(OH)

W3(OH) is another active, high-mass star formation site in the W3 molecular cloud. H_2O maser parallax measurements place the complex at a distance of 2.04 kpc (Hachisuka et al. 2006). W3(OH) consists of two main regions: a young, limb-brightened ultra-compact (UC) H II region with several OH masers, known as W3(OH) (Dreher & Welch 1981), and a younger, massive hot core with water masers $\sim6''$ east of W3(OH) known as W3(H_2O) or W3(TW) (Turner & Welch 1984). Both of these regions are within the TADPOL field-of-view. The UC H II region is ionized by a massive O9 star, and has a total luminosity of $7.1\times10^4\,\mathrm{L}_\odot$ (Hirsch et al. 2012). High resolution observations have revealed dense gas in a massive protobinary system ($\sim22\,\mathrm{M}_\odot$) towards W3(H_2O), without any associated ionized emission from UC H II region (Wilner et al. 1999; Wyrowski et al. 1999; Chen et al. 2006). Massive, collimated outflows and jets have been detected towards the W3(H_2O) system (Reid et al. 1995; Zapata et al. 2011).

SCUBA observations show significant polarization throughout the region (∼5%) with some evidence for depolarization towards the center (Matthews et al. 2009). Strong magnetic fields are also implied by single-dish CN Zeeman measurements, which find a ∼1.1 mG field strength towards this region (Falgarone et al. 2008).

See Figure 4.5 for maps.

4.8.3 L1448 IRS 2

L1448 IRS 2 is a Class 0 YSO (O'Linger et al. 1999) located in the Perseus molecular cloud at a distance of ∼ 230 pc (Hirota et al. 2011). Its well collimated bipolar outflow has been studied by CO mapping (e.g., Wolf-Chase et al. 2000), *Spitzer* IRAC (Tobin et al. 2007), and molecular hydrogen mapping (e.g., Eislöffel 2000). It is also one of the objects where Kwon et al. (2009) found that dust grains have grown significantly even in the youngest protostellar stage. The surrounding flattened structure was studied by *Spitzer* observations (Tobin et al. 2010). Recent SHARP observations by Chapman et al. (2013) show magnetic fields that are aligned with the bipolar outflow to within ∼ 10°.

See Figure 4.6 for maps.

4.8.4 L1448N(B)

L1448N(B) is a Class 0 YSO at the center of the L1448 IRS3 core (also called L1448N and IRAS 03225+3034) (Bachiller & Cernicharo 1986), at a distance of ∼ 230 pc (Hirota et al. 2011). It was first detected at 6 cm (Anglada et al. 1989), although it is weaker at centimeter wavelengths that its companion L1448N(A), which lies $\sim 7''$ to the northeast. L1448N(A) and L1448N(B) are suspected to be a gravitationally bound common-envelope binary (Kwon et al. 2006; Looney et al. 2000) with a separation of ∼ 2000 AU, even though they seem to be in different evolutionary stages. L1448N(B) is the stronger source at millimeter wavelengths (Terebey & Padgett 1997; Looney et al. 2000); it appears to be younger and more embedded than its companion (O'Linger et al. 2006).

CO observations of L1448N(B) show an outflow with a position angle estimated to be 129° on large (arc-minute) scales (Wolf-Chase et al. 2000) and 105° on small scales (Kwon et al. 2006). The redshifted lobe is easy to distinguish in channel maps, but the blueshifted lobe overlaps, and may even interact with, the outflow from L1448C, $\sim 75''$ to the south. High-resolution ($0.7'' \times 0.5''$) maps of the 2.7 mm continuum emission from L1448N(B) show a protostellar envelope elongated in a direction nearly perpendicular ($PA \sim 56°$) to the outflow (Looney et al. 2000). Observations of the linear polarization of 1.3 mm continuum emission made with the BIMA interferometer at $\sim 4''$ resolution (Kwon et al. 2006) imply that the magnetic field through the envelope is also approximately perpendicular to the outflow. This orientation is consistent with lower-resolution ($10''$) 850 μm polarization observations made with SCUPOL on the JCMT (Matthews et al. 2009).

See Figure 4.7 for maps.

4.8.5 L1448C

L1448C is the collective name for the embedded Class 0 YSOs located 75–80$''$ southeast of L1448N, at a distance of 232 pc (Hirota et al. 2011). L1448C has been the target of numerous observations in the IR continuum (e.g., Tobin et al. 2007), in the (sub)millimeter continuum (e.g., Jørgensen et al. 2007), in CO line emission (e.g., Nisini et al. 2000), and in SiO line emission (e.g., Nisini et al. 2007) because it is the point of origin of symmetrical, well collimated, high-velocity, and rapidly evolving (Hirano et al. 2010) outflows. The blueshifted outflow lobe extends to the north; the westward bend in the outflow at the point where it overlaps L1448N is strong evidence that the L1448C and L1448N outflows interact (Bachiller et al. 1995).

The multiplicity of YSOs in L1448C was revealed by observations of millimeter continuum emission (Volgenau 2004). The strongest millimeter source, called L1448C(N) (Jørgensen et al. 2006) or L1448mm A (Tobin et al. 2007), is the likely source of the outflows. A second source, $\sim 8''$ south of L1448mm A, is weaker in millimeter emission but prominent in maps of near- and mid-infrared emission made with IRAC and MIPS, respectively, on Spitzer. This source is called L1448C(S) (Jørgensen et al. 2006) or L1448mm B (Tobin et al. 2007).

SCUBA maps of linearly polarized 850 μm emission from the L1448 cloud only show significant polarization along the perimeter of the clump of 850 μm continuum emission coincident with L1448C. There is no obvious trend in the orientation of the magnetic field lines.

See Figure 4.8 for maps.

4.8.6 L1455 IRS 1

The dark cloud L1455 is located $\sim$1° south of the active star formation region NGC 1333 at a distance of 320 pc (de Zeeuw et al. 1999). L1455 IRS 1 (also known as L1455 FIR and IRAS 03245+3002) is the brightest far infrared source in the cloud. It is a low mass, Class I protostar, which was first detected in the far infrared with the Kuiper Airborne Observatory (Davidson & Jaffe 1984). High velocity CO emission was first detected by Frerking & Langer (1982) and was first mapped in CO($J = 1 \rightarrow 0$) by Goldsmith et al. (1984), who found extended blue- and redshifted emission over an area of more than $10'$, indicating the presence of more than one outflow, which they thought might be powered by RNO 15 and/or L1455 IRS 1. More recent studies (Hatchell et al. 2007; Curtis et al. 2010) have identified 4 outflows in L1455, each associated with a submillimeter core.

L1455 IRS 1 was first imaged in narrowband $H_2S(1)$ emission by Davis et al. (1997), who found three compact H_2 knots on the symmetry axis of IRS 1, outlining a highly collimated outflow at a position angle of 32°, while Curtis et al. (2010) determined a position angle of

42° from their CO($J = 3 \rightarrow 2$) imaging. This agrees well with the TADPOL CO($J = 2 \rightarrow 1$) imaging, which shows a well-defined bipolar molecular outflow. Although the dust polarization is not very strong, it is still a case where the B-field appears to be perpendicular to the outflow.

See Figure 4.9 for maps.

4.8.7 NGC 1333-IRAS 2A

The IRAS 2 (IRAS 03258+3104) core lies approximately 11′ south-southwest of the center of the NGC 1333 reflection nebula, at a distance of 320 pc (de Zeeuw et al. 1999). IRAS 2 hosts at least three deeply embedded YSOs (Sandell & Knee 2001). IRAS 2A, the strongest emitter at (sub)millimeter wavelengths, is a Class 0 object near the center of the core (Lefloch et al. 1998), at the intersection of nearly perpendicular CO outflows (Sandell et al. 1994; Engargiola & Plambeck 1999). One outflow (position angle ∼ 104°), with a blueshifted lobe that extends ∼ 100″ to the west and a redshifted lobe that extends ∼ 85″ to the east, is highly collimated and presumably young. The other outflow (position angle ∼ 25°), with blueshifted (south) and redshifted (north) lobes that extend at least 70″ in either direction, is poorly-collimated and older. The coincidence of IRAS 2A with the point of origin of the outflows suggests that IRAS 2A is an unresolved (< 65 AU) binary system (e.g., Jørgensen et al. 2004).

The magnetic field across the IRAS 2 core, as mapped with the SCUPOL on the JCMT (14″ resolution), was described as weak with a “random field pattern” (Curran et al. 2007). However, higher resolution (3″) data obtained by Curran et al. with the BIMA (Berkeley Illinois Maryland Array) interferometer shows magnetic field line with a roughly east-west orientation across most of the emitting region, which is consistent with the TADPOL observations.

See Figure 4.10 for maps.

4.8.8 SVS 13

SVS 13 was discovered as a near-infrared source by Strom et al. (1976) in the NGC 1333 star forming region. Using VLBI observations of 22 GHz H_2O masers, Hirota et al. (2008) found a distance of 235 pc. Observations at millimeter wavelengths reveal at least three continuum sources within SVS 13. These sources, which form a straight line in the plane of the sky from northeast to southwest, have been named as A, B, and C, respectively (Looney et al. 2000, and references therein). Source A is a Class 0/I source coincident with the infrared/optical counterparts of SVS 13; sources B and C are Class 0 sources. High resolution BIMA observations revealed a weak component of source A that is located 6″ to the southwest of the source and is coincident with centimeter continuum source VLA3 (Rodriguez et al. 1997; Rodríguez et al. 1999). TADPOL observations focus on sources A and B.

Observational evidence suggests that SVS 13 is powering the well studied chain of Herbig-Haro (HH) objects HH 7–11 (Bachiller et al. 2000; Looney et al. 2000). However, there is some debate as to the main exciting source of the outflow, which could be either VLA3 or SVS 13 (Rodriguez et al. 1997). This object is known to be one of the brightest H_2O maser sources among the known low-mass YSOs (Haschick et al. 1980; Claussen et al. 1996; Furuya et al. 2003).

See Figure 4.11 for maps.

4.8.9 NGC 1333-IRAS 4A

NGC 1333-IRAS 4A comprises two deeply embedded Class 0 YSOs at the south end of the NGC 1333 reflection nebula, located at a distance of 320 pc (de Zeeuw et al. 1999). The binarity of IRAS 4A, first detected in 0.84 mm CSO-JCMT baseline data (Lay et al. 1995), has been resolved interferometrically at millimeter (Looney et al. 2000), submillimeter (Jørgensen et al. 2007), and centimeter (Reipurth et al. 2002) wavelengths. The two components are $1.8''$ apart (580 AU at 320 pc) and share a common envelope with an estimated mass of $2.9\,M_\odot$ (Looney et al. 2003). High-resolution observations of molecular line emission from IRAS 4A have revealed both low-density (Jørgensen et al. 2007) and high-density (Di Francesco et al. 2001) tracers with inverse P-Cygni profiles, which have been interpreted as evidence that envelope material is falling onto the central protostars.

The outflows emanating from IRAS 4A have been mapped in several CO transitions (e.g., Blake et al. 1995; Knee & Sandell 2000; Jørgensen et al. 2007; Yıldız et al. 2012). The outflows are well collimated but are "bent" in the sky plane. Close ($< 0.5'$) to IRAS 4A, the outflows are oriented north-south; further from the protostars, the outflows have a position angle or $\sim 45°$. The redshifted lobe extends northward, and the blueshifted lobe extends southward. The extent of the outflows on the sky ($4'$) and the large range of line-of-sight velocities suggests that the outflow axis has an inclination $< 45°$.

Maps of linearly polarized dust emission from IRAS 4A have been made at 850 μm with the SCUBA polarimeter on the JCMT (Matthews et al. 2009). These maps imply a large-scale magnetic field that is fairly uniform in the northeast-southwest direction across the IRAS 4 core. Girart et al. (2006) also mapped IRAS 4A at high resolution with the Submillimeter Array (SMA), revealing one of the first "hourglass" B-field morphologies ever seen in a low-mass protostar.

See Figure 4.12 for maps.

4.8.10 NGC 1333-IRAS 4B and 4B2

NGC 1333-IRAS 4B and 4B2 are Class 0 sources in Perseus at a distance of 320 pc (de Zeeuw et al. 1999), and about $30''$ to the southeast of the well known Class 0 source NGC 1333-IRAS 4A. IRAS 4B hosts a slow ($\sim$10 km s^{-1}) bipolar molecular outflow oriented north-south. Single-dish maps from the SCUBA (Matthews et al. 2009) and Hertz (Dotson et al. 2010) polarimeters show polarization consistent with the prominent polarization detected by CARMA on the western edge of the core.

Strong water lines were detected toward IRAS 4B by the Spitzer infrared spectrograph (Watson et al. 2007) and Herschel HIFI (Herczeg et al. 2012). Watson et al. (2007) attributed the emission to shocked material falling from the protostellar envelope onto the dense surface of the circumstellar disk, which requires that the disk of IRAS 4B be oriented roughly face-on, thus allowing emission to escape from the cavity evacuated by the bipolar outflow. That assumption was called into question after VLBI measurements of the proper motions of water masers in the outflow of IRAS 4B that suggest that the object is in fact viewed edge-on (Marvel et al. 2008). The claim by Watson et al. (2007) that the water emission originates in the disk has been challenged by Herczeg et al. (2012), who argue that the emission originates in shocks within the bipolar outflow cavity.

IRAS 4B2 (also called IRAS 4BE, IRAS 4B′, and IRAS 4BII) is the weaker binary companion 10″ to the east of IRAS 4B. The source has been called IRAS 4C as well (e.g., Choi et al. 1999; Looney et al. 2000), but 4C is generally used as the name of a source ∼40″ east-northeast of IRAS 4A (e.g., Rodríguez et al. 1999; Smith et al. 2000; Sandell & Knee 2001). In their BIMA observations, Choi et al. (1999) saw IRAS 4B2 as an unresolved extension of continuum emission to the east of IRAS 4B. Sandell & Knee (2001) and Di Francesco et al. (2001) later resolved the 10″ IRAS 4B/IRAS 4B2 binary using the JCMT and the PdBI, respectively.

While prior to the TADPOL survey no spectral line emission had been detected toward IRAS 4B2, we see a small, faint E–W outflow in CO($J = 2 \rightarrow 1$).

See Figure 4.13 for maps.

4.8.11 HH 211 mm

HH 211 mm is the Class 0 YSO (Froebrich 2005) launching the well-known bipolar outflow HH 211. It is located in the IC 348 cluster at the eastern part of the Perseus molecular cloud, at a distance of 320 pc (de Zeeuw et al. 1999). The jet HH 211 was relatively recently detected by near-IR H_2 observations (McCaughrean et al. 1994). Gueth & Guilloteau (1999) showed that the driving object is HH 211 mm, and they distinguished between the collimated jet and the slow extended outflow components using interferometric millimeter-continuum and CO observations. The bipolar outflow has been studied extensively in various molecular line transitions (e.g., SiO($J = 1 \rightarrow 0$); Chandler & Richer 2001), and recently *Spitzer* IRS observations showed that the bipolar outflow material is mostly molecular (Dionatos et al. 2010). Based on the bipolar outflow velocity and extension, the kinematic age is estimated to be only ∼ 1000 yr. (e.g, Gueth & Guilloteau 1999). Recent submillimeter interferometric observations have revealed that the object is a protobinary system separated by about 0.3″ (Lee et al. 2009), and the kinematic structure of the envelope has been studied by CARMA N_2H^+ observations (Tobin et al. 2011). The SCUPOL map toward the HH 211 and IC 348 region showed polarization that is neither aligned with nor perpendicular to the the bipolar outflow (Matthews et al. 2009).

See Figure 4.14 for maps.

4.8.12 DG Tau

DG Tau is a Class II, 0.67 $M_\odot$ K5-M0 T Tauri star (Güdel et al. 2007, and references therein) located at a distance of roughly 140 pc in the Taurus-Auriga star-forming association (Kenyon et al. 1994; Torres et al. 2009). It is remarkable primarily for its well collimated jet, HH 158, and was among the first T Tauri stars known to exhibit such strong and clear accretion and outflow activity (Mundt & Fried 1983). The literature on its jet is correspondingly vast, as it has been studied extensively across the electromagnetic spectrum (see, e.g., Schneider et al. 2013; Rodríguez et al. 2012b; Lynch et al. 2013, and references therein). DG Tau is properly known as DG Tau A, since it has a common proper motion companion DG Tau B, a Class I source that launches the HH 159 jet (e.g., Rodríguez et al. 2012a).

The dust disk around DG Tau has the dubious distinction of being the most frequently observed by (sub)millimeter polarimeters. It was one of the first two T Tauri disks that seemed to exhibit a tentative ($3\,\sigma$) detection of unresolved 850 μm polarization using the single-dish JCMT (Tamura et al. 1999), apparently indicating a large-scale toroidal magnetic field threading the disk. Follow-up observations at 350 μm with the CSO did not confirm the 3% polarization fraction, but the wavelengths were too widely separated to rule out a spectral dependence of the polarization fraction (Krejny et al. 2009). As part of the TADPOL survey the JCMT detection was followed up at 1.3 mm using the CARMA polarimeter, which again resulted in a sensitive non-detection (Hughes et al. 2013). The CARMA results indicate that either the JCMT detection was spurious or the polarization originates from large spatial scales that are filtered out by the interferometer—an envelope, perhaps—rather than from the circumstellar disk itself.

See Figure 4.15 for maps.

4.8.13 L1551 NE

L1551 NE is a low-mass Class I protostar first discovered with IRAS (Emerson et al. 1984) and located a few arcminutes from L1551 IRS5 and at a distance of 140 pc (Kenyon et al. 1994). L1551 NE is a binary system with a bipolar molecular outflow and a Keplerian circumbinary disk (Moriarty-Schieven et al. 1995; Rodriguez et al. 1995; Reipurth et al. 2002; Takakuwa et al. 2012). SCUBA 850 μm measurements show polarization orientations in the extended dust envelope that are mostly perpendicular to the outflow direction, with no polarization detected at the continuum peak (Matthews et al. 2009). Our TADPOL observations show a clear pattern of polarization across the continuum peak, with B-field orientations perpendicular to the outflow direction.

See Figure 4.16 for maps.

4.8.14 L1527

L1527 is a Class 0/I YSO located in the Taurus molecular cloud at a distance of about 140 pc (e.g., Andre et al. 2000). Its bipolar outflow is oriented in the east-west direction and is nearly in the plane of the sky, which makes the object an ideal target for studying the disk and outflow structure at the earliest stage of low mass star formation (e.g., Jørgensen et al. 2007). Recently the disk was revealed to have Keplerian motion, and the protostellar mass was estimated to be ~ 0.2 $M_{\odot}$ using CARMA ^{13}CO observations (Tobin et al. 2012). In addition, detailed modeling of SMA and CARMA continuum observations found that the disk is large (about 125 AU in radius) and is thicker than the hydrostatic equilibrium case (Tobin et al. 2013a).

The source's orientation is also beneficial for magnetic field studies. SCUPOL detected quite irregular polarization at 850 μm, but at the center the B-field orientation is perpendicular to the bipolar outflow (Matthews et al. 2009), consistent with the TADPOL observations. In contrast, SHARP detected polarization in the outer regions at 350 μm that was consistent with B-fields that are aligned with the bipolar outflow (Davidson et al. 2011).

See Figure 4.17 for maps.

4.8.15 CB 26

CB 26 (Clemens & Barvainis 1988) is a Bok globule generally accepted to be associated with the Taurus-Auriga complex a distance of 140 pc (Launhardt & Sargent 2001; Henning et al. 2001). The embedded YSO located near the edge of the globule is a Class I source with a luminosity of $0.5\,L_{\odot}$ (Stecklum et al. 2004). Millimeter interferometric observations of dust continuum and molecular spectral line emission (Launhardt & Sargent 2001) show both an edge-on disk that sits at the center of a near-infrared bipolar reflection nebula (Stecklum et al. 2004), as well as a bipolar outflow (Launhardt et al. 2009) perpendicular to the disk.

SCUBA 850 μm measurements show polarization orientations both predominantly parallel to the disk (Henning et al. 2001) and predominantly perpendicular to the disk (Matthews et al. 2009). Our TADPOL observations detect polarization near the dust peak that is consistent with the latter SCUBA results.

See Figure 4.18 for maps.

4.8.16 Orion-KL

Orion-KL, the Kleinmann-Low Nebula in Orion, is the nearest region of high mass star formation, 415 pc away (Menten et al. 2007). It lies inside Orion Molecular Cloud 1 (OMC1), which in turn forms part of an integral shaped filamentary cloud that is more than 7 pc long (Johnstone & Bally 1999). Our map, a mosaic of 7 pointings, covers Orion-KL and its associated hot core, and a piece of the more quiescent "northern ridge" about $25''$ to the NE.

At least two massive stars, Source I (SrcI) and the Becklin-Neugebauer Object (BN) are associated with Orion-KL. Proper motion measurements show that these two stars are recoiling from one another at 35–40 km s^{-1}; they appear to have been ejected from a multiple system just 500 years ago (Gómez et al. 2008; Goddi et al. 2011). This explosive event also is thought to have created a set of bow shocks and fingers that form a poorly collimated, NW-SE high velocity outflow; a separate, lower velocity outflow emerges from SrcI in the perpendicular direction (Plambeck et al. 2009).

Extensive polarization maps from SCUBA, Hertz, and Stokes (Dotson et al. 2000) show that the large-scale magnetic field in OMC1 is perpendicular to the long axis of the molecular cloud, with evidence for an hourglass-shaped pinch centered on KL (Schleuning 1998). Higher resolution 345 GHz SMA observations show a remarkable circularly symmetric polarization pattern centered between SrcI and BN, near the site of the putative explosive event; a possible interpretation is that the explosion dragged the magnetic field outward into a radial pattern (Tang et al. 2010). However, within 500 AU of SrcI the magnetic field deduced from SiO v=0 maser[7] polarization observations is relatively straight. (Plambeck et al. 2003). The B-field orientation is highly uncertain because maser polarization may be either parallel or perpendicular to the field, and because of possible Faraday rotation by foreground plasma; Plambeck et al. argued that it is at PA 145°, roughly perpendicular to the low velocity outflow from SrcI.

The TADPOL map shows the radial magnetic field pattern previously detected with the SMA. Our map extends further north, and shows that the magnetic field orientation in the northern ridge cloud is consistent with the large scale field, except near the SW tip where it forms part of the radial pattern.

See Figure 4.19 for maps.

4.8.17 OMC3 MMS5 and MMS6

MMS5 and MMS6 are condensations in Orion Molecular Cloud 3 (OMC3)—a narrow ridge or filament about 1 pc long and at a distance of 415 pc (Menten et al. 2007). MMS6 is the brightest millimeter continuum source in OMC3, with an estimated mass of 36 $M_\odot$ (Chini et al. 1997b). It contains a compact core, MMS6-main, that probably is heated by an extremely young intermediate mass Class 0 protostar (Takahashi et al. 2012). A bipolar outflow, with a total length of only 4″ (2000 AU), emerges along a N-S axis from MM6-main; the dynamical age of the outflow is less than 100 years (Takahashi & Ho 2012). A more extended outflow emerges along an E-W axis from MMS5.

The large scale magnetic field orientation in OMC3 inferred from SCUBA data is perpendicular to the long axis of the cloud. Matthews et al. (2001) argue that the pattern of depolarization along the central axis is best explained by a field toroidally wrapped around a filament, rather than by a straight field perpendicular to a sheet. The field orientations that we measure for both the MMS5 and MMS6 cores are closely aligned with the large-scale field. Our results for MMS6 agree well with previous 3.6″ resolution observations of this source made with BIMA (Matthews et al. 2005).

See Figure 4.20 for maps.

---

[7] These masers, in the ground vibrational state, should not be confused with the stronger v=1 masers closer to the star; both the intensity and the polarization of the v=1 masers are time variable.

4.8.18 OMC2-FIR3 and 4

OMC2 is an intermediate mass star-forming region located north of the massive OMC1 complex in the so-called integral-shaped filament of Orion A. Located at a distance of 415 pc (Menten et al. 2007), it is one of the brightest regions in the Orion Nebula and is know to harbor several protostellar objects and pre-main-sequence stars. Earlier continuum studies at (sub)millimeter wavelengths have established it to be in a later evolutionary stage of star formation than the OMC3 region neighboring it to the north (Chini et al. 1997b; Lis et al. 1998). More recent studies have modeled several of its embedded sources as infalling protostars, young stars with disks, and binaries comprising both types of objects (Adams et al. 2012). More specifically, although OMC2-FIR4 is well modeled as a Class 0 protostar of approximately 50 $L_\odot$ and $10^{-4} M_\odot\,\mathrm{yr}^{-1}$ mass infall rate (Adams et al. 2012), recent high resolution measurements have resolved three spatially distinct sources in its core (López-Sepulcre et al. 2013).

The polarization of the OMC2 region and the FIR3 and 4 sources was first investigated at 350 μm by Houde et al. (2004) with Hertz at the CSO (see also Dotson et al. 2010). This region is characterized by extremely low polarization levels as well as a strong depolarization with increasing total intensity. For example, OMC2-FIR4 was found to have a mean polarization of 0.34% ± 0.08% within region of approximately $\pm\,0.3'$ from its peak (200 Jy within a beam of $20''$ FWHM at 350 μm), making it one of the most weakly polarized molecular cloud complexes ever observed at that wavelength. Although higher polarization was measured at 850 μm, the relatively low polarization as compared with other sources within the integral-shaped filament was confirmed by Matthews et al. (2009) and Poidevin et al. (2010). OMC2-FIR4 was also observed to be a region of transition in the orientation of the polarization. The mean polarization angle goes from $\sim 115°$ south of it to $\sim 175°$ to the north at OMC2-FIR3, where the polarization angle is relatively well aligned with the filament. This transition region is almost coincident with a location of intense outflow activity reported by Williams et al. (2003).

The aforementioned low levels of polarization obtained with single-dish measurements are in contrast with the results shown in Table 4.1 and Figure 4.21, where mean polarization fractions of ~ 6–8% are detected with CARMA, making FIR 3 and 4 two of the most polarized sources in our sample. This may be reconciled by the fact that the magnetic field, as measured at small scales with CARMA, significantly changes its orientation within just a few arcseconds towards the center of the map (i.e., at OMC2-FIR4). The change of nearly 90° observed could account for the exceedingly low polarization observed with Hertz, if the data were combined within a single Hertz beam.

See Figure 4.21 for maps.

4.8.19 CB 54

CB 54 (LBN1042; Lynds 1965; Clemens & Barvainis 1988) is a Bok globule at a distance of 1.1 kpc (Henning et al. 2001, and references therein). (Sub)millimeter and mid-infrared observations reveal two Class I YSOs coincident with source IRAS 07020-1618, with strong dust continuum emission and one or two bipolar outflows (Yun & Clemens 1994; Zhou et al. 1996; Ciardi & Gómez Martín 2007; de Gregorio-Monsalvo et al. 2009; Launhardt et al. 2010). SCUBA 850 μm measurements show weak polarization across the continuum source, with changing orientation and increased strength in the envelope (Henning et al. 2001; Matthews et al. 2009).

See Figure 4.22 for maps.

4.8.20 VLA 1623

VLA 1623 is the prototypical Class 0 source, discovered by Andre et al. (1993). It is located in the southern edge of the Ophiuchus A cloud at a distance of 125 pc (Loinard et al. 2008). It has a highly collimated outflow, as is typical of Class 0 sources, and this outflow extends over a large distance at a common position angle (Andre et al. 1990). The polarization toward VLA 1623 was measured by Holland et al. (1996) using the single bolometer UKT14, and the B-field was found to be perpendicular to the CO outflow. Holland et al. (1996) note that this alignment of the field implies that the large-scale field in the cloud cannot therefore collimate the outflow. The single dish polarization data from SCUBA (Matthews et al. 2009) and Hertz (Dotson et al. 2010) are consistent with this early picture, as are the CARMA data, which show that the central region has a preferred B-field orientation orthogonal to the outflow. This central region may be a flattened pseudo-disk, as discussed for other Class 0 sources by Davidson et al. (2011). The orientation of the field is aligned along the major axis of this pseudo-disk and orthogonal to the outflow, and even follows the emission extension to the north east. While the field orientation on small scales might alone suggest a toroidal field component, we note that in fact the CARMA field orientations are consistent with those of the large-scale emission.

See Figure 4.23 for maps.

4.8.21 Ser-emb 1, 6, 8, 8(N), and 17

Ser-emb 1, 6, 8, 8(N), and 17 are low-mass, Class 0 (Ser-emb 6, 8, 8(N), 17) and Class I (Ser-emb 1) protostars in the Serpens Main cluster, located at a distance of 415 pc (Dzib et al. 2010). All sources are discussed in Enoch et al. (2011), who made high-resolution 1.3 mm maps of nine low-mass cores in Serpens using CARMA. The results in Enoch et al. (2011) follow up on a large 1.1 mm survey of protostars using Bolocam on the CSO (Enoch et al. 2007).

Ser-emb 6 (also called Serp-FIR1 and Serp-SMM1) is the brightest (sub)millimeter source in the Serpens Main cluster. It harbors a Class 0 protostar at its center. Continuum observations at 6 cm using the Karl G. Jansky Very Large Array (VLA) resolved the continuum peak into three collinear sources, where the NW and SE components appear to be moving away from the central source (Rodriguez et al. 1989). While the three sources are not obviously present in the 1.3 mm maps from Enoch et al. (2011), it is possible that the outer two are associated with the lobes of the complicated bipolar outflow, which may be causing the disturbed B-field morphology on the E and W edges of the TADPOL map. The large-scale polarization properties of Ser-emb 6 are discussed at length in Chapman et al. (2013), who note that the polarization they measure with SHARP is not consistent with the small-scale morphology measured by CARMA. This could be because of projection effects, as the source and its complicated bipolar outflow are thought to be viewed at a high inclination angle with respect to the sky (Enoch et al. 2009).

Ser-emb 8 is also called S68N by McMullin et al. (1994), who examined the chemistry in the Serpens Main region. The two sources are notable for having the most distinct, well collimated SiO($J = 5 \rightarrow 4$) bipolar outflows in the entire TADPOL sample. It is also interesting to note that despite lying only $\sim 10''$ apart from one another, the pair of cores exhibit B-fields and outflows that are both parallel (Ser-emb 8) and perpendicular (Ser-emb 8(N)).

See Figures 4.24, 4.25, 4.26, and 4.27 for maps.

4.8.22 HH 108 IRAS

HH 108 IRAS (also known as IRAS 18331-0035) is a Class 0/I YSO (Froebrich 2005) in the Serpens molecular cloud, at a distance of about 310 pc (de Lara et al. 1991). The object was identified by 1.3 mm observations (Chini et al. 1997a) following the detection of the Herbig-Haro object HH 108 (Reipurth & Eiroa 1992). A colder millimeter object was discovered $70''$ northeast of HH 108 IRAS, and was named HH 108 MMS (Chini et al. 1997a). An elongated structure enclosing these two objects was also detected in submillimeter observations (Chini et al. 2001). Recently, Tobin et al. (2011) reported IRAM 30 m and CARMA data of N_2H^+ showing a velocity gradient perpendicular to the bipolar outflow. Siebenmorgen & Krügel (2000) have detected polarization of scattered light toward HH 108 IRAS and HH 108 MMS at 14 μm, which shows magnetic fields aligned with the elongated structure enclosing the two objects. However, no previous polarimetric observations of thermal dust emission have been reported toward this region.

See Figure 4.28 for maps.

4.8.23 G034.43+00.24 MM1 and MM3

G034.43+00.24 is a massive star-forming region associated with the IRAS source IRAS 18507+0121, located at a distance of 1.56 kpc (Kurayama et al. 2011). The most prominent source in the complex is the UC H II region G34.4+0.23, which is embedded in a massive (1000 $M_\odot$) dense core (Miralles et al. 1994; Molinari et al. 1996; Bronfman et al. 1996). At $\sim 5''$ resolution, 3 mm spectral line and continuum observations revealed another massive ($\sim$240 $M_\odot$) dense core north of the UC H II region known as G34.4MM. Near-infrared non-detection and the lack of a significant radio counterpart suggested a deeply embedded, high-mass protostar (Shepherd et al. 2004). Further millimeter continuum and Spitzer mid-IR observations revealed that the region is located in an $\sim 8'$ long infrared dark cloud known as

MSXDC G034.43+00.24 (Rathborne et al. 2005). Rathborne et al. identified four compact millimeter clumps labeled MM1–MM4, with MM1 corresponding to the millimeter core G34.4MM mentioned above. TADPOL observations focused on the cores MM1 and MM3.

The estimated masses and luminosities are 800 $\mathrm{M}_\odot$ and 32000 $\mathrm{L}_\odot$ for MM1, and 170 $\mathrm{M}_\odot$ and 12000 $\mathrm{L}_\odot$ for MM3 (Rathborne et al. 2005). SMA continuum observations at much higher resolution show that MM1 is a 29 $\mathrm{M}_\odot$ unresolved core with hot-core-like line emission (Rathborne et al. 2008). Recent ALMA observations by Sakai et al. (2013) show that MM3 is a hot core with a mass of $\lesssim 1.1\,\mathrm{M}_\odot$. Water maser emission, massive CO outflows, and excess 4.5 μm emission indicative of shocks have all been reported toward both MM1 and MM3 (Wang et al. 2006; Shepherd et al. 2007; Chambers et al. 2009; Sanhueza et al. 2010). Note that despite the significantly closer distance that Kurayama et al. (2011) found using maser parallax measurements, all of the above works (except for Sakai et al. 2013) have estimated physical parameters assuming a kinematic distance of 3.7–3.9 kpc.

The MM1 core was observed in both 3 mm continuum and CO($J = 1 \rightarrow 0$) line polarization with the BIMA array at $16''$ resolution (Cortes et al. 2008). Both the continuum and line polarization observations reveal a uniform polarization pattern with an orientation perpendicular to the major axis of the filament. TADPOL observations reveal a much more complex polarization pattern with significantly disturbed B-fields—and even hints of hourglass morphology—in the densest parts of the core.

See Figures 4.29 and 4.30 for maps.

4.8.24 B335 IRS

B335 IRS (Barnard 335, also called CB199 (Clemens & Barvainis 1988)) is an extremely isolated Bok globule harboring a low-mass Class 0 protostar. The distance to B335 is uncertain, but a recent estimate by Stutz et al. (2008) finds that it may be as close as 150 pc. Stutz et al. (2008) also derive a luminosity for B335 of 1.2 $L_\odot$. The protostellar nature of B335 was first uncovered by Keene et al. (1980, 1983) using far-infrared observations that were indicative of an embedded source. Frerking & Langer (1982) found evidence for an outflow in CO ($J = 1 \rightarrow 0$); B335 also presents a convincing infall signature with blue-asymmetric line profiles in optically thick tracers (Zhou et al. 1993). Harvey et al. (2003) found evidence for a circumstellar disk with a radius < 60 AU from modeling of interferometric visibilities. Kinematic data from ~ 1000 AU scales shown little evidence for rapid inner envelope rotation (Yen et al. 2013).

See Figure 4.31 for maps.

4.8.25 DR21(OH)

DR21(OH) is a massive star-forming clump located in the heart of the DR21 molecular ridge in Cygnus X. At a distance of 1.5 kpc (Rygl et al. 2010), Cygnus X is one of the nearest massive star forming complexes in our galaxy (Schneider et al. 2006; Motte et al. 2007). DR21(OH) has an estimated bolometric luminosity of $1.7\times10^4\,\mathrm{L}_\odot$ and a mass of 1800 $\mathrm{M}_\odot$

(Jakob et al. 2007). Millimeter observations have revealed two massive millimeter sources, MM1 and MM2 (Mangum et al. 1991; Liechti & Walmsley 1997), each with masses of a few $\times$ 100 $M_\odot$. At sub-arcsecond resolution, these two cores are resolved into a cluster of $\sim$10 compact massive cores between 5–24 $M_\odot$ (Zapata et al. 2012). DR21(OH) is rich in methanol, water and OH maser features (Plambeck & Menten 1990; Liechti & Walmsley 1997; Kurtz et al. 2004; Araya et al. 2009). Infrared observations have identified several deeply embedded YSOs in the region (Kumar et al. 2007; Davis et al. 2007). High-velocity bipolar outflows from both MM1 and MM2 have been detected in CO and other tracers (Lai et al. 2003; Zapata et al. 2012). Therefore, MM1/2 are excellent candidates for very young massive protostars. Our TADPOL observations encompass these two massive sources.

DR21(OH) has been part of several single-dish and interferometric polarization studies. At low resolution, a uniform large scale magnetic field perpendicular to the DR21 filament is observed (Vallée & Fiege 2006; Kirby 2009). At higher resolution, a more complex polarization pattern, consistent with our TADPOL observations, has been revealed toward DR21(OH) (Lai et al. 2003; Girart et al. 2013). The plane-of-sky component of the magnetic field is estimated to be 0.62 and 2.1 mG at scales of 0.34 and 0.08 pc respectively (Girart et al. 2013). These measurements are consistent with previous single-dish CN Zeeman measurements, which estimate the line-of-sight magnetic field strength to be 0.36 and 0.71 mG for MM1 and MM2, respectively (Crutcher 1999; Falgarone et al. 2008).

See Figure 4.32 for maps.

4.8.26 L1157

L1157-mm (IRAS 20386+6751) is a Class 0 source located in the Cepheus Flare region. The distance to L1157 is uncertain, with estimates between 250 pc and 440 pc (Viotti 1969; Straizys et al. 1992; Kun 1998; Kun et al. 2008); we adopt a distance of 250 pc (Looney et al. 2007). L1157 has a large ($\sim$ 20,000 AU) flattened envelope structure detected in 8 μm absorption (Looney et al. 2007) and molecular tracers N_2H^+ and NH_3 (Chiang et al. 2010; Tobin et al. 2011) that reveal complex kinematics from rotation, infall, and outflow. This large scale structure is perpendicular to the well known outflow from the central source (Gueth et al. 1996), affording an edge-on view of the system. The dust emission from the system has been observed at multiple wavelengths and resolutions at CARMA (Chiang et al. 2012) and was best modeled as an envelope with a unresolved disk ($<$ 40 AU). Recent high resolution ($\sim$ 0.06″) VLA 7.3 mm dust continuum observations have placed a limit on the size of the disk component of $<$ 20 AU (Tobin et al. 2013a). The magnetic field was shown to have a well defined hourglass shape and was estimated to have a plane-of-sky magnitude of 1–4 mG (Stephens et al. 2013).

See Figure 4.33 for maps.

4.8.27 CB 230

CB 230 (Clemens & Barvainis 1988) is an isolated globule located in the Cepheus flare region, at a distance of 325 pc (Straizys et al. 1992), although other more recent estimates range from 270–515 pc (Kun et al. 2009). The protostellar system is classified as Class 0/I (Launhardt et al. 2013). A large envelope is detected in both N_2H^+ and ammonia and exhibits a velocity gradient suggestive of rotation (Chen et al. 2007; Tobin et al. 2011). The protostellar source is also identified as a triple system (Yun 1996; Launhardt et al. 2013; Tobin et al. 2013b). The wide companion (CB 230 IRS2) is located 10″ from CB 230 IRS1 and is not observed at wavelengths longer than 24 μm (Launhardt et al. 2001; Massi et al. 2008; Launhardt et al. 2013); however, IRS2 does seem to drive a CO outflow (Launhardt 2001). The close companion to IRS1 (IRS1B) was recently discovered by Tobin et al. (2013b) and is separated from IRS1 by 0.3″ (100 AU).

See Figure 4.34 for maps.

4.8.28 L1165

The L1165 dark cloud has a L-shaped filament structure, and is located in the Cepheus region (e.g., Reipurth et al. 1997; Tobin et al. 2010). Two IRAS objects are in the kink of the filamentary structure; however, only the southern object IRAS 22051+5848 was detected at 850 μm and classified as a Class I YSO (Visser et al. 2002); this is the source we observe. The distance to the object is somewhat ambiguous in the literature: 750 pc (e.g., Reipurth et al. 1997) and 300 pc (e.g., Dobashi et al. 1994). We adopt the latter 300 pc, which gives a reasonable luminosity for a low mass YSO and has been used in previous (sub)millimeter studies. The bipolar outflow has been mapped in CO($J = 2 \rightarrow 1$) by the JCMT (Visser et al. 2002; Parker et al. 1991), and the near infrared nebula feature was imaged in K-band by the University of Hawaii 2.2 m telescope (Connelley et al. 2007). It has been imaged in 350 μm continuum emission by the SHARC-II camera at the CSO (Wu et al. 2007). In addition, *Spitzer* IRAC data have revealed that the bipolar outflow cavity and the elongated envelope structure (imaged in 8 μm emission) are perpendicular to each other (Tobin et al. 2010). Recently Tobin et al. (2011) detected a velocity gradient along the elongated envelope structure using IRAM 30 m observations in N_2H^+ and CARMA observations in N_2H^+ and HCO^+; these observations showed that the HCO^+ feature can be interpreted as rotation around a 0.5 $M_\odot$ central protostar. There have been no previous polarimetric observations toward this object.

See Figure 4.35 for maps.

4.8.29 NGC 7538 IRS 1

The hyper-compact H II region NGC 7538 IRS 1 was first discovered in a 2 μm and 20 μm survey of NGC 7538 (Wynn-Williams et al. 1974), which lies at a distance of 2.65 kpc (Moscadelli et al. 2009). IRS 1 is an extremely young high-mass star (type ∼O7), which powers a N-S ionized thermal jet (Gaume et al. 1995; Sandell et al. 2009), drives a molecular outflow (Scoville et al. 1986; Zhu et al. 2013), and excites a variety of molecular masers, including OH, H_2O, H_2CO, CH_3OH, NH_3, and $^{15}NH_3$ (Johnston et al. 1989). It is still heavily accreting with an accretion rate of $\sim 10^{-3}\,M_\odot\,yr^{-1}$, quenching the formation of an H II region. All the observational evidence suggests that IRS 1 should be surrounded by an E–W accretion disk, which has yet to be confirmed. Imaging with the SCUBA polarimeter at 850 μm indicates that the magnetic field is disturbed around IRS 1 (Momose et al. 2001). At the position of IRS 1 the degree of polarization is 2–3%, with a polarization (not B-field) position angle of 90°; however, immediately east the position angle is ∼50°, similar to what Flett & Murray (1991) obtained at 800 μm. It is not surprising that the magnetic field around IRS 1 is disturbed, because the molecular cloud core is forming a young cluster (Qiu et al. 2011). At least eight of the cluster members are seen as millimeter continuum sources and H_2O masers, suggesting that they are surrounded by accretion disks and are probably powering outflows.

See Figure 4.36 for maps.

4.8.30 CB 244

CB 244 (L1262) is an isolated globule in the Cepheus region with an estimated distance of 200 pc, which is the distance of the nearby cloud L1235 (Snell 1981; Benson & Myers 1989; Stutz et al. 2010). CB 244 harbors both a Class 0 protostar driving an outflow (Yun & Clemens 1994; Visser et al. 2002) and a neighboring starless core (Stutz et al. 2010). Chen et al. (2007) observed a filamentary distribution of N_2H^+ in the envelope surrounding the protostar; the velocity structure of the line was suggestive of rapid envelope rotation.

See Figure 4.37 for maps.

Bibliography

Adams, J. D., Herter, T. L., Osorio, M., et al. 2012, ApJ, 749, L24
Adatia, N. A., & Rudge, A. W. 1975, Electronics Letters, 11, 513
Agudo, I., Thum, C., Wiesemeyer, H., et al. 2012, A&A, 541, A111
Aitken, D. K., Wright, C. M., Smith, C. H., & Roche, P. F. 1993, MNRAS, 262, 456
Allen, A., Li, Z.-Y., & Shu, F. H. 2003, ApJ, 599, 363
Andersson, B.-G. 2012, ArXiv e-prints, arXiv:1208.4393 [astro-ph.GA]
Andre, P., Martin-Pintado, J., Despois, D., & Montmerle, T. 1990, A&A, 236, 180
Andre, P., Ward-Thompson, D., & Barsony, M. 1993, ApJ, 406, 122
—. 2000, Protostars and Planets IV, 59
Anglada, G., Rodriguez, L. F., Torrelles, J. M., et al. 1989, ApJ, 341, 208
Araya, E. D., Kurtz, S., Hofner, P., & Linz, H. 2009, ApJ, 698, 1321
Attard, M., Houde, M., Novak, G., et al. 2009, ApJ, 702, 1584
Bachiller, R., & Cernicharo, J. 1986, A&A, 168, 262
Bachiller, R., Gueth, F., Guilloteau, S., Tafalla, M., & Dutrey, A. 2000, A&A, 362, L33
Bachiller, R., Guilloteau, S., Dutrey, A., Planesas, P., & Martin-Pintado, J. 1995, A&A, 299, 857
Bachiller, R., & Perez Gutierrez, M. 1997, ApJ, 487, L93
Bai, X.-N. 2011, ApJ, 739, 50
Balbus, S. A., & Hawley, J. F. 1991, ApJ, 376, 214
—. 1998, Reviews of Modern Physics, 70, 1
Balbus, S. A., Hawley, J. F., & Stone, J. M. 1996, ApJ, 467, 76
Benson, P. J., & Myers, P. C. 1989, ApJS, 71, 89
Bethell, T. J., Chepurnov, A., Lazarian, A., & Kim, J. 2007, ApJ, 663, 1055
Blake, G. A., Sandell, G., van Dishoeck, E. F., et al. 1995, ApJ, 441, 689
Bock, D., Bolatto, A. D., Hawkins, D. W., et al. 2006, in Society of Photo-Optical Instrumentation Engineers (SPIE) Conference Series, Vol. 6267, 13
Boss, A. P. 2004, ApJ, 616, 1265
Bronfman, L., Nyman, L.-A., & May, J. 1996, A&AS, 115, 81
Campbell, M. F., Butner, H. M., Harvey, P. M., et al. 1995, ApJ, 454, 831
Chambers, E. T., Jackson, J. M., Rathborne, J. M., & Simon, R. 2009, ApJS, 181, 360
Chambers, J. E. 2006, ApJ, 652, L133
Chandler, C. J., & Richer, J. S. 2001, ApJ, 555, 139

Chandrasekhar, S., & Fermi, E. 1953, ApJ, 118, 113

Chapman, N. L., Davidson, J. A., Goldsmith, P. F., et al. 2013, ApJ, 770, 151

Chen, C.-Y., & Ostriker, E. C. 2014, ApJ, 785, 69

Chen, H.-R., Welch, W. J., Wilner, D. J., & Sutton, E. C. 2006, ApJ, 639, 975

Chen, X., Launhardt, R., & Henning, T. 2007, ApJ, 669, 1058

Chiang, H.-F., Looney, L. W., & Tobin, J. J. 2012, ApJ, 756, 168

Chiang, H.-F., Looney, L. W., Tobin, J. J., & Hartmann, L. 2010, ApJ, 709, 470

Chini, R., Reipurth, B., Sievers, A., et al. 1997a, A&A, 325, 542

Chini, R., Reipurth, B., Ward-Thompson, D., et al. 1997b, ApJ, 474, L135

Chini, R., Ward-Thompson, D., Kirk, J. M., et al. 2001, A&A, 369, 155

Choi, M., Panis, J.-F., & Evans, II, N. J. 1999, ApJS, 122, 519

Chu, T.-S., & Turrin, R. 1973, IEEE Transactions on Antennas and Propagation, 21, 339

Ciardi, D. R., & Gómez Martín, C. 2007, ApJ, 664, 377

Ciesla, F. J. 2007, Science, 318, 613

Claussen, M. J., Wilking, B. A., Benson, P. J., et al. 1996, ApJS, 106, 111

Clemens, D. P., & Barvainis, R. 1988, ApJS, 68, 257

Connelley, M. S., Reipurth, B., & Tokunaga, A. T. 2007, AJ, 133, 1528

Contopoulos, G., & Jappel, A., eds. 1974, Transactions of the IAU, Vol. XVB 1973, Proceedings of the Fifteenth General Assembly and Extraordinary General Assembly (Dordrecht: Reidel), 165

Cortes, P. C., Crutcher, R. M., Shepherd, D. S., & Bronfman, L. 2008, ApJ, 676, 464

Crutcher, R. M. 1999, ApJ, 520, 706

—. 2012, ARA&A, 50, 29

Crutcher, R. M., Roberts, D. A., Troland, T. H., & Goss, W. M. 1999, ApJ, 515, 275

Curran, R. L., & Chrysostomou, A. 2007, MNRAS, 382, 699

Curran, R. L., Chrysostomou, A., & Matthews, B. C. 2007, in IAU Symposium, Star-Disk Interaction in Young Stars, ed. J. Bouvier & I. Appenzeller, Vol. 243, 63

Curtis, E. I., Richer, J. S., Swift, J. J., & Williams, J. P. 2010, Monthly Notices of the Royal Astronomical Society, 408, 1516

Davidson, J. A., & Jaffe, D. T. 1984, Astrophysical Journal, 277, L13

Davidson, J. A., Novak, G., Matthews, T. G., et al. 2011, ApJ, 732, 97

Davies, R. D., & Gardner, F. F. 1966, Australian Journal of Physics, 19, 823

Davis, C. J., Kumar, M. S. N., Sandell, G., et al. 2007, MNRAS, 374, 29

Davis, C. J., Ray, T. P., Eisloeffel, J., & Corcoran, D. 1997, Astronomy and Astrophysics, 324, 263

Davis, Jr., L., & Greenstein, J. L. 1951, ApJ, 114, 206

de Gregorio-Monsalvo, I., Gómez, J. F., Anglada, G., et al. 2009, AJ, 137, 5080

de Lara, E., Chavarria-K., C., & Lopez-Molina, G. 1991, A&A, 243, 139

de Zeeuw, P. T., Hoogerwerf, R., de Bruijne, J. H. J., Brown, A. G. A., & Blaauw, A. 1999, AJ, 117, 354

Di Francesco, J., Myers, P. C., Wilner, D. J., Ohashi, N., & Mardones, D. 2001, ApJ, 562, 770

Dionatos, O., Nisini, B., Cabrit, S., Kristensen, L., & Pineau Des Forêts, G. 2010, A&A, 521, A7

Dobashi, K., Bernard, J.-P., Yonekura, Y., & Fukui, Y. 1994, ApJS, 95, 419

Dolginov, A. Z., & Mitrofanov, I. G. 1976, Ap&SS, 43, 291

Dotson, J. L. 1996, ApJ, 470, 566

Dotson, J. L., Davidson, J., Dowell, C. D., Schleuning, D. A., & Hildebrand, R. H. 2000, ApJS, 128, 335

Dotson, J. L., Vaillancourt, J. E., Kirby, L., et al. 2010, ApJS, 186, 406

Draine, B. T., & Weingartner, J. C. 1996, ApJ, 470, 551

Dreher, J. W., & Welch, W. J. 1981, ApJ, 245, 857

Dzib, S., Loinard, L., Mioduszewski, A. J., et al. 2010, ApJ, 718, 610

Eislöffel, J. 2000, A&A, 354, 236

Elmegreen, B. G., & Scalo, J. 2004, ARA&A, 42, 211

Emerson, J. P., Harris, S., Jennings, R. E., et al. 1984, ApJ, 278, L49

Engargiola, G., & Plambeck, R. L. 1999, in The Physics and Chemistry of the Interstellar Medium, Proceedings of the 3rd Cologne-Zermatt Symposium, ed. V. Ossenkopf, J. Stutzki, & G. Winnewisser (GCA-Verlag Herdecke), 291

Enoch, M. L., Corder, S., Dunham, M. M., & Duchêne, G. 2009, ApJ, 707, 103

Enoch, M. L., Glenn, J., Evans, II, N. J., et al. 2007, ApJ, 666, 982

Enoch, M. L., Corder, S., Duchêne, G., et al. 2011, ApJS, 195, 21

Falgarone, E., Troland, T. H., Crutcher, R. M., & Paubert, G. 2008, A&A, 487, 247

Fiedler, R. A., & Mouschovias, T. C. 1993, ApJ, 415, 680

Flett, A. M., & Murray, A. G. 1991, Monthly Notices of the Royal Astronomical Society (ISSN 0035-8711), 249, 4P

Franco, G. A. P., Alves, F. O., & Girart, J. M. 2010, ApJ, 723, 146

Frerking, M. A., & Langer, W. D. 1982, ApJ, 256, 523

Froebrich, D. 2005, ApJS, 156, 169

Furuya, R. S., Kitamura, Y., Wootten, A., Claussen, M. J., & Kawabe, R. 2003, ApJS, 144, 71

Galli, D., Lizano, S., Shu, F. H., & Allen, A. 2006, ApJ, 647, 374

Galli, D., & Shu, F. H. 1993a, ApJ, 417, 220

—. 1993b, ApJ, 417, 243

Gaume, R. A., Goss, W. M., Dickel, H. R., Wilson, T. L., & Johnston, K. J. 1995, Astrophysical Journal, 438, 776

Girart, J. M., Crutcher, R. M., & Rao, R. 1999, ApJ, 525, L109

Girart, J. M., Frau, P., Zhang, Q., et al. 2013, ApJ, 772, 69

Girart, J. M., Rao, R., & Marrone, D. P. 2006, Science, 313, 812

Goddi, C., Humphreys, E. M. L., Greenhill, L. J., Chandler, C. J., & Matthews, L. D. 2011, ApJ, 728, 15

Gold, T. 1952, MNRAS, 112, 215

Goldsmith, P. F., Heyer, M., Narayanan, G., et al. 2008, ApJ, 680, 428

Goldsmith, P. F., Snell, R. L., Hemeon-Heyer, M., & Langer, W. D. 1984, Astrophysical

Journal, 286, 599

Gómez, L., Rodríguez, L. F., Loinard, L., et al. 2008, ApJ, 685, 333

Güdel, M., Telleschi, A., Audard, M., et al. 2007, A&A, 468, 515

Gueth, F., & Guilloteau, S. 1999, A&A, 343, 571

Gueth, F., Guilloteau, S., & Bachiller, R. 1996, A&A, 307, 891

Hachisuka, K., Brunthaler, A., Menten, K. M., et al. 2006, ApJ, 645, 337

Hamaker, J. P., Bregman, J. D., & Sault, R. J. 1996, A&AS, 117, 137

Harvey, D. W. A., Wilner, D. J., Myers, P. C., & Tafalla, M. 2003, ApJ, 596, 383

Haschick, A. D., Moran, J. M., Rodriguez, L. F., et al. 1980, ApJ, 237, 26

Hatchell, J., Fuller, G. A., Richer, J. S., Harries, T. J., & Ladd, E. F. 2007, A&A, 468, 1009

Heiles, C. 1999, Arecibo Technical and Operations Memo Series (ATOMS), 2

—. 2000, AJ, 119, 923

Heiles, C., & Crutcher, R. 2005, in Lecture Notes in Physics, Berlin Springer Verlag, Vol. 664, Cosmic Magnetic Fields, ed. R. Wielebinski & R. Beck, 137

Heiles, C., Robishaw, T., Troland, T. H., & Roshi, D. A. 2003, GBT Commissioning Memos, 23

Heiles, C., & Troland, T. H. 2005, ApJ, 624, 773

Heiles, C., Perillat, P., Nolan, M., et al. 2001a, PASP, 113, 1247

—. 2001b, PASP, 113, 1274

Heiles, C. E., & Drake, F. D. 1963, Icarus, 2, 281

Hennebelle, P., & Ciardi, A. 2009, A&A, 506, L29

Hennebelle, P., & Fromang, S. 2008, A&A, 477, 9

Henning, T., Wolf, S., Launhardt, R., & Waters, R. 2001, ApJ, 561, 871

Herczeg, G. J., Karska, A., Bruderer, S., et al. 2012, A&A, 540, A84

Hildebrand, R. H. 1988, QJRAS, 29, 327

Hirano, N., Ho, P. P. T., Liu, S.-Y., et al. 2010, ApJ, 717, 58

Hirota, T., Honma, M., Imai, H., et al. 2011, PASJ, 63, 1

Hirota, T., Bushimata, T., Choi, Y. K., et al. 2008, PASJ, 60, 37

Hirsch, L., Adams, J. D., Herter, T. L., et al. 2012, ApJ, 757, 113

Hoang, T., & Lazarian, A. 2009, ApJ, 697, 1316

Högbom, J. A. 1974, A&AS, 15, 417

Hogerheijde, M. R., van Dishoeck, E. F., Blake, G. A., & van Langevelde, H. J. 1998, ApJ, 502, 315

Holland, W. S., Greaves, J. S., Ward-Thompson, D., & Andre, P. 1996, A&A, 309, 267

Houde, M., Dowell, C. D., Hildebrand, R. H., et al. 2004, ApJ, 604, 717

Howell, R. R., McCarthy, D. W., & Low, F. J. 1981, ApJ, 251, L21

Hughes, A. M., Hull, C. L. H., Wilner, D. J., & Plambeck, R. L. 2013, AJ, 145, 115

Hughes, A. M., Wilner, D. J., Cho, J., et al. 2009, ApJ, 704, 1204

Hull, C., Plambeck, R., & Engargiola, G. 2011, in General Assembly and Scientific Symposium, 2011 XXXth URSI (Istanbul, Turkey: IEEE), 1

Hull, C. L. H., Plambeck, R. L., Bolatto, A. D., et al. 2013, ApJ, 768, 159

Hull, C. L. H., Plambeck, R. L., Kwon, W., et al. 2014, ApJS, 213, 13

IEEE. 1997, IEEE Std 211-1997

Imai, H., Horiuchi, S., Deguchi, S., & Kameya, O. 2003, ApJ, 595, 285

Imai, H., Nakashima, K., Bushimata, T., et al. 2007, PASJ, 59, 1107

Jakob, H., Kramer, C., Simon, R., et al. 2007, A&A, 461, 999

Johnston, K. J., Stolovy, S. R., Wilson, T. L., Henkel, C., & Mauersberger, R. 1989, Astrophysical Journal, 343, L41

Johnstone, D., & Bally, J. 1999, ApJ, 510, L49

Jones, R. C. 1941, Journal of the Optical Society of America (1917-1983), 31, 488

Jones, R. V., & Spitzer, Jr., L. 1967, ApJ, 147, 943

Jones, T. J., Hyland, A. R., & Bailey, J. 1984, ApJ, 282, 675

Joos, M., Hennebelle, P., & Ciardi, A. 2012, A&A, 543, A128

Jørgensen, J. K., Hogerheijde, M. R., van Dishoeck, E. F., Blake, G. A., & Schöier, F. L. 2004, A&A, 413, 993

Jørgensen, J. K., Harvey, P. M., Evans, II, N. J., et al. 2006, ApJ, 645, 1246

Jørgensen, J. K., Bourke, T. L., Myers, P. C., et al. 2007, ApJ, 659, 479

Keene, J., Davidson, J. A., Harper, D. A., et al. 1983, ApJ, 274, L43

Keene, J., Hildebrand, R. H., Whitcomb, S. E., & Harper, D. A. 1980, ApJ, 240, L43

Kenyon, S. J., Dobrzycka, D., & Hartmann, L. 1994, AJ, 108, 1872

Kerr, A. R., Pan, S.-K., Claude, S. M. X., et al. 2013, ArXiv e-prints, arXiv:1306.6085 [physics.ins-det]

Killeen, N. E. B., Bicknell, G. V., & Ekers, R. D. 1986, ApJ, 302, 306

Kirby, L. 2009, ApJ, 694, 1056

Knee, L. B. G., & Sandell, G. 2000, A&A, 361, 671

Koch, P. M., Tang, Y.-W., & Ho, P. T. P. 2012, ApJ, 747, 79

Konigl, A., & Pudritz, R. E. 2000, Protostars and Planets IV, 759

Krasnopolsky, R., Li, Z.-Y., Shang, H., & Zhao, B. 2012, ApJ, 757, 77

Krejny, M., Matthews, T. G., Novak, G., et al. 2009, ApJ, 705, 717

Krumholz, M. R., Crutcher, R. M., & Hull, C. L. H. 2013, ApJ, 767, L11

Kumar, M. S. N., Davis, C. J., Grave, J. M. C., Ferreira, B., & Froebrich, D. 2007, MNRAS, 374, 54

Kun, M. 1998, ApJS, 115, 59

Kun, M., Balog, Z., Kenyon, S. J., Mamajek, E. E., & Gutermuth, R. A. 2009, ApJS, 185, 451

Kun, M., Kiss, Z. T., & Balog, Z. 2008, in Handbook of Star Forming Regions vol. 1, 136-239 (2008), ed. B. Reipurth (Astronomical Society of the Pacific), 136

Kurayama, T., Nakagawa, A., Sawada-Satoh, S., et al. 2011, PASJ, 63, 513

Kurtz, S., Hofner, P., & Álvarez, C. V. 2004, ApJS, 155, 149

Kwon, W., Looney, L. W., Crutcher, R. M., & Kirk, J. M. 2006, ApJ, 653, 1358

Kwon, W., Looney, L. W., Mundy, L. G., Chiang, H.-F., & Kemball, A. J. 2009, ApJ, 696, 841

Ladd, E. F., Deane, J. R., Sanders, D. B., & Wynn-Williams, C. G. 1993, ApJ, 419, 186

Lai, S.-P., Girart, J. M., & Crutcher, R. M. 2003, ApJ, 598, 392

Launhardt, R. 2001, in IAU Symposium, Vol. 200, The Formation of Binary Stars, ed. H. Zinnecker & R. Mathieu, 117

Launhardt, R., Sargent, A., & Zinnecker, H. 2001, in Astronomical Society of the Pacific Conference Series, Vol. 235, Science with the Atacama Large Millimeter Array, ed. A. Wootten, 134

Launhardt, R., & Sargent, A. I. 2001, ApJ, 562, L173

Launhardt, R., Pavlyuchenkov, Y., Gueth, F., et al. 2009, A&A, 494, 147

Launhardt, R., Nutter, D., Ward-Thompson, D., et al. 2010, ApJS, 188, 139

Launhardt, R., Stutz, A. M., Schmiedeke, A., et al. 2013, A&A, 551, A98

Lay, O. P., Carlstrom, J. E., & Hills, R. E. 1995, ApJ, 452, L73

Lazarian, A. 1994, MNRAS, 268, 713

—. 2003, J. Quant. Spec. Radiat. Transf., 79, 881

Lazarian, A. 2005, in American Institute of Physics Conference Series, Vol. 784, Magnetic Fields in the Universe: From Laboratory and Stars to Primordial Structures., ed. E. M. de Gouveia dal Pino, G. Lugones, & A. Lazarian, 42

—. 2007, J. Quant. Spec. Radiat. Transf., 106, 225

Lazarian, A., Andersson, B.-G., & Hoang, T. 2014, Understanding Polarization from Dust: Radiative Torques versus Paramagnetic Mechanism of Dust Alignment (Cambridge University Press)

Lazarian, A., & Draine, B. T. 1999a, ApJ, 520, L67

—. 1999b, ApJ, 516, L37

Lazarian, A., & Hoang, T. 2007, MNRAS, 378, 910

Lazarian, A., & Roberge, W. G. 1997, ApJ, 484, 230

Leão, M. R. M., de Gouveia Dal Pino, E. M., Santos-Lima, R., & Lazarian, A. 2013, ApJ, 777, 46

Lee, C.-F., Hirano, N., Palau, A., et al. 2009, ApJ, 699, 1584

Lefloch, B., Castets, A., Cernicharo, J., Langer, W. D., & Zylka, R. 1998, A&A, 334, 269

Li, H.-b., Dowell, C. D., Goodman, A., Hildebrand, R., & Novak, G. 2009, ApJ, 704, 891

Li, Z.-Y., Krasnopolsky, R., & Shang, H. 2011, ApJ, 738, 180

—. 2013, ApJ, 774, 82

Liechti, S., & Walmsley, C. M. 1997, A&A, 321, 625

Lis, D. C., Serabyn, E., Keene, J., et al. 1998, ApJ, 509, 299

Liu, H. B., Qiu, K., Zhang, Q., Girart, J. M., & Ho, P. T. P. 2013, ApJ, 771, 71

Loinard, L., Torres, R. M., Mioduszewski, A. J., & Rodríguez, L. F. 2008, ApJ, 675, L29

Loinard, L., Torres, R. M., Mioduszewski, A. J., et al. 2007, ApJ, 671, 546

Looney, L. W., Mundy, L. G., & Welch, W. J. 2000, ApJ, 529, 477

—. 2003, ApJ, 592, 255

Looney, L. W., Tobin, J. J., & Kwon, W. 2007, ApJ, 670, L131

López-Sepulcre, A., Taquet, V., Sánchez-Monge, Á., et al. 2013, A&A, 556, A62

Lynch, C., Mutel, R. L., Güdel, M., et al. 2013, ApJ, 766, 53

Lynds, B. T. 1965, ApJS, 12, 163

Machida, M. N., Matsumoto, T., Hanawa, T., & Tomisaka, K. 2006, ApJ, 645, 1227

Mangum, J. G., Wootten, A., & Mundy, L. G. 1991, ApJ, 378, 576

Marrone, D. P. 2006, PhD thesis, Harvard University

Marvel, K. B., Wilking, B. A., Claussen, M. J., & Wootten, A. 2008, ApJ, 685, 285

Massi, F., Codella, C., Brand, J., di Fabrizio, L., & Wouterloot, J. G. A. 2008, A&A, 490, 1079

Mathis, J. S. 1986, ApJ, 308, 281

Matthews, B. C., Fiege, J. D., & Moriarty-Schieven, G. 2002, ApJ, 569, 304

Matthews, B. C., Lai, S.-P., Crutcher, R. M., & Wilson, C. D. 2005, ApJ, 626, 959

Matthews, B. C., McPhee, C. A., Fissel, L. M., & Curran, R. L. 2009, ApJS, 182, 143

Matthews, B. C., Wilson, C. D., & Fiege, J. D. 2001, ApJ, 562, 400

McCaughrean, M. J., Rayner, J. T., & Zinnecker, H. 1994, ApJ, 436, L189

McKee, C. F. 1989, ApJ, 345, 782

McKee, C. F., & Ostriker, E. C. 2007, ARA&A, 45, 565

McKee, C. F., Zweibel, E. G., Goodman, A. A., & Heiles, C. 1993, in Protostars and Planets III, ed. E. H. Levy & J. I. Lunine (Tucson, Arizona: University of Arizona Press), 327

McMullin, J. P., Mundy, L. G., Wilking, B. A., Hezel, T., & Blake, G. A. 1994, ApJ, 424, 222

Megeath, S. T., Herter, T., Beichman, C., et al. 1996, A&A, 307, 775

Megeath, S. T., Wilson, T. L., & Corbin, M. R. 2005, ApJ, 622, L141

Mellon, R. R., & Li, Z.-Y. 2008, ApJ, 681, 1356

Ménard, F., & Duchêne, G. 2004, A&A, 425, 973

Menten, K. M., Reid, M. J., Forbrich, J., & Brunthaler, A. 2007, A&A, 474, 515

Mestel, L. 1985, in Protostars and Planets II, ed. D. C. Black & M. S. Matthews, 320

Mestel, L., & Spitzer, Jr., L. 1956, MNRAS, 116, 503

Miralles, M. P., Rodriguez, L. F., & Scalise, E. 1994, ApJS, 92, 173

Molinari, S., Brand, J., Cesaroni, R., & Palla, F. 1996, A&A, 308, 573

Momose, M., Tamura, M., Kameya, O., et al. 2001, The Astrophysical Journal, 555, 855

Moore, T. J. T., Bretherton, D. E., Fujiyoshi, T., et al. 2007, MNRAS, 379, 663

Moriarty-Schieven, G. H., Butner, H. M., & Wannier, P. G. 1995, ApJ, 445, L55

Moscadelli, L., Reid, M. J., Menten, K. M., et al. 2009, ApJ, 693, 406

Motte, F., Bontemps, S., Schilke, P., et al. 2007, A&A, 476, 1243

Mundt, R., & Fried, J. W. 1983, ApJ, 274, L83

Myers, A. T., McKee, C. F., Cunningham, A. J., Klein, R. I., & Krumholz, M. R. 2013, ApJ, 766, 97

Naghizadeh-Khouei, J., & Clarke, D. 1993, A&A, 274, 968

Napier, P. J. 1994, ALMA Memo Series, 115

Napier, P. J. 1999, in Astronomical Society of the Pacific Conference Series, Vol. 180, Synthesis Imaging in Radio Astronomy II, ed. G. B. Taylor, C. L. Carilli, & R. A. Perley, 37

Navarrini, A., & Plambeck, R. 2006, IEEE Transactions on Microwave Theory and Techniques, 54, 272

Nisini, B., Benedettini, M., Giannini, T., et al. 2000, A&A, 360, 297

Nisini, B., Codella, C., Giannini, T., et al. 2007, A&A, 462, 163

O'Linger, J., Wolf-Chase, G., Barsony, M., & Ward-Thompson, D. 1999, ApJ, 515, 696

O'Linger, J. C., Cole, D. M., Ressler, M. E., & Wolf-Chase, G. 2006, AJ, 131, 2601

Ostriker, E. C., Stone, J. M., & Gammie, C. F. 2001, ApJ, 546, 980

Padoan, P., Goodman, A., Draine, B. T., et al. 2001, ApJ, 559, 1005

Palmeirim, P., André, P., Kirk, J., et al. 2013, A&A, 550, A38

Pandian, J., Baker, L., Cortes, G., et al. 2006, Microwave Magazine, IEEE, 7, 74

Parker, N. D., Padman, R., & Scott, P. F. 1991, MNRAS, 252, 442

Pelkonen, V.-M., Juvela, M., & Padoan, P. 2009, A&A, 502, 833

Pereyra, A., & Magalhães, A. M. 2004, ApJ, 603, 584

Perley, R. A., & Butler, B. J. 2013, ApJS, 206, 16

Plambeck, R., & Engargiola, G. 2010, CARMA Memos, 54

Plambeck, R. L. 2000, BIMA Memo Series, 79

Plambeck, R. L., & Menten, K. M. 1990, ApJ, 364, 555

Plambeck, R. L., Wright, M. C. H., & Rao, R. 2003, ApJ, 594, 911

Plambeck, R. L., Wright, M. C. H., Friedel, D. N., et al. 2009, ApJ, 704, L25

Planck Collaboration, Ade, P. A. R., Aghanim, N., et al. 2014a, ArXiv e-prints, arXiv:1405.0871

—. 2014b, ArXiv e-prints, arXiv:1405.0872

—. 2014c, ArXiv e-prints, arXiv:1405.0873

Poidevin, F., Bastien, P., & Matthews, B. C. 2010, ApJ, 716, 893

Purcell, E. M. 1979, ApJ, 231, 404

Qiu, K., Zhang, Q., & Menten, K. M. 2011, ApJ, 728, 6

Rao, R., Crutcher, R. M., Plambeck, R. L., & Wright, M. C. H. 1998, ApJ, 502, L75

Rao, R., Girart, J. M., Lai, S.-P., & Marrone, D. P. 2014, ApJ, 780, L6

Rao, R., Girart, J. M., Marrone, D. P., Lai, S.-P., & Schnee, S. 2009, ApJ, 707, 921

Rathborne, J. M., Jackson, J. M., Chambers, E. T., et al. 2005, ApJ, 630, L181

Rathborne, J. M., Jackson, J. M., Zhang, Q., & Simon, R. 2008, ApJ, 689, 1141

Reid, M. J., Argon, A. L., Masson, C. R., Menten, K. M., & Moran, J. M. 1995, ApJ, 443, 238

Reipurth, B., Bally, J., & Devine, D. 1997, AJ, 114, 2708

Reipurth, B., & Eiroa, C. 1992, A&A, 256, L1

Reipurth, B., Rodríguez, L. F., Anglada, G., & Bally, J. 2002, AJ, 124, 1045

Robishaw, T. 2008, PhD thesis, University of California, Berkeley

Rodón, J. A., Beuther, H., Megeath, S. T., & van der Tak, F. F. S. 2008, A&A, 490, 213

Rodrigues, C. V., Sartori, M. J., Gregorio-Hetem, J., & Magalhães, A. M. 2009, ApJ, 698, 2031

Rodriguez, L. F., Anglada, G., & Curiel, S. 1997, ApJ, 480, L125

Rodríguez, L. F., Anglada, G., & Curiel, S. 1999, ApJS, 125, 427

Rodriguez, L. F., Anglada, G., & Raga, A. 1995, ApJ, 454, L149

Rodriguez, L. F., Curiel, S., Moran, J. M., et al. 1989, ApJ, 346, L85

Rodríguez, L. F., Dzib, S. A., Loinard, L., et al. 2012a, RMxAA, 48, 243

Rodríguez, L. F., González, R. F., Raga, A. C., et al. 2012b, A&A, 537, A123

Rudge, A. W., & Adatia, N. A. 1978, IEEE Proceedings, 66, 1592

Rybicki, G. B., & Lightman, A. P. 1979, Radiative processes in astrophysics (Wiley-VCH)

Rygl, K. L. J., Brunthaler, A., Reid, M. J., et al. 2010, A&A, 511, A2
Sabin, L., Zhang, Q., Zijlstra, A. A., et al. 2014, MNRAS, 438, 1794
Sakai, T., Sakai, N., Foster, J. B., et al. 2013, ApJ, 775, L31
Sandell, G., Goss, W. M., Wright, M., & Corder, S. 2009, The Astrophysical Journal Letters, 699, L31
Sandell, G., & Knee, L. B. G. 2001, ApJ, 546, L49
Sandell, G., Knee, L. B. G., Aspin, C., Robson, I. E., & Russell, A. P. G. 1994, A&A, 285, L1
Sanhueza, P., Garay, G., Bronfman, L., et al. 2010, ApJ, 715, 18
Sano, T., Miyama, S. M., Umebayashi, T., & Nakano, T. 2000, ApJ, 543, 486
Sault, R. J., Teuben, P. J., & Wright, M. C. H. 1995, in ASP Conf. Ser. 77: Astronomical Data Analysis Software and Systems IV, ed. R. A. Shaw, H. E. Payne, & J. J. E. Hayes, Vol. 4, 433
Schleuning, D. A. 1998, ApJ, 493, 811
Schleuning, D. A., Vaillancourt, J. E., Hildebrand, R. H., et al. 2000, ApJ, 535, 913
Schneider, N., Bontemps, S., Simon, R., et al. 2006, A&A, 458, 855
Schneider, P. C., Eislöffel, J., Güdel, M., et al. 2013, A&A, 550, L1
Scoville, N. Z., Sargent, A. I., Sanders, D. B., et al. 1986, Astrophysical Journal, 303, 416
Semenov, D., Wiebe, D., & Henning, T. 2006, ApJ, 647, L57
Shepherd, D. S., Nürnberger, D. E. A., & Bronfman, L. 2004, ApJ, 602, 850
Shepherd, D. S., Povich, M. S., Whitney, B. A., et al. 2007, ApJ, 669, 464
Shu, F. H., Adams, F. C., & Lizano, S. 1987, ARA&A, 25, 23
Shu, F. H., Najita, J. R., Shang, H., & Li, Z.-Y. 2000, Protostars and Planets IV, 789
Siebenmorgen, R., & Krügel, E. 2000, A&A, 364, 625
Smith, K. W., Bonnell, I. A., Emerson, J. P., & Jenness, T. 2000, MNRAS, 319, 991
Smith, R. J., Glover, S. C. O., Bonnell, I. A., Clark, P. C., & Klessen, R. S. 2011, MNRAS, 411, 1354
Snell, R. L. 1981, ApJS, 45, 121
Stapelfeldt, K. R., Duchêne, G., Perrin, M., et al. 2014, in IAU Symposium, Vol. 299, IAU Symposium, ed. M. Booth, B. C. Matthews, & J. R. Graham, 99
Stecklum, B., Launhardt, R., Fischer, O., et al. 2004, ApJ, 617, 418
Stephens, I. W., Looney, L. W., & Crutcher, R. M. 2014, Nature, submitted
Stephens, I. W., Looney, L. W., Dowell, C. D., Vaillancourt, J. E., & Tassis, K. 2011, ApJ, 728, 99
Stephens, I. W., Looney, L. W., Kwon, W., et al. 2013, ApJ, 769, L15
Straizys, V., Cernis, K., Kazlauskas, A., & Meistas, E. 1992, Baltic Astronomy, 1, 149
Strom, S. E., Vrba, F. J., & Strom, K. M. 1976, AJ, 81, 314
Stutz, A., Launhardt, R., Linz, H., et al. 2010, A&A, 518, L87
Stutz, A. M., Rubin, M., Werner, M. W., et al. 2008, ApJ, 687, 389
Takahashi, S., & Ho, P. T. P. 2012, ApJ, 745, L10
Takahashi, S., Ho, P. T. P., Tang, Y.-W., Kawabe, R., & Saito, M. 2009, ApJ, 704, 1459
Takahashi, S., Saigo, K., Ho, P. T. P., & Tomida, K. 2012, ApJ, 752, 10
Takakuwa, S., Saito, M., Lim, J., et al. 2012, ApJ, 754, 52

Tamura, M., Hough, J. H., Greaves, J. S., et al. 1999, ApJ, 525, 832

Tang, Y.-W., Ho, P. T. P., Koch, P. M., & Rao, R. 2010, ApJ, 717, 1262

Targon, C. G., Rodrigues, C. V., Cerqueira, A. H., & Hickel, G. R. 2011, ApJ, 743, 54

Tassis, K., Dowell, C. D., Hildebrand, R. H., Kirby, L., & Vaillancourt, J. E. 2009, MNRAS, 399, 1681

Terebey, S., & Padgett, D. L. 1997, in IAU Symposium, Vol. 182, Herbig-Haro Flows and the Birth of Stars, ed. B. Reipurth & C. Bertout, 507

Thompson, A. R., Moran, J. M., & Swenson, G. W., J. 2004, Interferometry and Synthesis in Radio Astronomy (2nd ed. New York: Wiley)

Tobin, J. J., Hartmann, L., Chiang, H.-F., et al. 2012, Nature, 492, 83

—. 2013a, ApJ, 771, 48

Tobin, J. J., Hartmann, L., Looney, L. W., & Chiang, H.-F. 2010, ApJ, 712, 1010

Tobin, J. J., Looney, L. W., Mundy, L. G., Kwon, W., & Hamidouche, M. 2007, ApJ, 659, 1404

Tobin, J. J., Hartmann, L., Chiang, H.-F., et al. 2011, ApJ, 740, 45

Tobin, J. J., Chandler, C. J., Wilner, D. J., et al. 2013b, ApJ, 779, 93

Tomisaka, K. 2011, PASJ, 63, 147

Torres, R. M., Loinard, L., Mioduszewski, A. J., & Rodríguez, L. F. 2009, ApJ, 698, 242

Turner, J. L., & Welch, W. J. 1984, ApJ, 287, L81

Turner, N. J., Sano, T., & Dziourkevitch, N. 2007, ApJ, 659, 729

Vaillancourt, J. E. 2006, PASP, 118, 1340

Vallée, J. P., & Fiege, J. D. 2006, ApJ, 636, 332

van der Tak, F. F. S., Tuthill, P. G., & Danchi, W. C. 2005, A&A, 431, 993

Vázquez-Semadeni, E., Banerjee, R., Gómez, G. C., et al. 2011, MNRAS, 414, 2511

Viotti, R. 1969, Ap&SS, 5, 323

Visser, A. E., Richer, J. S., & Chandler, C. J. 2002, AJ, 124, 2756

Volgenau, N. H. 2004, PhD thesis, University of Maryland, College Park, Maryland, USA

Wang, Y., Beuther, H., Zhang, Q., et al. 2012, ApJ, 754, 87

Wang, Y., Zhang, Q., Rathborne, J. M., Jackson, J., & Wu, Y. 2006, ApJ, 651, L125

Watson, D. M., Bohac, C. J., Hull, C., et al. 2007, Nature, 448, 1026

Weinreb, S. 1998, in Microwave Symposium Digest, 1998 IEEE MTT-S International, Vol. 2 (Baltimore, MD: IEEE), 673

White, T. L., & Cogdell, J. R. 1973, Moon, 6, 235

Williams, J. P., Plambeck, R. L., & Heyer, M. H. 2003, ApJ, 591, 1025

Wilner, D. J., Reid, M. J., & Menten, K. M. 1999, ApJ, 513, 775

Wolf-Chase, G. A., Barsony, M., & O'Linger, J. 2000, AJ, 120, 1467

Wright, C. M. 2007, Ap&SS, 311, 47

Wu, J., Dunham, M. M., Evans, II, N. J., Bourke, T. L., & Young, C. H. 2007, AJ, 133, 1560

Wynn-Williams, C. G., Becklin, E. E., & Neugebauer, G. 1972, MNRAS, 160, 1

Wynn-Williams, C. G., Becklin, E. E., & Neugebauer, G. 1974, Astrophys. J., 187, 473

Wyrowski, F., Schilke, P., Walmsley, C. M., & Menten, K. M. 1999, ApJ, 514, L43

Xu, Y., Reid, M. J., Zheng, X. W., & Menten, K. M. 2006, Science, 311, 54

Yen, H.-W., Takakuwa, S., Ohashi, N., & Ho, P. T. P. 2013, ApJ, 772, 22

Yıldız, U. A., Kristensen, L. E., van Dishoeck, E. F., et al. 2012, A&A, 542, A86

Yun, J. L. 1996, AJ, 111, 930

Yun, J. L., & Clemens, D. P. 1994, ApJS, 92, 145

Zapata, L. A., Loinard, L., Su, Y.-N., et al. 2012, ApJ, 744, 86

Zapata, L. A., Rodríguez-Garza, C., Rodríguez, L. F., Girart, J. M., & Chen, H.-R. 2011, ApJ, 740, L19

Zhou, S., Evans, II, N. J., Koempe, C., & Walmsley, C. M. 1993, ApJ, 404, 232

Zhou, S., Evans, II, N. J., & Wang, Y. 1996, ApJ, 466, 296

Zhu, L., Zhao, J.-H., Wright, M. C. H., et al. 2013, ApJ, 779, 51